Antibunching und Protonentransfer: Abstandshaltende Photonen als Instrument chemischer Kinetik

Dissertation

zur Erlangung des Grades

des Doktors der Naturwissenschaften

der Naturwissenschaftlich-Technischen Fakultät III

Chemie, Pharmazie, Bio- und Werkstoffwissenschaften

der Universität des Saarlandes

von

Michael Vester

Saarbrücken

2016

Tag des Kolloquiums:	02.09.2016
Dekan:	Prof. Dr.-Ing. Dirk Bähre
Berichterstatter:	Prof. Dr. Gregor Jung
	Prof. Dr. Christoph Becher
	/
Vorsitz:	Prof. Dr. Gerhard Wenz
akad. Mitarbeiter:	Dr. Bernd Morgenstern

Danksagung

Zuallererst möchte ich mich bei einer Reihe Menschen bedanken, ohne deren Dazutun diese Arbeit in ihrer Form sicherlich nicht bestehen würde.

Ich danke vielmals Herrn Prof. Gregor Jung dafür, dass er mir die Chance gegeben hat, mich dieser Herausforderung zu stellen. Ich bin dankbar für die sehr gute Betreuung, die mir Herr Jung hat zukommen lassen. Dabei habe ich stets das Gefühl gehabt, ich könne ihn jederzeit um Rat und Unterstützung fragen, die ich dann auch erhalten habe. Dieses Verhalten habe ich immer sehr geschätzt und erachte ich als vorbildlich.

Mein Dank gilt auch Herrn Prof. Christoph Becher für stimulierende fachliche Diskussionen und den so geleisteten Beitrag zur Arbeit. Außerdem danke ich für die Übernahme der Zweitkorrektur dieser Arbeit.

Ich bin dankbar für die Aufnahme in die Arbeitsgemeinschaft von Herrn Jung. Dabei verwende ich das Wort Arbeits*gemeinschaft* bewusst, denn das gemeinschaftliche Miteinander zeichnet diesen Arbeitskreis aus. Nicht nur habe ich die fachliche Zusammenarbeit mit meinen Kollegen gemocht. Durch die entstandenen Freundschaften kam auch der Spaß nicht zu kurz. So möchte ich mich bei euch, den Mitgliedern des Arbeitskreises Jung für eine schöne Zeit bedanken und für eure Hilfsbereitschaft. Und dafür, dass immer mal wieder dem ein oder anderen der Schalk im Nacken saß, was sehr zur Erheiterung beigetragen hat.

Ich danke meiner ganzen Familie und bin dankbar für ihre Unterstützung, deren Wert ich nicht bemessen kann. Dabei danke ich vor allem meinen Eltern Doris und Dieter Vester, die mir stets ihre bestmögliche Unterstützung haben zukommen lassen und mich in meinen Vorhaben bestärken.
Meiner Schwester Lisa-Marie, meiner Tante Karina und meinem Onkel Ralf bin ich dankbar für ihre ermutigenden Worte und ihren Rat, der mich einige Dinge hat klarer sehen lassen.

Ein gewaltiges Dankeschön gilt meiner Freundin Sarah Essner. Sie hat mir immer mit ihrem Zuspruch, ihrem Rat und ihrer Hilfe zur Seite gestanden und mir so Rückhalt und Standfestigkeit gegeben. Ich habe auch durch sie gelernt, manche Dinge nicht allzu ernst zu nehmen. So hat sie einen entscheidenden Beitrag an der Verwirklichung meiner Vorstellungen.

Inhalt

0. Zusammenfassung

Die zeitliche Entwicklung von angeregten Zuständen molekularer Systeme wird standardmäßig durch zeitaufgelöste Experimente mit gepulster Anregung abgebildet. Dabei bleibt die Kinetik der Grundzustände im Verborgenen oder raffinierte Pump-Probe-Experimente werden erforderlich. Im Kern dieser Arbeit stehen das sogenannte Photon-Antibunching (Engl., abstandshaltende Photonen), ein reiner Quanteneffekt, und die Beobachtung, dass dieses Phänomen es erlaubt Ratenkonstanten einer chemischen Reaktion im elektronischen Grundzustand zu extrahieren. Die Analyse der Zerfallskonstante der Korrelationsfunktion 2. Ordnung, d.h. die Evaluation der Zeitabstände zwischen einzelnen Detektionsereignissen, wird auf den Photozyklus einer Photosäure angewandt. In wässriger, gepufferter Umgebung ergibt sich so die bimolekulare Ratenkonstante der Reprotonierung im Grundzustand. Im aprotischen Solvens ist der Zerfall der Korrelationsfunktion komplexer: Eine lange Zeitkomponente wird der diffusionskontrollierten Rückprotonierung durch Säuremoleküle zugeordnet. Aus dem langsamen Zerfall kann die Wahrscheinlichkeit bestimmt werden, mit der das Proton den Coulomb-Käfig des Anions verlässt. Eine zusätzliche, schnelle Komponente kann mit dem s.g. solvens-getrennten Ionenpaar assoziiert werden, die angibt, wie schnell Proton und Anion im Coulomb-Käfig rekombinieren. Die Experimente dieser Arbeit verdeutlichen, dass quantenoptische Experimente Rückschlüsse auf fundamentale Reaktionsmechanismen zulassen können.

The analysis of excited-states and their time-evolution require time-resolved experiments with pulsed excitation. Ground-state kinetics remain hidden or demand more sophisticated and challenging approaches such as pump-probe excitation schemes. Rate constants of a chemical reaction in the ground-state are extracted from the so-called photon antibunching, a purely quantum optical effect, which is the main-finding of this work. The decay time of the second-order correlation function, $g^{(2)}$, is analyzed, i.e. inter-photon arrival times are evaluated, in the context of the Förster-cycle of photoacids. The bimolecular rate constant of the ground-state reprotonation by buffer molecules is obtained in aqueous solution. In aprotic solvent, the decay of $g^{(2)}$ is more complex: The long-time component of the biexponential decay is associated with the diffusion-controlled reprotonation in the ground-state. Moreover, the separation yield of proton and base is obtainable from the long-time component. The additional, short-time component hints to the so-called solvent-separated ion-pair, which lasts for 3 ± 1 ns in agreement with TCSPC results. This work demonstrates that mechanistic conclusions can be drawn from the implemetation of quantum-optical experiments and that open chemical issues can be resolved.

1. Einleitung

„Der Spaß fängt erst an, wenn man die Regeln kennt. Im Universum aber sind wir momentan noch dabei, die Spielanleitung zu lesen.“

Die Worte Richard Feynmans verleihen dem Streben der Naturwissenschaft Ausdruck, Prozesse innerhalb der Natur zu analysieren und fundamentale Gesetzmäßigkeiten, denen sie gehorchen, zu ergründen. In der Chemie gehört es zu den großen Herausforderungen, Reaktionsmechanismen ganzheitlich aufzuklären. So wurden bereits chemische Reaktionen auf Einzelmolekülniveau analysiert. Dabei wurden meist Änderungen der Fluoreszenzwellenlänge oder der Fluoreszenzintensität evaluiert.[1–8]

Zu den fundamentalen Reaktionstypen der Chemie zählt die Übertragung eines Protons. Die Protonenübertragung in Lösung spielt eine elementare Rolle in der Biologie, so in der Enzymkatalyse[9], dem Ansteuern von Ionenkanälen[10,11] oder der ATP Synthese[12]. Diese Beispiele sollen die Notwendigkeit weiter verdeutlichen, ein umfassendes Verständnis von Protonentransferreaktionen in Lösung zu erlangen.

Sogenannte Photosäuren, eine Klasse von Verbindungen, deren Charakteristikum eine mitunter beträchtliche Erhöhung der Säurestärke nach optischer Anregung ist,[13–15] eröffnen nicht nur die Möglichkeit der spektroskopischen Analyse des Protonentransfers.[16–19] Ferner erlauben sie die gezielte Freisetzung eines Protons und damit die Kontrolle des Startzeitpunktes der Protonenübertragung.[20,21] Der Protonentransfer im angeregten Zustand eines Moleküls wird ESPT genannt (Engl., Excited-State Proton Transfer).

Um 1950 untersuchte Theodor Förster den Protonentransfer der Photosäure HPTS (8-Hydroxypyren-1,3,6-trisulfonat, Pyranin) in Wasser mit stationärer Fluoreszenzspektroskopie.[22,23] Er beobachtete eine starke Verschiebung des Fluoreszenzlichts zu höheren Wellenlängen hin. Diese Rotverschiebung setzte er mit der Änderung der Säurestärke in Relation, d.h. mit der Änderung der pK_s Werte in Grund- und angeregtem Zustand. Damit war er als erster imstande das Phänomen der Photoazidität zu beschreiben.

Die Verwendung ausgeklügelter Verfahren mit hoher Zeitauflösung ermöglichte es, Prozesse, die auf die Photoanregung folgen, zu identifizieren und zu studieren – bis herab in die fs-Domäne.[24] So wurden verschiedene Klassen von Photosäuren mit fs-Pump-Probe,[14,25,26] Fluoreszenz Upconversion,[27–31] und zeitkorreliertem Einzelphotonenzählen[32,33] untersucht. Entsprechende Experimente wurden in einer Vielzahl verschiedener Lösemittel durchgeführt, darunter hauptsächlich protisch-polare, nämlich Wasser, Wasser-Alkohol-Mischungen[34] und Alkoholen verschiedener Kettenlänge[35]. Weniger Studien wurden in aprotischen

Lösungsmitteln wie DMSO[17,36,37] (Dimethylsulfoxid) vorgenommen. Alles in allem konnten intermediäre Spezies nachgewiesen werden, die nach optischer Anregung entstehen und die zerfallen noch bevor die zur Photosäure konjugierte Base im angeregten Zustand gebildet wird.[17,21,38–42]

Den ultraschnellen Methoden ist gemein, dass die Analytmoleküle initial in ihrem angeregten Zustand präpariert werden. Während der Messung wird dann die zeitliche Entwicklung der Potentialfläche des angeregten Zustandes erfasst. Dadurch ergibt sich zwangsläufig, dass Informationen über Prozesse im Grundzustand durch solche Methoden nur schwer zugänglich sind.[43,44]

In der vorliegenden Arbeit wird gezeigt, dass sich diese Lücke durch die Analyse des sogenannten Antibunchings, eines rein quantenoptischen Phänomens im Zusammenhang mit der Emissionscharakteristik einzelner Emitter,[45–47] schließen lässt. Ein Maß für das Antibunching ist die Korrelationsfunktion 2. Ordnung, kurz $g^{(2)}$.[48,49] Diese steht in diesem Kontext für die bedingte Wahrscheinlichkeit, ein Photon zu einem Zeitpunkt $t + \tau$ zu detektieren, nachdem zuvor ein Photon zu einem bestimmten Zeitpunkt t nachgewiesen wurde. Durch die Emission des „Startphotons“ werden die Moleküle in ihrem Grundzustand präpariert. Dann wird die Zeit τ bestimmt, die bis zur Detektion eines weiteren Photons der gleichen Energie verstreicht.[49,50] Dadurch, dass stets ein kompletter Photozyklus während einer solchen Messung durchlaufen wird, ist sämtliche Zeitinformation in der Zeitkonstante des Antibunchings enthalten. So werden Spezies fassbar, die während der Rückprotonierung im Grundzustand erzeugt werden und ihre Zerfallskonstanten bestimmbar.[51]

Einerseits wird das Emissionsverhalten einer Photosäure auf Pyrenbasis in gepufferter, wässriger Umgebung untersucht. Dabei wird ein monoexponentieller Zerfall von $g^{(2)}$ auf der ns-Zeitskala festgestellt. Durch eine Messreihe, bei der die Pufferkonzentration variiert wird, kann aus der Zerfallskonstante die bimolekulare Ratenkonstante für die Rückprotonierung der Base im Grundzustand extrahiert werden. Diese stimmt mit literaturbekannten Werten überein. Mit der neuartigen Ausnutzung des Antibunching Phänomens werden andererseits die Messungen mit mehreren pyrenolbasierten Photosäuren im aprotischen Solvens DMSO durchgeführt. Dabei soll zunächst die entsprechende bimolekulare Reprotonierungsrate bestimmt werden. Wider Erwarten zeigt $g^{(2)}$ einen biexponentiellen Zerfall mit langer und kurzer Zeitkomponente. Der kurze Zerfall wird mit dem sogenannten solvensgetrennten Ionenpaar (SSIP, engl. solvens separated ion pair) assoziiert, welches in wässriger Lösung, bedingt durch die wesentlich höhere Protonenmobilität, nicht gesehen wird. Der lange Zerfall entspricht der Bildung des SSIP aus der freien Base (FSIP, engl. fully separated ion pair). Ferner

können chemische Bedingungen etabliert werden, sodass der lange Zerfall nicht länger von der applizierten Anregungsrate abhängt. Dieser Sachverhalt wird durch ein Modell erklärt werden, in dem die Bildung des FSIP im angeregten Zustand und der Zerfall des FSIP im Grundzustand von den übrigen Prozessen im Photozyklus entkoppelt werden. Diffusive und nicht-diffusive Prozesse sind dann voneinander separiert.[52]

2. Protonentransfer

2.1 Das Phänomen der Photoazidität

Von photoaziden Molekülen wird gesprochen, wenn diese nach optischer Anregung eine Erhöhung ihrer Azidität erfahren, d.h. sich der pK_s beim Übergang vom Grund- in den angeregtem Zustand, im angeregten Zustand wird von pK_s^* gesprochen, signifikant ändert.[53] Diese Änderung kann viele Größenordnungen betragen. So ist $\Delta pK_s = pK_s^* - pK_s \approx 6$ im Falle des Moleküls HPTS (8-Hydroxypyren-1,3,6-trisulfonat, Pyranin, vgl. Abbildung 3).[54]
Der pK_s^* bzw. die Säurekonstante K_s^* ist dabei über das Protolysegleichgewicht der angeregten Zustände ROH^* und RO^{-*} definiert (vgl. Abbildung 1, Glg. (1)).[55] Dabei bewegt sich das Proton im attraktiven Coulomb-Potential V(r) des Anions. k_{espt} ist die Ratenkonstante des ESPT, k_{gr} die der Rückreaktion.

$$ROH^* \underset{k_{gr}}{\overset{k_{espt}}{\rightleftharpoons}} RO^{-*} + H^+$$

Abbildung 1: Zur Definition des pK_s^*.

$$K_s^* = \frac{k_{espt}}{k_{gr}} \cdot e^{V(r)} \qquad (1)$$

Als Modell zur Erklärung der bathochromen Verschiebung im Fluoreszenzlicht von HPTS entwickelte Theodor Förster ein zyklisches Schema, für das sich heute gemeinhin die Bezeichnung Förster-Schema oder Förster-Zyklus etabliert hat.[22,23] In diesem sind die Prozesse zusammengefasst, die auf die Anregung folgen (Abbildung 2 a)). Vom Grundzustand ROH aus gelangt das Molekül in den ersten angeregten Zustand ROH^*. Von dort wird ein Proton abstrahiert. Die assoziierte Ratenkonstante k_{espt} kann für bestimmte Pyrenolderivate um $2.5 \cdot 10^{11}$ s^{-1} in Wasser betragen und ist damit i.d.R. die größte Ratenkonstante im System.[31] Für bestimmte Super-Photosäuren werden ESPT Ratenkonstanten um $1.2 \cdot 10^{13}$ s^{-1} gemessen.[30,56] Ebenso wird ROH^* mit $k_{f,ROH}$, welches um $2 \cdot 10^8$ s^{-1} liegt,[57] entvölkert. Ein hohes Verhältnis $k_{espt}/k_{f,ROH}$ lässt sich durch das Fehlen einer ROH-Bande im Fluoreszenzspektrum (Abbildung 2c)) erkennen und auf einen sehr effizienten ESPT schließen. Folglich wird in sehr guter Näherung ROH^* alleine durch den ESPT depopuliert. Die korrespondierende Base RO^{-*} kann durch die Aufnahme des gleichen Protons geminant rekombinieren (vgl. Abbildung 2 a)). Die

entsprechende Rate k_{gr} in Glg. (1) kann über den pK_s^* und k_{espt} durch $pK_s^* = k_{espt}/k_{gr}$ auf $4 \cdot 10^8$ s^{-1} geschätzt werden.[31] Die korrespondierende Base RO^{-*} gelangt alternativ unter der Aussendung eines Fluoreszenzsphotons mit k_f in ihren Grundzustand RO^-. RO^- wird mit der Ratenkonstanten k_p reprotoniert; dieser Prozess schließt den Förster-Zyklus. Unter bestimmten experimentellen Bedingungen spielen die in Abbildung 2 a) grau dargestellten Prozesse eine unwesentliche Rolle. Wichtig dafür ist ein pH-Wert, der so gewählt ist, dass das Grundzustandsgleichgewicht auf die ROH Seite geschoben wird. Gleichzeitig soll das Protolysegleichgewicht auf RO^{-*} Seite liegen. Folglich muss $pK_s^* << pH << pK_s$ gelten.

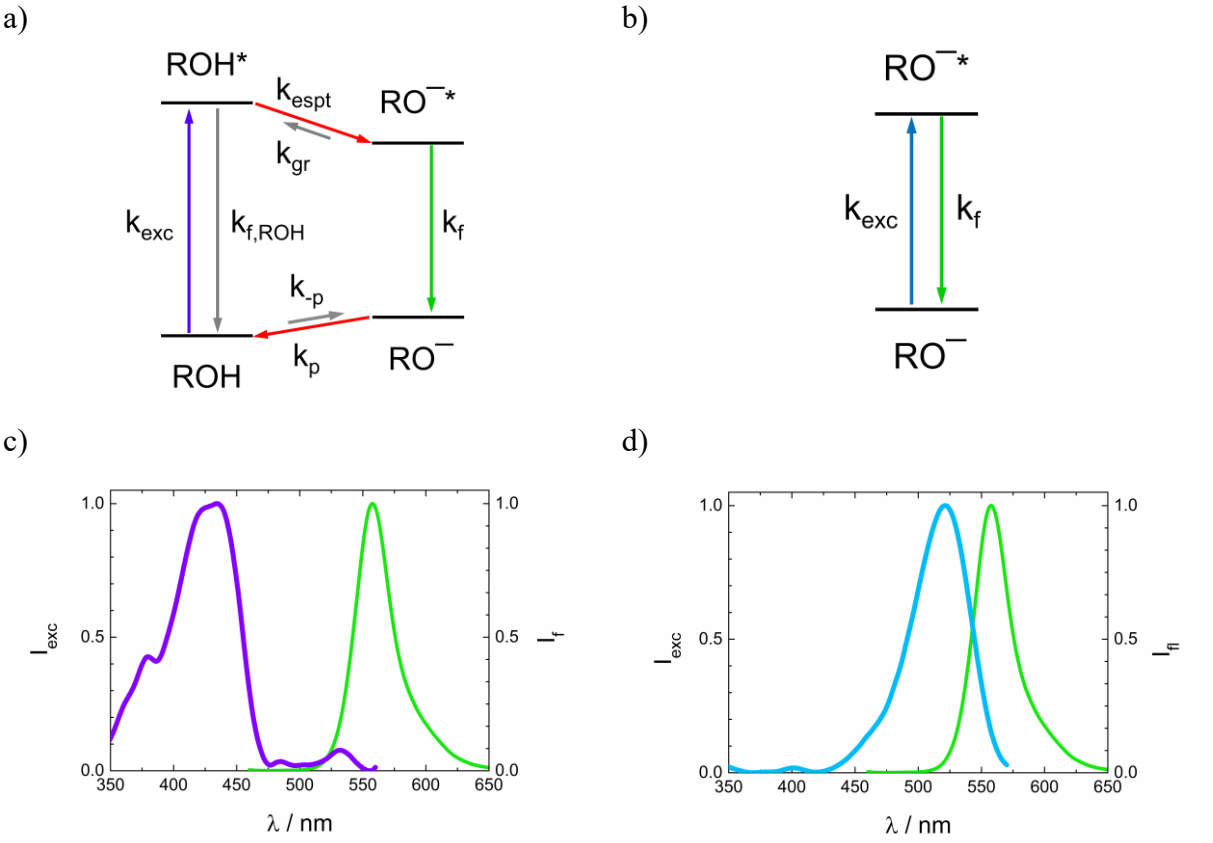

Abbildung 2: Zur spektroskopischen Charakterisierung von Photosäuren.
a) Förster-Zyklus einer Photosäure für $pK_s^* < pH < pK_s$. b) Niveauschema einer Photosäure für $pH >> pK_s$.
c) Anregungsspektrum und Emissionsspektrum der Photosäure bei $pK_s^* < pH < pK_s$.
d) Anregungsspektrum und Emissionsspektrum der Photosäure bei $pH >> pK_s$.

Die Verschiebung zwischen 0-0-Übergang der Säure und 0-0-Übergang der Base ist dabei ein direktes Maß für die Zunahme der Säurestärke nach der optischen Anregung (Glg. (2)).[55,58,59]

$$\Delta pK_s = \frac{h(\upsilon_{ROH} - \upsilon_{RO^-})}{k_B T \cdot \ln(10)} \qquad (2)$$

2.2 Strukturmerkmale und Ursprung der Photoazidität

Strukturmerkmal aller photoaziden Moleküle ist ein aromatisches Ringsystem, an das eine Gruppe mit azidem Proton, hier eine Hydroxylfunktion, kovalent gebunden ist.[53,60,61] Der einfachste Vertreter dieser aromatischen Alkohole ist das Phenol (P) mit $pK_s = 9{,}8$ und $pK_s^* = 4{,}0$ (vgl. Abbildung 3).

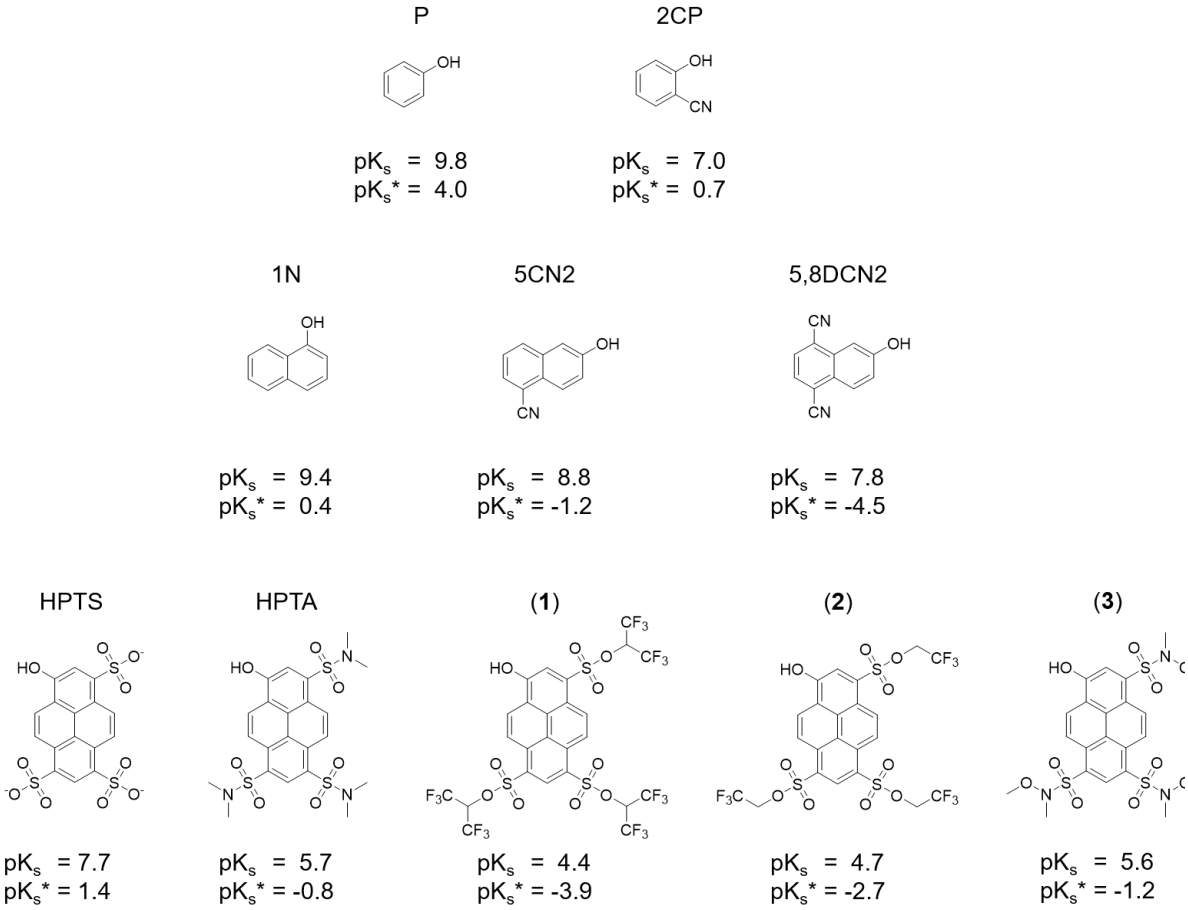

Abbildung 3: Photosäuren auf der Basis aromatischer Alkohole.
Phenol (**P**)[62], 2-Cyano-Phenol (**2CP**)[63],
1-Naphthol (**1N**)[64], 5-Cyano-2-Naphthol (**5CN2**)[13], 5,8-Dicyano-2-Naphthol (**5,8DCN2**)[13],
8-Hydroxypyren-1,3,6-Trisulfonat (**HPTS**)[65], 8-Hydroxypyren-1,3,6-Trisulfonamid (**HPTA**)[57],
Tris(1,1,1,3,3,3-Hexafluorpropan-2-yl)-8-Hydroxypyren-1,3,6-Trisulfonat (**1**)[57], Tris-(2,2,2-Trifluorethyl)-8-Hydroxypyren-1,3,6-Trisulfonat (**2**)[57], 8-Hydroxy-N,N′,N″-Trimethoxy-N,N′,N″-Trimethylpyrene-1,3,6-Trisulfonamid (**3**)[57].

Durch die Einführung von elektronenziehenden Gruppen wie der Cyano-Funktion, -CN, oder Sulfonatfunktionen lassen sich die Säurestärken K_s und K_s^* erhöhen (2-Cyanophenol, 2CP).[62,63] Mit dem einfachsten kondensierten aromatischen Alkohol, dem Naphthol (2N), lassen sich durch zwei Cyano-Substituenten (5,8-Dicyanonaphthol, kurz 5,8DCN2) bereits Säurestärken im angeregten Zustand erzielen, die mit Säurestärken starker Mineralsäuren vergleichbar sind.[55]

Da diese Cyanonaphthole azide genug sind, um organische Lösungsmittel zu protonieren, konnte erstmals der Protonentransfer in nicht-wässrigen Lösungsmitteln wie diversen Alkoholen sowie im aprotischen Lösemittel DMSO untersucht werden.[66]

Der Elektronendruck bzw. –zug eines Substituenten auf das aromatische System wird mit dem sogenannten Hammet-Koeffizienten σ erfasst. Der Elektronenzug ist umso höher, je größer der Hammet-Koeffizient σ ist. Prémont-Schwarz et al.[67] haben Derivate von 1-Naphthol mit unterschiedlichen Substituenten an 5. Stelle hinsichtlich des pK_s und des pK_s^* Wertes untersucht und sind dabei auf Zusammenhänge gestoßen, die in Abbildung 4 dargestellt sind. Es ist eine lineare Abhängigkeit der Säurestärken in Grund- und angeregtem Zustand vom Hammet-Koeffizienten zu verzeichnen. Dabei fällt die Erhöhung der Azidität mit zunehmendem σ im angeregten Zustand merklicher aus (vgl. Tabelle 1).

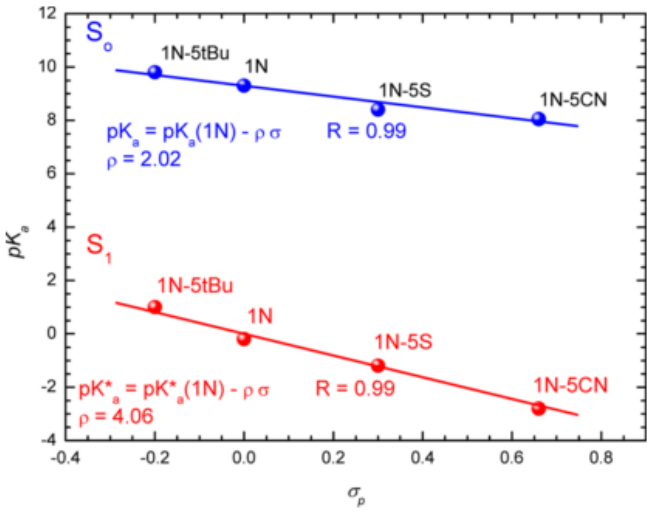

Abbildung 4: Säurestärke und Hammet-Koeffizient.
Abhängigkeit der Säurestärken verschieden 5-substituierter Naphthole vom Hammet-Koeffizienten σ des Substituenten.[67]
Reprinted with permission from M. Prémont-Schwarz, T. Barak, D. Pines et al., *J. Phys. Chem. B*, 2013, **117**, 4594-4603. Copyright 2013 American Chemical Society.

Tabelle 1: 5-substituierte Naphthole und pK_s-Werte.[67]

	1N	1N-5tBu	1N-4S	1N-5S	1N-3,6diS	1N-5CN
	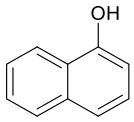	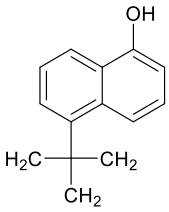	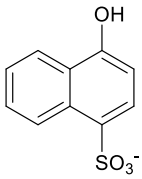	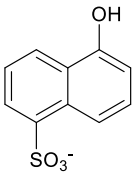	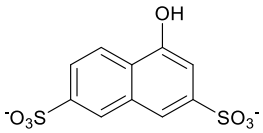	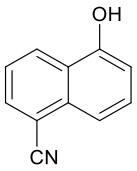
pK_s	9.4	9.8	8.3	8.4	8.6	8.05
pK_s^*	-0.2	1.0	-0.1	-0.7	-2.6	-2.8

Ursachen für die Photoazidität können sowohl auf der Eduktseite als auch auf der Produktseite des ESPT gefunden werden. Weller[68] führte 1952 stationär-spektroskopische Studien an verschiedenen Naphtholen durch und war der erste, der einen n-π*-Ladungstransfer vom Hydroxylsauerstoff in das aromatische System nach Anregung in S_1 postulierte. Die dadurch geschwächte OH-Bindung würde die Abstraktion des Protons dann begünstigen und zu einem niedrigeren pK_s^* führen. Agmon et al. wiesen durch differenzielle Solvatochromie[55] an 2-Naphthol ein Erstarken der Wasserstoffbrückenbindung zwischen Proton und Solvensmolekül nach. Dafür wurde eine Positivierung des Hydroxylsauerstoffs im angeregten Zustand als ursächlich angesehen, welche durch unabhängige semiempirische Verfahren[69] gezeigt wurde. Weitere ab initio Rechnungen[70] in Bezug auf Wasser-Phenol Cluster weisen auf eine Verkürzung und damit auf ein Erstarken der ROH---S Bindung hin.

Für das Photoprodukt, also die anionische Base, lässt sich durch differenzielle Solvatochromie eine signifikante Elongation der Wasserstoffbrückenbindung, der RO^----HS^+ Bindung, verzeichnen.[55] Dies wird auf eine deutlich reduzierte Ladung am Hydroxylsauerstoff zurückgeführt und dadurch ein entsprechender n-π*-Ladungstransfer auf anionischer Seite belegt.

Grundsätzlich kann auch von einem produktseitigen Ladungstransfer ausgegangen werden.[16] Zum einen liefern die bereits o.g. semiempirischen Verfahren einen deutlichen Beleg dafür. Hier zeigt sich (Abbildung 5), dass im Falle der Base durch Photoanregung ein deutlich höherer Ladungsbetrag in den distalen Ring transferiert wird als dies bei der Säure der Fall ist. Ein weiter empirischer Beleg für produktseitigen Ladungstransfer ist schließlich die Reduktion der pK_s-Werte, insbesondere des pK_s^*, durch die Einführung elektronenziehender Substituenten an den Positionen 5 und 8. Dadurch wird die negative Mulliken-Ladung an den jeweiligen Kohlenstoffatomen gesenkt und so das Molekül thermodynamisch stabilisiert.[55] So wird im

Falle von 5,8DCN ein um gut vier logarithmische Einheiten kleinerer pK_s^* erreicht, verglichen mit dem 2N.

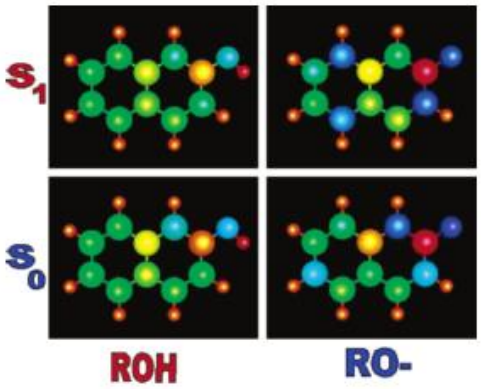

Abbildung 5: Elektronendichteverteilung in 2-Naphthol.[55]
Je röter, desto größere positive Partialladung, grün ist neutral, je blauer desto größere negative Partialladung.
Reprinted with permission from N. Agmon, *J. Phys. Chem. A*, 2005, **109**, No. 1, 13-35. Copyright 2005 American Chemical Society.

Gerade in Bezug auf die photoaziden Pyrenolderivate wurde ein der Protonenabstraktion vorausgehender Ladungstransfer als Ursache ihrer Säurestärke im angeregten Zustand ausgemacht.[71] Zusätzlich spielt für neutrale pyrenolbasierte Photosäuren der elektronische Zustand, in den das Molekül angeregt wird, eine übergeordnete Rolle. So ist das elektrische Dipolmoment des Moleküls signifikant größer, wenn es in den s.g. ^1L_a Zustand promoviert wird.[72] Im ^1L_a Zustand liegt das Dipolmoment parallel zur Längsachse des Pyrenolgrundgerüstes (vgl. Abbildung 6).[73] Ob das Molekül protoniert oder deprotoniert vorliegt, spiele dann eine untergeordnete Rolle.[72]

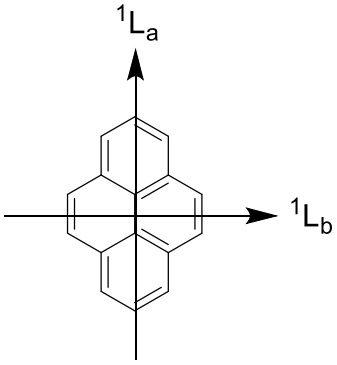

Abbildung 6: ^1L_a und ^1L_b Zustände des Pyrens.

2.3 Protonentransfer in Lösung: Kinetische Betrachtung

Abbildung 7 zeigt Fluoreszenzzerfälle des Pyrenolderivats HPTA in DMSO.[57]

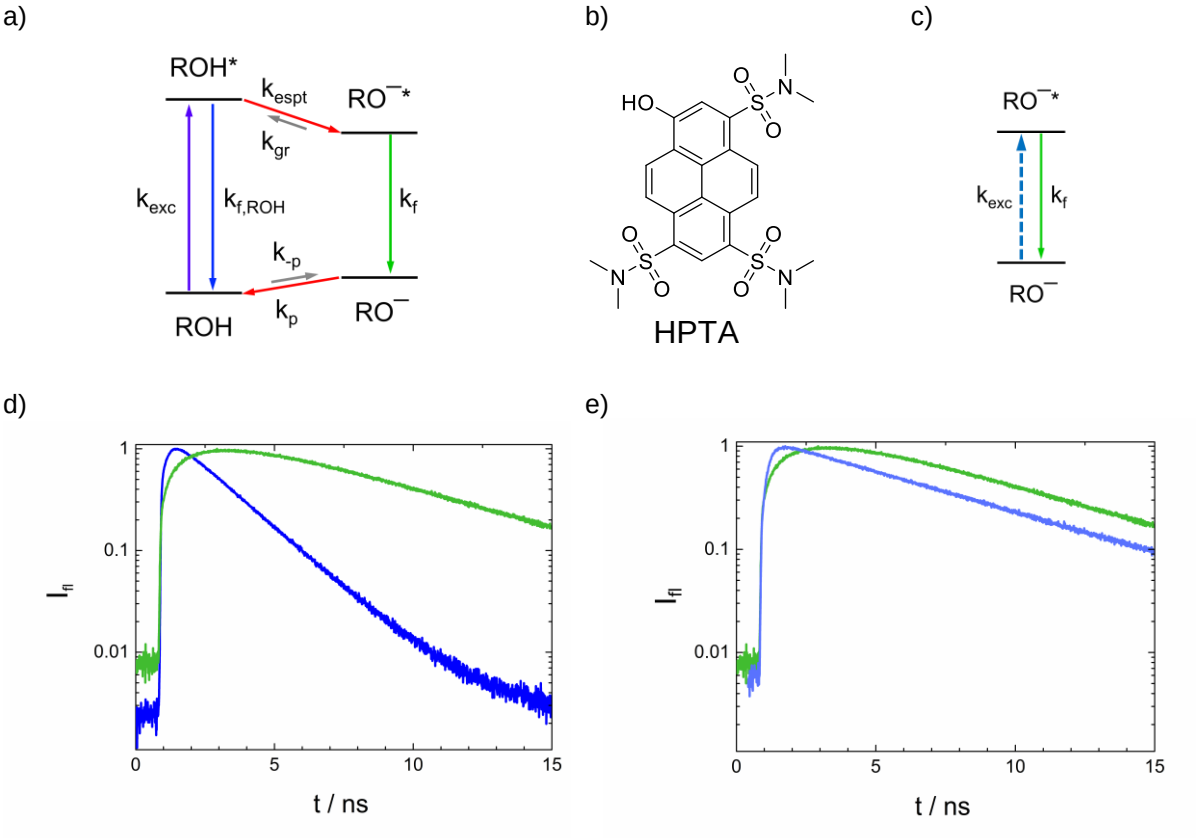

Abbildung 7: Zur Kinetik des ESPT einer mittelstarken Photosäure.
a) Förster-Zyklus einer Photosäure in angesäuertem DMSO.
b) HPTA
c) Niveauschema einer mittelstarken Photosäure in reinem DMSO.
d) Fluoreszenzzerfall von HPTA in angesäuertem DMSO. Anregung der ROH Form mit 405 nm und Detektion der ROH Fluoreszenz (blaue Kurve). Anregung der ROH Spezies und Detektion der RO^- Spezies (grüne Kurve).
e) Fluoreszenzzerfall von HPTA in DMSO. Anregung der ROH Spezies und Detektion der RO^- Spezies (grüne Kurve) verglichen mit Anregung von RO^- und Detektion der RO^- Fluoreszenz (hellblaue Kurve). d)-e) Datengenerierung durch C. Spies.

In Abbildung 7 d) sind Zerfälle dargestellt, die durch Anregung der Säurebande mit 405 nm (20 MHz) und der Detektion mit 470/40 nm (Säurebande) erhalten werden (blaue Kurve). Im Bereich weniger Nanosekunden weist die ROH-Fluoreszenz einen monoexponentiellen Zerfall mit der Zerfallskonstanten $k_{Säureform} = k_{f,ROH} + k_{espt} \approx 1/1.8\ ns^{-1}$ auf. Zu höheren Zeiten zeigt sich eine weitere Zerfallskomponente. Diese wird durch die geminante Rekombination mit der Ratenkonstante k_{gr} im angeregten Zustand verursacht, die zu der Population von ROH^* einen Beitrag liefert.[57]

a)

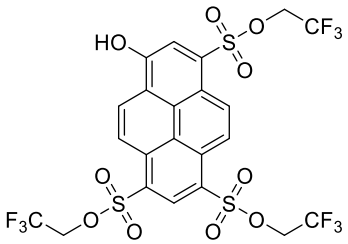

(**2**)

b)

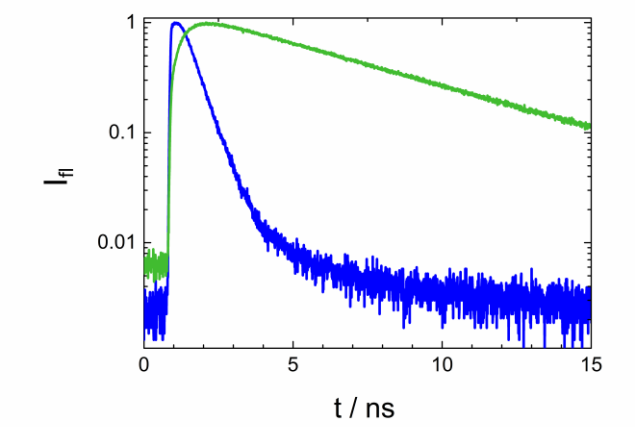

c)

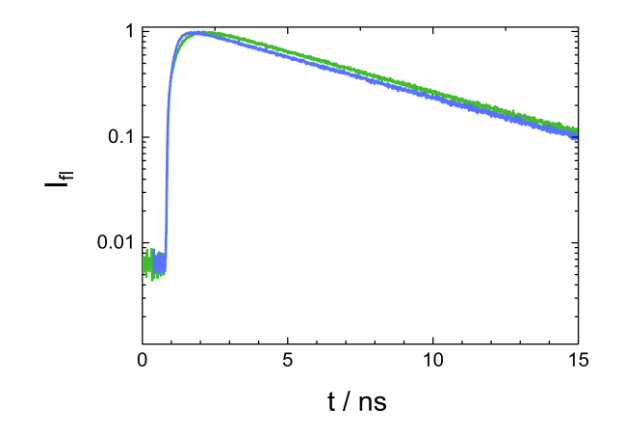

d)

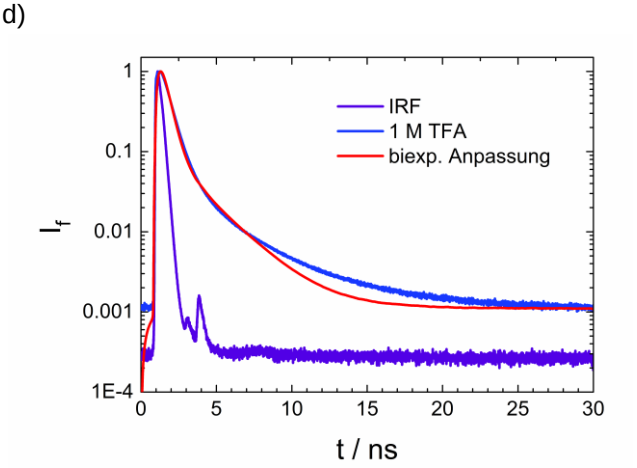

e)

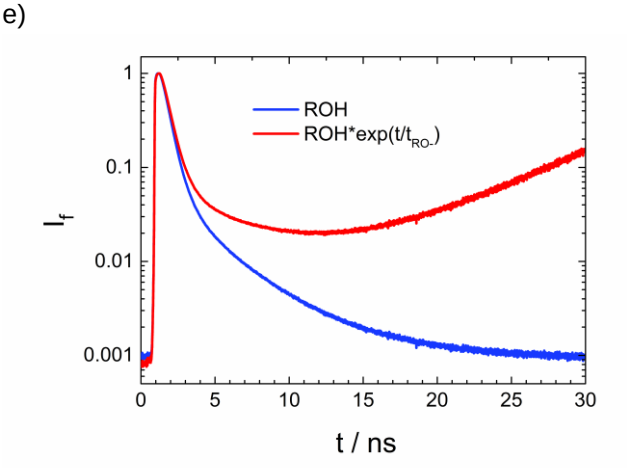

Abbildung 8: Kinetik des ESPT einer starken Photosäure.
a) (**2**)
b) Fluoreszenzzerfall von (**2**) in angesäuertem DMSO. Anregung der ROH Form mit 405 nm und Detektion der ROH Fluoreszenz (blaue Kurve). Anregung der ROH Spezies und Detektion der RO^- Spezies (grüne Kurve).
c) Fluoreszenzzerfall von (**2**) in DMSO. Anregung der ROH Spezies und Detektion der RO^- Spezies (grüne Kurve) verglichen mit Anregung von RO^- und Detektion der RO^- Fluoreszenz (hellblaue Kurve).
d) Zerfall der ROH-Fluoreszenz in DMSO mit 1 M TFA (blaue Kurve). Zu höheren Zeiten weicht der Zerfall vom biexponentiellen Verhalten ab (rote Kurve).
e) Die Abweichung wird deutlicher, wenn das ROH-Signal (blaue Kurve) mit dem Fluoreszenzzerfall der Base verrechnet wird (rote Kurve).
b)-c) Datengenerierung durch C. Spies. d)-e) Datengenerierung durch A. Grüter.

Im Fall von (**2**) ist der Fluoreszenzzerfall von ROH deutlich schneller (blaue Kurve, Abbildung 8 b)). Das ist auf die wesentlich höhere ESPT Ratenkonstante k_{espt} zurückzuführen, die mit dem deutlich niedrigeren pK_s^* einhergeht. Auch hier ist die geminante Rekombination erkennbar, deren Ratenkonstante k_{gr} bei höheren TFA Konzentrationen (TFA: Trifluoressigsäure) (Abbildung 8 d)) signifikant größer ist. Besonders deutlich wird die Abweichung des Zerfalls der ROH Fluoreszenz vom eigentlich biexponentiellen Verhalten, wenn der Zerfall mit $\exp(-t/\tau_f)$ multipliziert wird (Abbildung 8 e)). Dabei ist $\tau_f = 5.6$ ns die Fluoreszenzlebensdauer der Base.[65,74–77]

Den zeitlichen Verläufen der ROH Fluoreszenz sind in Abbildung 7 d) und Abbildung 8 b) die Zerfälle der RO^- Fluoreszenz gegenübergestellt, die nach der Anregung von ROH erhalten werden. Diese Zerfälle verlaufen biexponentiell, mit ansteigender und fallender Komponente. Die kurze, ansteigende Komponente kann der Bildung von RO^- mit der Ratenkonstante k_{espt} zugeordnet werden. Die längere, abfallende Komponente liefert die Fluoreszenzlebensdauer des Anions, τ_f, als Zerfallskonstante.[31,57]

Die in Abbildung 7 e) und Abbildung 8 c) als hellblaue Kurven dargestellten Zerfälle werden durch Anregung der Photosäuren in DMSO mit 470 nm und der Detektion bei 583/120 nm erhalten (Emissionsbande der Base). Diese weisen keine ansteigende Komponente auf, wenn von der ansteigenden Komponente durch die Population von RO^- mit k_{exc} abgesehen wird. Der Zerfall liefert wieder die Lebensdauer der anionischen Spezies. Im Fall von (**2**) ist der Unterschied zwischen den RO^- Zerfällen nach ROH und RO^- Anregung geringer verlichen mit HPTA. Die Bildungsgeschwindigkeit von RO^- ist im Fall von (**2**) sehr groß, was ein weiteres Mal der deutlich höheren ESPT Ratenkonstante von (**2**) zuzuschreiben ist.

Bei der Verwendung von Methoden höherer Zeitauflösung, insbesondere fs-Pump-Probe Spektroskopie und Fluoreszenz-Upconversion, werden Reaktionsintermediate ausgemacht, deren Entstehung und Zerfall mitunter mehr als zwei Größenordnungen schneller verlaufen als die Emission aus den S_1 Zuständen.[78] Diese Experimente wurden in erster Linie an HPTS, HPTA und diversen Naphtholderivaten in protisch-polaren Lösungsmitteln, nämlich Wasser, Wasser-Alkohol-Mischungen und kurzkettigen Alkoholen durchgeführt. So hat sich ein wesentlich differenziertes Bild des Protonentransfers etabliert, das mit dem sogenannten Eigen-Weller Schema (Abbildung 9) kinetisch beschrieben wird.[17,21,38,41,60,79,80]

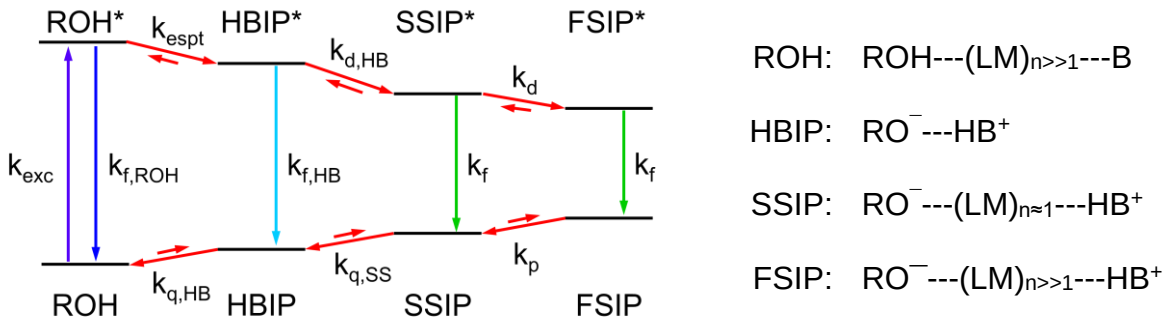

Abbildung 9: Eigen-Weller Schema: ein erweitertes kinetisches Modell.
Eigen-Weller Schema für ein beliebiges Lösungsmittel LM und ein beliebiges Akzeptormolekül B.

Im Eigen-Weller Bild verläuft die Reaktion von der Säure zur Base und umgekehrt stets über zwei weitere intermediäre Spezies, das HBIP (Engl. Hydrogen-Bonded Ion Pair) und das SSIP (Engl. Solvent-Separated Ion Pair). Im HBIP sind die anionische Base und das protonierte Akzeptormolekül HB^+ über eine Wasserstoffbrücke verbunden, ohne dass ein weiteres Solvensmolekül beteiligt wäre. Im SSIP sind Base und protonierter Akzeptor durch wenige Solvensmoleküle separiert, das Proton bewegt sich nach wie vor im zentralsymmetrischen Coulomb-Potenzial der Base.[60,74,79,81] Ist der FSIP Zustand (engl. Fully-Separated Ion Pair) erreicht, welcher im Förster-Bild der RO^- Spezies entspricht, sind Base und Proton vollständig separiert und bewegen sich unabhängig voneinander. Die Reprotonierung verläuft analog: RO^- und HB^+ diffundieren zueinander, bis sich die Coulomb'sche Wechselwirkung einstellt und das SSIP gebildet wird. Die Annäherung setzt sich fort, bis RO^- und H^+ über eine Wasserstoffbrücke verbunden sind. Schließlich folgt die Rekombination. Bildung und Zerfall von HBIP und SSIP sind dabei unimolekularer, die des FSIP bimolekularer Natur.

Konkret bildet sich im Fall von HPTS in Wasser das HBIP innerhalb bis zu 10 ps nach Anregung, nach weiteren ca. 30 ps das SSIP.[39,40] Der ESPT von (**1**) zu Wasser findet innerhalb

von ungefähr 3 ps statt, in Ethanol ist der ESPT derselben Verbindung bereits rund 60 mal langsamer.[31]

Obschon der Protonentransfer verschiedener Photosäuren in diversen protischen Lösungsmitteln im Fokus etlicher Studien stand,[29,55,78,81–85] wurden bisweilen weniger Anstrengungen unternommen, den Protonentransfers in aprotischen Lösungsmitteln zu untersuchen. Außerdem beschränken sich die zeitaufgelösten Studien meist auf die Kinetik der Intermediate im angeregten Zustand. Über die Rekombination des FSIP und des Intermediats SSIP in ihren Grundzuständen ist bislang wenig bekannt. Das Proton weist in DMSO einen Diffusionskoeffizienten von $D_{DMSO}(H^+) \approx 4.5 \cdot 10^{-6}$ cm² s^{-1} [86] und von $D_{H2O}(H^+) = 7 \cdot 10^{-5}$ cm² s^{-1} in Wasser[87] auf. Demnach ist anzunehmen, dass der Protonentransfer in aprotischem Solvens etwa eine Größenordnung langsamer abläuft als in protischen Lösungsmitteln. Durch die wesentlich geringere Protonenmobilität in DMSO ist im Besonderen der Zerfall des SSIP so verlangsamt, dass dieser im Grundzustand mit TCSPC Zählelektronik beobachtet werden kann.[52]

3. Abstandshaltende Photonen und Korrelationsfunktion

3.1 das Phänomen abstandshaltender Photonen (engl. Antibunching)

Zunächst wird von einem molekularen System ausgegangen, das lediglich zwei elektronische Zustände S_0 und S_1 einnehmen kann, das an einem Ort fixiert ist und das kontinuierlich angeregt wird (Abbildung 10 a)). Die Anregungsrate k_{exc} und die Fluoreszenzrate k_f führen zur Limitierung der maximalen Emissionsrate eines solchen Moleküls. Einzelne Photonen sind zeitlich separiert. Der Zeitabstand wird durch $\tau_{AB} = (k_{exc} + k_f)^{-1}$ bestimmt (Abbildung 10 b)).[88–90] Für dieses Phänomen abstandshaltender Photonen wird im Folgenden der aus dem Englischen stammende Begriff Antibunching verwendet. Das Antibunching rührt daher, dass im Fall einzelner Moleküle exakt ein Photon pro Photozyklus generiert wird und so nie zwei Photonen des gleichen Moleküls gleichzeitig erfasst werden.[45,46,48,91–95]

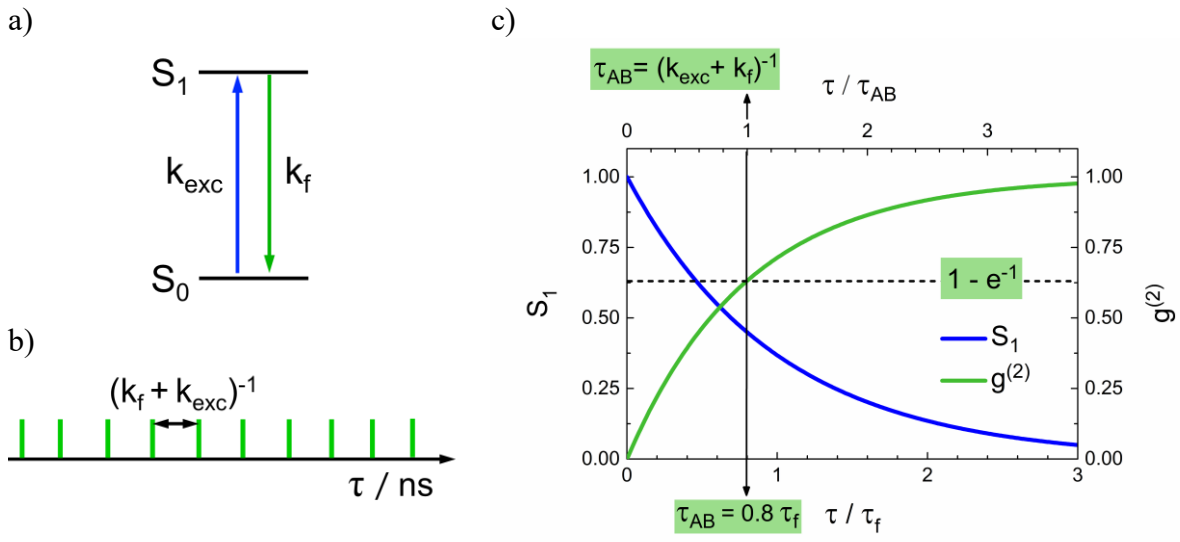

Abbildung 10: Zur Erklärung des Antibunchings.
a) Zwei-Zustandssystem mit Anregungsratenkonstante k_{exc} und Fluoreszenzratenkonstante k_f.
b) Photonenstrom eines Moleküls mit den Zuständen S_0 und S_1.
c) Vergleichende Darstellung der Besetzung des S_1 Zustandes und der Korrelationsfunktion 2. Ordnung $g^{(2)}$. Im vorliegenden Beispiel sei k_{exc} = 50 MHz und k_f = 200 MHz.

Antibunching ist ein inhärentes Charakteristikum einzelner Emitter, im Besonderen auch einzelner Atome, Quantenpunkte, Nanodiamanten und Kohlenstoffnanoröhren, und gilt als deren eindeutiger Nachweis.[47,49,96–99] Die absolute Amplitude des Antibunchings erlaubt es, Moleküle zu zählen.[100,101] Über die relativen Amplituden kann die Stöchiometrie in Komplexen bestimmt werden.[102] Die Zeitkonstante gibt Aufschlüsse über die Kinetik von Prozessen, so

über die Kinetik von exzitonischen Übergängen in Halbleiter-Quantenpunkten[99] und Nanodiamanten[103] oder über die FRET-Dynamik[104] und damit über die Faltungsdynamik von Proteinen[105].

Der experimentellen Erfassung dieses Phänomens dient das Konzept der Photonenkorrelation bzw. mathematisch der Korrelationsfunktion 2. Ordnung, kurz $g^{(2)}$.[48,49,99] In diesem Kontext ist $g^{(2)}$ ein Maß für die bedingte Wahrscheinlichkeit, nach der Detektion eines Photons zum Zeitpunkt t ein weiteres Photon zu einem späteren Zeitpunkt $t + \tau$ zu detektieren. Dabei entspricht $g^{(2)}$ der zeitlichen Besetzung des emittierenden Niveaus, normiert auf die stationäre Besetzung desselben Zustands (vgl. Abbildung 10 c)).[88,106] Für das ortsgebundene, kontinuierlich getriebene Zwei-Zustands-System ergibt sich Glg. (3).[88]

$$g^{(2)}(\tau) \equiv \frac{[S_1](\tau)}{[S_1(\infty)]} = 1 - e^{-(k_{exc}+k_f)\tau} \tag{3}$$

Nach Glg. (3) steigt die Chance, nach der Detektion eines Photons zum Zeitpunkt null das nachfolgende Photon zu detektieren, monoexponentiell an (Abbildung 10 c)). Ist die Zeit $\tau_{AB} = (k_{exc} + k_f)^{-1}$ verstrichen, wurde das zweite Photon mit einer Wahrscheinlichkeit von $1 - e^{-1} \approx 0.63$ detektiert, wenn von einer Detektionseffizienz von 100 % ausgegangen wird. Im vorliegenden Fall in Abbildung 10 beträgt k_{exc} 50 MHz, die Fluoreszenzrate belaufe sich auf 200 MHz. Dann ergibt sich $\tau_{AB} = 4\ \text{ns} < 5\ \text{ns} = \tau_f$.

Werden diffundierende Moleküle in Lösung konfokal beobachtet, ist die Wahrscheinlichkeit der zeitgleichen Besetzung des Beobachtungsvolumens mit mehr als einem Molekül verschieden von null. So führt die Detektion von Fluoreszenzphotonen verschiedener Emitter zum Zeitpunkt null zu $g^{(2)}(0) \neq 0$. Glg. (3) muss dann modifiziert werden:[88]

$$g^{(2)}(\tau) = \frac{1}{N}\left(1 - e^{-(k_{exc}+k_f)\tau}\right) \tag{4}$$

Die Detektion von unkorrelierten Untergrundphotonen führt ebenfalls zu einer Erhöhung von $g^{(2)}(0)$.[49,107] Über die $g^{(2)}$-Messung wurden so bereits Anregungsraten einzelner, diffundierender Rhodamin 6G Moleküle in Lösung bestimmt, welche sich bei niedrigeren Anregungsintensitäten (< 100 kW/cm²) als Zwei-Zustandssystem verhalten.[88] Durch Messen der Korrelationsfunktion 2. Ordnung oder höherer Ordnung lässt sich das Beugungslimit

mikroskopischer Systeme umgehen und hochauflösende Mikroskopie realisieren. Dies wurde sowohl mit konfokalen Systemen als auch Weitfeld-Mikroskopen umgesetzt.[100,108,109]

3.2 Beiträge anderer Fluktuationsquellen zur Korrelationsfunktion

Grundsätzlich werden durch $g^{(2)}$ sämtliche Prozesse erfasst, die zu zeitlichen Fluktuationen des Fluoreszenzlichts führen.[110,111] Neben dem Antibunching können im Falle frei diffundierender Moleküle die Diffusion,[112–114] die Rotation,[115] photophysikalische Prozesse wie Interkombinationsübergänge[90,94,97,116,117] und photochemische Reaktionen wie cis-trans-Isomerisierungen[118,119] zu Fluoreszenzfluktuationen führen (Abbildung 11). Das Bleichverhalten eines Fluorophors hat ebenfalls einen Einfluss auf die Korrelationsfunktion.[120]

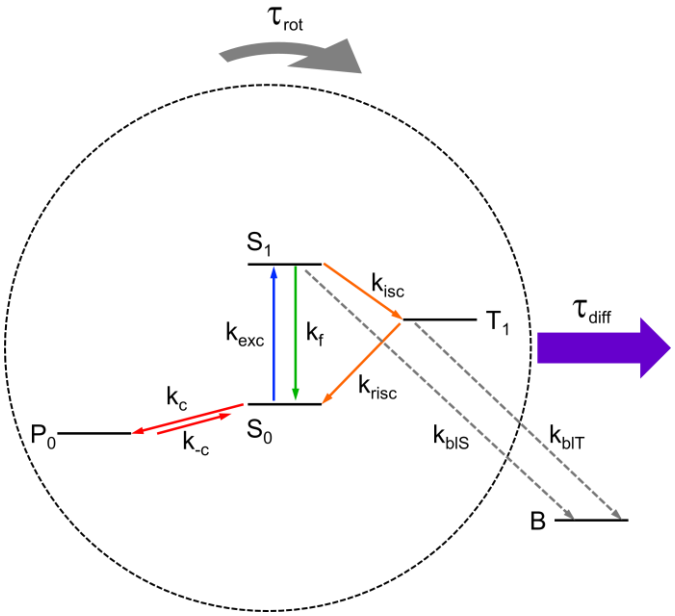

Abbildung 11: Allgemeine Darstellung eines Photozyklus und möglichen Fluktuationsquellen. Diffusion mit der Zeitkonstanten τ_{diff}, Rotation mit der Zeitkonstanten τ_{rot}, Interkombinationsübergänge vom S_1 in den Triplett Zustand T_1 mit k_{isc} und zurück (k_{risc}). Chemische Reaktion zum Produkt P_0 mit k_c und zurück mit k_{-c}. Der S_1 wird mit k_{exc} populiert, der Fluoreszenzzerfall wird wesentlich durch k_f bestimmt. Das Photobleichen führt aus dem S_1 mit k_{blS} bzw. aus dem T_1 mit k_{blT} irreversibel in den Dunkelzustand B.

Laufen nun diese Prozesse auf unterschiedlichen Zeitskalen ab, kann die Korrelationsfunktion des Systems als Produktfunktion der $g_i^{(2)}$'s dargestellt werden. Die respektiven $g_i^{(2)}$, d.h. die jeweiligen Prozesse, die zur korrelierten Photonenemission führen, gelten dann als separabel.[110]

$$g^{(2)} = \prod_i g_i^{(2)} = g_{bl}^{(2)} \cdot g_{diff}^{(2)} \cdot g_{Du}^{(2)} \cdot g_{AB}^{(2)} \cdot g_{rot}^{(2)} \tag{5}$$

Eine Korrelationsfunktion 2. Ordnung eines molekularen Systems mit verschiedenen Fluktuationsbeiträgen ist in

Abbildung 12 dargestellt. Die Zeitskalen, auf denen die zugrundeliegenden Prozesse ablaufen, können sich in der Praxis von Sekunden bis Nanosekunden erstrecken. Aus folgend genannten Gründen wird auf eine weitere Darstellung des Einflusses der Molekülrotation auf $g^{(2)}$ abgesehen. Erstens können Rotationszeiten kleiner Moleküle im Bereich weniger Pikosekunden[121] liegen, d.h. es gilt $\tau_{rot} << \tau_f$, sodass dann Fluktuationen aufgrund der Rotation keinen Einfluss auf $g^{(2)}$ haben. Zweitens sind Molekülrotationen in der Korrelationsfunktion dann nachweisbar, wenn im Emissionsstrahlengang eine bestimmte Polarisationsrichtung selektiert wird.[89] Dies wird hier experimentell nicht realisiert. Die übrigen Prozesse und ihre Einflüsse auf $g^{(2)}$ werden im Folgenden konkretisiert.

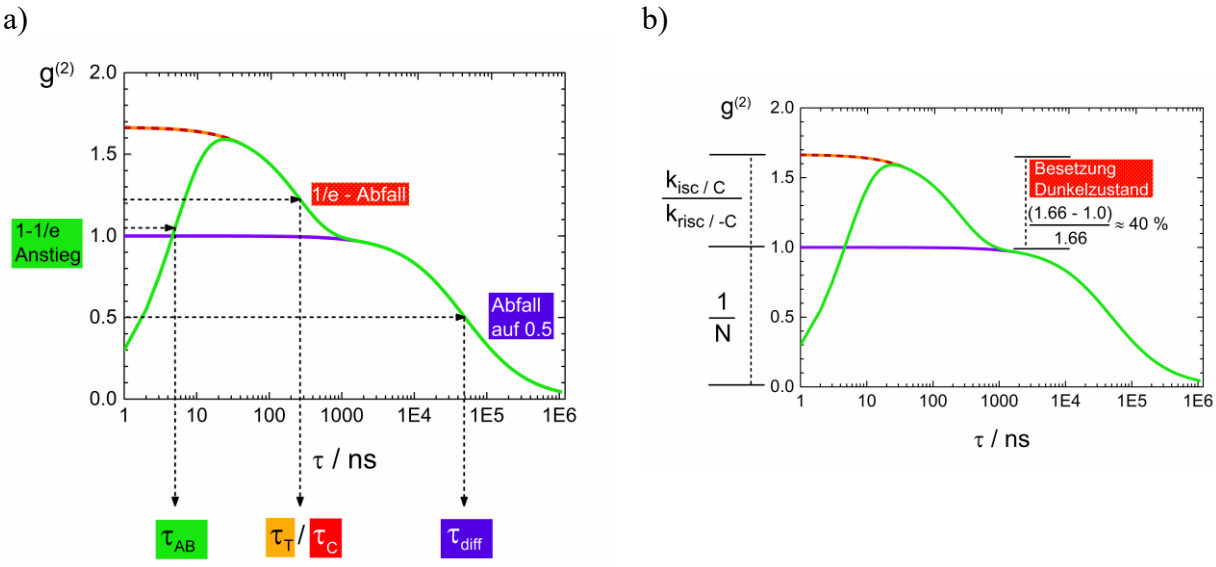

Abbildung 12: Der Einfluss verschiedener Fluktuationsquellen auf die Korrelationsfunktion.
a) Gesamte Korrelationsfunktion. Diffusion, schnelle Kinetik (ISC, chem. Reaktion) und Antibunching modulieren $g^{(2)}$. Jeder Prozess wird durch eine bestimmte Zeitkonstante charakterisiert. Diese liegen mitunter um mehrere Größenordnungen auseinander. Die Prozesse gelten dadurch als separabel.
b) Gesamte Korrelationsfunktion eines molekularen Systems. Die relativen Amplituden werden durch die effektive Teilchenzahl und die Ratenkonstanten der kinetischen Prozesse bestimmt.

3.2.1 Diffusion und Analyse der Photostabilität

Typische Farbstoffmoleküle weisen Diffusionskoeffizienten um $D \approx 3 \cdot 10^{-6}$ $cm^2 s^{-1}$ auf.[112] Ihre Diffusionszeiten durch einen beugungsbegrenzt fokussierten Laserstrahl, d.h. durch ein konfokales Volumen in der Größenordnung weniger Femtoliter, liegt damit im Bereich von 100 µs ($\tau_{diff} \approx 2\omega^2/4D$ [121]). Die Diffusion der Farbstoffteilchen in das bzw. aus dem Beobachtungsvolumen führt zu zeitlichen Konzentrationsänderungen und damit zu Fluktuationen im Fluoreszenzsignal. Diese führen wiederum zu einem hyperbolischen Abfall von $g^{(2)}$ nach Glg. (6).[122,123] Darin ist τ die Korrelationszeit und τ_{diff} die Zeit, für die $g^{(2)}(\tau_{diff}) = ½\, g^{(2)}(0)$ gilt. ω_0 entspricht dem minimalen Strahlradius und z_0 der Raygleigh-Länge. V_{eff} bezeichnet das effektive konfokale Volumen und $< C >$ die mittlere Teilchenkonzentration. Damit ist $V_{eff} \cdot < C >$ gerade die mittlere Besetzungszahl des Beobachtungsvolumens, diese entspricht der inversen Korrelationsamplitude $g^{(2)}(0)$ (vgl. Abbildung 12 b)). Die mittlere Diffusionszeit der Moleküle ergibt sich aus dem $g^{(2)}$-Abfall auf ½ (vgl. Abbildung 12 a)). Die Diffusionszeiten um 100 µs sind um mehrere Größenordnungen langsamer als die Fluoreszenzlebensdauer typischer Farbstoffe (um 1-10 ns). Folglich können solche Moleküle als stationär angesehen werden, während elektronische Übergänge stattfinden. Das durch die Diffusion bedingte Korrelationssignal (Glg. (6)) kann dann isoliert analysiert werden (violette Kurve in Abbildung 12 a), b)).[123]

$$g_{diff}^{(2)} = \frac{1}{V_{eff}\langle C\rangle} \cdot \frac{1}{1+\frac{\tau}{\tau_{diff}}} \cdot \frac{1}{\sqrt{1+\left(\frac{\omega_0}{z_0}\right)^2 \frac{\tau}{\tau_{diff}}}} \quad [123,122] \tag{6}$$

Gleichung (6) kann zu Gleichung (7) reduziert werden, falls die rückseitige Objektivapertur nur partiell ausgeleuchtet wird.[124] Die partielle Ausleuchtung führt zu einer Homogenisierung der Laserintensität in axialer Richtung, sodass die Diffusion von Teilchen in dieser Richtung wenige Schwankungen in der Fluoreszenzintensität verursachen. Lediglich die Diffusion in lateraler Richtung ist dann von Gewicht.

$$g_{diff}^{(2)} = \frac{1}{V_{eff}\langle C\rangle} \cdot \frac{1}{1+\frac{\tau}{\tau_{diff}}} \tag{7}$$

Die Anregung von Farbstoffmolekülen mit relativ hohen Laserintensitäten kann zum raschen Photobleichen, d.h. zur Zerstörung des chromophoren Systems, führen.[124,125] Solche Intensitäten liegen in der Größenordnung von 100 kW/cm², was bei manchen Farbstoffen der Sättigungsintensität entsprechen kann.[126] Das Photobleichen eines Moleküls während der Passage durch den Laserfokus führt zu kleineren Diffusionszeiten τ_{diff} und zu einer scheinbar schnelleren Diffusion. Dabei ist die Abnahme der Diffusionszeit proportional zur Anregungsintensität (Glg. (8)). Darin ist $\tau_{diff}(I_{exc})$ die Diffusionszeit bei gegebener Anregungsintensität, $\tau_{diff}(0)$ die extrapolierte Diffusionszeit bei 0 kW/cm² und k_{bl} bezeichnet die Bleichrate. Je geringer k_{bl}, desto photostabiler der Farbstoff. Demnach erlaubt die intensitätsabhängige Messung der Diffusionszeit die Bestimmung der Photostabilitäten von Farbstoffen.[57,124–126]

$$\frac{\tau_{diff}(0)}{\tau_{diff}(I_{exc})} = 1 + k_{bl} \cdot \tau_{diff}(0) \cdot I_{exc} \tag{8}$$

3.2.2 Korrelationsfunktion und Photon-Bunching

Weitere physikalische oder chemische Prozesse können dazu führen, dass Farbstoffmoleküle in einen Dunkelzustand gelangen, von dem aus keine Fluoreszenzphotonen emittiert werden. Das führt zu einem zusätzlichen Zerfall in der $g^{(2)}$ Funktion, dessen Zeitkonstante τ_B sich aus der Ratenkonstante in den Dunkelzustand k_{Du} und der Ratenkonstante aus dem Dunkelzustand k_{-Du} zu $\tau_B = (k_{Du} + k_{-Du})^{-1}$ ergibt (Glg. (9)).

$$g_{Du}^{(2)} = 1 - Du + Du \cdot exp(-\tau/\tau_B) \tag{9}$$

Zu Zeiten, die in der Größenordnung von τ_B liegen, ist $g^{(2)} > 1$. Demnach werden Photonen mit höherer Wahrscheinlichkeit zeitgleich detektiert. Das System emittiert Photonen bündelweise (Abbildung 13 b)). Das Faktum, dass auf einer Zeitskala der Kinetik des Dunkelzustands Photonen in Bündeln detektiert werden, wird als Bunching (Engl. Bündeln) bezeichnet.[94]

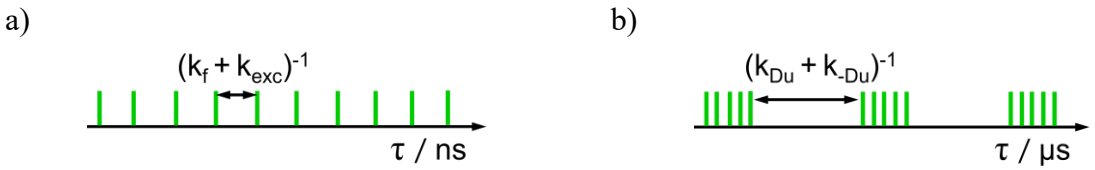

Abbildung 13: Vergleich zweier Photonenströme.
a) Antibunching in der Größenordnung der Fluoreszenzlebensdauer.
b) Bunching auf einer Zeitskala, auf der der Dunkelzustand zerfällt. Dabei wird der Dunkelzustand mit k_{Du} populiert bzw. mit k_{-Du} entleert.

Dabei ist die Art des Dunkelzustandes für das Zustandekommen von $g^{(2)} > 1$ zunächst unerheblich. Lediglich die Tatsache, dass eine Besetzung des Dunkelzustandes erfolgt, induziert Fluoreszenzfluktuationen auf der Zeitskala der Besetzungsdynamik.[90,115]

3.2.3 Bunching Analyse und Interkombinationsübergänge

So kann, wie in Abbildung 11 plakativ gezeigt, das Triplett-Niveau T_1 oder ein protonierter Zustand P_0 ein Dunkelzustand darstellen. Im Folgenden wird näher beleuchtet, wie sich die Triplettkinetik durch die Korrelationsanalyse quantifizieren lässt. Daran schließt sich die Analyse des Protolysegleichgewichts einer Photosäure in ihrem Grundzustand auf der Grundlage des Bunching-Zerfalls von $g^{(2)}$ an.

Der Triplettdynamik, deren Zeitkonstante hier um 0.1 – 10 µs liegen kann, wird durch $g_T^{(2)}$ (Glg. (10)) Rechnung getragen. Dabei repräsentiert $T = k_{isc}^{eff}/(k_{isc}^{eff} + k_{risc})$ das Kontingent an Molekülen im Triplettzustand, $\tau_T = (k_{isc}^{eff} + k_{risc})^{-1}$ bezeichnet die Zeitkonstante, die zwischen der Detektion konsekutiver Photonenbündeln verstreicht.[90,106,110,116,127,128] Mit der Interkombinationsratenkonstante k_{isc} wird der Zustand T_1 bevölkert, und mit k_{risc} entleert. Die effektive Ratenkonstante k_{isc}^{eff} ist dabei eine Funktion der Anregungsrate k_{exc}. Nach Glg. (11) ergibt sie sich aus der intensitätsunabhängigen Rate k_{isc} multipliziert mit der Besetzungswahrscheinlichkeit des S_1-Zustandes.[124,128]

$$g_T^{(2)} = 1 - T + T \cdot exp(-\tau/\tau_T)$$ [90,106,110,116,128] (10)

$$k_{isc}^{eff} = k_{isc} \cdot \frac{k_{exc}}{k_{exc} + k_f}$$ (11)

Durch die exponentielle Anpassung des Bunching-Zerfalls von $g^{(2)}$ können so τ_B und damit k_{isc}^{eff} und k_{risc} bestimmt werden. Über eine intensitätsabhängige Messung kann mit Glg. (11) schließlich k_{isc} erhalten werden. Die Zeitkonstante τ_B hängt empfindlich von der vorliegenden Sauerstoff-Konzentration ab,[127,129] da es sich hierbei um einen effizienten Triplett-Quencher handelt. So ist allgemein $\tau_B \approx 1 – 10$ µs in Anwesenheit von Sauerstoff, unter Sauerstoffausschluss werden Triplettlebensdauern um 50 ms erreicht.[127,129] Die Bunching-Zeitkonstante liegt im Fall der Photosäuren bei Anregungsraten um 30 MHz im Bereich von 1 µs. Die Fluoreszenzlebensdauern liegen um 5 ns. Demnach kann die Triplettkinetik von $g^{(2)}_{diff}$ und $g^{(2)}_{AB}$ isoliert analysiert werden.

3.2.4 Bunching Analyse und Protonentransfer

In den folgenden Publikationen wird der Protonentransfer im Grundzustand von Photosäuren u.a. dadurch analysiert, dass die Zeitkonstante des Bunchingzerfalls bestimmt wird.[51,57] Dieses Vorgehen ist der Bestimmung der Interkombinationsratenkonstante sehr ähnlich. Im Kontext der Analyse des Protonentransfers werden unterschiedliche Anregungsschemata appliziert, die sich hinsichtlich Anregungswellenlänge ($\lambda_{abs}(RO^-)$ oder $\lambda_{abs}(ROH)$) und der vorliegenden Protonenkonzentration ($pH >> pK_s$ oder $pH \approx pK_s$,) unterscheiden (vgl. Abbildung 14 a) und c)).

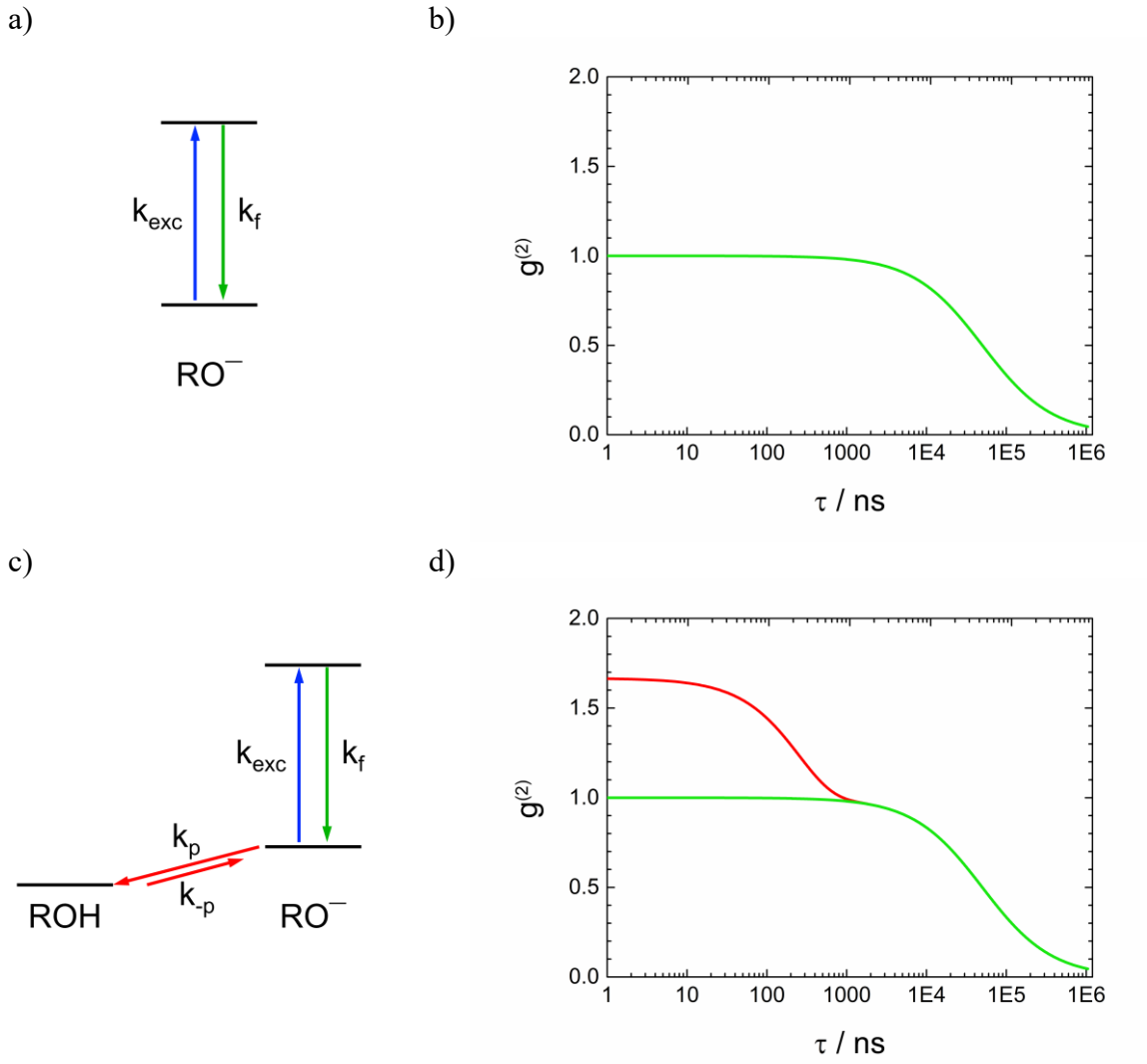

Abbildung 14: Vergleich zwischen a) Zwei-Zustandssystem und c) System mit Dunkelzustand ROH. b) Im Idealfall, unter Vernachlässigung von Interkombinationsübergängen und Photobleichen, zeigt die Korrelationsfunktion einen hyperbolischen Zerfall aufgrund der diffusiven Entleerung des konfokalen Volumens.
d) Besetzt ein gewisser Grad an Molekülen den Dunkelzustand ROH, so zeigt sich die exponentiell zerfallende Schulter im Bereich von $\tau = 1/(k_p + k_{-p})$. Das ist der Fall, wenn $pH \approx pK_s$.

Zunächst wird pH >> pK_s eingestellt, so dass eine komplette Entvölkerung des ROH Zustandes gewährleistet ist (Abbildung 14 a)). Unter dieser Bedingung kann durch Variation der Anregungsintensität eine eventuelle Triplettdynamik der betreffenden Photosäure untersucht werden. Zeichnet sich eine Verbindung durch eine Triplettdynamik aus, kann so eine Anregungsintensität gefunden werden, bei der die Population des Triplettniveaus zu vernachlässigen ist. Die Protonierungskinetik kann dann für sich analysiert werden.
Zur Analyse der Protonierungskinetik werden $\lambda_{exc} \approx \lambda_{abs}(RO^-)$ und pH ≈ pK_s gewählt, wobei der pH etwas unterhalb des pK_s liegen soll, damit das Protolysegleichgewicht auf ROH Seite liegt (Abbildung 14 c)).[57] Der ROH Zustand ist ein Dunkelzustand und durch die Wahl des pH ist dieser relativ stark populiert. Dies führt einerseits zu einer schnellen Kinetik mit Zeitkonstanten um 1µs. Ferner ist die Kinetik umso ausgeprägter je höher die Population des ROH Niveaus ist (vgl. Glg. (12)). Die beiden Reaktionsraten k_p und k_{-p} ergeben sich nach Glg. (12) aus der Zerfallskonstanten bzw. der relativen Bunching-Amplitude, sprich der Besetzung des ROH Zustandes.[130]

$$g^{(2)} = \frac{1}{V_{eff}\langle C\rangle}\frac{1}{1+\frac{\tau}{\tau_{diff}}}\left(1+\frac{k_p^{eff}}{k_{-p}^{eff}}\exp\left(-\left(k_p^{eff}+k_{-p}^{eff}\right)\tau\right)\right) \tag{12}$$

Mit Glg. (13) lässt sich der pK_s Wert der untersuchten Verbindung bis auf zwei Nachkommastellen genau bestimmen.[57]

$$pK_s = pH + log\frac{k_p^{eff}}{k_{-p}^{eff}} \tag{13}$$

Wichtig ist der Hinweis, dass es sich bei k_p^{eff} und k_{-p}^{eff} um effektive Ratenkonstanten handelt. Beide hängen von der verwendeten Konzentration des Säure-Base Puffers ab (vgl. Glg. (14) und (15)). Darin sind k_p^{bi} und k_{-p}^{bi} konzentrationsunabhängige, bimolekulare Ratenkonstanten. Diese lassen sich nach Glg. (14) und (15) durch Variation der Pufferkonzentration bestimmen.[51,57,130]

$$k_p^{eff} = k_p^{bi}\cdot[HB^+] \tag{14}$$

$$k_{-p}^{eff} = k_{-p}^{bi}\cdot[B] \tag{15}$$

Die Ratenkonstante k_p^{bi} dient außerdem als Referenz zur bimolekularen Reprotonierungsratenkonstante, die aus dem Antibunching extrahiert wird. Wie k_p^{bi} aus dem Antibunching-Zerfall von $g^{(2)}$ erhalten wird, wird als Nächstes betrachtet.

4. Abstandshaltende Photonen und Protonentransfer

4.1 Antibunching-Experimente

Im „Antibunching-Experiment“ wird zunächst die Zerfallskonstante τ_{AB} des Referenz-Systems $RO^- \leftrightarrow RO^{-}*$ ermittelt (Abbildung 15 a)). Dazu wird wieder $pH >> pK_s$ eingestellt oder es wird in reinem DMSO gemessen, in dem sämtliche benutzte Photosäuren deprotoniert vorliegen. Der ROH Zustand ist in beiden Fällen entvölkert. Es wird für alle verwendeten Photosäuren wird eine reduzierte Lebensdauer $\tau_{AB} = 1/(k_{exc} + k_f)$ nachgewiesen (Abbildung 15 b)).[88]

a) b)

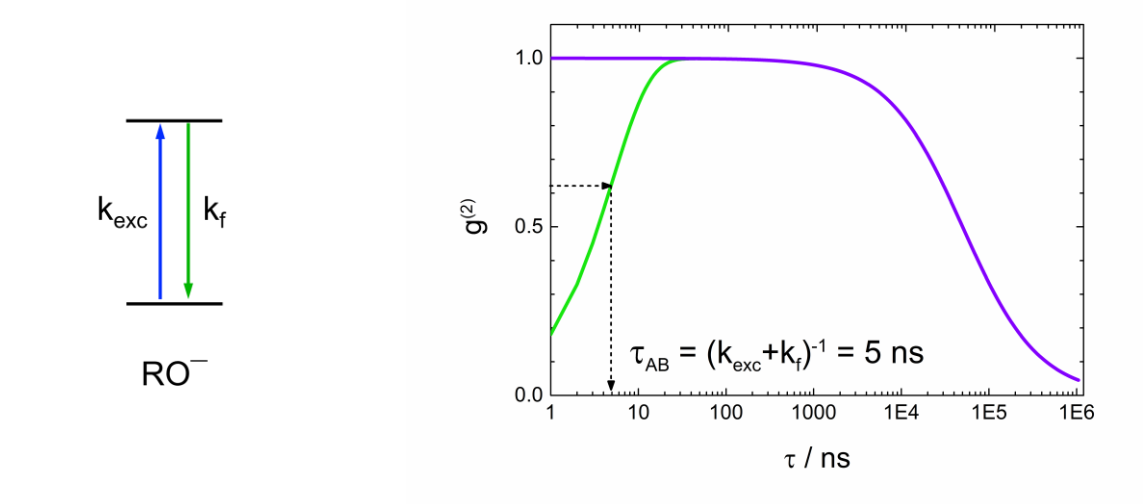

c) d)

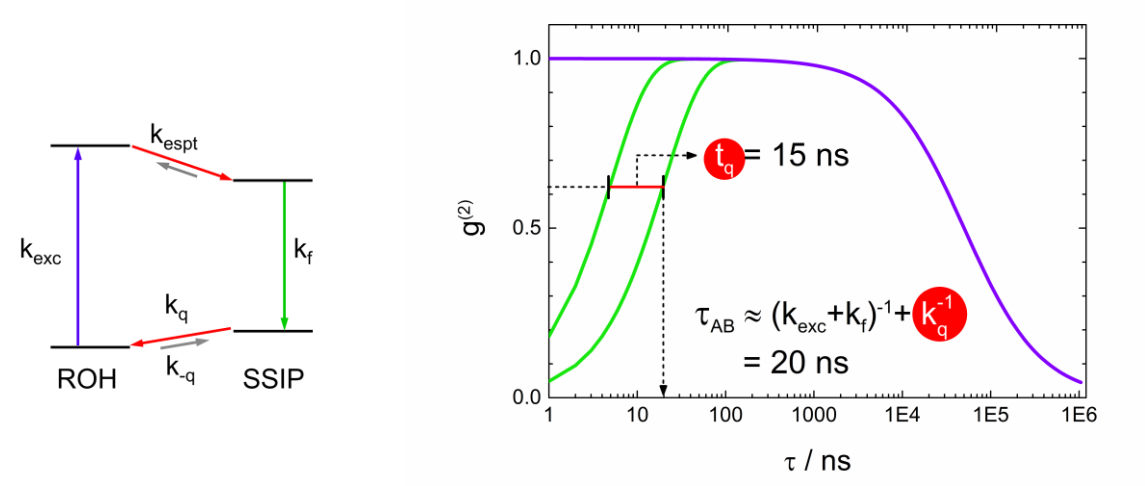

Abbildung 15: Vergleich zwischen a) Zwei-Zustands-System und c) Vier-Zustands-System.
b) Die Zeitkonstante des Antibunchings ist, wie zu erwarten, $\tau_{AB} = (k_{exc} + k_f)^{-1}$.
d) Beim Vier-Zustands-System ist die Zeitkonstante τ_{AB} vergrößert. Im Fall des Protonentransfers DMSO, wo das SSIP beobachtet werden kann, ist τ_{AB} um genau $1/k_q$, der Zeitkonstanten der Rückprotonierung verlängert.

Im nächsten Schritt werden Anregungswellenlänge und Protonenkonzentration so etabliert, dass der Förster-Zyklus häufig durchlaufen wird ($\lambda_{exc} \approx \lambda_{abs}(ROH)$ und $pH << pK_s$). Die Kopplung zweier optisch anregbarer Spezies im Grundzustand und im angeregten Zustand über den Protonentransfer führt dabei zu einer deutlichen Vergrößerung von τ_{AB}.[51] Durch Variation der Pufferkonzentration [B] werden unterschiedliche Zerfallskonstanten $k_{AB}([B])$ erhalten. Für verschiedene k_p wird $g^{(2)}_{AB}$ simuliert und die theoretischen $k_{AB}(k_p)$ bestimmt. Durch Vergleich der experimentellen $k_{AB}([B])$ mit den simulierten $k_{AB}(k_p)$ lässt sich die bimolekulare Ratenkonstante der Rückprotonierung k_p^{bi} gewinnen. Der ermittelte Wert der Ratenkonstante stimmt mit literaturbekannten Werten und den Werten aus dem Bunching-Experiment gut überein.[130]

Wird DMSO als Lösungsmittel verwandt, gestaltet sich der $g^{(2)}$-Zerfall in der ns-Domäne als komplexer (

Abbildung 16). Der biexponentielle Zerfall von $g^{(2)}$ kann einzig durch die Annahme zweier emissiver Spezies erklärt werden.[52]

a)

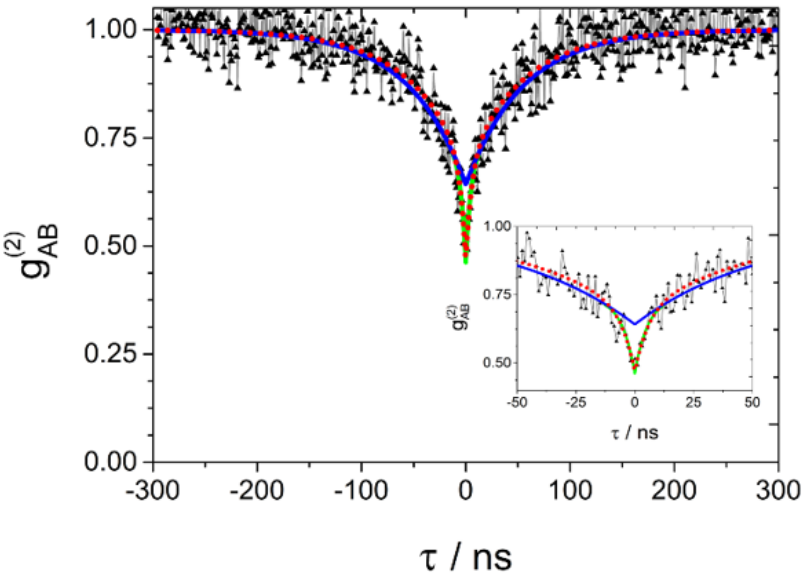

b)

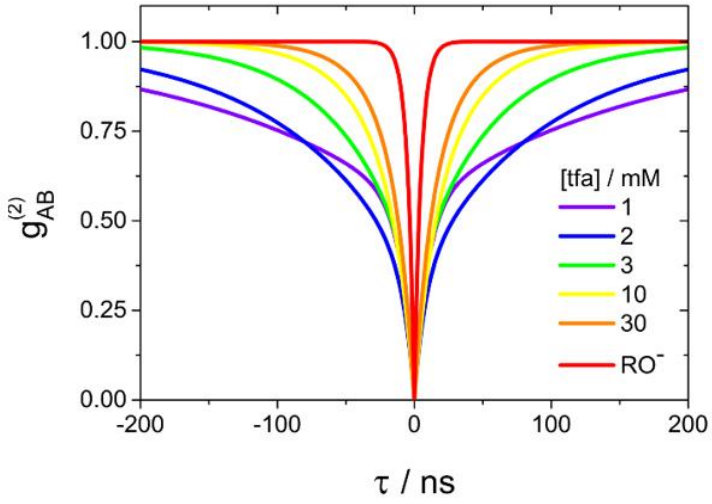

Abbildung 16: Korrelationsanalyse der Fluoreszenz von (**1**).
a) Biexponentieller $g^{(2)}$-Zerfall von (**1**) in DMSO mit TFA.
b) Abhängigkeit von $g^{(2)}$ von der verwandten TFA Konzentration (hier sind normierte Fitfunktionen dargestellt, die sich aus dem Experiment ergeben).
Reproduced from M. Vester, A. Grüter, B. Finkler et al., PCCP, 2016, DOI: 10.1039/C6CP00718J with permission from the PCCP Owner Societies.

Das zugrundeliegende Eigen-Weller Schema wird zunächst auf ein 5-Zustände System reduziert (vgl. Abbildung 17). Die Annahmen bzw. Näherungen, die dabei getroffen werden, basieren zum einen Teil auf dem vorhergehenden Antibunching-Versuch in wässriger Lösung[51]. Zum anderen fußen die Überlegungen auf früher durchgeführten solvatochromischen Studien am Protonentransfer und Ultrakurzzeitexperimenten mit Photosäuren.[31,71]

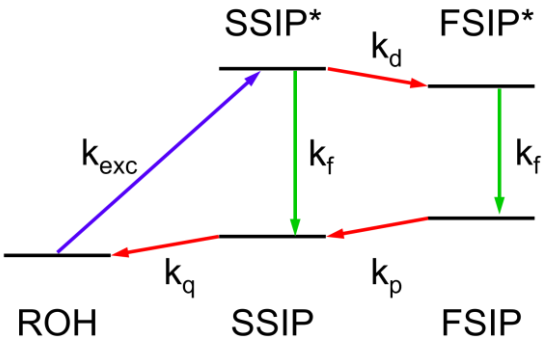

Abbildung 17: Reduziertes Eigen-Weller-Schema.
Reproduced from M. Vester, A. Grüter, B. Finkler et al., PCCP, 2016, DOI: 10.1039/C6CP00718J with permission from the PCCP Owner Societies.

Im Zuge der weiteren Analyse der Zeitkomponenten werden die diffusiven Prozesse, d.h. die Bildung und der Zerfall des FSIP und die nicht-diffusiven Prozesse entkoppelt. Eine Separation

der Zeitskalen ist dabei ausreichend gewährleistet. So wird das 5-Zustände-System als Kombination aus zyklischem 3-Zustände-System und 2-Zustandssystem beschrieben (Abbildung 18). Die Kinetik des FSIP Zerfalls hängt dann primär von den Ratenkonstanten k_d^{eff} und k_p ab. Damit können Antibunching Zeitkonstanten erklärt werden, die mitunter größer sind als Zeitkonstanten, die der inversen Anregungsrate entsprechen.[52]

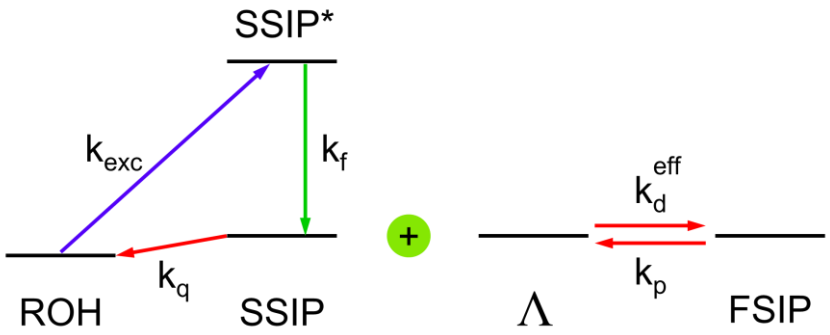

Abbildung 18: Zur Reduktion des Fünf-Zustandssystems.
Entkopplung der diffusiven und der nicht-diffusiven Prozesse im System. Λ repräsentiert das 3-Zuständesystem.
Reproduced from M. Vester, A. Grüter, B. Finkler et al., PCCP, 2016, DOI: 10.1039/C6CP00718J with permission from the PCCP Owner Societies.

Schließlich werden im folgenden Teil Eigenschaften der ausgewählten Photosäuren betrachtet, die notwendig sind, um das Antibunching-Experiment durchzuführen.

4.2 Über die Eignung der verwandten Pyrenolderivate

Damit der Protonentransfer durch die Fluoreszenzkorrelationsanalyse untersucht werden kann, werden Farbstoffe gesucht, die sich durch eine möglichst hohe, zeitlich stabile Emissionsrate auszeichnen. Um den Protonentransfer in DMSO entsprechend untersuchen zu können, müssen außerdem die Photosäuren azide genug sein, das Lösemittel DMSO zu protonieren.

In Tabelle 3 sind wichtige Eigenschaften der drei häufig verwandten Pyrenolderivate (**1**)-(**3**) dargestellt. Allen ist das Pyrenolgrundgerüst gemein; auch werden die Moleküle durch Substitution mit Sulfonsäureresten erhalten. Von (**3**) nach (**1**) steigt der Elektronenzug der Substituenten. Dies führt zu einer Erniedrigung der pK_s Werte, wobei die Reduktion des pK_s^* wesentlich größer ausfällt. Beide Umstände sind völlig konsistent mit den Ausführungen in Kapitel 2.2.

Tabelle 2: Übersicht über verwandte Pyrenolderivate.[57]

Eigenschaft		(**1**)	(**2**)	(**3**)
Struktur		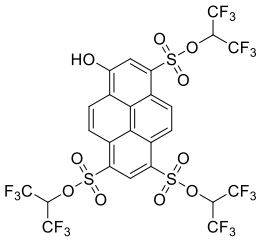	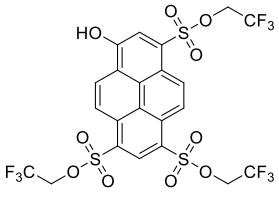	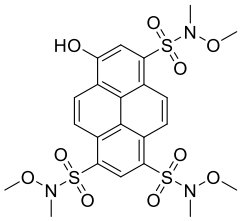
λ_{abs}/nm	ROH	449	440	438
	RO^-	576	568	568
λ_{em}/nm	ROH	c	c	506
	RO^-	580	574	576
τ_f / ns	ROH	0.2	0.4	1.4
	RO^-	5.6	5.6	5.7
pK_s		[a]4.4	[a]4.7	[b]5.6
pK_s^*		-3.9	-2.7	-1.2

λ_{abs} : Absorptionswellenlänge in DMSO, λ_{em} Emissionswellenlänge in DMSO, τ_f Fluoreszenzlebensdauer in DMSO, [a] pK_s Werte in Wasser, durch FCS bestimmt, [b] pK_s Werte in Wasser durch Absorptionstitration bestimmt, pK_s^* Werte in Wasser mit Gleichung 2 bestimmt. [c] nicht bestimmbar wegen hoher ESPT Ratenkonstante.

Ein möglichst großer ΔpK_s, wobei insbesondere $pK_s^* << 0$ gelten soll, ist aus zweierlei Gründen essentiell. Erstens müssen im Antibunching-Experiment Bedingungen etabliert werden, so dass möglichst viele Förster-Zyklen pro Zeiteinheit durchlaufen werden. Dadurch

ist die Ausbeute an Fluoreszenzphotonen pro Zeiteinheit möglichst hoch. Dazu muss für die Besetzung der Grundzustände [ROH] und [RO^-] zum Startzeitpunkt eines Start-Stop-Experimentes gelten: [ROH](t = 0) ≈ 1 >> [RO^-](t = 0). Es muss also bei niedrigen pH-Werten bzw. hohen Protonenkonzentrationen gearbeitet werden. Gleichzeitig darf das Protolysegleichgewicht im angeregten Zustand nicht allzu stark auf ROH* Seite verschoben werden, da der ESPT nach wie vor effizient ablaufen soll, damit genügend RO^- Photonen erzeugt werden. Hier muss also gelten: [ROH*] ≈ 0 << [RO*]. Zweitens muss die genutzte Photosäure azide genug sein, um das Lösungsmittel DMSO zu protonieren, wenn DMSO als Solvens und Protonenakzeptor verwendet werden soll. Dass sich solche Bedingungen etablieren lassen, ist in den betreffenden Absorptions- und Emissionsspektren zu erkennen (vgl. Abbildung 19). So wird im Falle des Lösemittels DMSO das Protolysegleichgewicht des Grundzustandes durch [TFA] > 300 µM (Protonendonor) völlig auf ROH Seite gebracht (Abbildung 19 a)). Gleichzeitig fällt die Änderung im angeregten Zustand weniger stark aus, da die Emissionsbande der Base das Spektrum dominiert (Abbildung 19 b)). Als wässrige Lösung wird eine gepufferte Lösung bei pH 3 verwendet, so dass aufgrund von [ROH]/[RO^-] α $K_s/[H^+]$ ≈ 50 von k_{-p} << k_p ausgegangen werden kann. Gleichzeitig bleibt das Säure-Base Gleichgewicht im angeregten Zustand davon unberührt (pK_s^* ≈ -3 << pK_s ≈ 4,5 → K_s^* >> K_s).

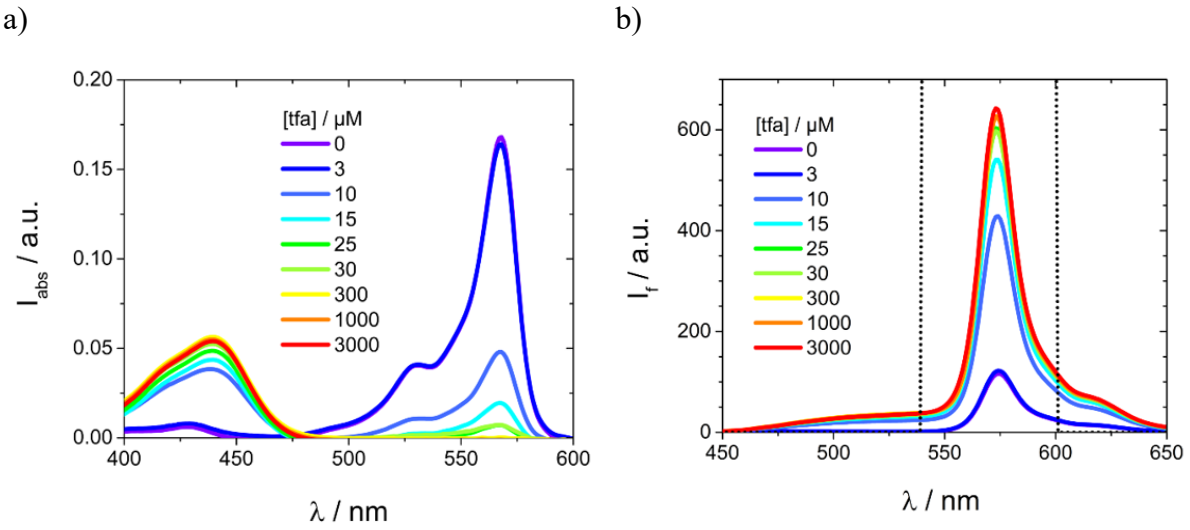

Abbildung 19: Spektrale Eigenschaften von (**2**).
a) Absorptions und b) Emissionsspektren von (**2**) in DMSO bei verschiedenen TFA Konzentrationen. Das Transmissionsprofil des Emissionsfilters (570/60 ET Bandpass) ist in Schwarz eingezeichnet.

Das Einbringen elektronenziehender Funktionen in das Molekül führt nicht nur zu einer starken Erniedrigung des pK_s^* bei vergleichsweise konstantem pK_s. Es bewirkt zudem eine zunehmende bathochrome Verschiebung in der Emission.[57] Ein größerer Stokes-Shift erlaubt eine bessere Abtrennbarkeit von Anregungs- und Emissionslicht und so prinzipiell bessere Signal-zu-Untergrund Verhältnisse.

Der nächste zentrale Molekülparameter, der Garant einer stabilen Fluoreszenzemission ist, ist die Photostabilität. Diese ist invers proportional zur Bleichrate k_{bl}, des Fluorophors, welche wiederrum angibt, wie rasch ein Farbstoff bei gegebener Anregungsintensität zerstört wird.[124–126] In Abbildung 20 werden die Bleichraten verschiedener Pyrenolderivate verglichen. Dabei wurde k_{bl} jeweils über eine intensitätsabhängige Messung von τ_{diff} und über Glg. (8) ermittelt.[57] Rhodamin 6G, ein Derivat des Xanthens, welches bereits auf Einzelmolekülebene detektiert[131,132] und sogar abgebildet[133,134] wurde, dient dabei als Referenz für einen vergleichsweise stabilen Farbstoff.[135]

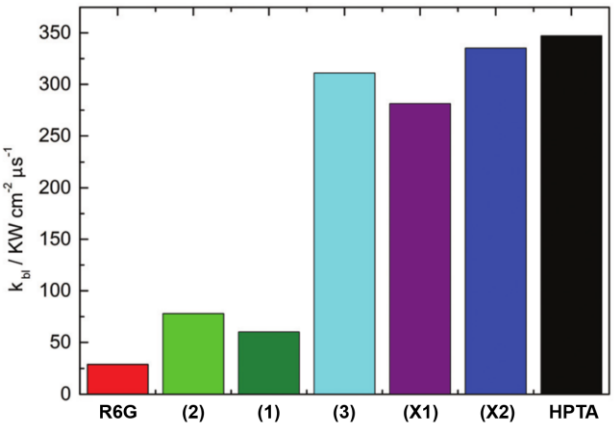

Abbildung 20: Photostabilitäten verschiedener Farbstoffe.
Vergleich der Bleichraten, k_{bl}, verschiedener Pyrenolderivate mit Rhodamin 6G (R6G).[57] (**1**), (**2**), (**3**) sind die Substanzen, die in den Antibunching-Experimenten verwendet werden. X1 und X2 sind Pyrenolderivate, die dort nicht verwendet werden.
Reproduced from Ref. „B. Finkler, C. Spies, M. Vester et al., *Photochem. Photobiol. Sci., 2014, 13, 548–562*“ with permission from the European Society for Photobiology, the European Photochemistry Association, and the Royal Society of Chemistry.

Die größten Erhöhungen der Azidität im angeregten Zustand werden durch die Einführung von mehrfach fluorierten Sulfonsäureestern erzielt (Verbindungen (**1**) und (**2**)). Es wird in Abbildung 20 ersichtlich, dass diese fluorierten Sulfonsäurereste außerdem zur Erhöhung der Photostabilität beitragen.[136,137] Ferner führen Mehrfachsubstitutionen mit Fluor zu einer erhöhten chemischen Stabilität und zur weiteren Erhöhung der Photostabilität.[57,126,136,137] Es wird davon ausgegangen, dass eine Redoxreaktion für die Photodestruktion eines Fluorophors ursächlich ist. Oft findet eine Elektronenabgabe aus dem angeregten Zustand des Fluorophors

an das Lösungsmittel statt. Demnach führt eine Erhöhung des Oxidationspotentials des Fluorophors zur Erhöhung der Photostabilität.[136] Ferner können Lösemitteleinflüsse bei der Stabilisierung des durch die Photooxidation freigesetzten Elektrons eine Rolle spielen. So gilt Glg. (16) für die Abhängigkeit der Reaktionsgeschwindigkeitskonstante zweier ionischer Reaktionspartner von der Dielektrizitätskonstanten des Lösungsmittels im Fall stark verdünnter Lösungen.[138] Daraus kann geschlossen werden, dass die Photooxidation eines Fluorophors in einem weniger polaren Lösungsmittel als Wasser, nämlich DMSO, langsamer abläuft, da das Elektron vom Lösungsmittel weniger gut stabilisiert werden kann. Demnach ist ein Farbstoff in DMSO photostabiler als im Lösungsmittel Wasser.

$$lnk = lnk_0 + \frac{1}{4\pi\varepsilon_0}\frac{z_a z_b e^2 N_A}{RTr_{ab}}\left(1 - \frac{1}{\varepsilon_r}\right) \tag{16}$$

Als weitere essentielle Molekülgröße gilt im Allgemeinen die Fluoreszenzquantenausbeute, die möglichst nahe an 100 % liegen soll. Im Falle der verwandten Photosäuren (**1**), (**2**), (**3**) liegt sie bei 91 %, 87 % und 98 % (vgl. Tabelle 2).[57]
Schließlich hängt die Emissionsrate pro Molekül von der Triplettkinetik des Moleküls ab (Glg. (17) und (18)).

$$k_{em} = \frac{k_{exc}\Phi_f}{1 + \frac{k_{exc}}{k_s}} \tag{17}$$

Dabei ist die Sättigungsrate k_s gegeben durch, falls $k_f >> k_{isc}$ gilt:

$$k_s = \frac{k_f}{\frac{k_{isc}}{k_{risc}} + 1} \tag{18}$$

Damit also die Emissionsrate pro Molekül möglichst hoch ist, sollte die Ratenkonstante für den Interkombinations-Übergang, k_{isc}, möglichst klein sein.[139,140] Tabelle 3 gibt in Spalte 2 einen Überblick der intensitätsunabhängigen Interkombinationsraten k_{isc} der Pyrenolderivate (**1**) - (**3**) in DMSO und zusätzlich von (**2**) in wässriger Lösung. Diesen werden literaturbekannte Werte von k_{isc} der häufig gebrauchten Fluoreszenzfarbstoffe Rhodamin 6G (Rh6G) und Fluoreszeinisothiocyanat (FITC) gegenübergestellt. Die Photosäuren sind hinsichtlich ihrer Interkombinationsratenkonstanten mit dem guten Fluoreszenzfarbstoff Rh6G vergleichbar.

FITC, welches bekanntermaßen eine ausgeprägte Triplettdynamik aufweist, zeigt eine signifikant höhere Konstante k_{isc}.[90,124]

Tabelle 3: Parameter von Interkombinationsübergängen in verschiedenen Farbstoffen. Dazu zählen die genutzten Pyrenolderivate in DMSO. Diese werden mit literaturbekannten Werten der häufig genutzten Farbstoffe Rhodamin 6G (Rh6G) und Fluoreszeinisothiocyanat (FITC) verglichen. [w]in wässriger Lösung.

		k_{exc} = 30 MHz		k_{exc} = 30 MHz
Farbstoff	k_{isc} / MHz	k_{isc}^{eff} / MHz	k_{risc} / MHz	t_B / µs
(**1**)	0.98 ± 0.03	0.13 ± 0.01	0.63 ± 0.07	1.5
(**2**)	1.15 ± 0.04	0.26 ± 0.01	0.74 ± 0.03	1.3
(**3**)	0.85 ± 0.06	0.15 ± 0.02	1.41 ± 0.14	0.7
(**2**)[w]	1.4[51]			
Rh6G[w]	1.1[90]			
FITC[w]	5.7[90]-8.1[124]			

Zusammengefasst bleibt festzuhalten, dass sich die verwendeten Farbstoffe aufgrund einer hohen Quantenausbeute, einer hohen Photostabilität, einem niedrigen pK_s^*, und niedrigen Interkombinationsraten sehr gut zur Analyse des Antibunchings eignen.

5. Publikationen

1) B. Finkler, C. Spies, M. Vester et al., *Photochem. Photobiol. Sci.*, 2014, **13**, 548–562
„Highly Photostable „Super“-Photoacids for Ultrasensitive Fluorescence Spectroscopy“

2) M. Vester, T. Staut, J. Enderlein and G. Jung, , *J. Phys. Chem. Lett.*, 2015, **6**, 1149–1154
„Photon Antibunching in a Cyclic Chemical Reaction Scheme“

3) M. Vester, A. Grüter, B. Finkler, R. Becker and G. Jung, *PCCP*, 2016, Accepted Manuscript
„Biexponential Photon Antibunching: Recombination Kinetics within the Förster-Cycle in DMSO“

5.1 B. Finkler, C. Spies, M. Vester et al., *Photochem. Photobiol. Sci.*, 2014, 13, 548–562

„Highly Photostable „Super“-Photoacids for Ultrasensitive Fluorescence Spectroscopy“

Cite this: DOI: 10.1039/c3pp50404b

Highly Photostable "Super"-Photoacids for Ultrasensitive Fluorescence Spectroscopy

Björn Finkler[a], Christian Spies[a], Michael Vester[a], Frederick Walte[a], Kathrin Omlor[a], Iris Riemann[b], Manuel Zimmer[c], Frank Stracke[b], Markus Gerhards[c], Gregor Jung[a*]

Received 27th November 2013,
Accepted 14th January 2014

DOI: 10.1039/c3pp50404b

www.rsc.org/pps

The photoacid 8-hydroxypyren-1,3,6-trisulfonic acid (HPTS, pyranine) is a widely used model compound for the examination of excited state proton transfer (ESPT). We synthesized five "super"-photoacids with varying hydrophilicity and acidity on the basis of HPTS. By chemical modification of the three sulfonic acid substituents, the photoacidity is enhanced by up to more than five logarithmic units from pK_a* ≈ 1.4 to ~ -3.9 for the most acidic compound. As a result, nearly quantitative ESPT in DMSO can be observed. The novel photoacids were characterized by steady-state and time-resolved fluorescence techniques showing distinctively red shifted spectra compared to HPTS while maintaining a high quantum yield near 90%. Photostability of the compounds was checked by fluorescence correlation spectoscopy (FCS) and found to be adequately high for ultrasensitive fluorescence spectroscopy. The described photoacids present a valuable palette for a wide range of applications, especially when the properties of HPTS, i.e. highly charged, low photostability and only moderate excited state acidity, are limiting.

Introduction

Many aromatic alcohols like phenol-[1–5] and naphthol-derivatives[5–23] undergo an increase of acidity upon electronic excitation, facilitating an excited state proton transfer (ESPT) to the solvent or an appropriate base molecule. Among these, the pyrenol derivative HPTS (8-Hydroxypyren-1,3,6-trisulfonic acid, pyranine) is one of the most investigated photoacids.[5,24–46] Theodor Förster was the first to describe ESPT of HPTS to water more than 60 years ago,[24,25] but this molecule is still under investigation.[40,41] One important reason for the ongoing interest in this dye is that the use of short excitation pulses to trigger proton transfer reactions allows for monitoring the molecular events which follow the dissociation of the acid (ROH) by time-resolved fluorescence spectroscopy.[28,30,31,33,35,39,42–45] Besides the examination of proton transfer, HPTS has been used for various biological applications due to its high water solubility[47] and low toxicity. Hence, a fluorogenic substrate for different enzymes was developed by modification of the hydroxyl group of the molecule.[48] Having a pK_a within the physiological range, the chromophore has been suggested for measuring of cytoplasmic and acidic organelle pH in different cell types.[49] However, the lack of cell permeability due to of the negatively charged sulfonic acid substituents yet limits the use of HPTS as intracellular indicator.[50]
The pK_a of HPTS drops from 7.3[49] to 1.4 upon excitation (pK_a*).[27] The latter value indicates a rather moderate photoacidity in the excited state. 8-Hydroxypyren-*N,N,N',N',N'',N''*-hexamethyl-1,3,6-trisulfonamide (HPTA, **3f**) is a more recently introduced derivative of HPTS which also exhibits photoacidic properties.[5,44,45,51,52] The substitution of the three sulfonic acid groups of HPTS with more electron-withdrawing dimethyl sulfonamide groups results in an increased aqueous acidity in the ground state (pK_a = 5.6) and even more in the excited state (pK_a* ~ -0.8). Suchlike molecules with pK_a* < 0 are referred to as "super"-photoacids.[15,53] The high acidity in the excited state induces ESPT to non-aqueous solvents like methanol, dimethylformamide or dimethyl sulfoxide,[8] which in turn enables the investigation of solvent effects on the process.[18] Furthermore, proton transfer in organic solvents is characterized by simpler kinetics than in water.[9] In fact, HPTA is hardly soluble in water.[52]
In the past years, significant efforts were undertaken to develop even stronger photoacids. Tolbert and co-workers modified and intensively studied 1- and 2-naphthol derivatives with several electron-withdrawing functional groups to enhance the photoacidity of the dye.[8,9,14] The most acidic compound among these is 5,8-dicyano-2-naphthol (DCN2) with a pK_a* = -4.5 calculated by use of the Förster cycle.[9] DCN2 has become an elaborately studied and valuable compound for examination of ESPT.[19–22,53] However, the examination of proton transfer to water is challenging, because DCN2 is nearly insoluble in this solvent as well.[54]

This limitation was overcome with N-methyl-6-hydroxyquinolinium ($NM6HQ^+$) iodide.[53,55–57] Analysis of the time-resolved data of its ESPT in water revealed a pK_a* of -7. This high photoacidity was attributed to an intramolecular charge transfer from the hydroxylate group to the positively charged pyridinium ring.53 In another recent publication, quinone cyanine photoacids were reported.54,58,59 The aqueous pKa* of these dyes was estimated to be ~ -6 and below. Compared to the ground state pKa of ~ 4.5, electronic excitation results in an increase by at least 10 orders of magnitude. For both classes of molecules, deprotonation rate constants above 1012 s-1 were reported, which are the highest values recorded up to date. Nevertheless, the positive charge present in both classes of photoacids aggravates the analysis of ESPT kinetics, since the typical description, by the spherically symmetric Debye-Smoluchowski equation for reversibility cannot be applied.53,54 In addition, quantum yield of the RO*- form of the cyanine based dyes hardly reaches 10%.54 Finally, virtually all systems on the basis of naphthol and hydroxyquinoline are excited by UV- or near UV-light. As a consequence Raman scattering, photodestruction and background fluorescence are intensified, which complicates the investigation of ESPT by ultrasensitive spectroscopic methods and their application for live-cell imaging.

The above mentioned shortcomings of existing photoacids kindled our interest in the searchfor the search of new "super"-photoacids for various purposes. In the present manuscript, we describe several highly photostable, bright "super"-photoacids on the basis of pyranine. Sulfonic acid groups of HPTS were converted by use of amines and alcohols to more electron-withdrawing sulfonamide and sulfonic ester groups. All described molecules exhibit a higher photoacidity than HPTS and partially even higher than HPTA. Two of these derivatives are well soluble in water. The lack of the negatively charged substituents in contrast to HPTS enables the use of the more lipophilic compounds as a fluorescent probe for intracellular use *in vivo*. Photostability, as verified by fluorescence correlation spectroscopy (FCS), is comparable to rhodamine 6G.

Results

Scheme 1 displays the overall synthesis of the photoacids starting from HPTS. Compounds **3d** and **3e** were conceived as highly hydrophilic probes. To achieve this aim, we used substituents with structural elements which are known for good water solubility while maintaining the similar electron withdrawing capability as the dimethyl sulfonamides of HPTA.

The rationale of dyes **3a-c** was to increase photoacidity. Fluorinated alcohols were chosen for the synthesis of **3a** and **3b** due to higher chemical stability of the corresponding sulfonic esters compared to the hydrocarbon analogs.[60] The synthesis of **3a-f**, as illustrated in Scheme 1, followed a modified procedure of Singaram *et al*.[61] HPTS was converted into 8-acetoxypyrene-1,3,6-trisulfonic acid (**1**) for protection of the hydroxyl group in the following reaction. Subsequently, the sulfonic acid groups of **1** were activated as sulfonyl chloride substituents (**2**) by use of thionyl chloride. Photoacids **3a-f** were obtained from a reaction of **2** with the corresponding alcohols and amines in moderate to good overall yields (62-91%). The complete substitution of the three sulfonic acid groups could be proven by NMR-spectroscopy for all compounds, while the pyrene core itself remained unaltered.

Spectroscopic characterization with absorption and steady-state fluorescence spectroscopy

For spectroscopic characterization, DMSO was chosen as aprotic solvent due to its excellent dissolving properties and because putative ESPT of "super"-photoacids might occur in this medium. Other solvents are discussed in a parallel publication[62] and time-resolved data with higher time-resolution will be presented elsewhere.[63]

In pure DMSO, all compounds dissociate to a large extent without addition of a base, as can be anticipated from the absorption spectra (Figure 1a). A tentative explanation of this high degree of dissociation is that it could originate from the acidity constant in DMSO which is similar to that in water, in combination with the low dye concentration. This effect would not be surprising due to the highly delocalized charge in the anion.[64] Also, spurious amounts of water might support the dissiciation.[65] The absorption maxima $\lambda_{abs,\,max}$ of anionic compounds 3a-f are found between λ = 554 and 576 nm (Table 1).

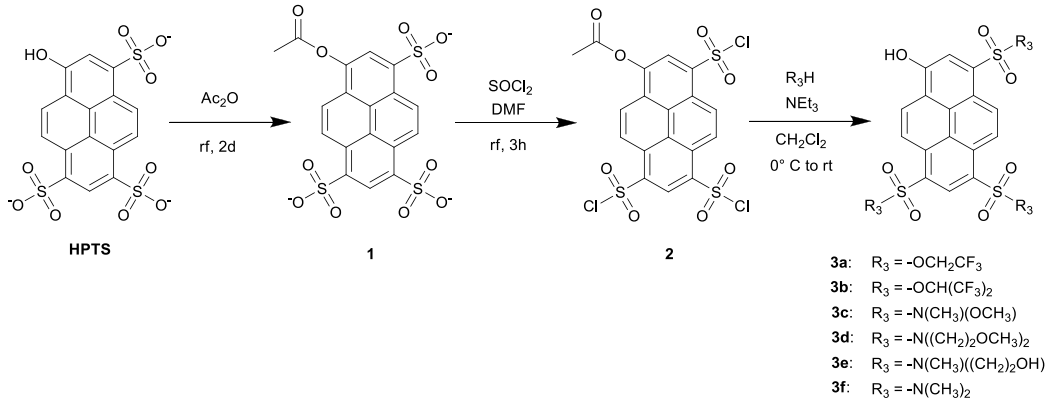

Scheme 1: Synthesis of HPTS-derivatives **3a-f**.

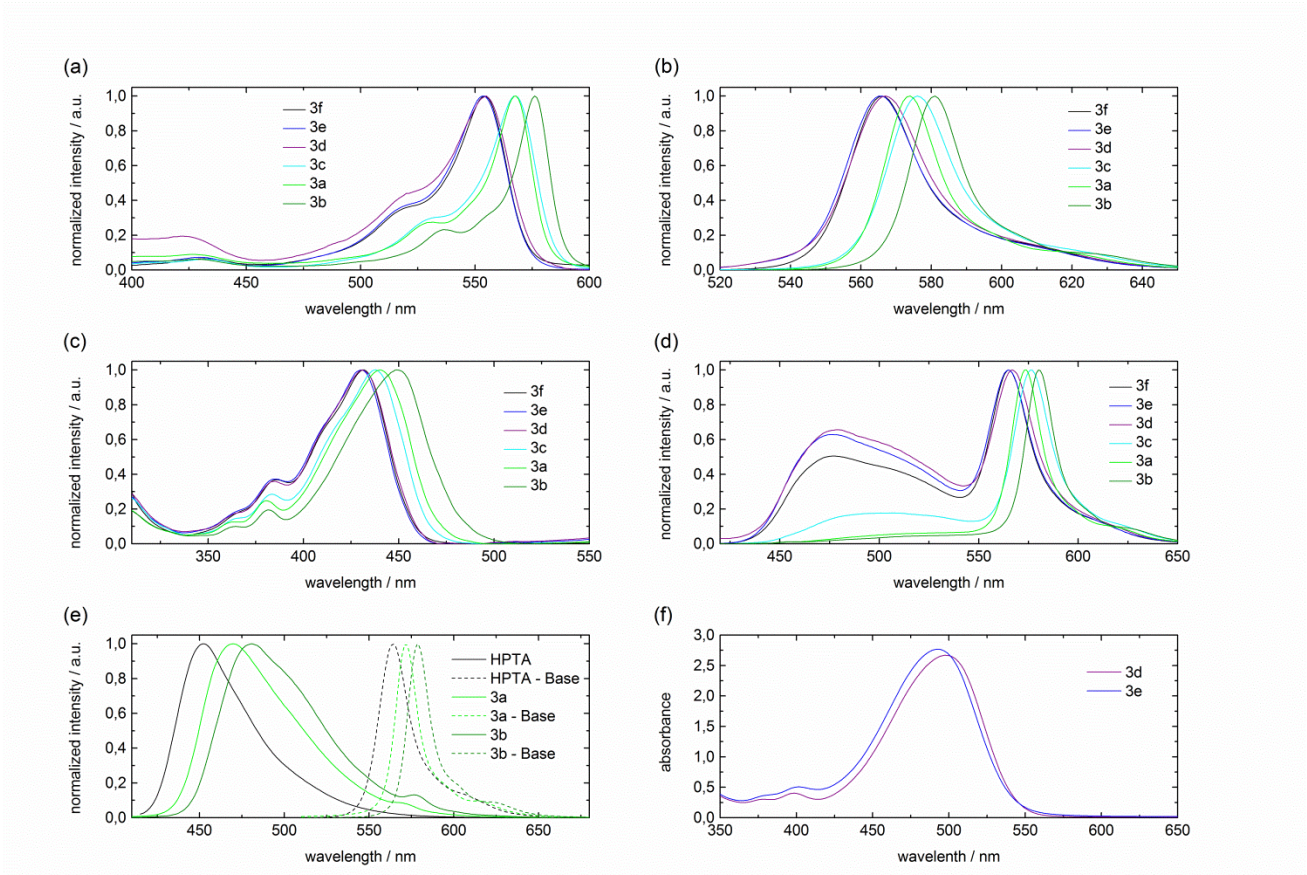

Figure 1: (a) Absorption and (b) emission spectra (λ_{exc} = 500 nm or 520 nm) of the base form of the photoacids. (c) Absorption and (d) emission spectra (λ_{exc} = 400 nm) of the neutral photoacids in DMSO. (e) Emission spectra of the photoacids (solid line, acetone+TFA) and their base forms (dashed, acetone+NaOH). (f) Absorption spectra of two photoacids in water before normalization, showing the excellent water solubility of **3d** (10 mm path length) and **3e** (1 mm path length).

Emission spectra in pure DMSO (Figure 1b) exclusively exhibit fluorescence of the anionic dyes ($\lambda_{em,\ max}$ = 565-581 nm). Stokes shifts of the anionic species decrease from $\Delta\tilde{\nu}$ = 380 cm^{-1} (12 nm) for **3e** to $\Delta\tilde{\nu}$ = 150 cm^{-1} (5 nm) for the sulfonic ester derivative **3b**. Molar absorption coefficients (Table 1) are highest for the sulfonic esters (**3a**, **3b**) and slightly smaller for the sulfonamide derivatives.Molar absorption coefficients (Table 1) are highest for the sulfonic esters (**3a**, **3b**) and slightly smaller for the sulfonamide derivatives. Addition of 3 µL trifluoroacetic acid to DMSO (1 mL) assures a complete protonation of the dyes in the electronic ground state (Figure 1c, 1d). The normalized absorption spectra (Figure 1c) display a shape similar to that previously

Photochem. Photobiol. Sci., 2014, DOI: 10.1039/C3PP50404B

described for neutral **3f**[5] ($\lambda_{abs,\ max}$ = 430-449 nm), whereas no absorption of the anionic species is discernible. Absorption spectra of neutral and anionic **3d** and **3e** almost coincide with those of **3f**,[5] whereas absorption bands of **3a-c** are distinctly red shifted. A similar red shift is also present in the fluorescence emission of the excited RO^- form, only the order of the close lying maxima of **3a** and **3c** is reversed.

All corresponding fluorescence emission spectra (Figure 1d) show maxima at λ = 565-581 nm, which coincide with those of the excited base. This finding hints to the occurrence of ESPT to DMSO. A second maximum at higher energies in the spectra of **3c-f** arises from the excited photoacid.[5] While the peak height at $\lambda_{em,\ max}$ (ROH) is about 50-70% of the anionic emission for **3d-f**, it is just around 20% for compound **3c**. In the spectra of **3a** and **3b** nearly no emission of an excited neutral photoacid is visible, indicating a high efficiency of the ESPT process for these compounds in DMSO. Stokes shifts as the phenomenological difference between absorption of ROH and emission maxima of the conjugated base RO^- lie in the range between $\Delta\tilde{\nu}$ = 5000 and 5600 cm^{-1} (132-138 nm).

The pure emission of the neutral species can be observed in less polar solvents. Fluorescence emission spectra of **3a**, **3b** and **3f** in acetone are shown in Figure 1e. Interestingly, whereas **3f** shows exclusive emission of the excited neutral species, a second distinct band at higher wavelength is discernible in the spectrum of **3a** and even more **3b**.

Table 1: Spectroscopic properties of **3a-f** in DMSO.

	3a	**3b**	**3c**	**3d**	**3e**	**3f**
$\lambda_{abs,\ max}$, nm(ROH)	440	449	438	431	430	431
$\lambda_{em,\ max}$, nm (ROH)	-[a]	-[a]	506	479	477	477
$\lambda_{abs,\ max}$, nm (RO^-)	568	576	568	555	554	554
$\lambda_{em,\ max}$, nm(RO^-)	574	581	576	567	566	565
Φ_{fl}	0.87[b]	0.91[b]	0.98[b]	0.87[c]	0.95[c]	0.84[c]
$\varepsilon_{abs,\ max}$ (RO^-), L mol^{-1} cm^{-1}	60000	60000	53000	-[d]	35000	37000

[a] could not be determined due to nearly quantitative ESPT in DMSO.

[b] comparative quantum yield; sulforhodamine 101 (Φ_{fl} = 0.95 (EtOH)[70]) and rhodamine 101(Φ_{fl} = 1.00 (EtOH)[71]) used as reference.

[c] comparative quantum yield; rhodamine 6G (Φ_{fl} = 0.94 (EtOH)[72]) and fluorescein (Φ_{fl} = 0.95 (0.1M NaOH)[73]) used as reference.

[d] could not be determined due to hygroscopy of the compound.

The maximum of this peak ($\lambda \approx$ 570 nm) coincides with that of the excited RO^-species in this solvent. Consequently, we attribute this observation to some ESPT of **3a** and **3b** to the solvent acetone.Finally, absorption spectra before normalization demonstrate the solubility of compounds **3d** and **3e** in water (Figure 1f). Both compounds are readily soluble in concentrations > 10^{-4} mol/L, yielding an optical density above 2. From the necessary dilution, we could estimate a saturation concentration of **3e** above 10 mM. This should be adequately high for biological use and for transient absorption measurements in water.[66–69]

Acidity constants

Photoacids are characterized by their acidity constants in ground and excited state. pK_a values of **3c-f** were analyzed in aqueous solution via absorption titration. Absorption spectra of **3e** in buffer solution with various pH values are shown in Figure 2a. An isosbestic point indicates a proper conversion from ROH to RO^- with increasing pH. Fluorescence correlation spectroscopy, which provides an alternative access to pK_a at very low concentrations, was used for pK_a determination of the hardly water-soluble sulfonic ester derivatives **3a** and **3b** (see *supporting information* for details).[74] pK_a values are roughly the same within the experimental error for all sulfonamide based photoacids (p$K_a \approx$ 5.6), but formal substitution of the sulfonamide by sulfonic ester groups decreases the pK_a by roughly one logarithmic unit (p$K_a \approx$ 4.4-4.7).

Fluorescence titration and Förster calculations were used to evaluate the pK_a* of the photoacids **3a-f**. Figure 2b shows absorption and emission spectra of compound **3a** in perchloric acid of different concentration, characterized by their Hammett acidity values H_0.[75,76] At all H_0 values, only the neutral species is present in the

Photochem. Photobiol. Sci., 2014, DOI: 10.1039/C3PP50404B

http://xlink.rsc.org/?doi=C3PP50404B

ground state. Its absorption is deformed at H_0 = -0.2 presumably due to the formation of non-fluorescent aggregates as a result of reduced solubility at low perchloric acid concentrations, i.e. high water content. For the same reason, fluorescence emission intensity is diminished at low acid concentrations. Nevertheless, with decreasing H_0 values the emission of anionic molecule decreases, since the high proton concentration shifts the dissociation equilibrium towards the fluorescence emission of the excited ROH form. Figure 2c illustrates the fluorescence intensity ratios of acid to base emission for all photoacids. pK_a* values (Table 2) were evaluated according to equation 1.[77]

$$R = R_1 + (R_2 - R_1)\frac{1}{1+10^{\mathrm{pH}-\mathrm{p}K_a}} \quad (1)$$

In equation 1, R is the fluorescence or absorbance ratio of λ_{max} (ROH) and λ_{max} (RO^-), whereas R_1 resp. R_2 represent the minimal and maximal ratio values observed at very high and low proton concentrations. Among the sulfonamide based dyes, **3f** seems to be the less acidic compound, whereas **3c** and **3e** are the strongest, which is slightly different to the ordering of the RO^-/ROH ratios in the steady-state fluorescence spectra in DMSO (Table 2). However, the differences are cancelled in the excited state acidities calculated by use of the Förster cycle. The change of the pK_a value ΔpK_a can be calculated from the fluorescence excitation and emission maxima in aqueous solution according to equation 2. The so determined pK_a* values will be refered to as Förster-pK_a* (see Table 2). With exception of **3a** and **3d**, the Förster-pK_a* values are found to be lower than those calculated from ratiometric titration.

(2)

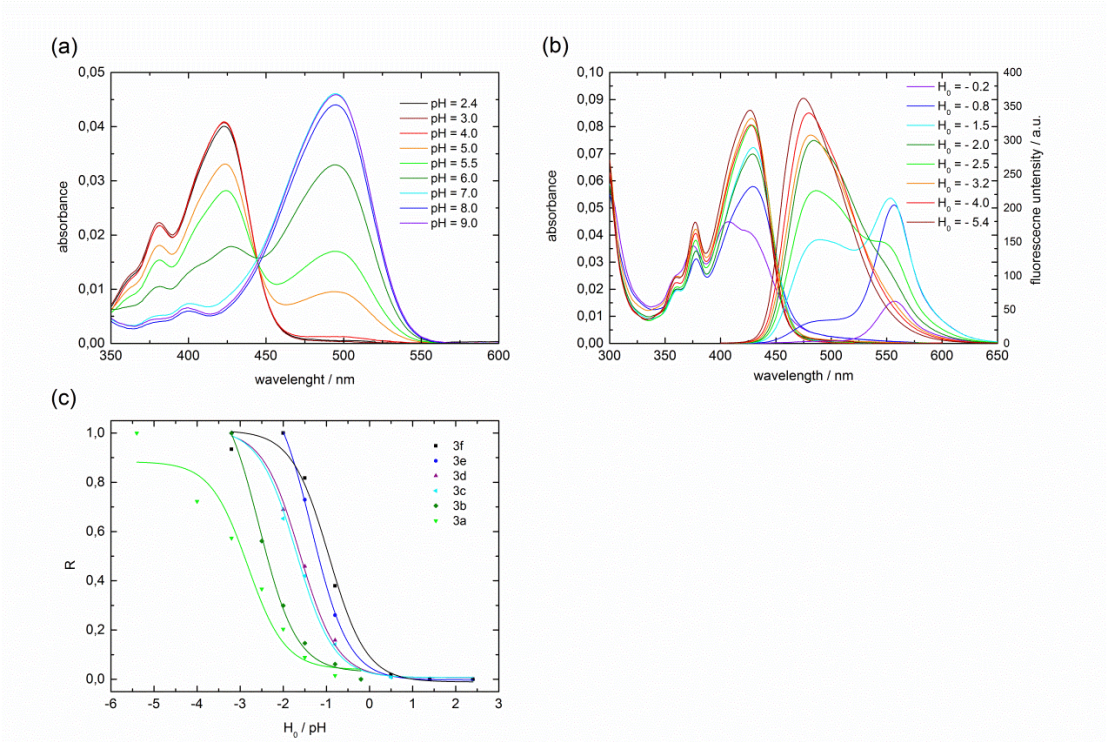

Figure 2: (a) Absorption titration of **3e** in buffer with the acid form absorbing at λ = 423 nm and the base form at λ = 495 nm. (b) Absorption and emission spectra of **3a** in perchloric acid of different concentration. The solubility decreases with higher water content. (c) Fluorescence intensity ratios of acid to base peak signals (λ_{max} see Table 1).

Table 2: pK_a -values; $\lambda_{abs,\,max}$ (H_2O) and $\lambda_{em,\,max}$ (H_2O) given in nm. Perchloric acid was used for acidification.

	3a		**3b**		**3c**		**3d**		**3e**		**3f**	
	RO^-	ROH	RO^-	ROH	RO^-	ROH	RO^-	ROH	RO^-	ROH	RO^-	ROH
$\lambda_{abs,\,max}$	516	426	526	414	509	429	499	427	495	423	494	422
$\lambda_{em,\,max}$	558	480	564	490	555	481	551	478	548	476	547	473
pK_a	4.7[a]		4.4[a]		5.6[b]		5.7[b]		5.6[b]		5.6[b]	
pK_a*[c]	-2.7		-3.9		-1.2		-0.8		-0.9		-1.0	
pK_a*[d]	-2.9		-2.5		-1.0		-1.0		-0.6		-0.3	

[a] determined by FCS.

[b] determined via absorption titration.

Photochem. Photobiol. Sci., 2014, DOI: 10.1039/C3PP50404B

[c] determined via Förster cycle.

[d] evaluated by fluorescence titration.

In any case, the sulfonic ester derivatives turned out to be about two logarithmic units more acidic than the sulfonamide based molecules independent of the method.

$$\Delta \mathrm{p}K_\mathrm{a} = \frac{(\mathrm{h}\nu_{\mathrm{ROH}} - \mathrm{h}\nu_{\mathrm{RO}^-})}{kT\ln(10)} \qquad (2)$$

Time-resolved spectroscopy

ESPT of the photoacids to DMSO was studied in more detail by time-correlated single-photon counting (TCSPC). The TCSPC histograms of the excited bases in neat DMSO (Figure 3a) follow a mono-exponential decay. Fluorescence lifetimes for all bases lie between 5.5 and 5.7 ns (see Table 3) indicating that the variation of the substituents does not greatly affect the fluorescence lifetime of the excited RO^- form in this solvent. A similar value was previously reported for **3f**.[45] In agreement to this long fluorescence lifetime, the fluorescence quantum yield in DMSO is found to be close to 90% or even higher for all excited RO^- species (Table 1).

Both the mono-exponential decay and the high quantum yield indicate that competitive processes to fluorescence are negligible. Furthermore, no distinct triplet population can be found in FCS experiments (see below).

In TFA acidified DMSO (Figure 3b) the fluorescence decay of neutral **3a-f** (λ_{det} = 420-460 nm) follows complex kinetics, which could not be entirely resolved by our experimental setup (IRF ~ 300 ps). Average decay time constants ($\tau_{\mathrm{fl,avg}}$) are in the range of 2.2-0.4 ns (see Table 3). The fluorescence signals of neutral **3d-f** appear to decay similar, but slower than those of the further photoacids. Especially **3a** and **3b** exhibit rapid fluorescence decays.

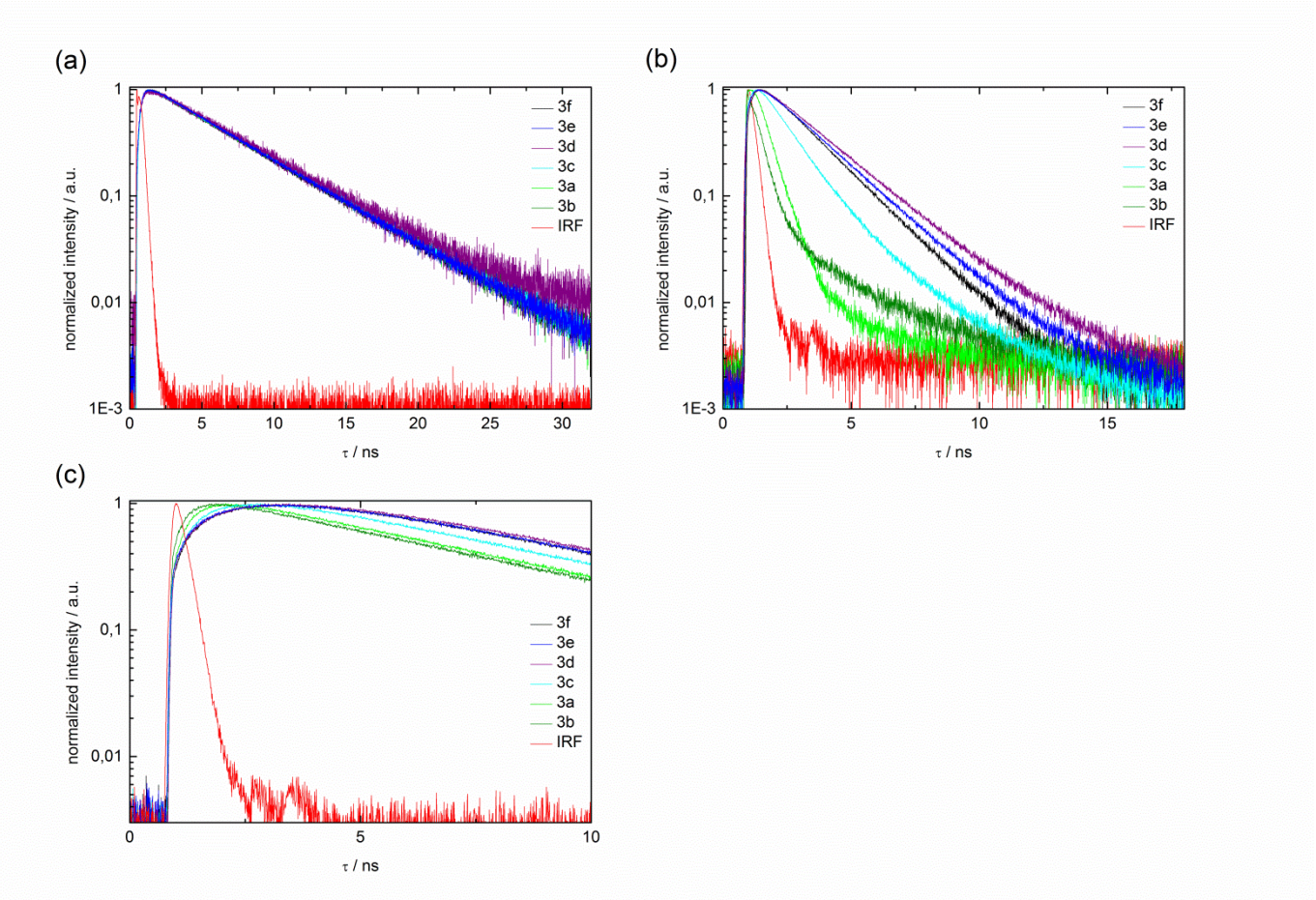

Figure 3: TCSPC-Histograms of the various photoacids: (a) λ_{ex} = 470 nm, λ_{det}= 550-600 nm, DMSO. (b) λ_{ex} = 405 nm λ_{det} = 420-460 nm, DMSO+TFA. (c) λ_{ex} = 405 nm, λ_{det}= 560-610 nm, DMSO+TFA.

Fluorescence decay of the excited acid ROH ($\tau_{\mathrm{fl,ROH}}$) is expected to be determined by the sum of the natural radiative rate constant of the photoacid k_{rad} and the rate constant of the proton transfer in the excited state k_{ESPT}

Photochem. Photobiol. Sci., 2014, DOI: 10.1039/C3PP50404B

http://xlink.rsc.org/?doi=C3PP50404B

(equation 3).[46] A mono-exponential decay is thus anticipated.

$$\tau_{\mathrm{fl,ROH}} = \frac{1}{k_{\mathrm{rad}} + k_{\mathrm{ESPT}}} \qquad (3)$$

However, the observed fluorescence decay is non-exponential and deviates especially at longer times from purely exponential progression. This indicates that more processes influence the fluorescence lifetime of the ROH form. Aberration from an exponential decay of the ROH* fluorescence has been observed for different photoacids in water and was attributed to arise from a geminate proton recombination process.[19,26,27,46] Currently, experiments are undertaken to explore whether diffusional processes or recombination in the excited state could be the reason for the unexpected behavior here as well.

At λ_{det} = 560-610 nm, TCSPC histograms of **3a-f** (Figure 3c) are described by two exponentials. The longer time component,

i.e. the decay, agrees with the lifetime of the anionic species determined by the histograms in Figure 3a. The short, rise time component with negative amplitude is attributed to the formation of the excited RO^- form caused by ESPT. Short time-components obtained by reconvolution analysis span the range between 1.8 and 0.2 ns and show similar values as the component determined at λ_{det} = 420-460 nm but are slightly smaller. Yet, the average decay time of **3b** at λ_{det} = 420-460 nm obtained by reconvolution fit ($\tau \sim 0.8$ ns) seems to differ from this trend. This constant is about four times longer than the rise time component at λ_{det} = 560-610 nm ($\tau \sim 0.2$ ns), which in turn is in good agreement with the excited state acidity of this compound (see discussion). This deviation is attributed to an enhanced detection of background fluorescence due to the low intensity of the ROH emission in the case of this strong photoacid. However, it is assumed that the rise time component of the RO^- form mirrors the same process as the main decay component of the ROH fluorescence. Consequently, these values reflect time component of the proton transfer in the excited state (τ_{ESPT}) (see Table 3).

Table 3: Fluorescence lifetimes of **3a-f**.

	3a	**3b**	**3c**	**3d**	**3e**	**3f**
$\tau_{\mathrm{fl,avg}}$, ns (DMSO, ROH)	0.4	0.8	1.4	2.2	2.0	1.8
τ_{ESPT}, ns (DMSO, RO^-)	0.4	0.2	0.9	1.8	1.7	1.6
$\tau_{\mathrm{fl,RO^-}}$, ns (DMSO, RO^-)	5.6	5.6	5.7	5.5	5.5	5.5

Photostability

A fundamental factor for usability of a chromophore in ultrasensitive spectroscopy is the resistance to photobleaching. The use of HPTS in such assays is hampered by its low photostability which is assumed to arise from the permanent negative charges.[78,79] Especially for microscopic applications, a good photostability is a key feature. Since all dyes are sufficiently soluble in water for FCS measurements, we determined their relative photostability in aqueous buffer solution (pH = 7.5) by use of this technique.[80] At the employed pH, almost two units above the highest pK_a values, all dyes exist solely in the anionic RO^- form. Furthermore, RO^- is the exclusively emissive form in water and its direct excitation with green light results in a lower background and simplifies the analysis since protonation can be ignored as a competitive source of fluctuations.

Shortly, fluorescence fluctuations arising from molecules into and out of the detection volume are autocorrelated. The longest time component of the autocorrelation decay, hence, results from diffusion through the detection volume. However, any light-driven, irreversible process competing with diffusion, leads to a smaller apparent diffusion time τ_{diff}. The extent, by which τ_{diff} is reduced upon increased excitation intensities, is a measure of the photostability. Equation 4 represents the kinetic description of photobleaching as competitive process to diffusion in analogy to the Stern-Volmer analysis.[80] k_{bl} is the photobleaching rate constant and can be determined by plotting $\tau_{\mathrm{diff}}(0)/\tau_{\mathrm{diff}}(I)$ against the excitation intensity I.

$$\frac{\tau_{\mathrm{diff}}(0)}{\tau_{\mathrm{diff}}(I)} = 1 + k_{\mathrm{bl}} \cdot \tau_{\mathrm{diff}}(0) \cdot I \qquad (4)$$

Photochem. Photobiol. Sci., 2014, DOI: 10.1039/C3PP50404B

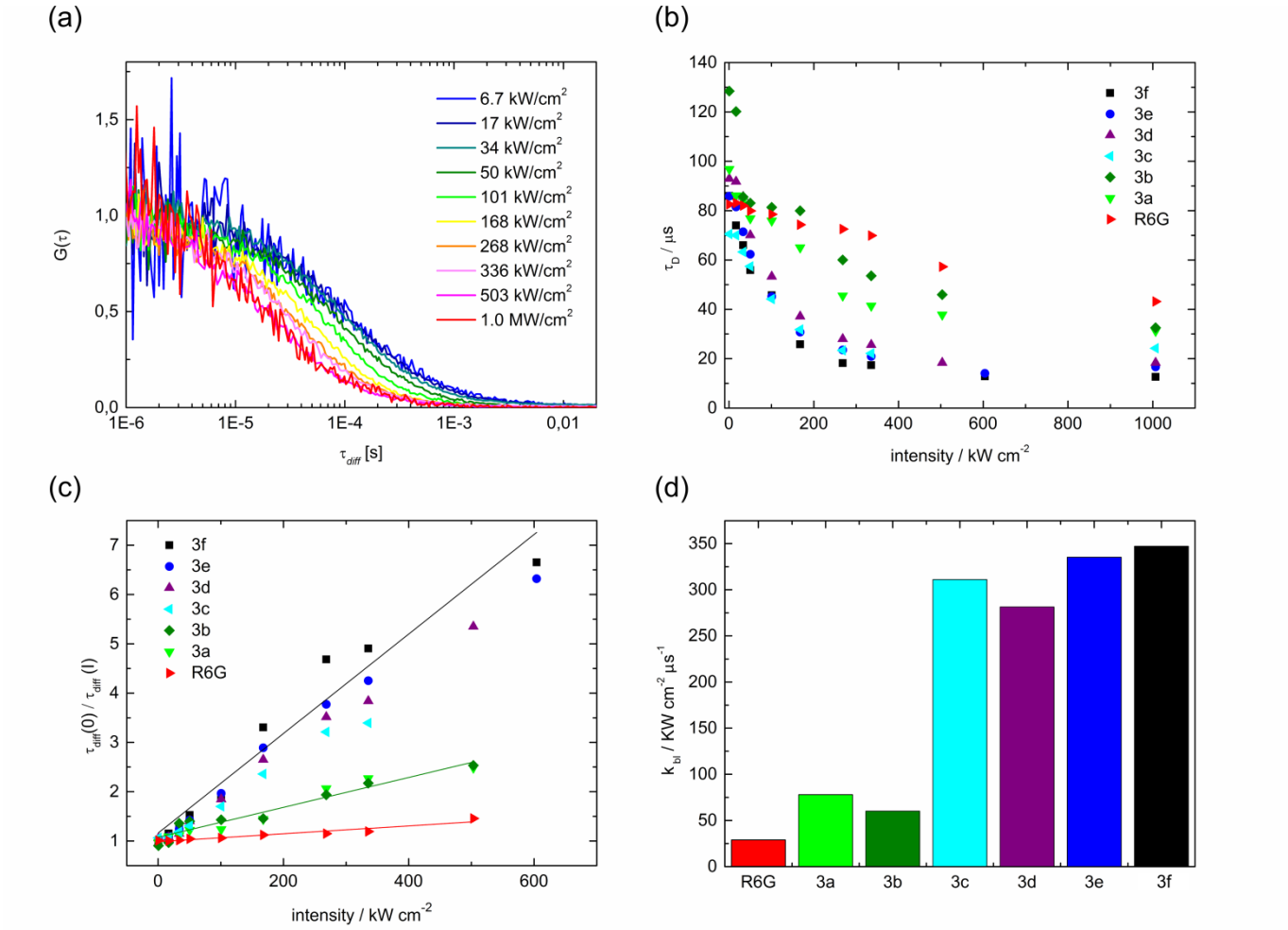

Figure 4: Investigation of the photostabilities of the photoacids in an aqueous medium. (a) Normalized FCS-curves of **3d** at various laser-intensities (λ_{exc} = 488 nm). (b) Measured diffusion times for all photoacids. (c) Stern-Volmer type analysis. (d) Rate constants of photobleaching after correction with the relative excitation cross sections.

All dyes were excited with intensities spanning more than two orders of magnitude. As reference, we selected rhodamine 6G (R6G) which is used for single-molecule experiments and known for its excellent photostability.[81,82] Its excitation and emission maxima beneficially are similar to those of deprotonated **3a-f**. Figure 4a shows the normalized auto-correlation functions of compound **3d** at intensities ranging from 6.7 to 1000 kW cm^{-2}. It turns out that the higher the laser intensity, the shorter τ_{diff}. This behavior is also observed for all other measured dyes (Figure 4b) and obeys the linear form of equation 4. Electronic saturation of all analyzed dyes was calculated to occur above 300 kW cm^{-2}. Accordingly, deviations of the linear relation at high intensities (> 500 kW cm^{-2}) likely result from saturation[80] and were therefore excluded from the analysis. The k_{bl} values shown in Figure 4d were obtained from dividing the slope of Figure 4c by $\tau_{\mathrm{diff}}(0)$ and further correction by the varying extinction coefficient at λ = 488 nm. Thus, the photostability of the examined molecules can be unequivocally compared due to the same experimental conditions.

It turns out, that the photostabilities of the fluorinated sulfonic esters are very close to the reference dye R6G. **3a** exhibits a bleaching rate constant k_{bl} less than the triple of R6G, while this value is even more lowered for **3b** being only about twice as high. All sulfonamide derivatives are commonly less photostable. Nevertheless, even the sulfonamide derivatives show sufficient photostability for *in vivo* fluorescence measurements.

Perspectives for biological application

Finally, we also investigated the capability of the photoacids for a potential *live cell* use. As mentioned before, highly negatively charged HPTS cannot penetrate intact cell membranes leading to a negative fluorescence staining (Figure 5a).

Although **3d** and especially **3e** can be dissolved in millimolar concentrations (Figure 1f), incubation for all cultures can be performed at lower concentrations. Unfortunately, compound **3e** does not cross the membrane of an intact cell, presumably due to the high hydrophilicity. Subsequently, we chose dyes with higher lipophilicity **3a** and **3c** and incubated Hep-G2 cells. Figure 5b-d show multiphoton fluorescence micrographs after treatment of Hep-G2 cells with **3a** and **3c**. The used dyes apparently cross the cell membrane within 20 minutes (**3c**) to 1 hour (**3a**) and accumulate in the cytosol. The accumulation may be due to adsorption of the lipophilic molecules to cellular compounds which are absent in the nucleus. Especially compound **3c** appears appropriate as fluorescence in the cytoplasma can be found within 1 minute after incubation (Figure 5c). A further staining of the nucleus is not observed.

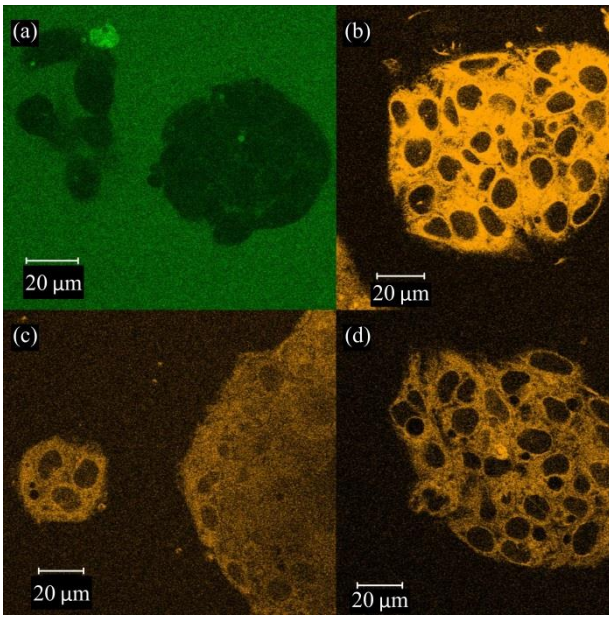

Figure 5: Clusters of Hep-G2 cells (λ_{ex}= 800 nm) incubated with (a) HPTS, λ_{det} = 495-591 nm, after 60 minutes; (b) **3a**, λ_{det} = 495-623 nm, after 60 minutes; (c) **3c**, λ_{det} = 495-591 nm, after 1 minutes and (d) 20 minute.

Discussion

A series of new photoacids, all derived from pyranine as starting material, is presented. They can be divided into two groups, i.e. the sulfonamides and sulfonic esters. The variation of the acidity of the sulfonamide derivatives can be understood by comparing the properties of the substituents. The acidity of the protonated 2-methoxy-N-(2-methoxyethyl)ethanamine and 2-(methylamino)ethanol lies in a similar range as that of dimethylamine (pK_a ~ 9-10).[83–85] Consequently, the electron-withdrawing strength of the corresponding sulfonamides is expected to be similar to that of **3f**. In contrast, the protonated form of N,O-dimethylhydroxylamine shows a pK_a of 4.75,[83] indicating an increased electron withdrawing strength of the corresponding sulfonamide in relation to the above mentioned amines. An even higher electron-withdrawing strength is anticipated for the sulfonic esters, due to the higher electronegativity of the oxygen atoms of **3a** and **3b** compared to the nitrogen atoms of the sulfonamides **3c-f**. A pK_a of 9.3[86] for 1,1,1,3,3,3-hexafluoro-2-propanol in contrast to pK_a = 12.4 for 2,2,2-trifluoroethanol[86] reveals the reduced charge density of the oxygen atom and hence points to a higher electron-withdrawing strength of the corresponding sulfonic ester. Accordingly, compound **3b** is expected to exhibit the highest acidity of all derivatives, even higher than that of **3a**. Therefore, although the Hammett-coefficients are not known for all substituents, acidity is expected to decrease in the order **3b** > **3a** > **3c** > **3d** ≈ **3e** ≈ **3f**. Actually, the substituents influence the experimental ground state acidity in the anticipated order with exception of **3c**.

The small change in pK_a by only one unit from the esters to the sulfonamides compared to the enhancement of the excited state acidity by more than two orders of magnitude, illustrates the greater impact of the substituents on the excited state properties. This behavior is also observed for substituted 1-naphtols.[17] The tendency of the excited state acidity is established in the computed Förster-pK_a* values. While **3d** and **3e** exhibit the lowest and **3c** the highest acidity of the sulfonamide photoactids, the pK_a* of **3b** was calculated to be the lowest of all compounds. As these values are calculated from spectroscopic data, i.e. Stokes shifts, it is understandable that absorption maxima of the ROH species as well as the emission maxima of RO^- largely follow the same ordering. However, specific interactions are analyzed elsewhere.[62]

The ESPT kinetics observed by TCSPC correlate well with the Förster-pK_a values, yielding a good agreement between thermodynamical and kinetic analysis. The acceleration of the fluorescence decay is attributed to the rising efficiency of the ESPT from **3e** to **3b**. The ESPT time constants τ_{ESPT} of **3a** and **3b** are more than twice as small as for the strongest sulfonamide based acid **3c** (0.9 ns), which is half of the ESPT time constant of the other sulfonamide derivatives. Accordingly, the ratio of the emission intensity of the neutral species to that of the corresponding base by excitation of the ROH species is a measure of the ESPT efficiency. While compounds with the most electron-withdrawing substituents **3a** and **3b** show nearly quantitative ESPT in DMSO, **3d** and **3e** which contain less electron withdrawing groups only partly dissociate after excitation.

Besides some minor variations like the different rate constants for the similar sulfonamides **3d-f**, noteworthy deviations from the general tendency derived above can

Photochem. Photobiol. Sci., 2014, DOI: 10.1039/C3PP50404B

be found. pK_a^* values determined by fluorescence titration do not exactly match the ordering of the ROH/RO$^-$ ratios observed in the steady-state spectra in DMSO. Especially the weakly water soluble derivative **3b** points to lower excited state acidities by more than one order of magnitude compared to pK_a* determined via Förster calculations. In addition, the pK_a* of **3f** (pK_a* ≈ -0.3) is slightly different to previous results[5] and does not fit to the above mentioned ordering. Also, the apparent higher pK_a* of **3a** in comparison to that of **3b** also contradicts the findings of the steady-state and time-resolved fluorescence spectroscopy in acidic DMSO. The divergence is ascribed to the fact that especially neutral **3b**, and to a lesser extent **3a** as well, is hardly soluble in water, which results in a low absorption and fluorescence intensity. The weak solubility of these two compounds is likely due to the increasing quantity of fluorine atoms in the molecule. Hence, titration experiments are affected by the low solubility of some neutral species as the ratio of the ROH and RO$^-$ form at low pH-values is vague. This hypothesis is supported by the observation that the values of the strongly water-soluble photoacids are distinctly less diverse. Nevertheless, the experimentally determined pK_a* values serve as a good approximation as a change of the ratio is clearly visible, but the ordering of the excited state acidities determined by Förster calculation is in better agreement with all other spectroscopic observations. Yet, it should be noted that also the Förster-pK_a* values present an approximation, since changes in the molecular geometry and solvation relaxation are not taken into account.[9,11]

Some more correlations of the Förster-pK_a* values with other spectroscopic data can be found. The Stokes shift of the bases and also the width of the anionic fluorescence emission band from λ_{FWHM} = 25 nm for **3d** and **3e** to λ_{FWHM} = 18 nm for **3b**, are diminished in the same order. Both observations could be qualitatively understood if one takes into account that the excited bases are the conjugated bases to the photoacids. Therefore, their spectroscopic behavior reflects the tendency of the acid in reversed order, i.e. the corresponding base of the strongest photoacid is the less interacting with the surrounding.

It is also worth to note that the photostability follows the trend **3b** > **3a** > sulfonamides. A unified picture, which comprises all mechanisms of photobleaching, is still lacking. Triplet states, higher excited states and/in combination with molecular oxygen are commonly regarded as reason for this degradation process.[80,87,88] It was reported for numerous chromophores that fluorination or trifluoromethylation of the aromatic core leads to an enhanced photostability.[89–93] Yet, the stabilizing effect of core-fluorination and -trifluoromethylation is ascribed mainly to the strong electron withdrawing properties of fluorine substituents.[91] Moreover, there are several examples of chromophores substituted with electron withdrawing cyano groups, that are also characterized by higher photostability compared to the unsubstituted molecule.[94–96] So, the electron withdrawing strength of the substituents could be the explanation for the enhanced photostability of the sulfonate based compounds **3a** and **3b**, and could explain why photoacidity and photostability are related. The fact that a clear and reproducible FCS-trace is observed for each dye can be interpreted as hint for sufficiently high photostability for further single-molecule experiments, especially as no triplet population could be detected by FCS.

Conclusions

We have synthesized a series of five new derivatives of HPTS. The physical- and photophysical properties of the HPTS backbone can be greatly modified to give a palette of photoacids with varying properties. Substitution of the sulfonic acid substituents can increase the excited state acidity up by to ~ 5 logarithmic units. Especially the chemical and photostable sulfonic ester derivatives exhibit almost quantitative ESPT in DMSO. In contrast to HPTS, all compounds lack negative charges and are sufficiently photostable for ultrasensitive fluorescence spectroscopy. All derivatives exhibit high quantum yields. While showing similar photochemical properties as **3f**, compounds **3d** and **3e** exhibit a significant solubility in aqueous media, whereas **3c** is strongly membrane permeable. Various applications in life sciences can be foreseen. Recently, we have addressed the origin of the enhanced photoacidity compared to HPTS in detail by solvatochromic studies.[62] Furthermore, the kinetics of the ESPT are investigated by femtosecond time-resolved spectroscopy and allow for examining its solvent-dependence.[63] Altogether, worthwhile and improved alternatives to HPTS are reported.

Experimental Section

General

8-Hydroxypyrene-1,3,6-trisulfonic acid (purity > 98%) was purchased from Acros Organics. All other reagents and solvents were obtained from Sigma-Aldrich, Merck or Acros Organics and used without further purification. For the chromatographic purification of **3e**, silica gel was washed prior to use with an 8:2 mixture of methylene chloride and methanol and dried in vacuo.

UV/Vis and Fluorescence Spectroscopy

Absorption spectra were recorded with Jasco Spectrophotometer V-650, fluorescence emission and

Photochem. Photobiol. Sci., 2014, DOI: 10.1039/C3PP50404B

http://xlink.rsc.org/?doi=C3PP50404B

excitation spectra with Jasco Spectrofluorometer FP-6500. Concentrations of the measured solutions were in micromolar range if not otherwise stated.

Time-Correlated Single-Photon Counting

TCSPC measurements were performed with a home-built setup. Excitation was done with pulsed laser diodes (PicoQuant, LDH-P-C-405, λ = 405 nm resp. PicoQuant, LDH-P-C-470, λ = 470 nm; pulse width = 60-120 ps) which were controlled by a diode laser driver unit (PDL 808 MC SEPIA, PicoQuant). A single-photon avalanche detector (PDM 100ct SPAD, Micro Photon Devices) in combination with a photon counting device (PicoHarp 300, PicoQuant) was used for detection. The overall instrumental response function was ~ 300 ps (FWHM). Obtained data were analysed by the SymPhoTime (PicoQuant) and FluoroFit (PicoQuant) software.

Fluorescence Correlation Spectroscopy

FCS measurements were performed using a custom built setup. Continuous-wave lasers (Picarro, Soliton, λ = 488 nm resp. Guided Laser Technologies, Fiber Laser FL546, λ = 546 nm) with a beam diameter of 0.7 mm were used as excitation source. The laser was coupled into an inverted microscope (Axiovert 200, Zeiss) and reflected by a dichroic mirror (495 DRLP resp. 555 DRLP Omega) into a water-immersion objective lens (PlanApo 63x, NA 1.2 WI, Zeiss). The beam was focused into a diffraction limited spot above the cover slide (0.17 ± 0.01 mm, Assistent). A drop of nanomolar dye solution placed on top of the cover slip served as sample. Emitted fluorescence was collected by the same objective, passed the dichroic mirror and focused by the tube lens onto a 50 µm pinhole. After filtering through a band pass filter (HQ 585/50 or HQ 590/70, AHF Analysentechnik), the light was split into two beams by 50:50 beam splitter. Photons were detected by two avalanche photodiodes (SPCM-14-AQR, Perkin-Elmer Optoelectronics). The output of these modules was cross-correlated by a hardware correlator (FLEX 02-01D/C, Correlator.com). Laser power was varied from 20 µW to 3 mW, corresponding to an intensity of 6.7-1000 kW/cm^2. Correlation data was analysed according to the 2D model consistent with Ref [80].

Two-photon-excitation laser scanning microscopy

Laser scanning microscopy was performed with a confocal laser microscope (LSM510 META, Zeiss; Objective: Plan-Neofluar 40x/1.3, Zeiss). Excitation was performed with a Ti:Sa laser (Chameleon XR, Coherent) operating at λ = 800 nm.

Cell culture

HepG2 cells were grown in IBIDI µ-dishes (Ø 35 mm ibiTreat 33327), RPMI 1640 medium with 10% FCS (Gibco, w/o phenol red) and incubated at 37°C, 5% CO_2 for 1-2 days. Before the experiment the cells were washed with PBS and new medium was added.

FTIR-spectroscopy

FTIR measurements were performed with a Bruker Vertex 80v spectrometer using a home-built liquid cell with a path length of 1 cm. This cell contains a stainless steel housing, PTFE spacer, a viton gasket and CaF_2-windows. In case of **3e**, a home-built liquid cell with a variable pathlength has been used, in case of **3e** a space of 75 µm was chosen. The IR spectra are measured by a using a HgCdTe photoconductive detector. An average of 64 spectra (in case of **3e** 128 spectra) at a resolution of 1 or 2 cm^{-1} has been recorded. All substances (except **3e**) have been solved in CCl_4 by using concentrations in the 10^{-4} mol/L range. Species **3e** has been solved in CD_3OD with a concentration of $2*10^{-2}$ mol/L. The IR measurements are used to characterize the structure of the investigated substances in the electronic ground state.

Syntheses

Trisodium 8-acetoxypyrene-1,3,6-trisulfonic acid (1): Trisodium 8-hydroxypyrene-1,3,6-trisulfonic acid (2.28 g; 4.35 mmol) and sodium acetate (35.7 mg, 0.44 mmol) were suspended in acetic anhydride (25 mL) and refluxed for 35 hours. After the suspension was cooled down to room temperature, it was diluted with THF and filtered off. The residue was washed with acetone and dried in vacuum yielding a grey powder (2.26 g, 3.99 mmol, 92%). UV/Vis (H_2O): λ_{max} = 368 nm; fluorescence (H_2O): λ_{max} = 389 nm. ^{1}H-NMR (400 MHz, DMSO-d6, 25°C): δ = 9.24 (1 H, d, ^3J(H,H)= 9.6 Hz, Ar-*H*), 9.15 (1 H, d, ^3J(H,H) = 9.6 Hz, Ar-*H*), 9.12 (1 H, d, ^3J(H,H) = 9.6 Hz, Ar-*H*), 9.08 (1 H, s, Ar-*H*), 8.27 (1 H, s, Ar-*H*), 8.13 (1 H, d, ^3J(H,H) = 9.6 Hz, Ar-*H*), 2.57 ppm (3 H, s, COC*H*$_3$), ^{13}C-NMR (100 MHz, DMSO-d6, 25°C): δ = 169.9, 143.0, 142.6, 141.1, 140.9, 127.7, 127.3, 127.0, 125.9, 125.7, 125.1, 124.7, 124.6, 124.5, 122.9, 119.8, 119.2, 20.8 ppm. MS (ESI): *m/z* calc. for $C_{18}H_9Na_3O_{11}S_3$: 565.90 $[M]^+$, found: 566.48.

8-Acetoxypyrene-1,3,6-trisulfonyl chloride (2): Compound **1** (1.09 g, 1.93 mmol) was suspended in thionylchloride (5 mL). After addition of dimethylformamide (30 µL), the mixture was heated to reflux for 5 hours. The solution was cooled down to ambient temperature and poured on ice. After precipitation, **2** was filtered off and was obtained as orange powder after drying in vacuo. (1.04 g, 1.88 mmol, 97%). ^{1}H-NMR (400 MHz, DMSO-d6, 25°C): δ = 9.67 (1 H, d, ^3J (H,H) = 10.0 Hz, Ar-*H*), 9.62 (1 H, s, Ar-*H*), 9.50 (1 H, d, ^3J (H,H) = 10.0 Hz, Ar-*H*), 9.44 (1 H, d, ^3J (H,H) = 9.6 Hz, Ar-*H*), 8.91 (1 H, s, Ar-*H*), 8.82

Photochem. Photobiol. Sci., 2014, DOI: 10.1039/C3PP50404B

http://xlink.rsc.org/?doi=C3PP50404B

(1 H, d, ^3J (H,H) = 10.0 Hz, Ar-*H*), 2.68 ppm (3 H, s, COC*H*$_3$).

General procedure for synthesis of derivatives 3a-e: Triethylamine (see individual procedure) was added to a solution of alcohols resp. amines in methylene chloride (1 mL / 0.5 mmol of reagent) and the mixture was cooled to 0 °C. Compound **2** was dissolved in methylene chloride (5 mL / 0.1 mmol of **2**) and added drop-wise to the reaction mixture. After warming up to room temperature and stirring for 48 h, hydrochloric acid (1 M, 20 mL) was added to the solution. The organic phase was separated, extracted three times with hydrochloric acid (1 M) and saturated sodium chloride-solution before being dried over sodium sulfate. After evaporation, the crude product was purified via column chromatography.

Tris(2,2,2-trifluoroethyl) 8-hydroxypyrene-1,3,6-trisulfonate (3a): Following the general procedure, 2,2,2-trifluoroethanol (118.5 mg, 1.18 mmol) was reacted with **2** (131.2 mg, 0.24 mmol) after addition of trietylamine (132.3 mg, 1.30 mmol). Column chromatographic purification (eluent: ethyl acetate/petrolether 40-65 = 3.5 : 6.5) gave a yellow powder of **3a** (121,0 mg, 0.17 mmol, 73%). UV/Vis (DMSO+TFA): λ_{max} = 440 nm, (DMSO): λ_{max} = 568 nm, $\varepsilon_{(568)}$ (RO$^-$) = 60000 L mol^{-1} cm^{-1}, fluorescence (DMSO; DMSO+TFA): λ_{max} = 574 nm. IR (CCl_4): $\tilde{\nu}$ = 1377, 1742, 2855, 2928, 2959, 3118, 3531 cm^{-1}. ^{1}H-NMR (400 MHz, acetone-d6, 25°C): δ = 9.38 (1 H, s, Ar-*H*), 9.27 (1 H, d, ^3J (H,H) = 10.0 Hz, Ar-*H*), 9.15 (1 H, d, ^3J (H,H) = 9.2 Hz, Ar-*H*), 9.04 (1 H, d, ^3J (H,H) = 9.2 Hz, Ar-*H*), 8.99 (1 H, d, ^3J (H,H) = 10.0 Hz, Ar-*H*), 8.62 (1 H, s, Ar-*H*), 4.90 ppm (6 H, m, 3 C*H*$_2$-CF$_3$). ^{13}C-NMR (100 MHz, acetone-d6, 25°C): δ = 156.5, 135.4, 134.1, 133.6, 132.4, 130.5, 129.1, 127.1, 126.9, 126.4, 126.1 (q, ^1J (C,F) = 277.3 Hz, 3 C, 3 *C*F$_3$), 125.2, 123.3, 122.9, 122.0, 121.0, 118.4, 66.5 ppm (q, ^2J (C,F) = 37.4 Hz, 3 C, 3 *C*H$_2$-CF$_3$), ^{19}F-NMR (376 MHz, DMSO-d6, 25°C): δ = -74.96, -74.98, -74.99 ppm. MS (ESI): *m/z* calc. for $C_{22}H_{13}F_9O_{10}S_3$: 702.94 [M-H]$^-$, found: 702.84.

Tris(1,1,1,3,3,3-hexafluoropropan-2-yl) 8-hydroxypyrene-1,3,6-trisulfonate (3b): Compound **3b** was obtained following the general procedure. After application of triethylamine (213.3 mg, 2.11 mmol), 1,1,1,3,3,3-hexafluoroisopropanol (322.1 mg, 1.92 mmol) was reacted with compound **2** (214.2 mg, 0.38 mmol). Compound **3b** was purified by column chromatography (eluent: ethyl acetate/petrolether 40-65 = 3 : 7) and was obtained as orange powder (274.0 mg, 0.30 mmol, 79%). UV/Vis (DMSO+TFA): λ_{max} = 449 nm, (DMSO): λ_{max} = 576 nm, $\varepsilon_{(576)}$ (RO$^-$) = 60000 L mol^{-1} cm^{-1}, fluorescence (DMSO; DMSO+TFA): λ_{max} = 581 nm. IR (CCl_4): $\tilde{\nu}$ = 1053, 1112, 1186, 1300, 1380, 1413, 1622, 2857, 2928, 2975, 3129, 3464 cm^{-1}. ^{1}H-NMR (400 MHz, acetone-d6, 25°C): δ = 9.41 (1 H, s, Ar-*H*), 9.36 (1 H, d, ^3J (H,H) = 9.8 Hz, Ar-*H*), 9.25 (1 H, d, ^3J (H,H) = 9.5 Hz, Ar-*H*), 9.08 (1 H, d, ^3J (H,H) = 9.5 Hz, Ar-*H*), 9.06 (1 H, d, ^3J (H,H) = 9.8 Hz, Ar-*H*), 8.67 (1 H, s, Ar-*H*), 6.48 (1 H, hep, ^3J (H,F) = 5.8 Hz, C*H*(CF$_3$)$_2$), 6.39 (1 H, hep, ^3J (H,F) = 5.8 Hz, C*H*(CF$_3$)$_2$), 6.35 ppm (1 H, hep, ^3J (H,F) = 5.8 Hz, C*H*(CF$_3$)$_2$), ^{13}C-NMR (100 MHz, acetone-d6, 25°C): δ = 157.3, 136.0, 134.5, 134.0, 132.4, 131.2, 130.3, 126.7, 126.5, 126.4, 126.1, 125.0, 123.3, 123.2, 120.9, 119,8 (6 C, q, ^1J (C,F) = 278.8 Hz, 6 *C*F$_3$), 118.8, 73.4 ppm (3 C, hep, ^2J (C,F) = 35.2 Hz, 3 *C*H-(CF$_3$)$_2$), ^{19}F-NMR (376 MHz, DMSO-d6, 25°C): δ = -74.34; -74.37, -74.41 ppm. MS (ESI): *m/z* calc. for $C_{25}H_{10}F_{18}O_{10}S_3$: 906.91 [M-H]$^-$, found: 906.97.

8-Hydroxy-*N,N',N''*-trimethoxy-*N,N',N''*-trimethylpyrene-1,3,6-trisulfonamide (3c): Synthesis of compound **3c** follows the general procedure. N,O-Dimethylhydroxylamine hydrochloride (164.4 mg, 1.69 mmol) was deprotonated with triethylamine (312.8 ml, 3.09 mmol) and reacted with **2** (156.1 mg, 0.23 mmol). After column chromatographic purification (eluent: ethyl acetate/petrolether 40-65 = 6 : 4), **3c** was obtained as yellow powder (103.0 mg, 0.18 mmol, 62%). UV/Vis (DMSO+TFA): λ_{max} = 438 nm, (DMSO): λ_{max} = 568 nm, $\varepsilon_{(568)}$ (RO$^-$) = 53000 L mol^{-1} cm^{-1}, fluorescence (DMSO; DMSO+TFA): λ_{max} = 576 nm. IR (CCl_4): $\tilde{\nu}$ = 1157, 1346, 2856, 2929, 2980, 3137, 3452, 3589 cm^{-1}. ^{1}H-NMR (400 MHz, acetone-d6, 25°C): δ = 9.51 (1 H, d, ^3J (H,H) = 9.8 Hz, Ar-*H*), 9.48 (1 H, d, ^3J (H,H) = 9.5 Hz, Ar-*H*), 9.32 (1 H, d, ^3J (H,H) = 9.8 Hz, Ar-*H*), 9.29 (1 H, s, Ar-*H*), 9.01 (1 H, d, ^3J (H,H) = 9.5 Hz, Ar-*H*), 8.50 (1 H, s, Ar-*H*), 3.78 (3 H, s, OC*H*$_3$), 3.76 (6 H, s, 2 OC*H*$_3$), 2.96 (3 H, s, NC*H*$_3$), 2.95 (3 H, s, NC*H*$_3$), 2.92 ppm (3 H, s, NC*H*$_3$), ^{13}C-NMR (100 MHz, acetone-d6, 25°C): δ = 154.9, 136.5, 135.5, 135.3, 131.3, 131.0, 127.3, 126.8, 126.7, 126.3, 125.8, 125.7, 124.0, 123.5, 123.0, 119.1, 63.9, 63.8, 63.7, 39.2, 39.1, 39.0 ppm. MS (ESI): *m/z* calc. for $C_{22}H_{25}N_3O_{10}S_3$: 586.06 [M-H]$^-$, found: 586.07.

8-Hydroxy-*N,N,N',N',N'',N''*-hexakis(2-methoxyethyl)pyrene-1,3,6-trisulfonamide (3d): Following the general procedure, **2** (62.3 mg, 0.11 mmol) was reacted with 2-methoxy-N-(2-methoxyethyl)ethanamine (51.2 mg, 0.39 mmol) in presence of triethylamine (61.2 mg, 0.61 mmol). The crude product was purified by column chromatography (eluent: ethyl acetate/petrolether 40-65 = 9 : 1). After the solvent was removed in vacuo, **3d** was obtained as yellow, highly hygroscopic powder (Yield could not be determined). UV/Vis (DMSO+TFA): λ_{max} = 431 nm, (DMSO): λ_{max} = 555 nm, fluorescence (DMSO;

http://xlink.rsc.org/?doi=C3PP50404B

DMSO+TFA): λ_{max} = 567 nm. IR (CCl_4): $\tilde{\nu}$ = 1115, 1151, 1373, 1687, 2931, 2984, 3591 cm^{-1}. ^{1}H-NMR (400 MHz, acetone-d6, 25°C): δ = 9.26 (1 H, d, ^3J (H,H) = 10.0 Hz, Ar-*H*), 9.24 (1 H, s, Ar-*H*), 9.09 (1 H, d, ^3J (H,H) = 9.8 Hz, Ar-*H*), 9.01 (1 H, d, ^3J (H,H) = 10.0 Hz, Ar-*H*), 8.90 (1 H, d, ^3J (H,H) = 9.8 Hz, Ar-*H*), 8.44 (1 H, s, Ar-*H*), 3.65 (12 H, m, 6 NCH_2CH_2O), 3.48 (12 H, m, 6 NCH_2CH_2O), 3.13 (6 H, s, 2 OCH_3), 3.08 (6 H, s, 2 OCH_3), 3.07 ppm (6 H, s, 2 OCH_3), ^{13}C-NMR (100 MHz, DMSO-d6, 25°C): δ = 154.6, 136.9, 132.1, 131.8, 130.9, 130.8, 130.7, 128.9, 128.1, 126.1, 125.8, 125.5, 123.7, 121.6, 119.1, 115.5, 70.1 (2 C), 70.0 (2 C), 69.9 (2 C), 58.0 (2 C), 57.9 (4 C), 47.3 (2 C), 46.9 (4 C) ppm. MS (ESI): *m/z* calc. for $C_{34}H_{49}N_3O_{13}S_3$:826.23 $[M+Na]^+$, found: 826.21.

8-Hydroxy-*N,N',N''*-tris(2-hydroxyethyl)-*N,N',N''*-trimethylpyrene-1,3,6-trisulfonamide (3e): Compound **3e** was synthesized according the general procedure. 2-(Methylamino)ethanol (55.9 mg, 0.74 mmol) was reacted with **2** (82.7 mg, 0.15 mmol) after addition of triethylamine (82.9 mg, 0.82 mmol). Crude **3e** was purified by column chromatography (eluent: methanol/methylene chloride = 1 : 9) to give a yellow powder (85.4 mg, 0.14 mmol, 91%). UV/Vis (DMSO+TFA): λ_{max} = 430 nm; (DMSO): λ_{max} = 554 nm; $\varepsilon_{(554)}$ (RO^-) = 35000 L mol^{-1} cm^{-1}, fluorescence (DMSO; DMSO+TFA): λ_{max} = 566 nm. IR (CD_3OD): $\tilde{\nu}$ = 1337, 1415, 2615, 3345 cm^{-1}. ^{1}H-NMR (400 MHz, DMSO-d6, 25°C): δ = 9.14 (1 H, d, ^3J (H,H) = 9.8 Hz, Ar-*H*), 8.97 (1 H, d, ^3J (H,H) = 9.6 Hz, Ar-*H*), 8.94 (1 H, s, Ar-*H*), 8.86 (1 H, d, ^3J (H,H) = 9.8 Hz, Ar-*H*), 8.80 (1 H, d, ^3J (H,H) = 9.6 Hz, Ar-*H*), 8.23 (1 H, s, Ar-*H*), 3.49 (6 H, m, 3 NCH_2CH_2O), 3.26 (6 H, m, 3 NCH_2CH_2O), 2.88 (3 H, s; NCH_3), 2.86 (3 H, s, NCH_3), 2.85 ppm (3 H, s, NCH_3), ^{13}C-NMR (100 MHz, DMSO-d6, 25°C): δ = 154.6, 135.6, 132.2, 131.0, 129.8, 129.6, 129.0, 128.3, 126.1, 126.0, 125.6, 123.7, 121.6, 120.5, 119.2, 115.5, 59.1, 59.0 (2C), 51.7, 51.5 (2 C), 35.4, 35.2 ppm (2 C). MS (ESI): *m/z* calc. for $C_{25}H_{31}N_3O_{10}S_3$: 652.11 $[M+Na]^+$, found: 652.27.

8-Hydroxypyren-*N,N,N',N',N'',N''*-hexamethyl-1,3,6-trisulfonamide (3f, HPTA): Compound **2** (168.5 mg, 0.30 mmol) was suspended in a cooled (0° C) 5 mL dimethyl amine solution (40% in H_2O). After stirring for 24h and warming up to room temperature, the solution was acidified with hydrochloric acid (1M) causing a precipitation of crude **3f**. The yellow solid was filtered off, dissolved in ethyl acetate and washed twice with saturated sodium chloride-solution. After being dried over sodium sulfate and evaporation, **3f** was purified by column chromatography (eluent: ethyl acetate/petrolether 40-65 = 6 : 4) and obtained as yellow powder (102.8 mg, 0,190 mmol, 63%). UV/Vis (DMSO+TFA): λ_{max} = 431 nm, (DMSO): λ_{max} = 554 nm, $\varepsilon_{(554)}$ (RO^-) = 37000 L mol^{-1} cm^{-1}, fluorescence (DMSO; DMSO+TFA): λ_{max} = 565 nm. IR (CCl_4): $\tilde{\nu}$ = 1114, 1162, 2855, 2928, 2960, 3280 cm^{-1}. ^{1}H-NMR (400 MHz, DMSO-d6, 25°C): δ = 9.27 (1 H, d, ^3J (H,H) = 10.0 Hz, Ar-*H*), 9.15 (1 H, d, ^3J (H,H) = 10.0 Hz, Ar-*H*), 9.02 (1 H, d, ^3J (H,H) = 10.0 Hz, Ar-*H*), 8.98 (1 H, s, Ar-*H*), 8.87 (1 H, d, ^3J (H,H) = 10.0 Hz, Ar-*H*), 8.31 (1 H, s, Ar-*H*), 2.83 (6 H, s, 2 NCH_3), 2.81 ppm (12 H, s, 4 NCH_3), ^{13}C-NMR (100 MHz, DMSO-d6, 25°C): δ = 154.7, 133.8, 132.7, 131.6, 130.0, 128.0, 127.8 (2 C), 126.3, 125.5 (2 C), 123.8, 121.7, 120.7, 119.6, 116.3, 37.4 (2 C), 37.3 ppm (4 C). MS (ESI): *m/z* calc. for $C_{22}H_{25}N_3O_7S_3$: 539.09 $[M]^+$, found: 539.10.

Acknowledgements

Financial support by the German Science Foundation (DFG, JU650/3-1) is gratefully noticed. Furthermore we thank Devid Hero, Saarland University, for the recording of the mass spectra.

Notes and references

[a]Biophysical Chemistry, Saarland University, Campus B2 2, 66123 Saarbrücken, Germany.
[b]Fraunhofer-IBMT, Ensheimer Straße 48, 66386 St. Ingbert, Germany.
[c]Technische Universität Kaiserslautern & Research Center Optimas, Fachbereich Chemie, Erwin-Schrödinger-Str., 67663 Kaiserslautern, Germany.

Electronic Supplementary Information (ESI) available: [details of any supplementary information available should be included here]. See DOI: 10.1039/b000000x/

1. J. Steadman and J. A. Syage, Picosecond mass • selective measurements of phenol • (NH3)n acid-base chemistry in clusters, *J. Chem. Phys.*, 1990, **92**, 4630–4632.
2. J. Syage and J. Steadman, Picosecond measurements of phenol excited-state proton transfer in clusters, *J. Chem. Phys.*, 1991, **95**, 2497–2510.
3. J. A. Syage, Tunneling mechanism for excited-state proton transfer in phenol-ammonia clusters, *J. Phys. Chem.*, 1993, **97**, 12523–12529.
4. S. Kaneko, S. Yotoriyama, H. Koda, and S. Tobita, Excited-state proton transfer to solvent from phenol and cyanophenols in water, *J. Phys. Chem. A*, 2009, **113**, 3021–3028.
5. E. Pines, in *The Chemistry of Phenols*, ed. Z. Rappoport, John Wiley & Sons, Ltd. **2003**, pp. 491–527.
6. I. Martynov, A. Demyashkevich, B. M. Uzhinov, M. G. Kuz'min, Proton transfer reactions in the excited electronic states of aromatic molecules, *Russ. Chem. Rev.*, 1977, **46**, 3–31.

7. A. Jankowski, P. Stefanowicz, and P. Dobryszycki, Excited state proton transfer in 2-naphthol derivatives bound to selected sites of proteins, *J. Photochem. Photobiol. A Chem.*, 1992, **69**, 57–66.
8. L. M. Tolbert and J. E. Haubrich, Enhanced photoacidities of cyanonaphthols, *J. Am. Chem. Soc.*, 1990, **112**, 8163–8165.
9. L. M. Tolbert and J. E. Haubrich, Photoexcited proton transfer from enhanced photoacids, *J. Am. Chem. Soc.*, 1994, **116**, 10593–10600.
10. S. Kim, J. Breen, D. Willberg, L. W. Peng, A. Heikal, J. A. Syage and A. H. Zewail, Solvation ultrafast dynamics of reactions. 8. Acid-base reactions in finite-sized clusters of naphthol in ammonia, water, and piperidine, *J. Phys. Chem.*, 1995, **99**, 7421–7435.
11. D. Huppert, L. M. Tolbert, and S. Linares-Samaniego, Ultrafast excited-state proton transfer from cyano-substituted 2-naphthols, *J. Phys. Chem. A*, 1997, **101**, 4602–4605.
12. K. Solntsev, D. Huppert, L. M. Tolbert and N. Agmon, Solvatochromic shifts of “super” photoacids, *J. Am. Chem. Soc.*, 1998, **120**, 7981–7982.
13. R. Knochenmuss, K. M. Solntsev, and L. M. Tolbert, Molecular beam studies of the “super”photoacid 5-cyano-2-naphthol in solvent clusters, *J. Phys. Chem. A*, 2001, **105**, 6393–6401.
14. C. Clower, K. M. Solntsev, J. Kowalik, L. M. Tolbert, and D. Huppert, Photochemistry of “super” photoacids. 3. Excited-state proton transfer from perfluoroalkylsulfonyl-substituted 2-naphthols, *J. Phys. Chem. A*, 2002, **106**, 3114–3122.
15. L. M. Tolbert and K. M. Solntsev, Excited-state proton transfer: from constrained systems to “super”photoacids to superfast proton transfer, *Acc. Chem. Res.*, 2002, **35**, 19–27.
16. F. De Vleeschouwer, W. Yang, D. N. Beratan, P. Geerlings, and F. De Proft, Inverse design of molecules with optimal reactivity properties: acidity of 2-naphthol derivatives, *Phys. Chem. Chem. Phys.*, 2012, **14**, 16002–16013.
17. M. Prémont-Schwarz, T. Barak, D. Pines, E. T. J. Nibbering, and E. Pines, Ultrafast excited state proton transfer reaction of 1-naphthol-3,6-disulfonate and several 5-substituted 1-naphthol derivatives, *J. Phys. Chem. B*, 2013, **117**, 4593–4594.
18. K. M. Solntsev, D. Huppert, and N. Agmon, Photochemistry of “super”-photoacids. Solvent effects, *J. Phys. Chem. A*, 1999, **103**, 6984–6997.
19. I. Carmeli, D. Huppert, L. M. Tolbert, and J. E. Haubrich, Ultrafast excited-state proton transfer from dicyano-naphthol, *Chem. Phys. Lett.*, 1996, **260**, 109–114.
20. B. Cohen, J. Segal, and D. Huppert, Proton transfer from photoacid to solvent, *J. Phys. Chem. A*, 2002, **106**, 7462–7467.
21. K. M. Solntsev, L. M. Tolbert, B. Cohen, D. Huppert, Y. Hayashi, and Y. Feldman, Excited-state proton transfer in chiral environments. 1. Chiral solvents, *J. Am. Chem. Soc.*, 2002, **124**, 9046–9047.
22. N. Agmon, Elementary steps in excited-state proton transfer, *J. Phys. Chem. A*, 2005, **109**, 13–35.
23. D. Pines, E. T. J. Nibbering, and E. Pines, Relaxation to equilibrium following photoacid dissociation in mineral acids and buffer solutions, *J. Phys. Condens. Matter*, 2007, **19**, 065134 1-14.
24. T. Förster, Fluoreszenzspektrum und Wasserstoffionenkonzentration, *Naturwissenschaften*, 1949, **6**, 186–187.
25. T. Förster, Dissoziation angeregter Moleküle, *Zeitschrift für Elektrochemie*, 1950, **54**, 42–46.
26. E. Pines, D. Huppert, and N. Agmon, Geminate recombination in excited-state proton-transfer reactions: Numerical solution of the Debye–Smoluchowski equation with backreaction and comparison with experimental results, *J. Chem. Phys.*, 1988, **88**, 5620–5630.
27. N. Agmon, E. Pines, and D. Huppert, Geminate recombination in proton-transfer reactions. II. Comparaison of diffusional and kinetic schemes, *J. Chem. Phys.*, 1988, **88**, 5631–5638.
28. T.-H. Tran-Thi, T. Gustavsson, C. Prayer, S. Pommeret, and J. T. Hynes, Primary ultrafast events preceding the photoinduced proton transfer from pyranine to water, *Chem. Phys. Lett.*, 2000, **329**, 421–430.
29. J. T. Hynes, T.-H. Tran-Thi, and G. Granucci, Intermolecular photochemical proton transfer in solution: new insights and perspectives, *J. Photochem. Photobiol. A Chem.*, 2002, **154**, 3–11.
30. P. Leiderman, L. Genosar, and D. Huppert, Excited-state proton transfer : Indication of three steps in the dissociation and recombination process, *J. Phys. Chem. A*, 2005, **109**, 5965–5977.
31. D. B. Spry, A. Goun, and M. D. Fayer, Deprotonation dynamics and stokes shift of pyranine (HPTS), *J. Phys. Chem. A*, 2007, **111**, 230–237.
32. G. Jung, S. Gerharz, and A. Schmitt, Solvent-dependent steady-state fluorescence spectroscopy for searching ESPT-dyes: Solvatochromism of HPTS revisited, *Phys. Chem. Chem. Phys.*, 2009, **11**, 1416–1426.
33. W. Liu, F. Han, C. Smith, and C. Fang, Ultrafast conformational dynamics of pyranine during excited state proton transfer in aqueous solution revealed by femtosecond stimulated Raman spectroscopy, *J. Phys. Chem. B*, 2012, **116**, 10535–10550.
34. E. Pines, D. Huppert, and N. Agmon, Salt effects on steady-state quantum yields of ultrafast, diffusion-influenced, reversible photoacid dissociation reactions, *J. Phys. Chem.*, 1991, **25**, 666–674.
35. M. Rini, B.-Z. Magnes, E. Pines, and E. T. J. Nibbering, Real-time observation of bimodal proton transfer in acid-base pairs in water, *Science*, 2003, **301**, 349–352.
36. E. Pines and D. Huppert, Observation of geminate recombination in excited state proton transfer, *J. Chem. Phys.*, 1986, **84**, 3576–3577.

Photochem. Photobiol. Sci., 2014, DOI: 10.1039/C3PP50404B

http://xlink.rsc.org/?doi=C3PP50404B

37. D. Pines, E. Pines, in *Hydrogen-Transfer Reactions*, ed. J. T. Hynes, J. P. Klinman, H.-H. Limbach, R. L. Schowen, Wiley-VCH Verlag GmbH & Co. KGaA, Weinheim **2006**, pp. 377–415.
38. N. Barrash-Shiftan, B. B. Brauer, and E. Pines, Solvent dependence of pyranine fluorescence and UV-visible absorption spectra, *J. Phys. Org. Chem.*, 1998, **11**, 743–750.
39. D. Pines and E. Pines, Direct observation of power-law behavior in the asymptotic relaxation to equilibrium of a reversible bimolecular reaction, *J. Chem. Phys.*, 2001, **115**, 951–953.
40. Y. Wang, W. Liu, L. Tang, B. Oscar, F. Han, and C. Fang, Early time excited-state structural evolution of pyranine in methanol revealed by femtosecond stimulated Raman spectroscopy, *J. Phys. Chem. A*, 2013, **117**, 6024–6042.
41. F. Han, W. Liu, and C. Fang, Excited-state proton transfer of photoexcited pyranine in water observed by femtosecond stimulated Raman spectroscopy, *Chem. Phys.*, 2013, **422**, 204–219.
42. T.-H. Tran-Thi, C. Prayer, P. Millié, P. Uznanski, and J. T. Hynes, Substituent and solvent effects on the nature of the transitions of pyrenol and pyranine. identification of an intermediate in the excited-state proton-transfer reaction, *J. Phys. Chem. A*, 2002, **106**, 2244–2255.
43. O. F. Mohammed, D. Pines, J. Dreyer, E. Pines, and E. T. J. Nibbering, Sequential proton transfer through water bridges in acid-base reactions, *Science*, 2005, **310**, 83–86.
44. D. B. Spry and M. D. Fayer, Charge redistribution and photoacidity: Neutral versus cationic photoacids, *J. Chem. Phys.*, 2008, **128**, 084508 1–9.
45. D. B. Spry and M. D. Fayer, Observation of slow charge redistribution preceding excited-state proton transfer, *J. Chem. Phys.*, 2007, **127**, 204501 1–10.
46. E. Pines and D. Huppert, Geminate recombination proton-transfer reactions, *Chem. Phys. Lett.*, 1986, **126**, 88–91.
47. Z. Zhujun and R. W. Seitz, A fluorescence sensor for quantifying pH in the range from 6.5 to 8.5, *Anal. Chim. Acta*, 1984, **160**, 47–55.
48. O. S. Wolfbeis and E. Koller, Fluorimetric assay of hydrolases at longwave excitation and emission wavelengths with new substrates possessing unique water solubility, *Anal. Biochem.*, 1983, **129**, 365–370.
49. O. S. Wolfbeis, E. Fürlinger, H. Kroneis, and H. Marsoner, A study on fluorescent indicators for measuring near neutral ("physiological") pH-Values, *Fresenius Zeitschrift für Anal. Chemie*, 1983, **314**, 119–124.
50. J. Han and K. Burgess, Fluorescent indicators for intracellular pH, *Chem. Rev.*, 2010, **110**, 2709–2728.
51. E. Pines, D. Pines, Y.-Z. Ma, and G. R. Fleming, Femtosecond pump-probe measurements of solvation by hydrogen-bonding interactions, *ChemPhysChem*, 2004, **5**, 1315–1327.
52. D. B. Spry and M. D. Fayer, Proton transfer and proton concentrations in protonated Nafion fuel cell membranes, *J. Phys. Chem. B*, 2009, **113**, 10210–10221.
53. E.-A. Gould, A. V Popov, L. M. Tolbert, I. Presiado, Y. Erez, D. Huppert, and K. M. Solntsev, Excited-state proton transfer in N-methyl-6-hydroxyquinolinium salts: solvent and temperature effects, *Phys. Chem. Chem. Phys.*, 2012, **14**, 8964–8973.
54. N. Karton-Lifshin, I. Presiado, Y. Erez, R. Gepshtein, D. Shabat, and D. Huppert, Ultrafast excited-state intermolecular proton transfer of cyanine fluorochrome dyes, *J. Phys. Chem. A*, 2012, **116**, 85–92.
55. T. G. Kim and M. R. Topp, Ultrafast excited-state deprotonation and electron transfer in hydroxyquinoline derivatives, *J. Phys. Chem. A*, 2004, **108**, 10060–10065.
56. J. L. Pérez Lustres, S. A. Kovalenko, M. Mosquera, T. Senyushkina, W. Flasche, and N. P. Ernsting, Ultrafast solvation of N-methyl-6-quinolone probes local IR spectrum, *Angew. Chem. Int. Ed. Engl.*, 2005, **44**, 5635–5639.
57. J. L. Pérez-Lustres, F. Rodriguez-Prieto, M. Mosquera, T. A. Senyushkina, N. P. Ernsting, and S. A. Kovalenko, Ultrafast proton transfer to solvent: Molecularity and intermediates from solvation- and diffusion-controlled regimes, *J. Am. Chem. Soc.*, 2007, **129**, 5408–5418.
58. I. Presiado, N. Karton-Lifshin, Y. Erez, R. Gepshtein, D. Shabat, and D. Huppert, Ultrafast proton transfer of three novel quinone cyanine photoacids, *J. Phys. Chem. A*, 2012, **116**, 7353–7363.
59. R. Simkovitch, N. Karton-Lifshin, S. Shomer, D. Shabat, and D. Huppert, Ultrafast excited-state proton transfer to the solvent occurs on a hundred-femtosecond time-scale, *J. Phys. Chem. A*, 2013, **117**, 3405–3413.
60. S. C. Miller, Profiling sulfonate ester stability: Identification of complementary protecting groups for sulfonates, *J. Org. Chem.*, 2010, **75**, 4632–4635.
61. F. E. Cappuccio, J. T. Suri, D. B. Cordes, R. A. Wessling, and B. Singaram, Evaluation of pyranine derivatives in boronic acid based saccharide sensing: Significance of charge interaction between dye and quencher in solution and hydrogel, *J. Fluoresc.*, 2004, **14**, 521–533.
62. C. Spies, B. Finkler, N. Acar, and G. Jung, Solvatochromism of pyranine-derived photoacids, *Phys. Chem. Chem. Physic*, 2013, **15**, 19893–19905.
63. C. Spies, S. Shomer, B. Finkler, D. Pines, E. Pines, D. Huppert, and G. Jung, Solvent dependence of excited-state proton transfer from pyranine-derived photoacids, *submitted*.
64. F. G. Bordwell, Equilibrium acidities in dimethyl sulfoxide solution, *Acc. Chem. Res.*, 1988, **21**, 456–463.
65. C. A. Reed, The nature of H+ in condensed media, *Acc. Chem. Res.*, 2013, **46**, 2567–2575.
66. G. Schweitzer, L. Xu, B. Craig, and F. DeSchryver, A double OPA femtosecond laser system for transient absorption spectroscopy, *Opt. Commun.*, 1997, **142**, 283–288.

Photochem. Photobiol. Sci., 2014, DOI: 10.1039/C3PP50404B

67. C. Buehler, C. Y. Dong, P. T. So, T. French, and E. Gratton, Time-resolved polarization imaging by pump-probe (stimulated emission) fluorescence microscopy, *Biophys. J.*, 2000, **79**, 536–549.
68. M. Fukuda, O. Kajimoto, M. Terazima, and Y. Kimura, Application of the transient grating method to the investigation of the photo-thermalization process of malachite green in room temperature ionic liquids, *J. Mol. Liq.*, 2007, **134**, 49–54.
69. R. Berera, R. van Grondelle, and J. T. M. Kennis, Ultrafast transient absorption spectroscopy: principles and application to photosynthetic systems, *Photosynth. Res.*, 2009, **101**, 105–118.
70. R. a Velapoldi and H. H. Tønnesen, Corrected emission spectra and quantum yields for a series of fluorescent compounds in the visible spectral region, *J. Fluoresc.*, 2004, **14**, 465–72.
71. T. Karstens and K. Kobs, Rhodamine B and rhodamine 101 as reference substances for fluorescence quantum yield measurements, *J. Phys. Chem.*, 1980, **84**, 1871–1872.
72. M. Fischer and J. Georges, Fluorescence quantum yield of rhodamine 6G in ethanol as a function of concentration using thermal lens spectrometry, *Chem. Phys. Lett.*, 1996, **260**, 115–118.
73. J. H. Brannon and D. Magde, Absolute quantum yield determination by thermal blooming. Fluorescein, *J. Phys. Chem.*, 1978, **82**, 705–709.
74. J. Widengren, B. Terry, and R. Rigler, Protonation kinetics of GFP and FITC investigated by FCS - aspects of the use of fluorescent indicators for measuring pH, *Chem. Phys.*, 1999, **249**, 259–271.
75. L. P. Hammett and A. J. Deyrup, A series of simple basic indicators. I. The acidity functions of mixtures of sulfuric and perchloric acids with water, *J. Am. Chem. Soc.*, 1932, **54**, 2721–2739.
76. M. J. Jorgenson and D. R. Hartter, A Critical re-evaluation of the hammett acidity function at moderate and high acid concentrations of sulfuric acid. New H 0 values based solely on a set of primary aniline indicators, *J. Am. Chem. Soc.*, 1963, **85**, 878–883.
77. Y. Avnir and Y. Barenholz, pH determination by pyranine: Medium-related artifacts and their correction, *Anal. Biochem.*, 2005, **347**, 34–41.
78. A. B. Kotlyar, N. Borovok, S. Raviv, L. Zimanyi, and M. Gutman, Fast redox perturbation of aqueous solution by photoexcitation of pyranine, *Photochem. Photobiol.*, 1996, **63**, 448–454.
79. J. Yang, X.-P. Xing, X.-B. Wang, L.-S. Wang, A. P. Sergeeva, and A. I. Boldyrev, Negative electron binding energies observed in a triply charged anion: Photoelectron spectroscopy of 1-hydroxy-3,6,8-pyrene-trisulfonate, *J. Chem. Phys.*, 2008, **128**, 091102 1–4.
80. B. Hinkeldey, A. Schmitt, and G. Jung, Comparative photostability studies of BODIPY and fluorescein dyes by using fluorescence correlation spectroscopy, *Chemphyschem*, 2008, **9**, 2019–2027.
81. V. Vukojevic, M. Heidkamp, Y. Ming, B. Johansson, L. Terenius, and R. Rigler, Quantitative single-molecule imaging by confocal laser scanning microscopy, *Proc. Natl. Acad. Sci. U. S. A.*, 2008, **105**, 18176–18181.
82. J. Hu and C.-Y. Zhang, Simple and accurate quantification of quantum yield at the single-molecule/particle level, *Anal. Chem.*, 2013, **85**, 2000–2004.
83. H. K. J. Hall, Correlation of the base strengths of amines, *J. Am. Chem. Soc.*, 1957, **79**, 5441–5444.
84. J. King, M. Gill, and P. Ciubotaru, Benzenesulfonyl chloride with primary and secondary amines in aqueous media–Unexpected high conversions to sulfonamides at high pH, *Can. J. Chem.*, 2005, **1535**, 1525–1535.
85. E. Hamborg and G. Versteeg, Dissociation constants and thermodynamic properties of amines and alkanolamines from (293 to 353) K, *J. Chem. Eng. Data*, 2009, **54**, 1318–1328.
86. A. Kundu and N. Kishore, 1,1,1,3,3,3-Hexafluoroisopropanol induced thermal unfolding and molten globule state of bovine alpha-lactalbumin: Calorimetric and spectroscopic studies, *Biopolymers*, 2004, **73**, 405–420.
87. J. Widengren, U. Mets, and R. Rigler, Fluorescence correlation spectroscopy of triplet states in solution: A theoretical and experimental study, *J. Phys. Chem.*, 1995, **99**, 13368–13379.
88. T. Ha and P. Tinnefeld, Photophysics of fluorescent probes for single-molecule biophysics and super-resolution imaging, *Annu. Rev. Phys. Chem.*, 2012, **63**, 595–617.
89. W.-C. Sun, K. R. Gee, D. H. Klaubert, and R. P. Haugland, Synthesis of fluorinated fluoresceins, *J. Org. Chem.*, 1997, **62**, 6469–6475.
90. W.-C. Sun, K. R. Gee, and R. P. Haugland, Synthesis of novel fluorinated coumarins: Excellent UV-light excitable fluorescent dyes, *Bioorg. Med. Chem. Lett.*, 1998, **8**, 3107–3110.
91. G. Y. Yang, M. Hanack, Y. W. Lee, Y. Chen, M. K. Y. Lee, and D. Dini, Synthesis and nonlinear optical properties of fluorine-containing naphthalocyanines, *Chem. - An Eur. J.*, 2003, **9**, 2758–2762.
92. Z. R. Woydziak, L. Fu, and B. R. Peterson, Synthesis of fluorinated benzophenones, xanthones, acridones, and thioxanthones by iterative nucleophilic aromatic substitution, *J. Org. Chem.*, 2012, **77**, 473–481.
93. H. Sun, A. Putta, J. P. Kloster, and U. K. Tottempudi, Unexpected photostability improvement of aromatics in polyfluorinated solvents, *Chem. Commun.*, 2012, **48**, 12085–12087.
94. S. H. Kim and S. H. Hwang, Synthesis and photostability of functional squarylium dyes, *Dye. Pigment.*, 1997, **35**, 111–121.

95. A. Toutchkine, D.-V. Nguyen, and K. M. Hahn, Merocyanine dyes with improved photostability, *Org. Lett.*, 2007, **9**, 2775–2777.
96. N. I. Shank, K. J. Zanotti, F. Lanni, P. B. Berget, and B. A. Armitage, Enhanced photostability of genetically encodable fluoromodules based on fluorogenic cyanine dyes and a promiscuous protein partner, *J. Am. Chem. Soc.*, 2009, **131**, 12960–12969.

Photochem. Photobiol. Sci., 2014, DOI: 10.1039/C3PP50404B

Photochem. Photobiol. Sci., 2014, DOI: 10.1039/C3PP50404B

http://xlink.rsc.org/?doi=C3PP50404B

Supporting Information

Highly Photostable "Super"-Photoacids for Ultrasensitive Fluorescence Spectroscopy

Björn Finkler[a], Christian Spies[a], Michael Vester[a], Frederick Walte[a], Kathrin Omlor[a], Iris Riemann[b], Manuel Zimmer[c], Frank Stracke[b], Markus Gerhards[c], Gregor Jung[a]

[a] *Biophysical Chemistry, Saarland University, Campus B2 2, 66123 Saarbrücken, Germany.*

[b] *Fraunhofer-IBMT, Ensheimer Straße 48, 66386 St. Ingbert, Germany.*
[c] *Technische Universität Kaiserslautern & Research Center Optimas, Fachbereich Chemie, Erwin-Schrödinger-Str.*
67663 Kaiserslautern, Germany.

Email corresponding author: g.jung@mx.uni-saarland.de

Photochem. Photobiol. Sci., 2014, **13**, 548-562

http://xlink.rsc.org/?doi=C3PP50404B

Determination of pK_a values via fluorescence correlation spectroscopy (FCS)

For determination of the pK_a values of the weakly water soluble photoacids, we followed the experimental procedure of Widegren *et al*. [S1]

The actual system consists of an acid, the corresponding base and buffer HB^+/B for stabilizing the equilibrium. A 20 mM HPCE-buffer (citric acid / sodium citrate, Fluka) was employed for the pH values 4 and 4.5. Protonation and deprotonation is widely mediated by HB^+ and B with the bimolecular rate constants k_{prot}^{bi} and k_{deprot}^{bi} (Equation S1), which are experimentally determined to lie in the range of ~ 10^8 $M^{-1}s^{-1}$. At a total buffer concentration of 20 mM, where $[HB^+] \approx [B]$, direct, diffusion-controlled protonation by H^+ and deprotonation can be neglected at pH-values > 4.[S1]

$$ROH + B \underset{k_{prot}^{bi}}{\overset{k_{deprot}^{bi}}{\rightleftharpoons}} RO^- + HB^+ \qquad (S1)$$

The kinetic description for the equilibrium leads to:

$$\frac{d[RO^-]}{dt} = -k_{prot}^{bi}[RO^-][HB^+] + k_{deprot}^{bi}[ROH][B] = 0 \qquad (S2)$$

The effective rates are defined as $k_{prot}^{eff} = k_{prot}^{bi} \cdot [HB^+]$ and $k_{deprot}^{eff} = k_{deprot}^{bi} \cdot [B]$, so equation S2 can be converted into:

$$\frac{[ROH]}{[RO^-]} = \frac{k_{prot}^{eff}}{k_{deprot}^{eff}} \qquad (S3)$$

$$K_a^{-1} = \frac{[ROH]}{[H^+][RO^-]} \qquad (S4)$$

Combination of (S3) and (S4) leads to a relation for the pK_a:

$$pK_a = pH + log\frac{k_{prot}^{eff}}{k_{deprot}^{eff}} \qquad (S5)$$

http://xlink.rsc.org/?doi=C3PP50404B

The rate constants k_{prot}^{eff} and k_{deprot}^{eff} are directly accessible in a FCS-experiment by photoexcitation of RO^- and detection of its fluorescence (Figure S1).

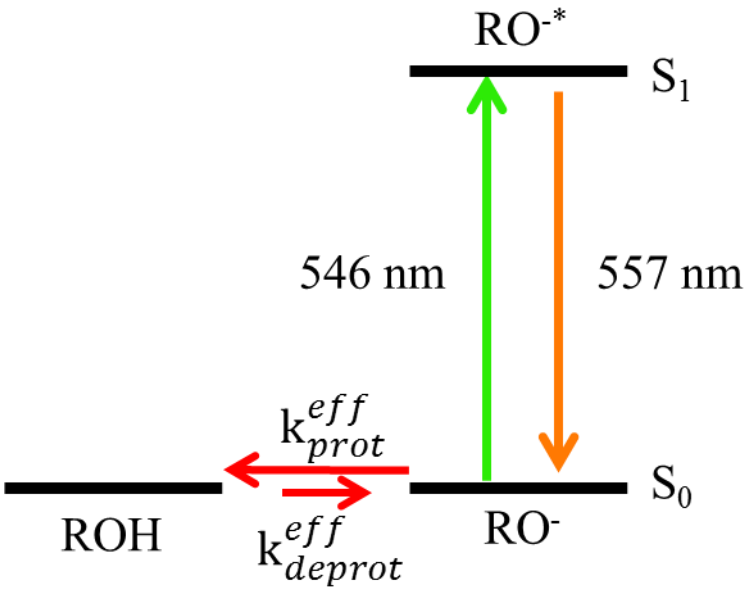

Figure S1: Schematic representation for pK_a-determination: excitation of RO^- (**3b**) was performed at λ_{exc} = 546 nm ($\lambda_{abs,\,max}$ = 515 nm at pH 4; $\lambda_{em,\,max}$ = 557 nm at pH 4), fluorescence was detected at λ_{det} = 555-625 nm. The dark state ROH is populated with the rate constant k_{prot}^{eff}, whereas k_{deprot}^{eff} describes the depopulation the dark state.

Fitting the obtained correlation functions G(τ) according to equation S6 (Figure S2) gives the rates k_{prot}^{eff}, k_{deprot}^{eff} and consequently the pK_a value depicted in Table 2. The outcome of this approach was verified with **3f**.

$$G(\tau) = \frac{1}{\langle N \rangle} \frac{1}{1+\frac{\tau}{\tau_D}} \left(1 + \frac{k_{prot}^{eff}}{k_{deprot}^{eff}} \exp\left(-(k_{prot}^{eff} + k_{deprot}^{eff})\tau\right) \right) \qquad \text{(S6)}$$

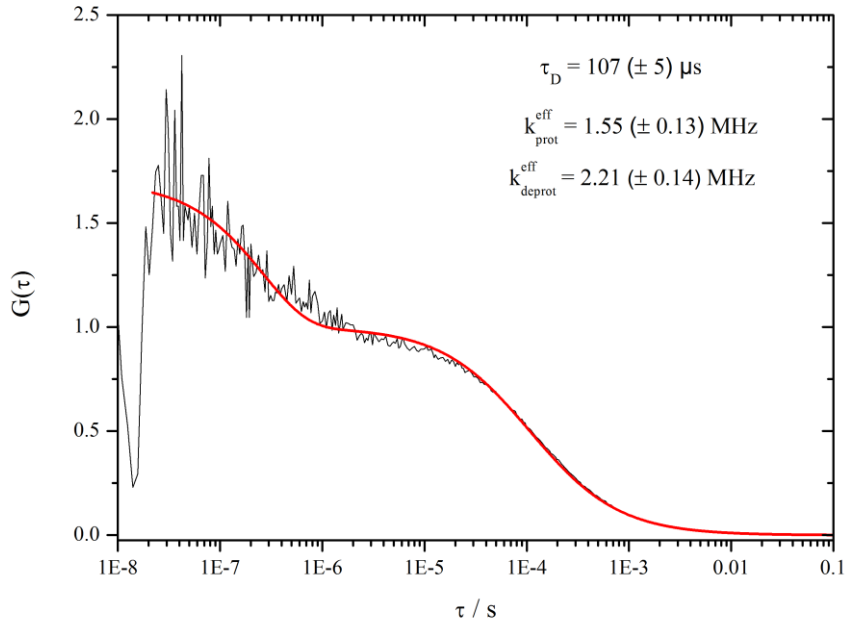

Figure S2: Normalized correlation function of **3b**. Excitation was performed at λ = 546 nm with a laser intensity of 168 kW cm^{-1} in a 20 mM citrate-buffer at pH 4.5. Fluorescence was detected at λ_{det} = 555-625 nm. A pK_a of 4.4 is calculated as a mean value of two measurements.

Characterisation of the described compounds with NMR- and mass spectroscopy:

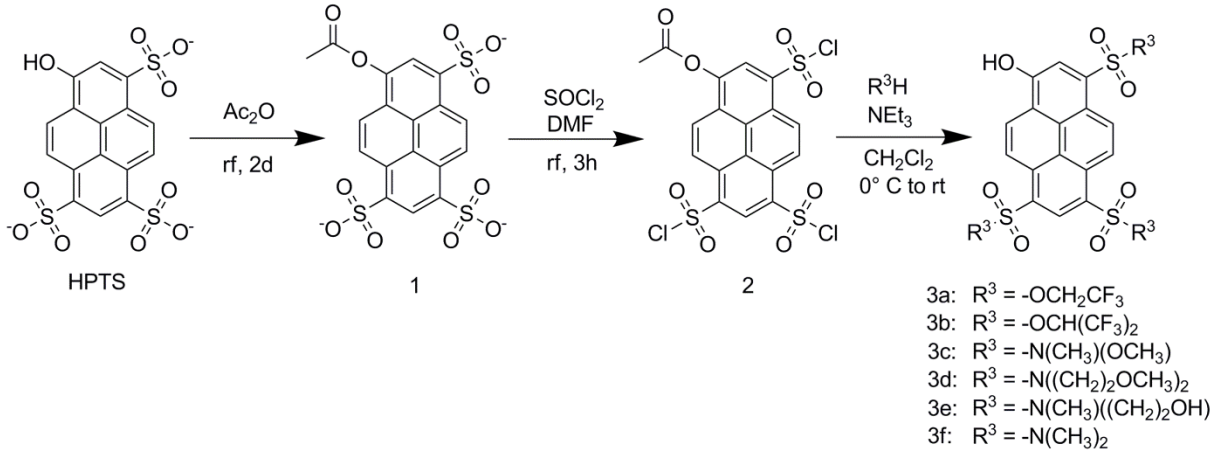

Scheme S1: Synthesis of HPTS-derivatives **3a-f**.

Compound **1**:

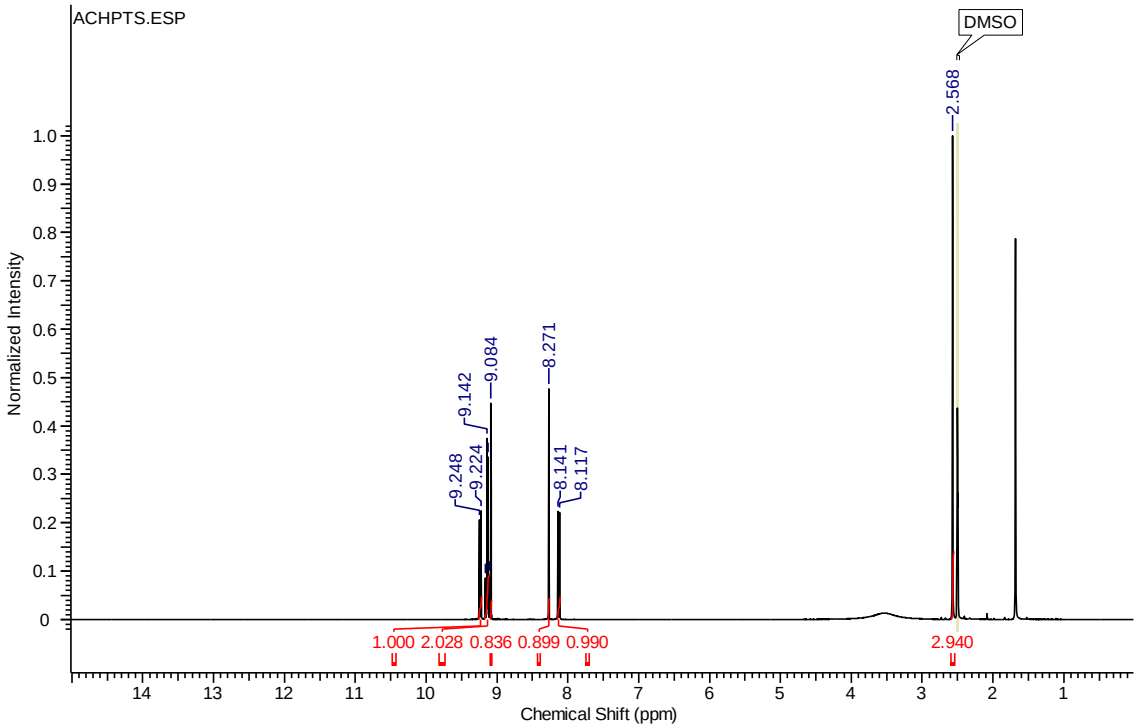

Figure S3: ^{1}H-NMR spectrum of **1**.

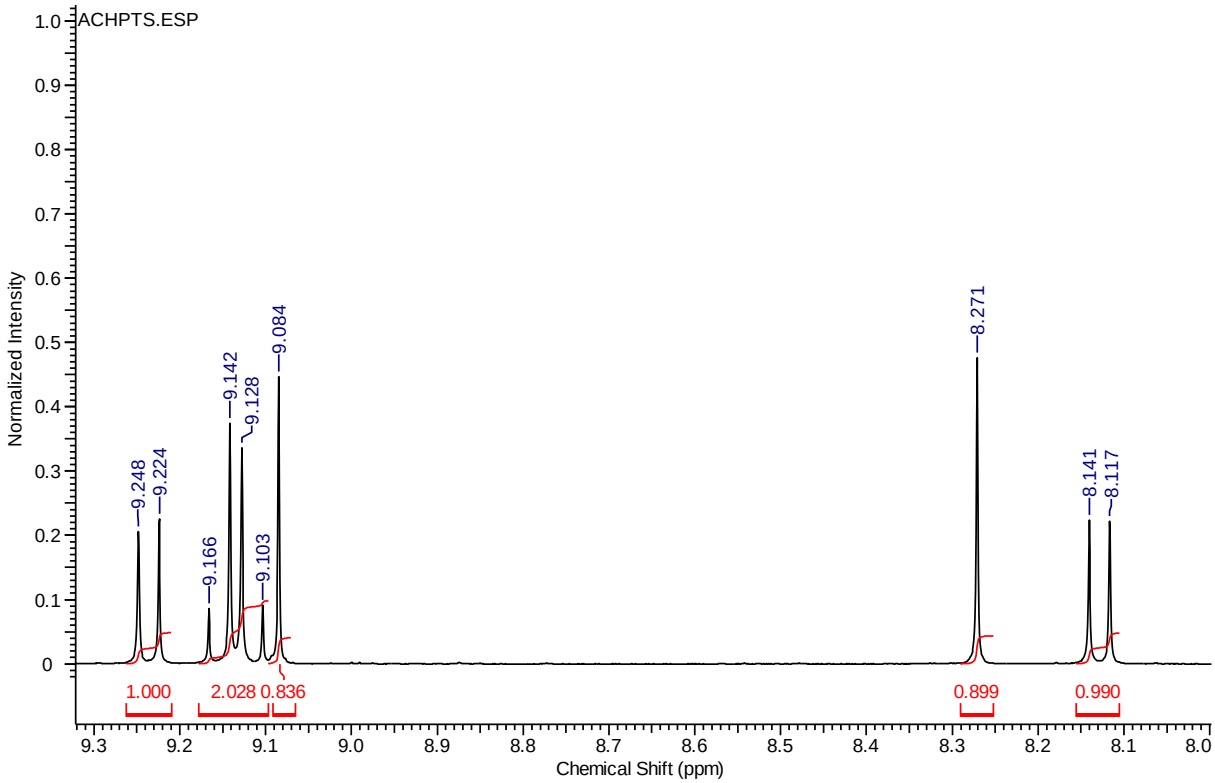

Figure S4: ^{1}H-NMR spectrum of **1** (zoomed).

http://xlink.rsc.org/?doi=C3PP50404B

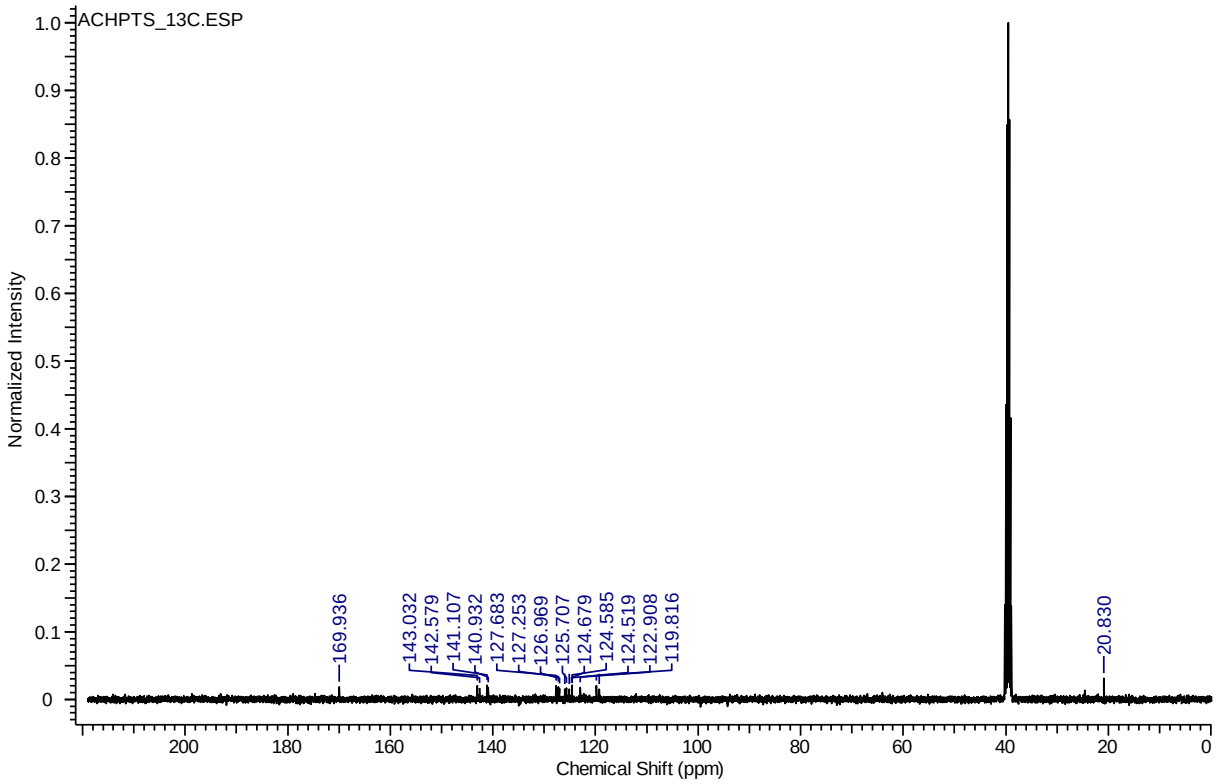

Figure S5: ^{13}C-NMR spectrum of **1**.

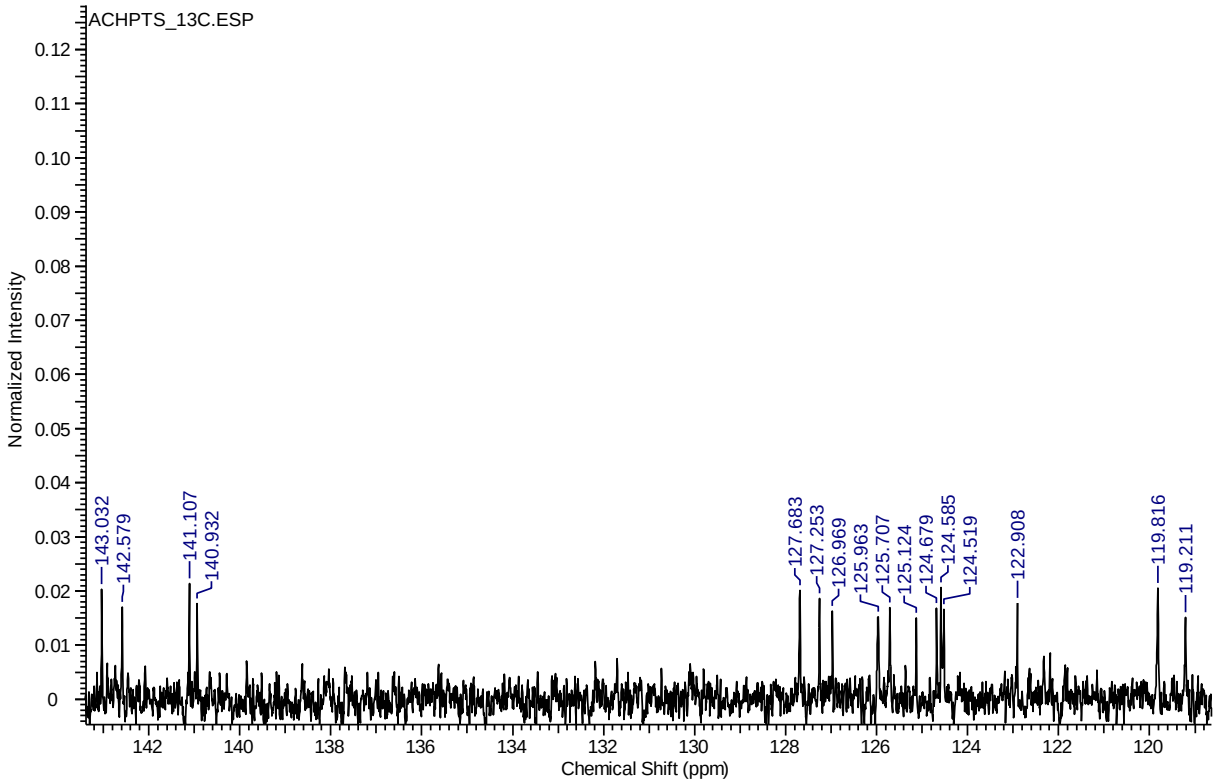

Figure S6: ^{13}C-NMR spectrum of **1** (zoomed).

http://xlink.rsc.org/?doi=C3PP50404B

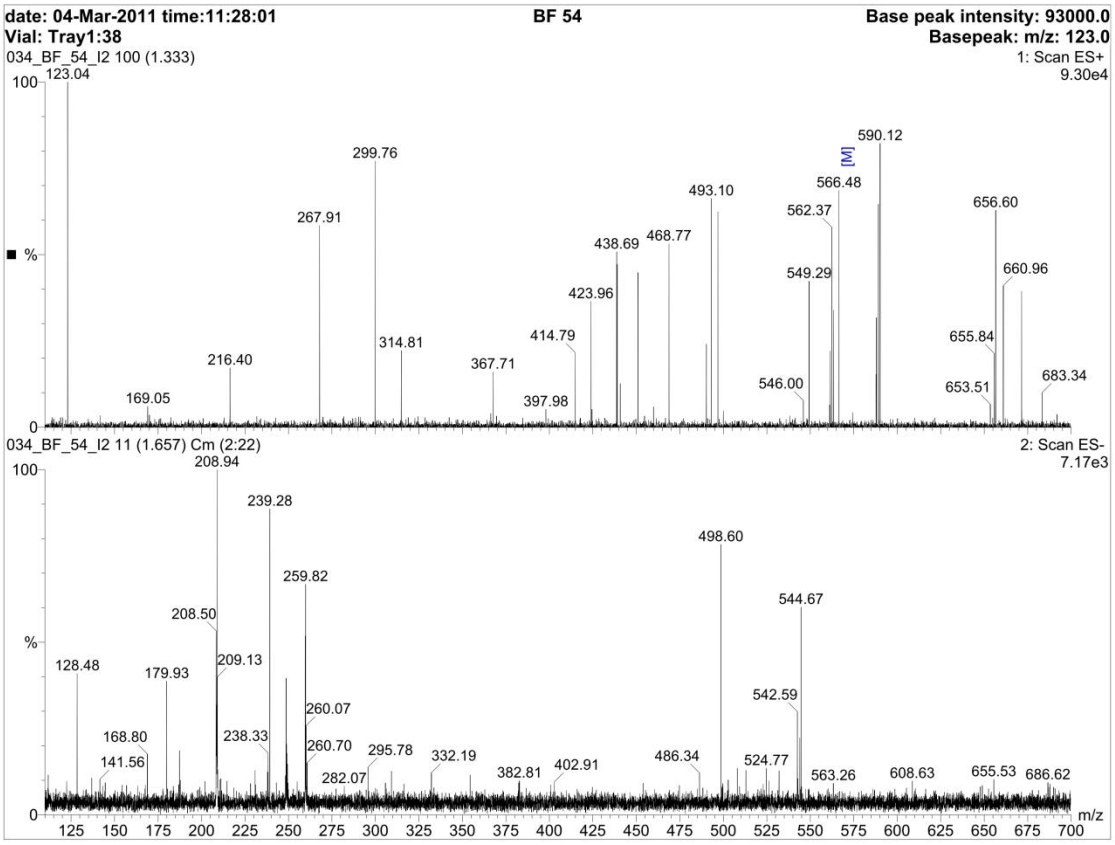

Figure S7: mass spectrum of **1**.

Compound **2**:

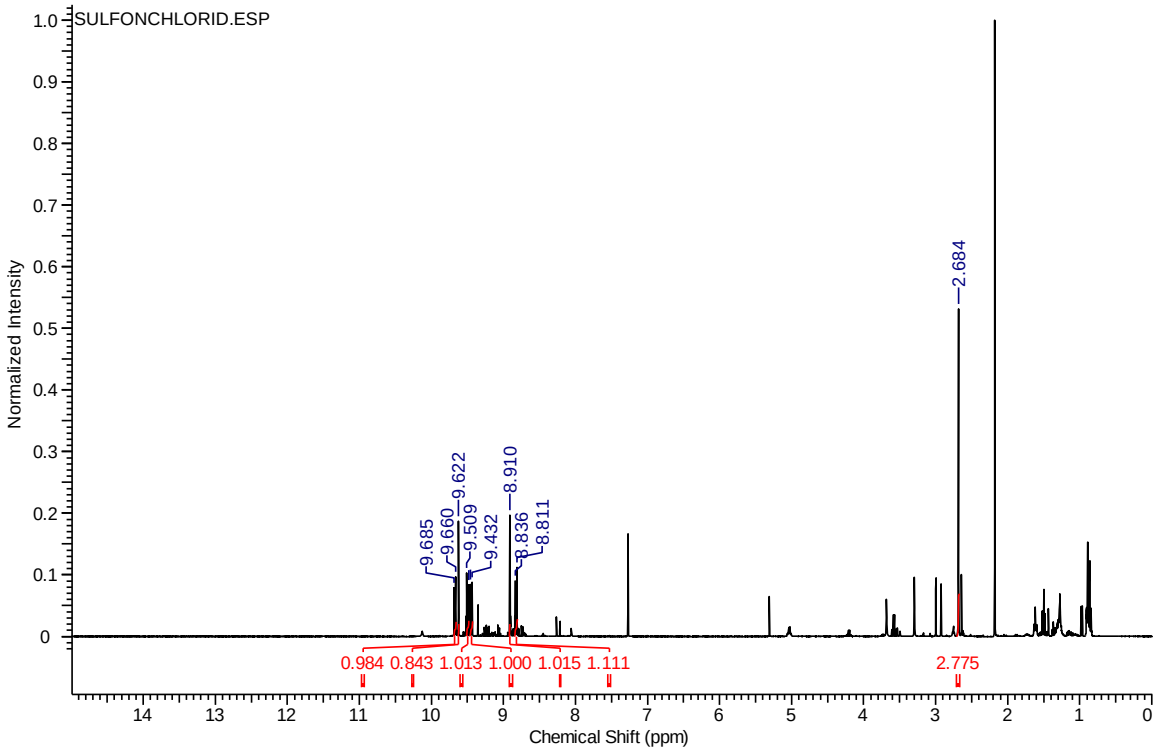

Figure S8: ^{1}H-NMR spectrum of **2**.

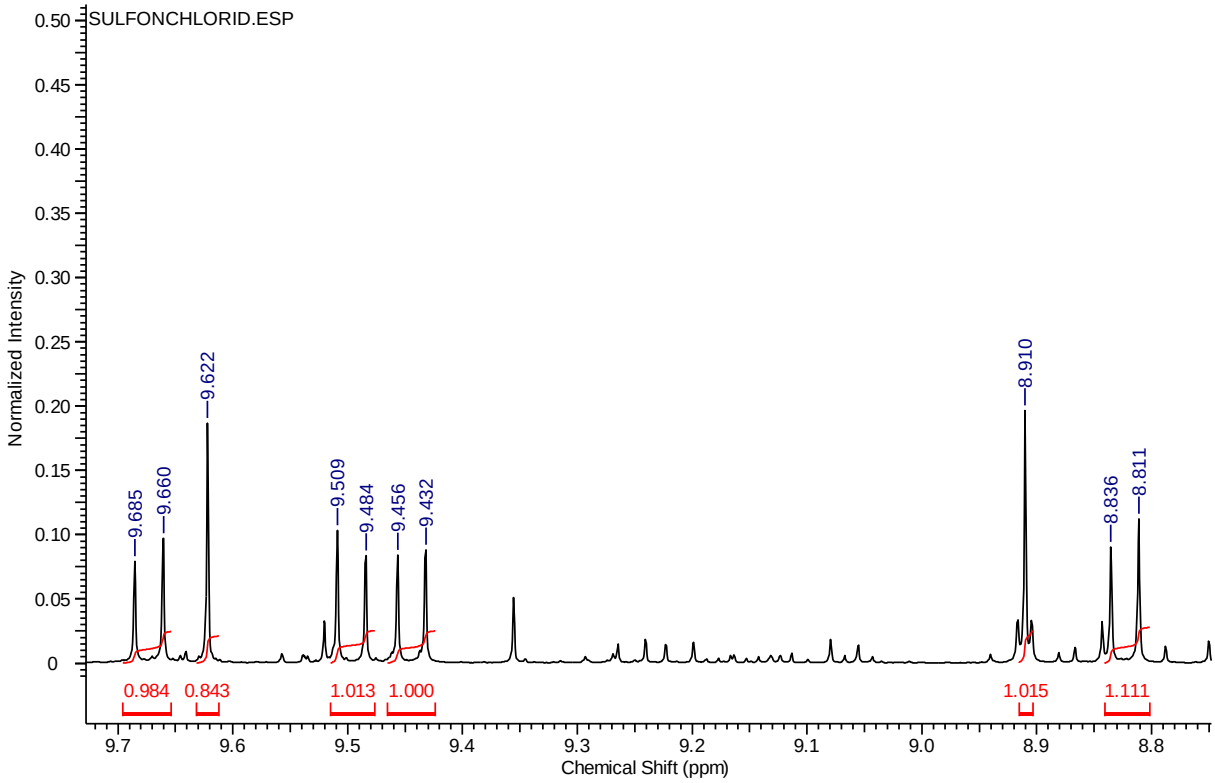

Figure S9: ^{1}H-NMR spectrum of **2** (zoomed).

Compound **3a**:

http://xlink.rsc.org/?doi=C3PP50404B

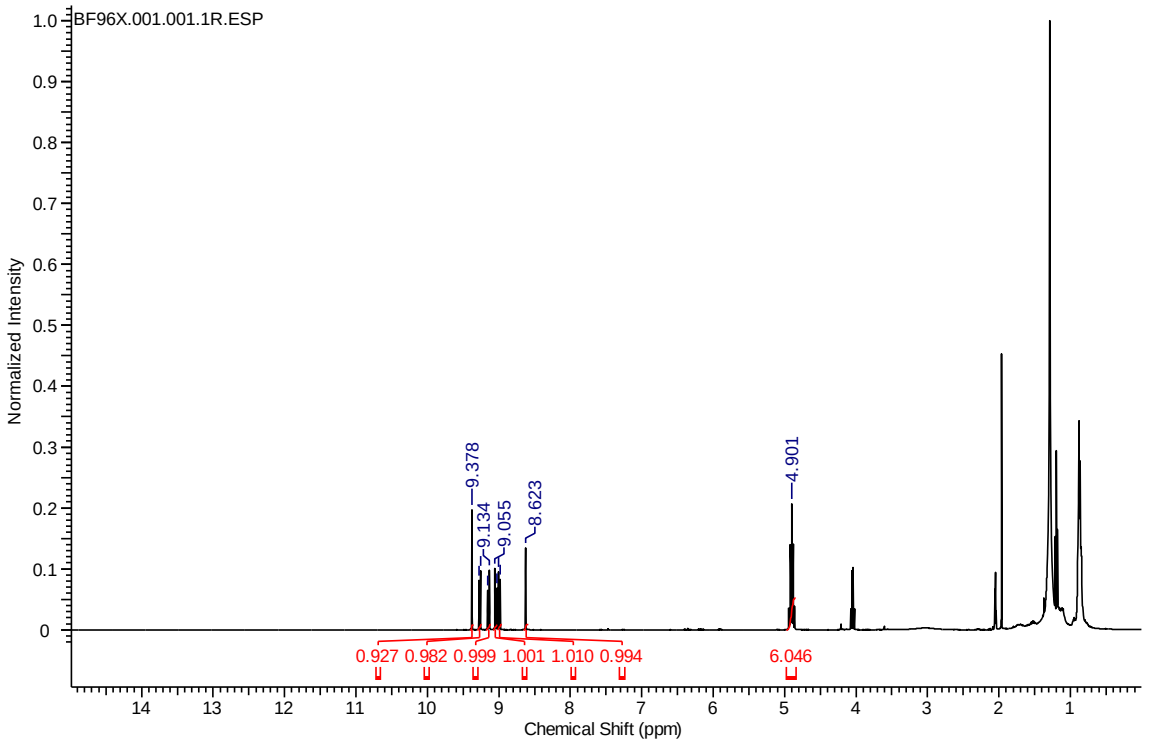

Figure S10: ^{1}H-NMR spectrum of **3a**.

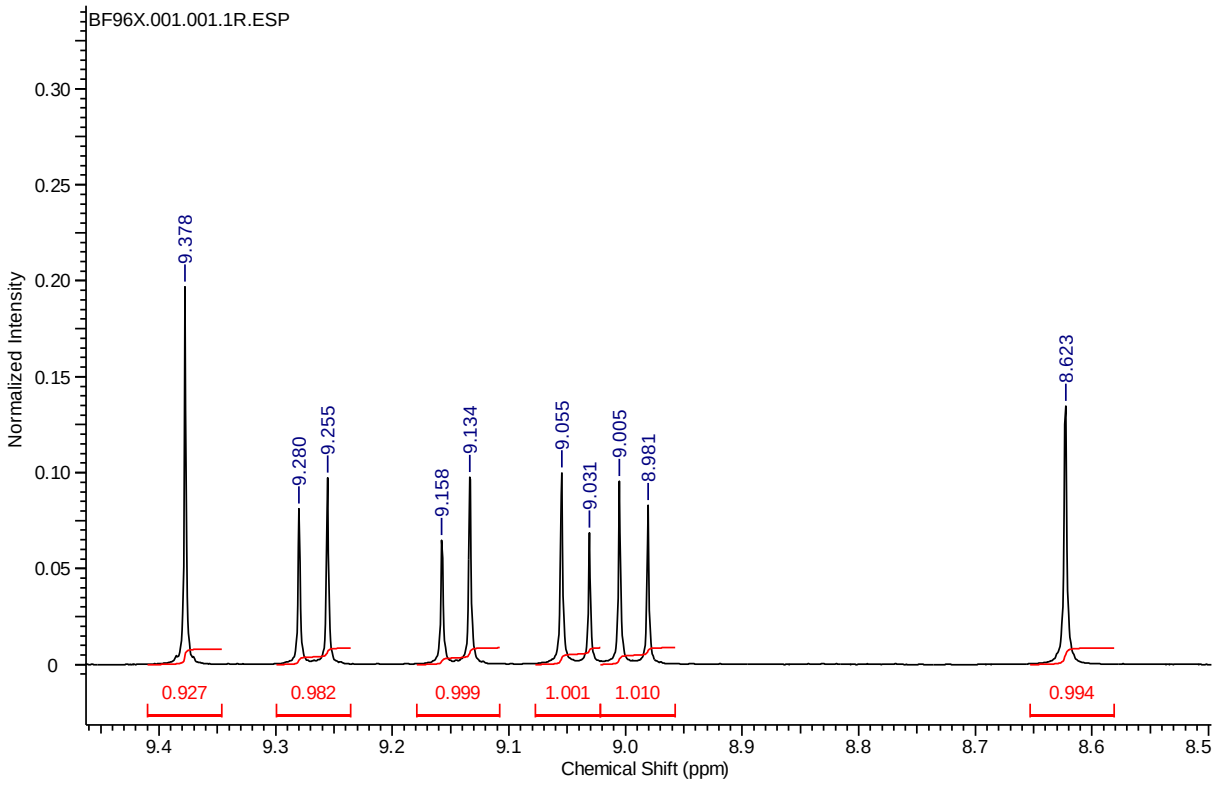

Figure S11: ^{1}H-NMR spectrum of **3a** (zoomed).

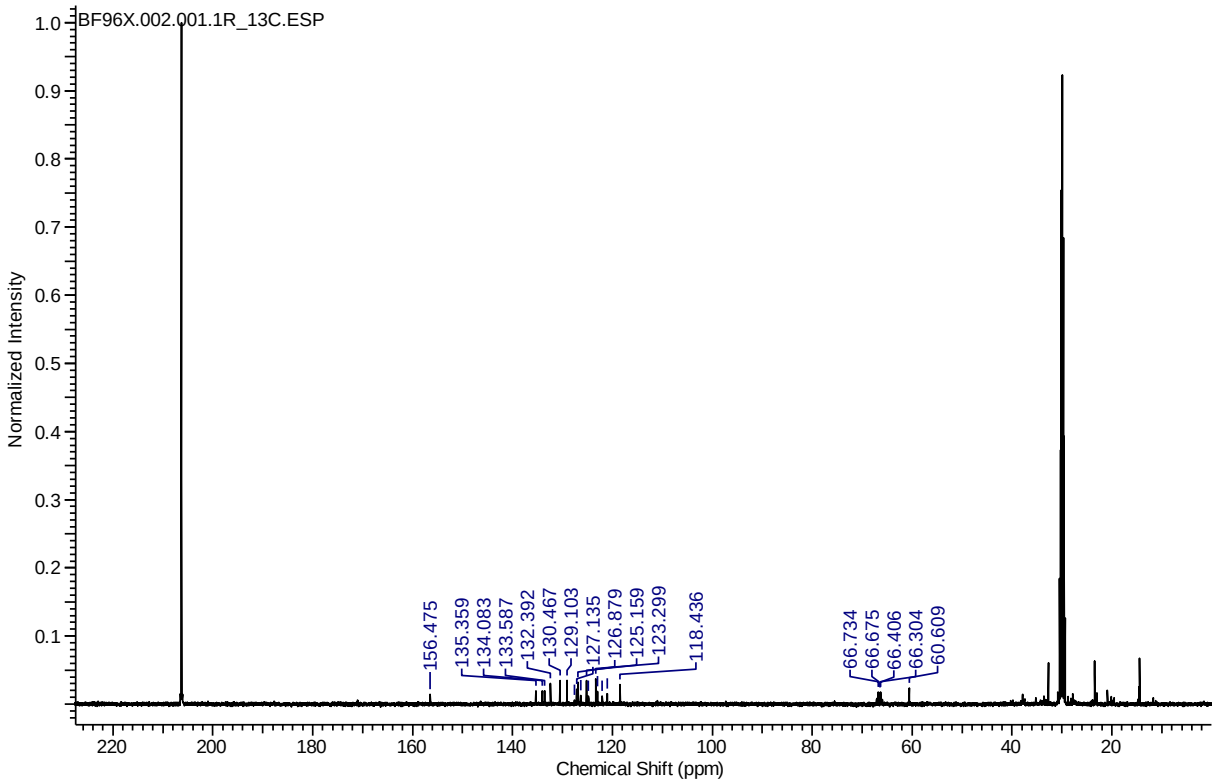

Figure S12: ^{13}C-NMR spectrum of **3a**.

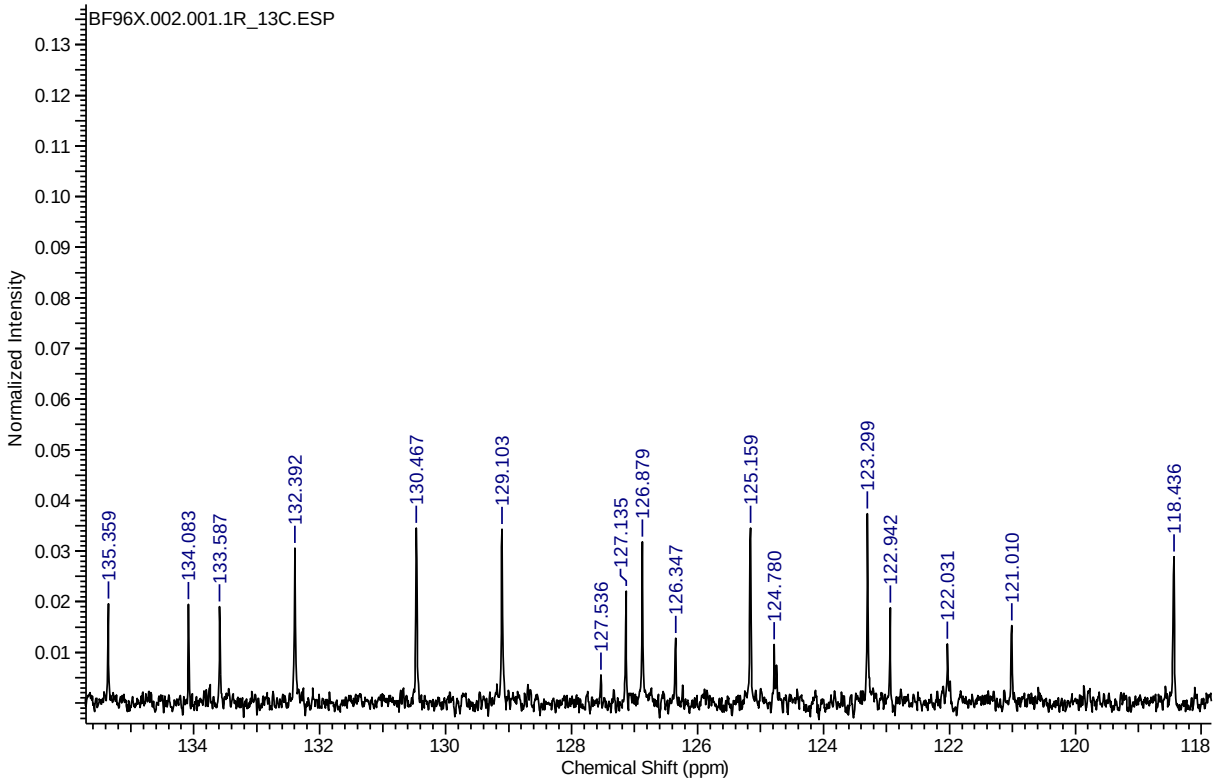

Figure S13: ^{13}C-NMR spectrum of **3a** (zoomed).

http://xlink.rsc.org/?doi=C3PP50404B

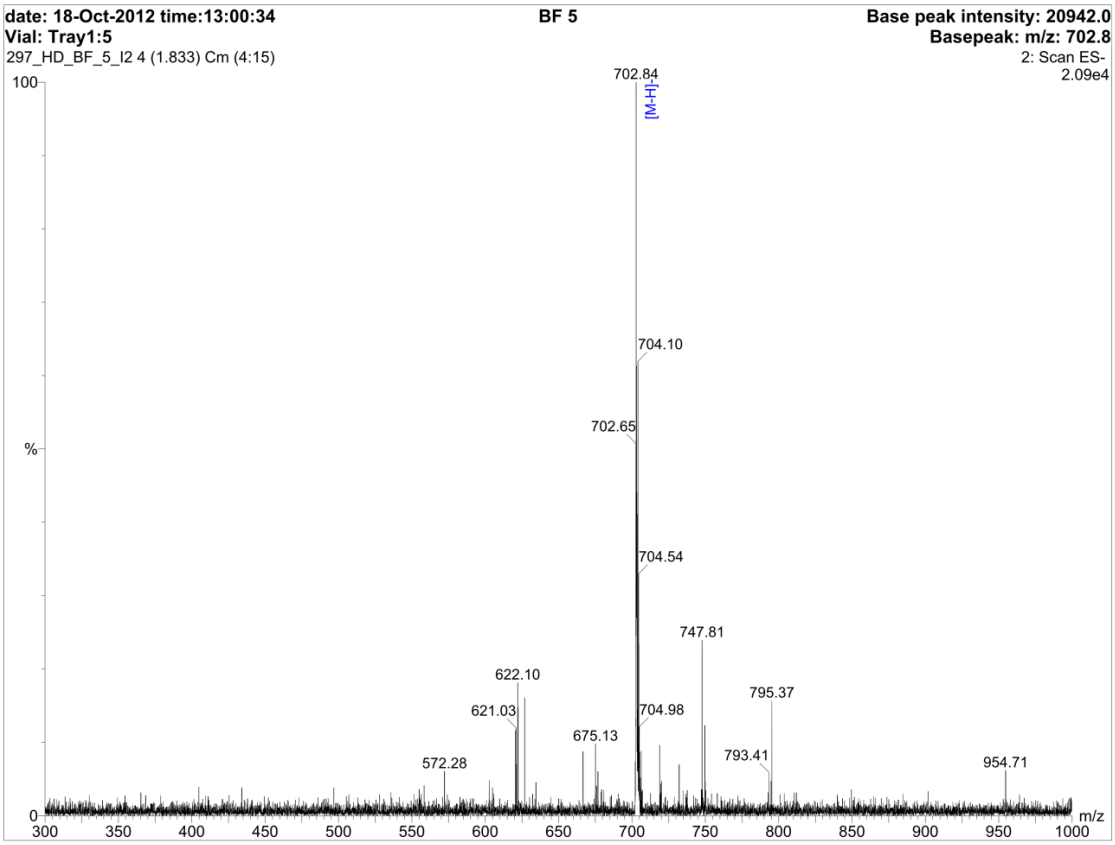

Figure S14: mass spectrum of **3a**.

Compound **3b**:

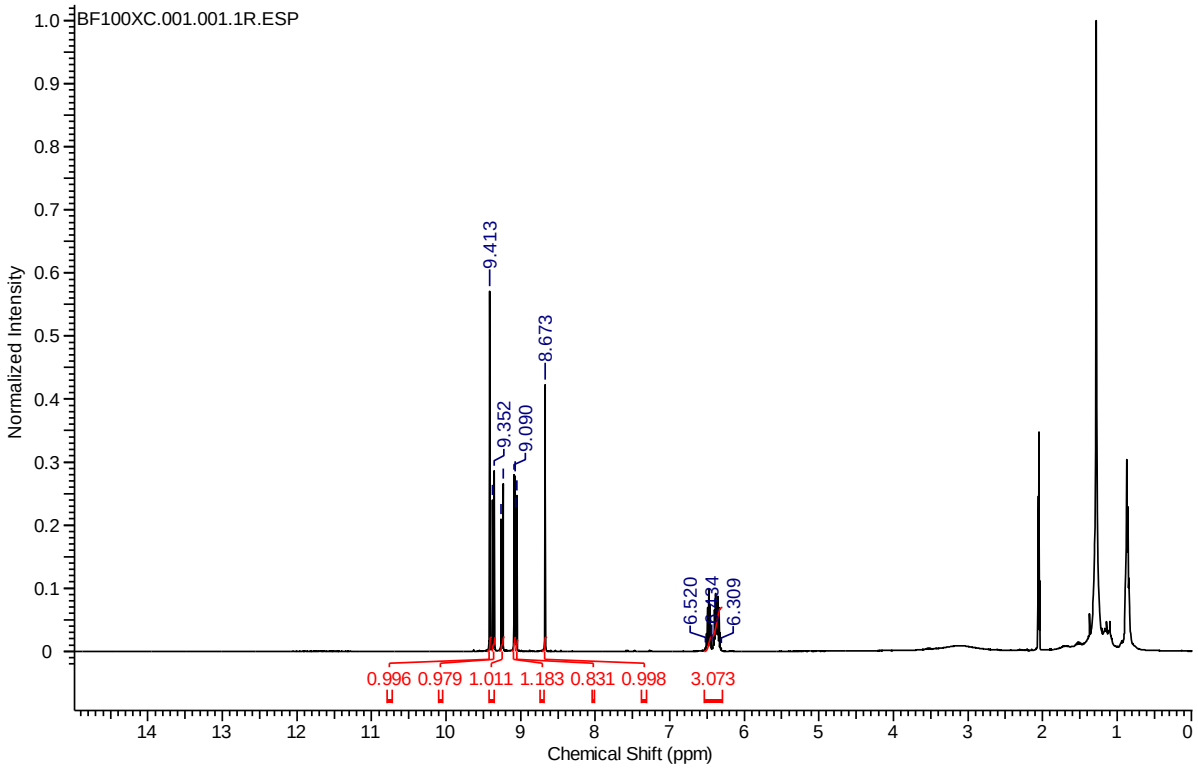

Figure S15: ^{1}H-NMR spectrum of **3b**.

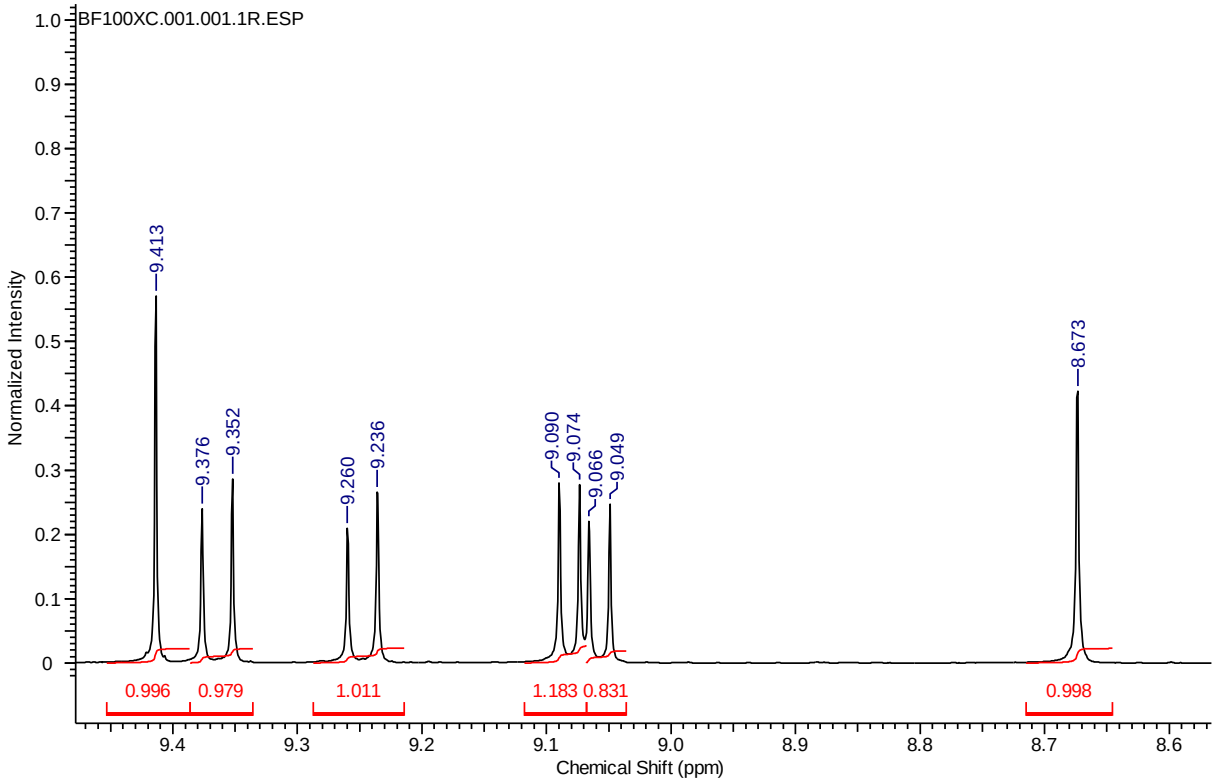

Figure S16: ^{1}H-NMR spectrum of **3b** (zoomed).

http://xlink.rsc.org/?doi=C3PP50404B

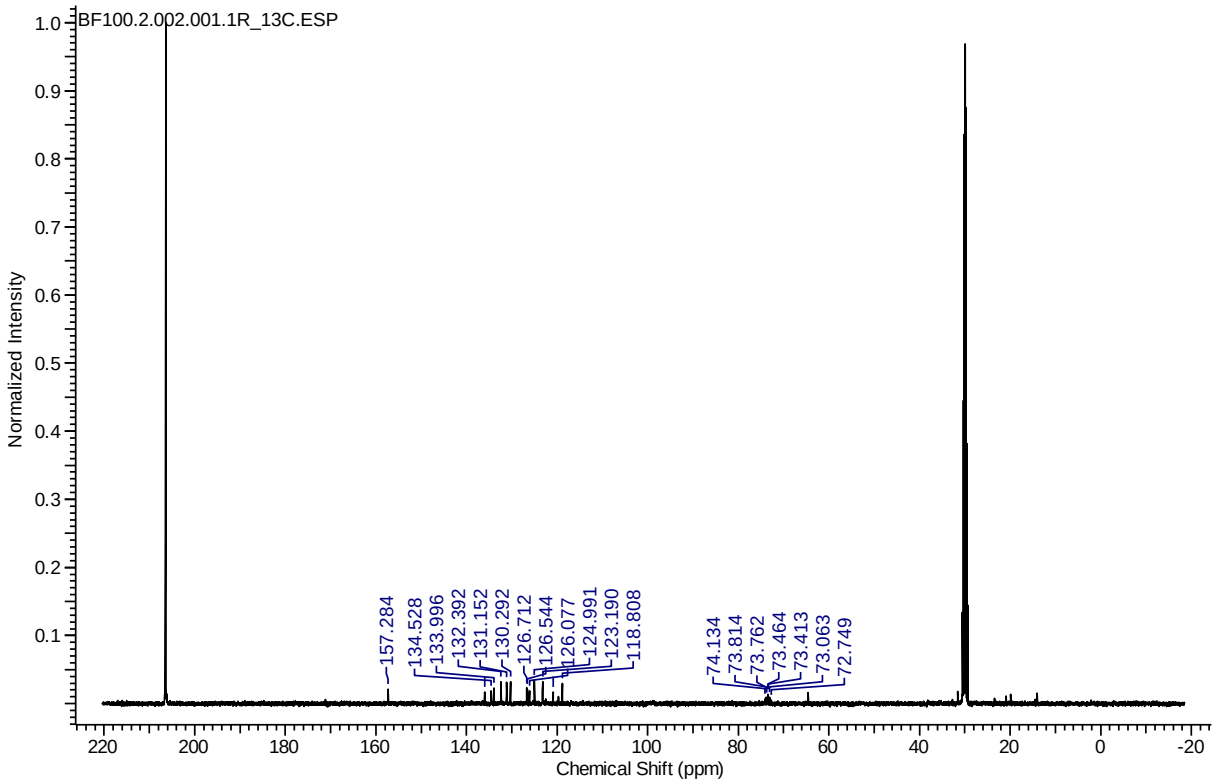

Figure S17: ^{13}C-NMR spectrum of **3b**.

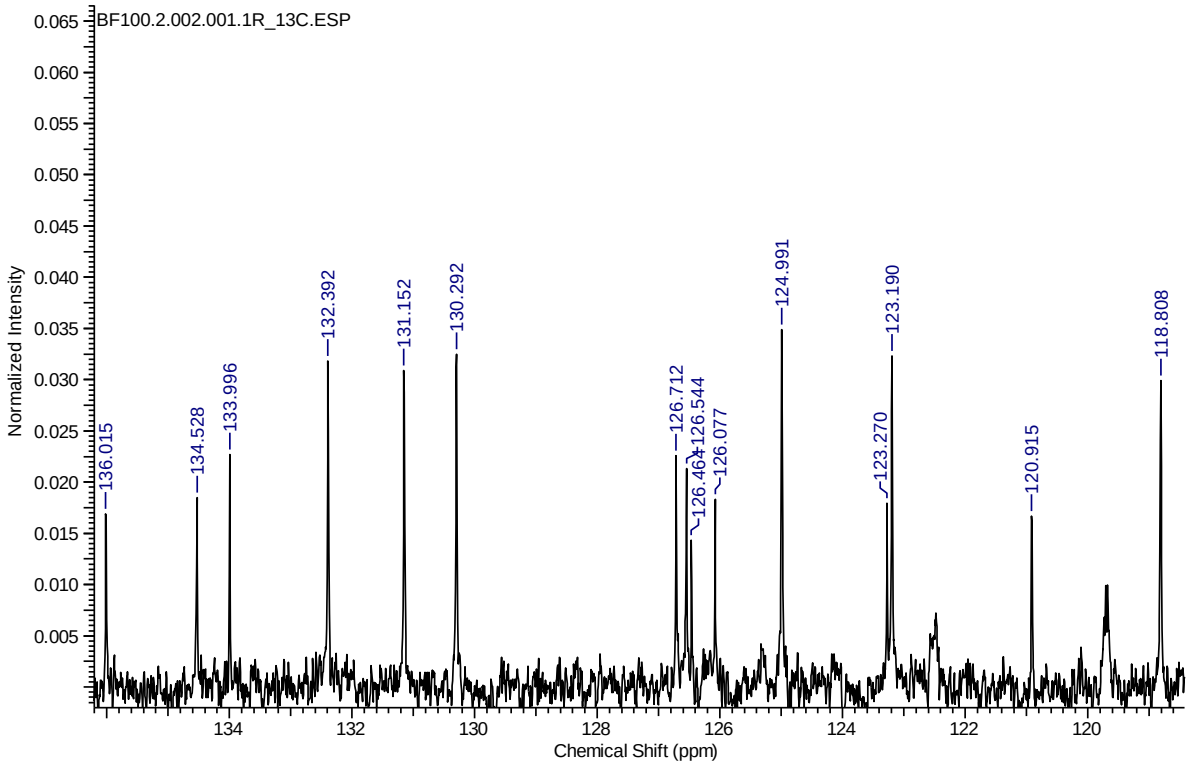

Figure S18: ^{13}C-NMR spectrum of **3b** (zoomed).

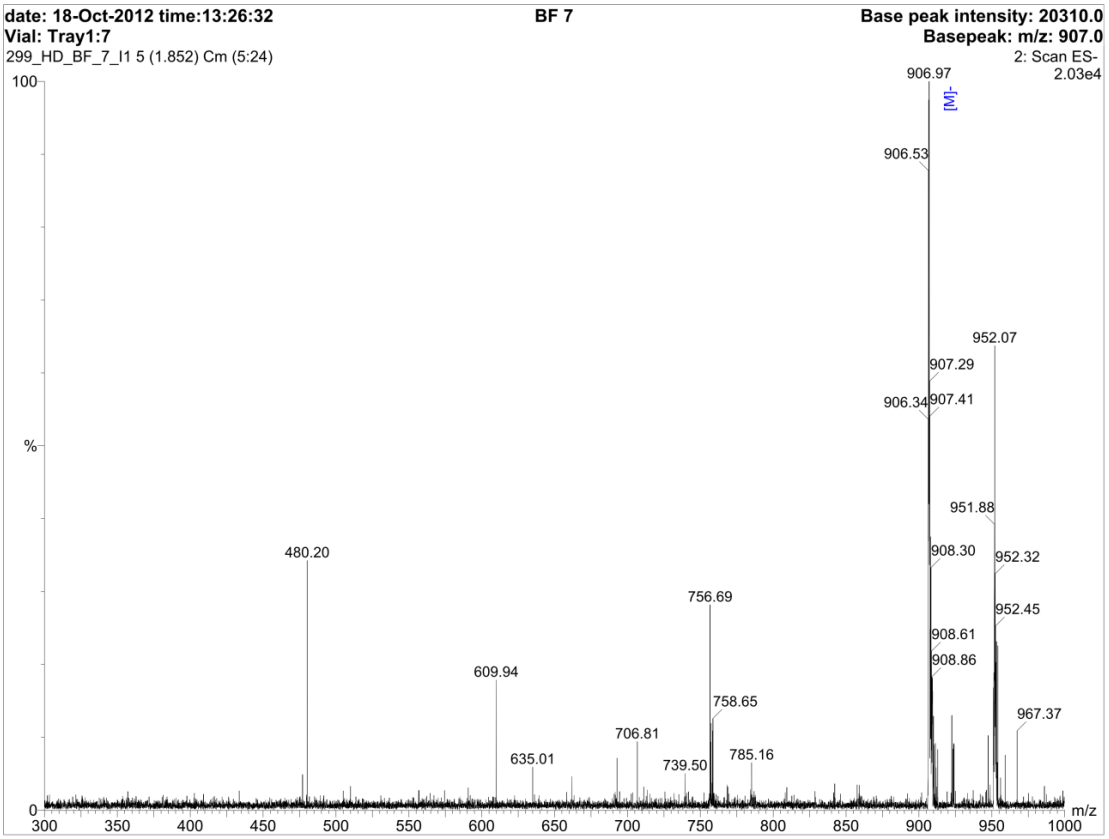

Figure S19: mass spectrum of **3b**.

http://xlink.rsc.org/?doi=C3PP50404B

Compound **3c**:

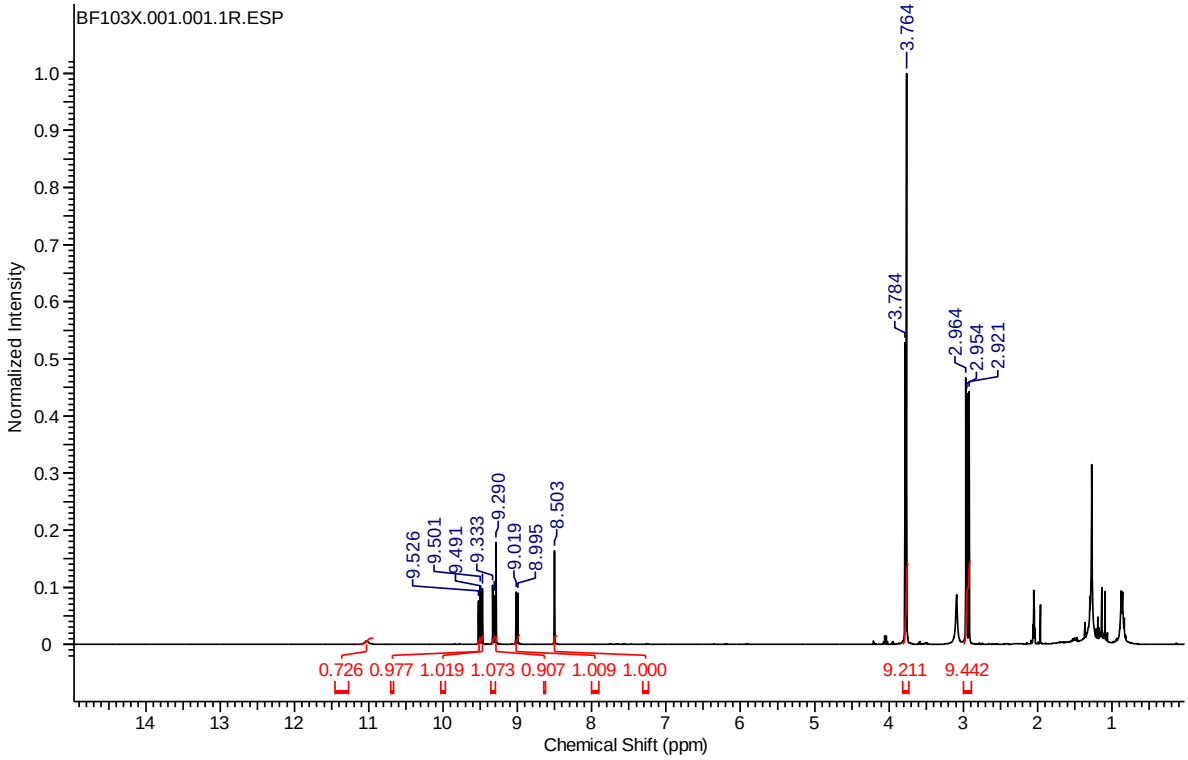

Figure S20: ^{1}H-NMR spectrum of **3c**.

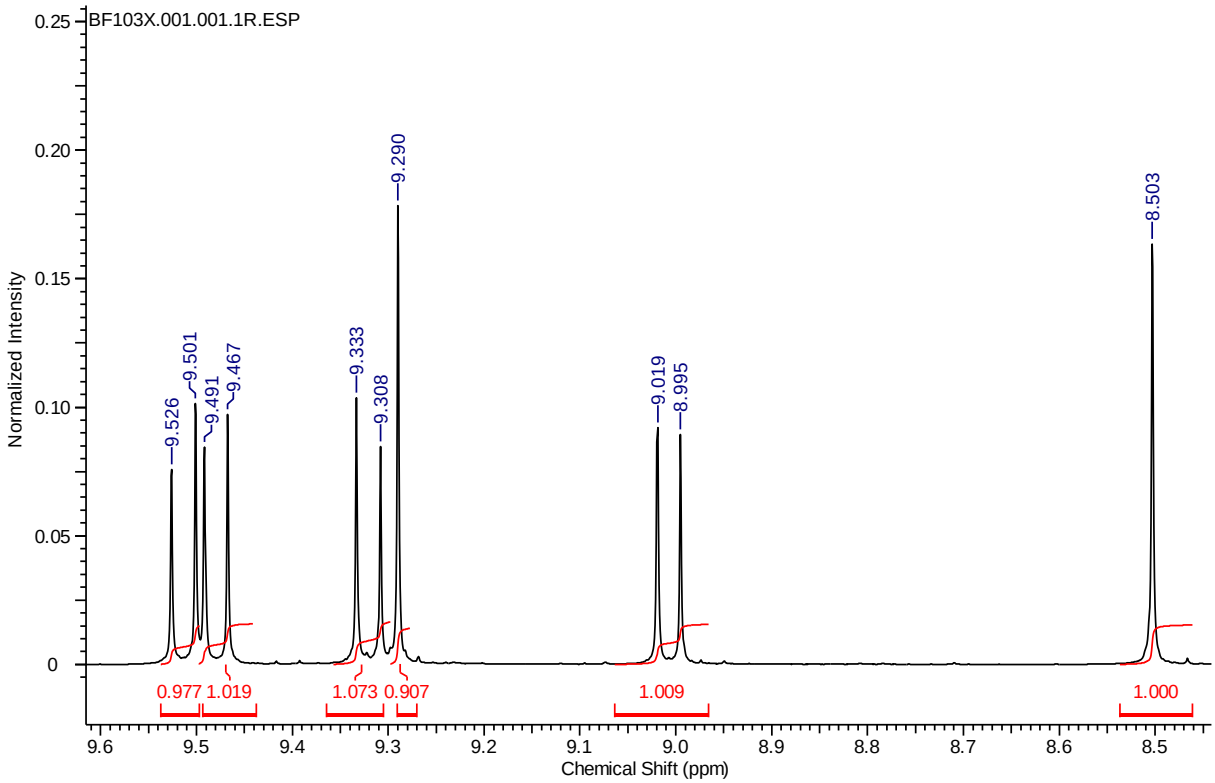

Figure S21: ^{1}H-NMR spectrum of **3c** (zoomed).

Photochem. Photobiol. Sci., 2014, **13**, 548-562

http://xlink.rsc.org/?doi=C3PP50404B

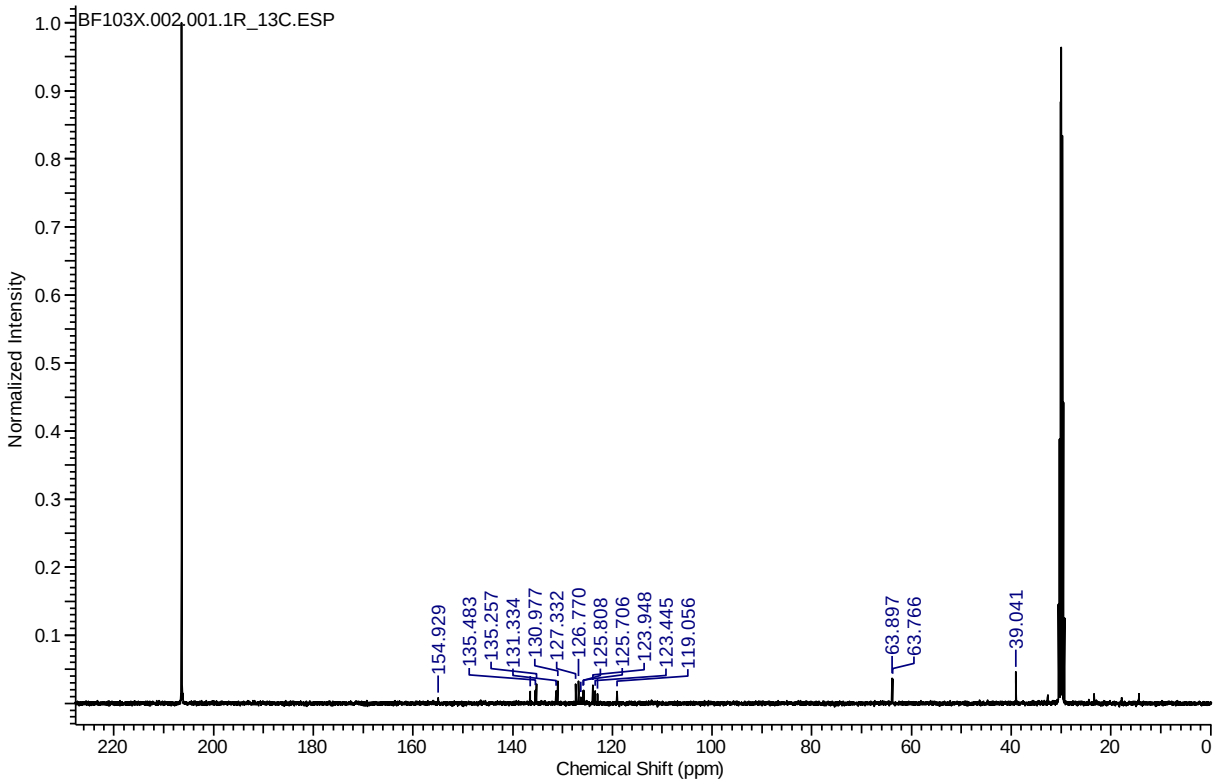

Figure S22: ^{13}C-NMR spectrum of **3c**.

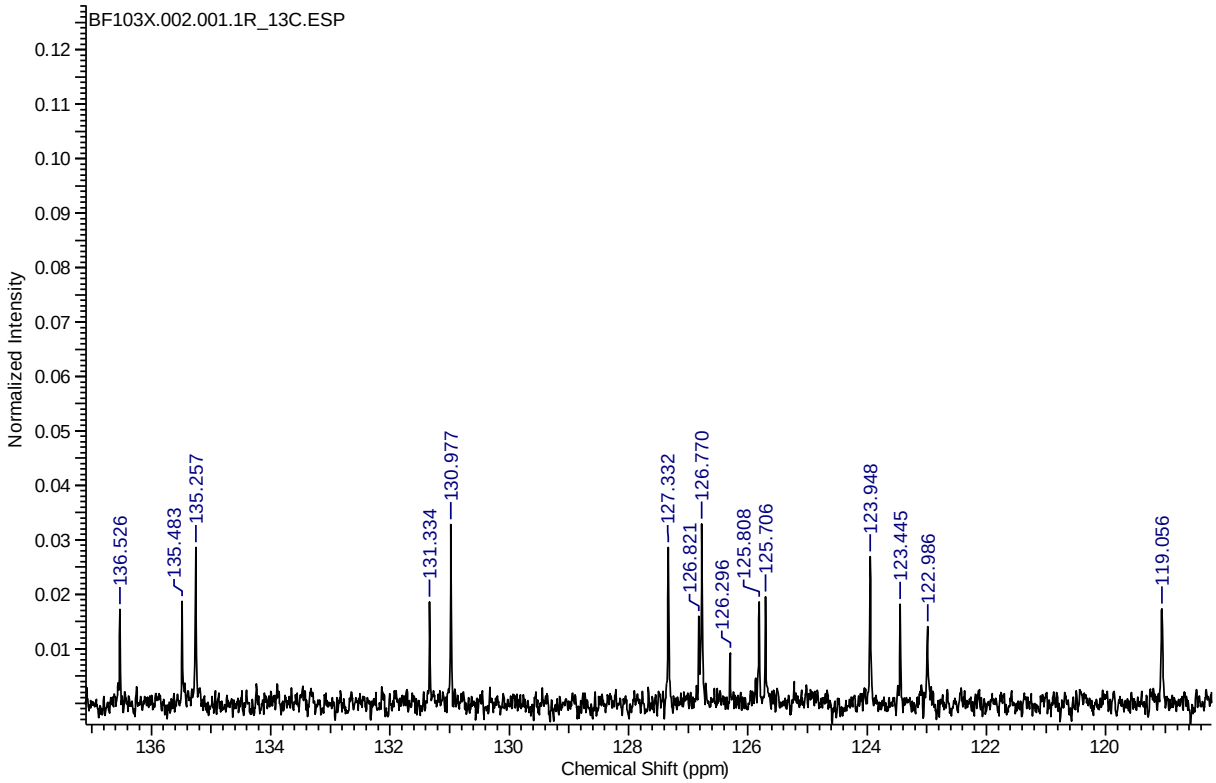

Figure 23: ^{13}C-NMR spectrum of **3c** (zoomed).

http://xlink.rsc.org/?doi=C3PP50404B

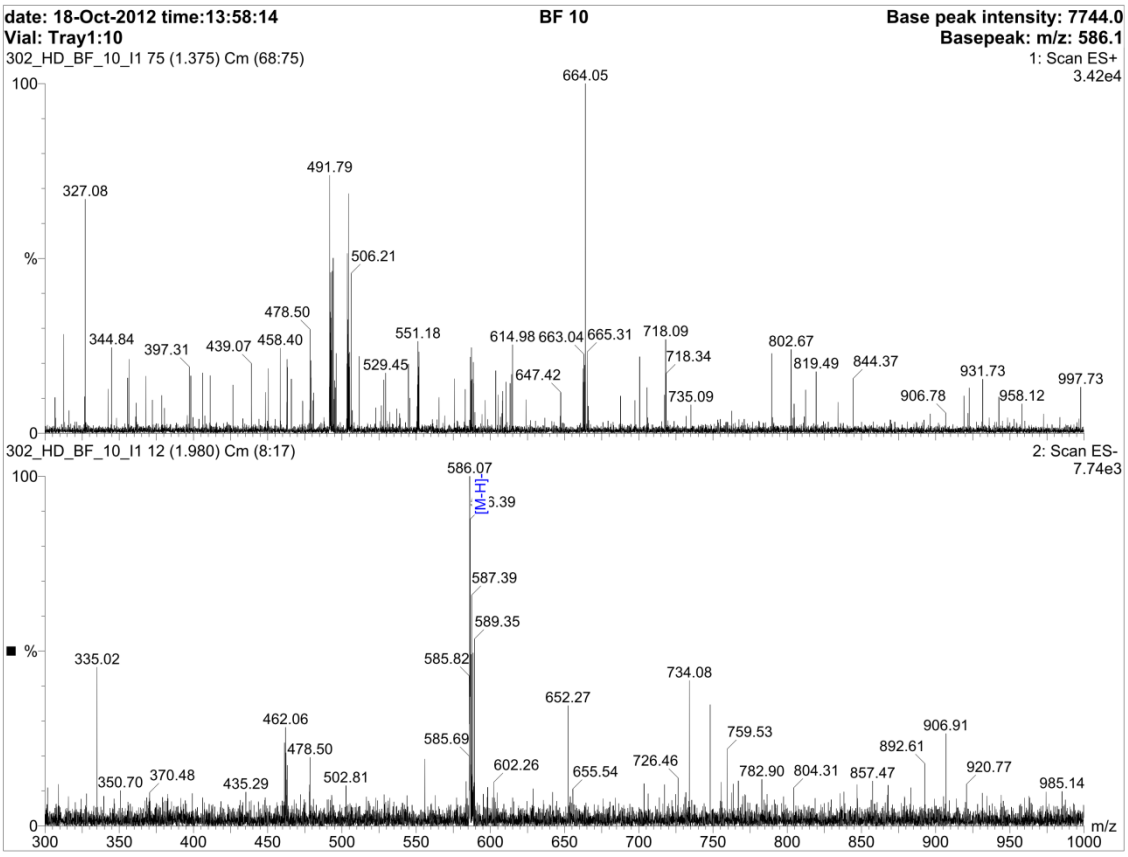

Figure S24: mass spectrum of **3d**.

Compound **3d**:

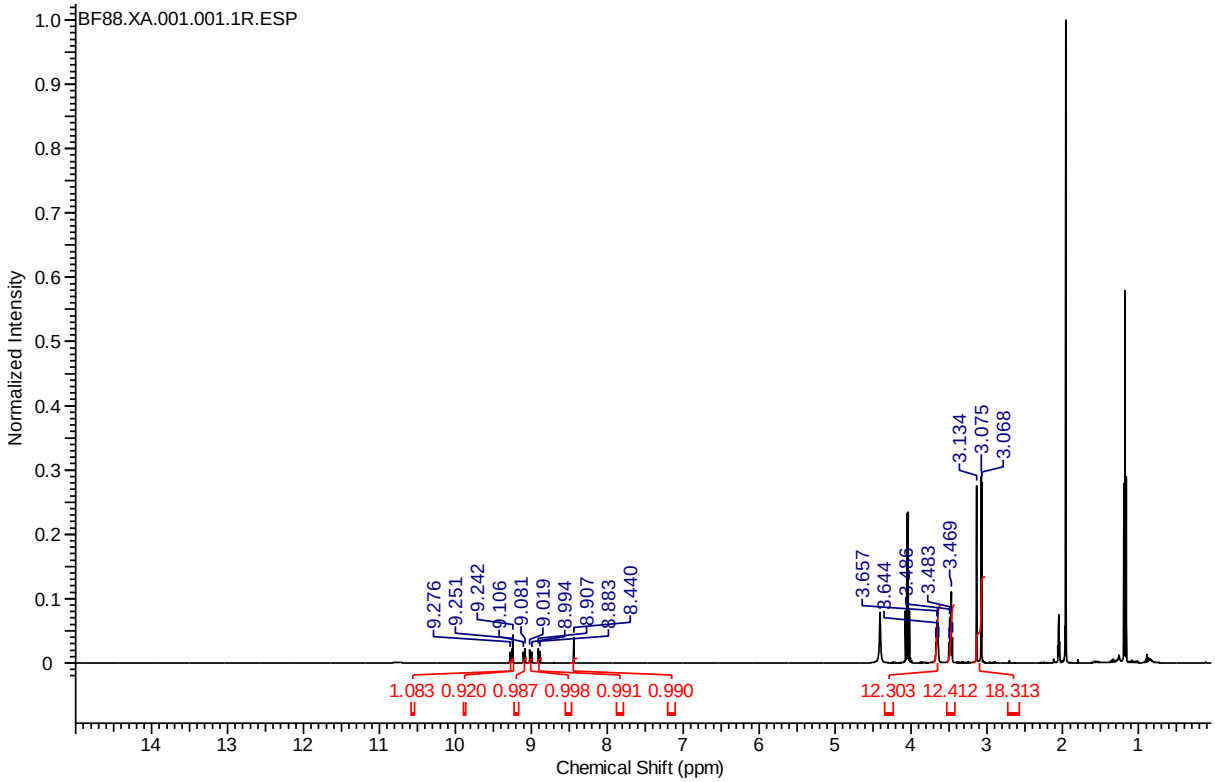

Figure S25: ^{1}H-NMR spectrum of **3d**.

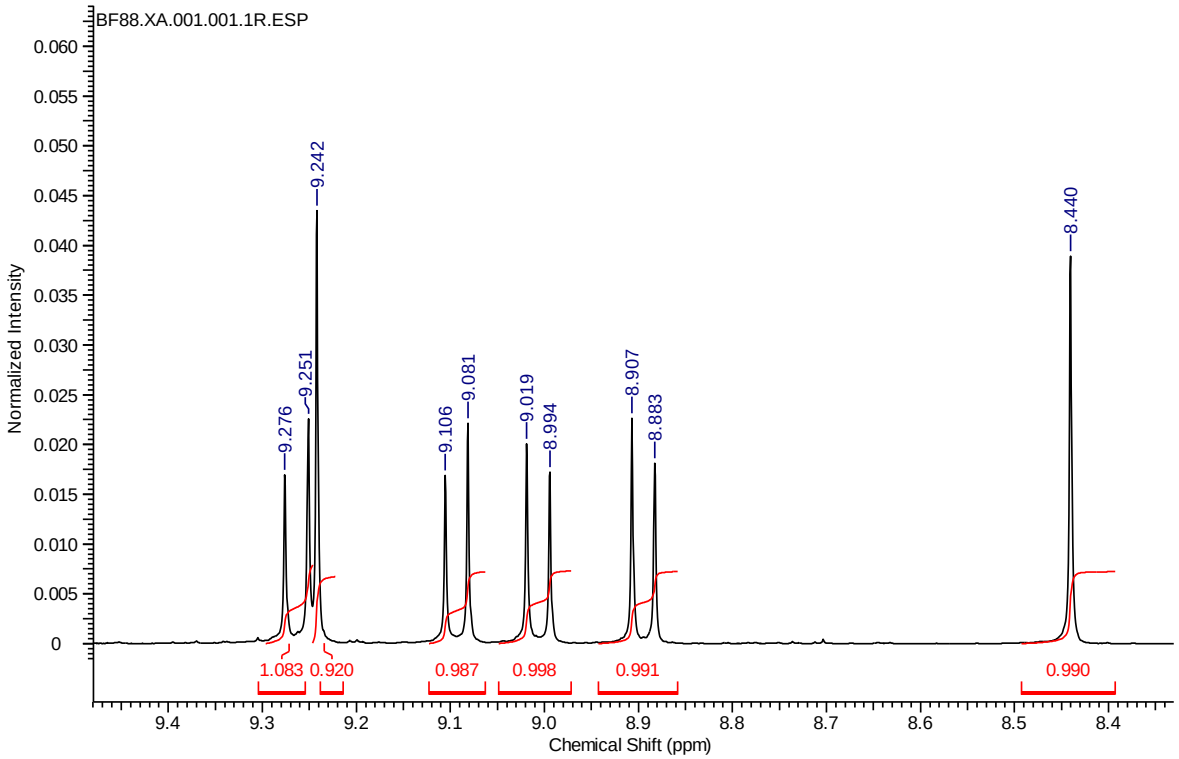

Figure S26: ^{1}H-NMR spectrum of **3d** (zoomed).

http://xlink.rsc.org/?doi=C3PP50404B

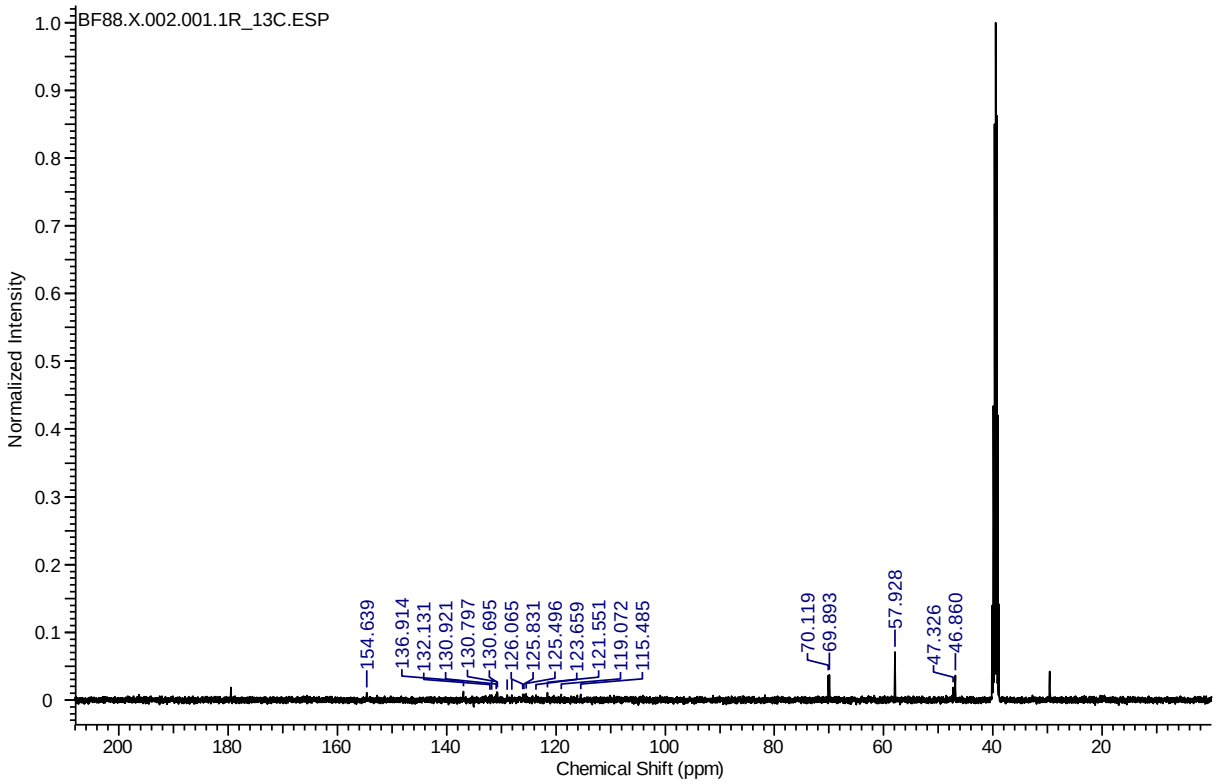

Figure S27: ^{13}C-NMR spectrum of **3d**.

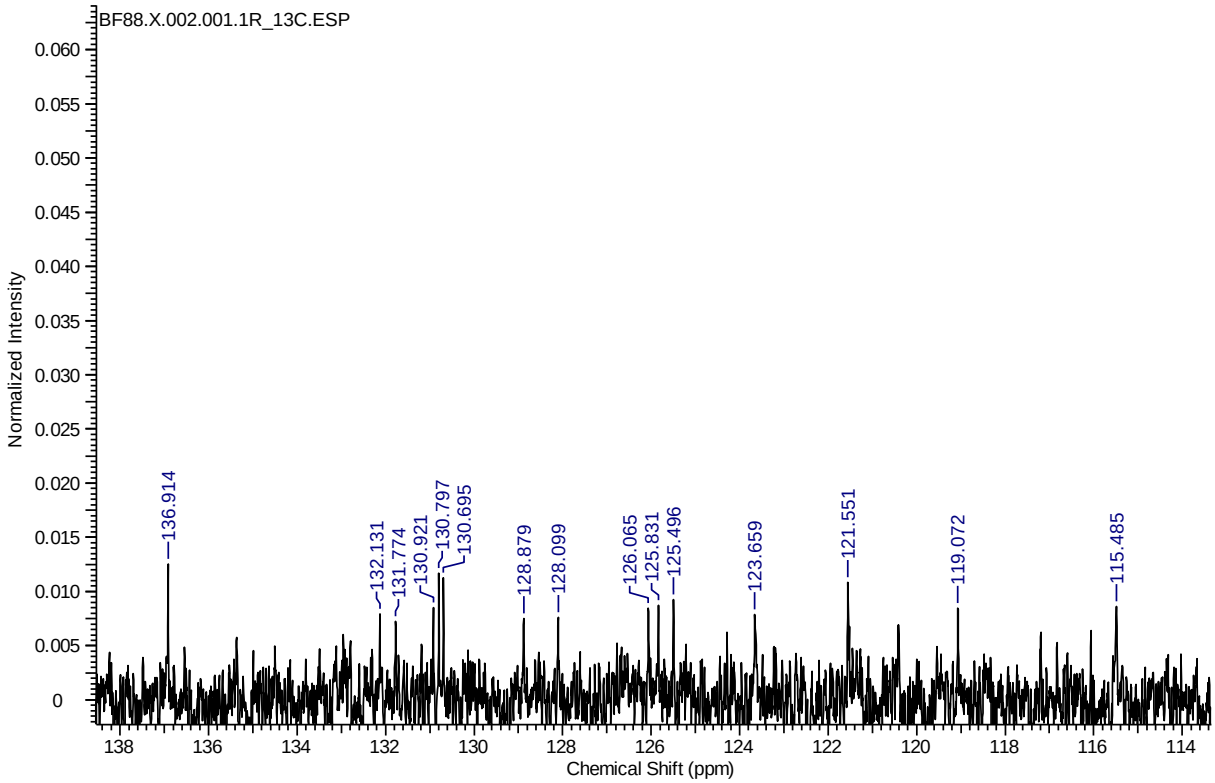

Figure S28: ^{13}C-NMR spectrum of **3d** (zoomed).

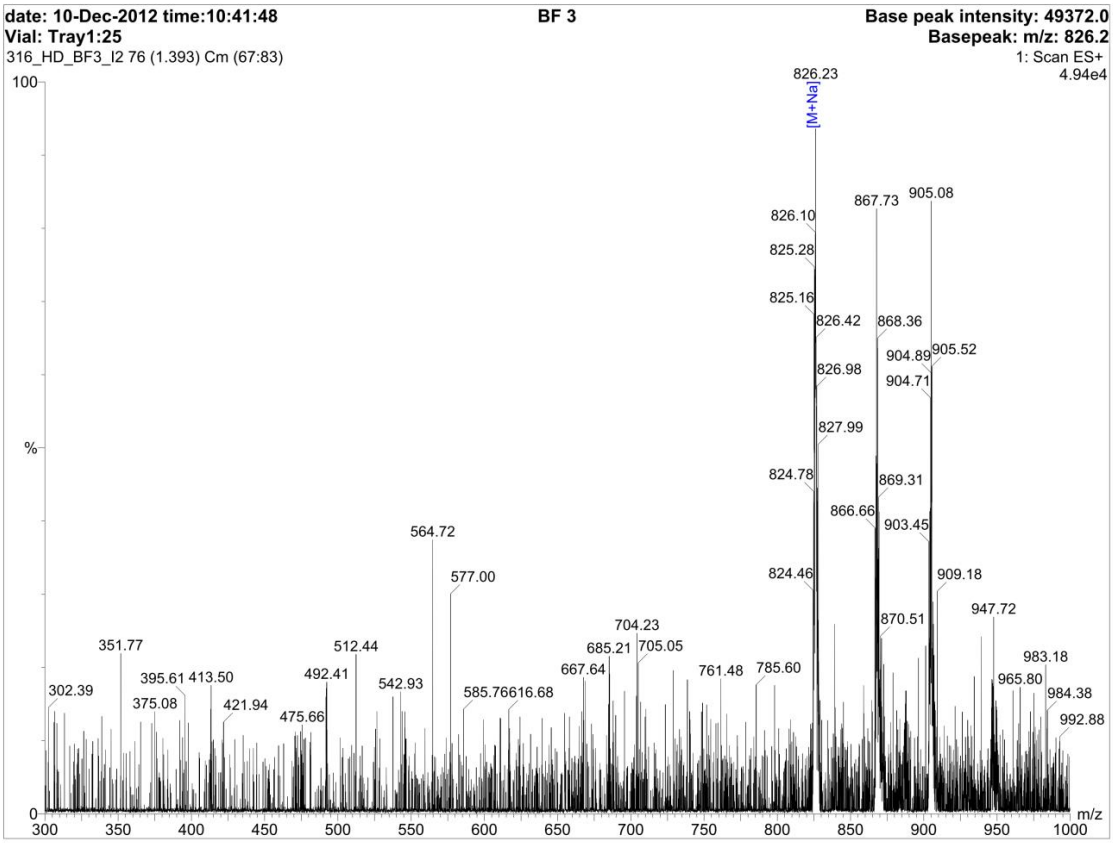

Figure S29: mass spectrum of **3d**.

http://xlink.rsc.org/?doi=C3PP50404B

Compound **3e**:

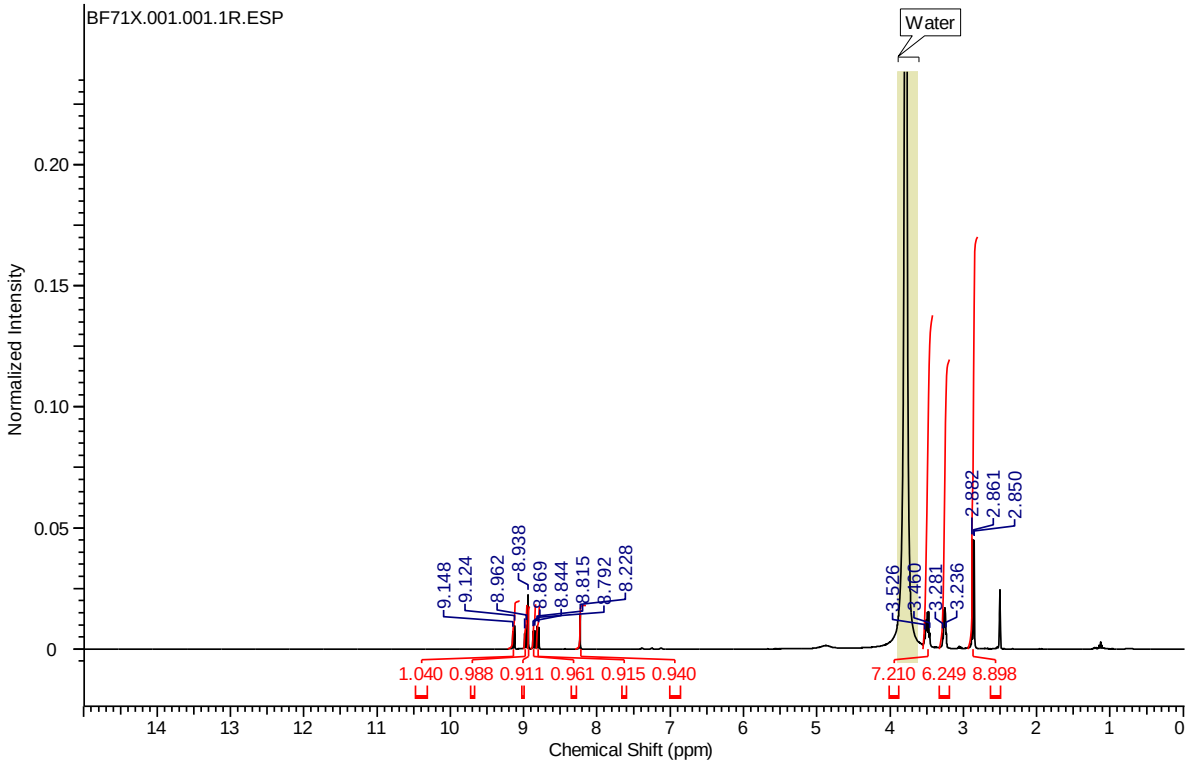

Figure S30: ^{1}H-NMR spectrum of **3e**.

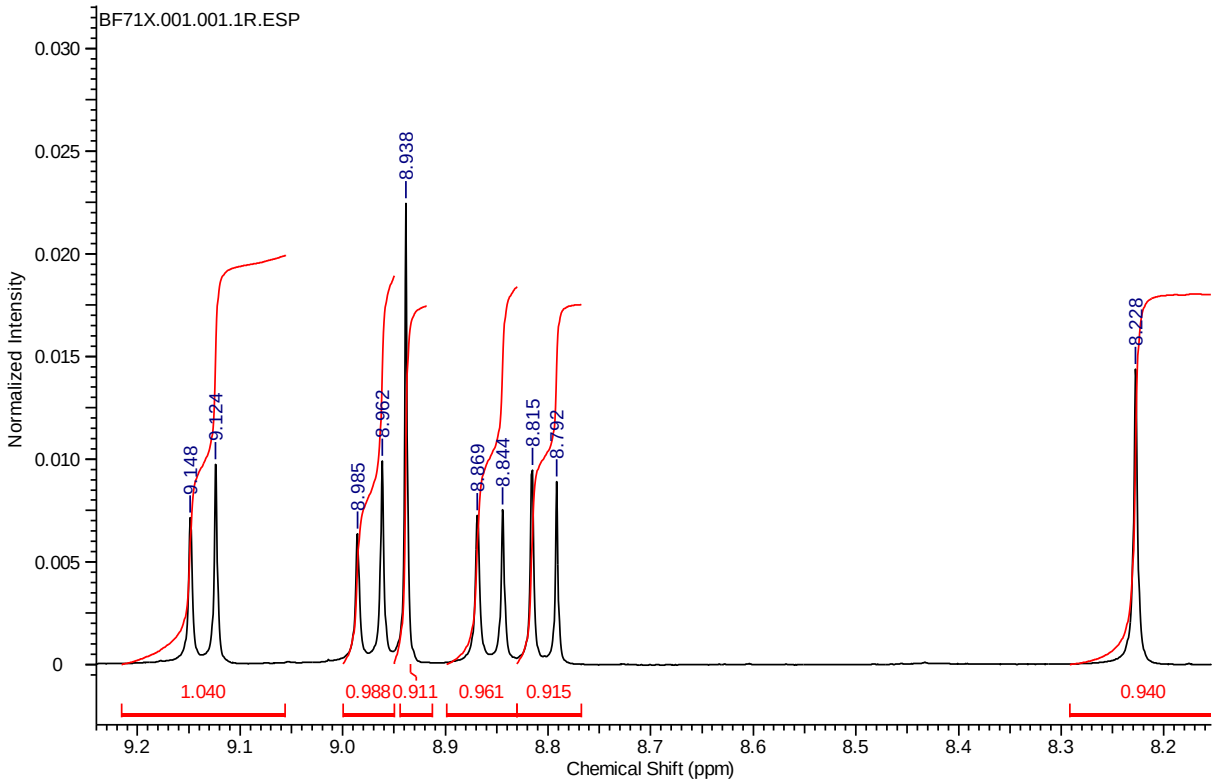

Figure S31: ^{1}H-NMR spectrum of **3e** (zoomed).

Photochem. Photobiol. Sci., 2014, **13**, 548-562

http://xlink.rsc.org/?doi=C3PP50404B

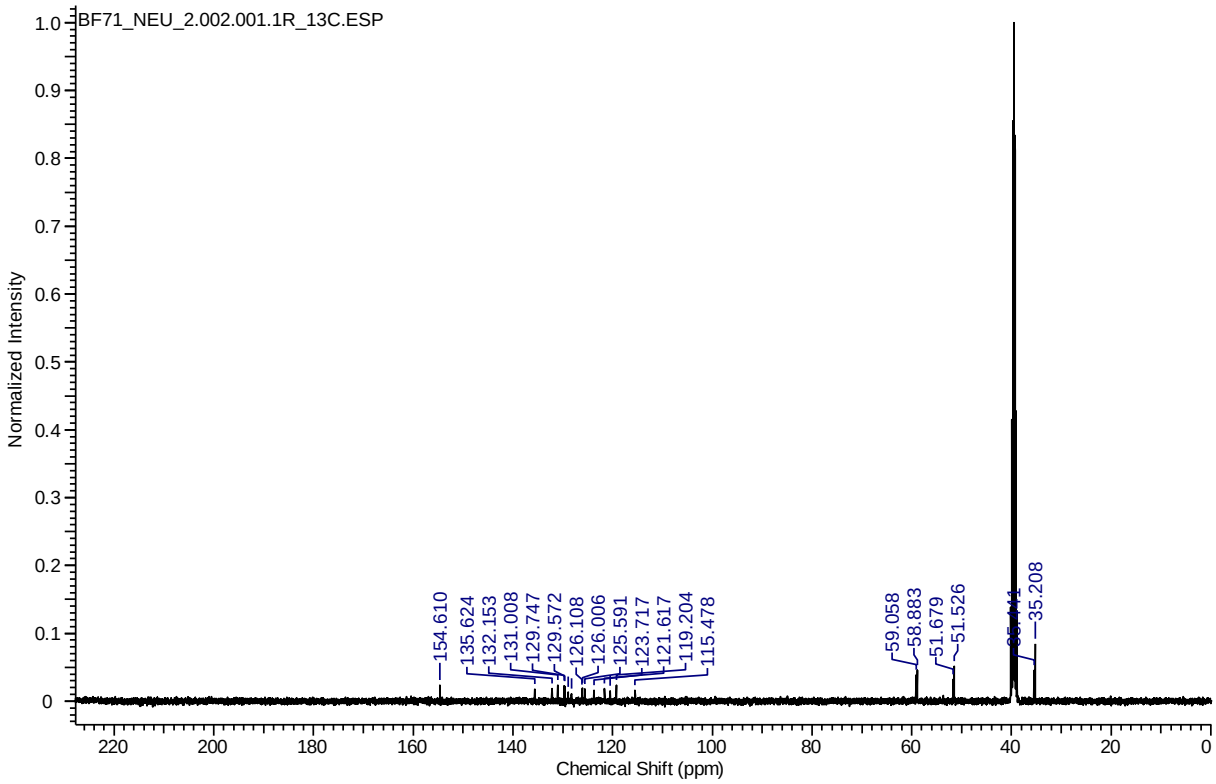

Figure S32: ^{13}C-NMR spectrum of **3e**.

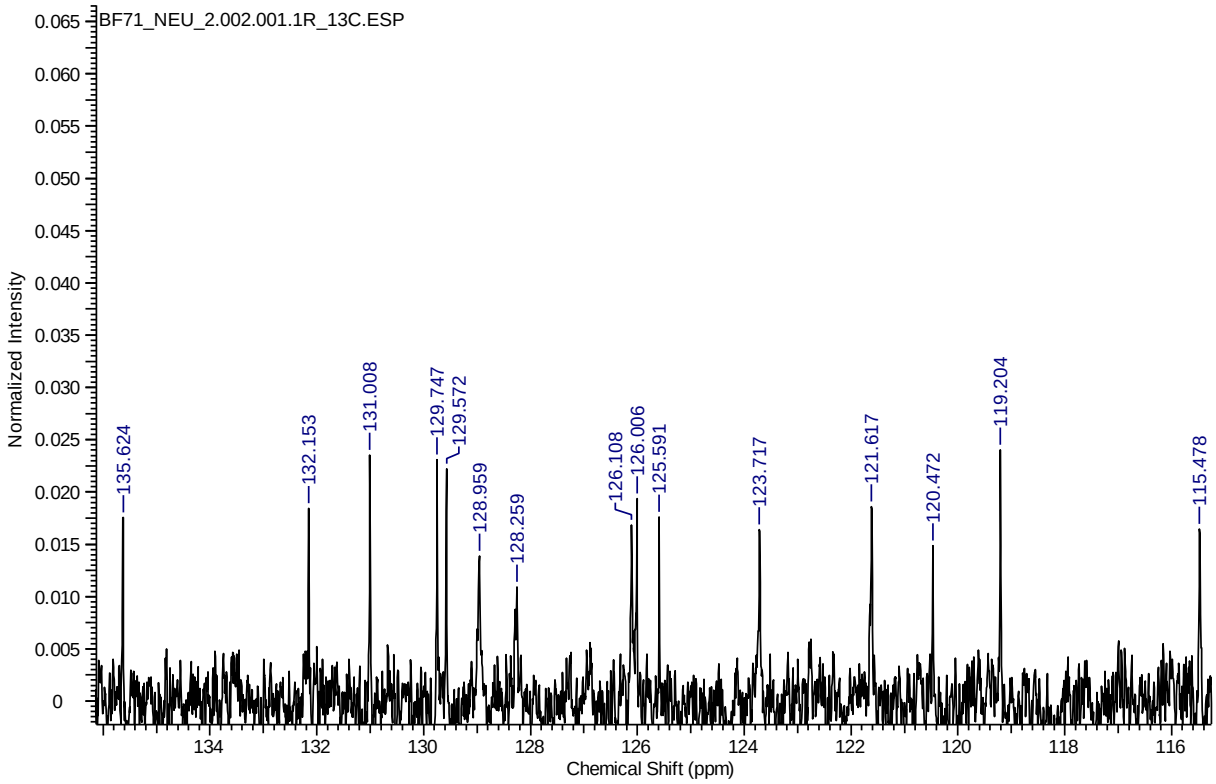

Figure S33: ^{13}C-NMR spectrum of **3e** (zoomed).

http://xlink.rsc.org/?doi=C3PP50404B

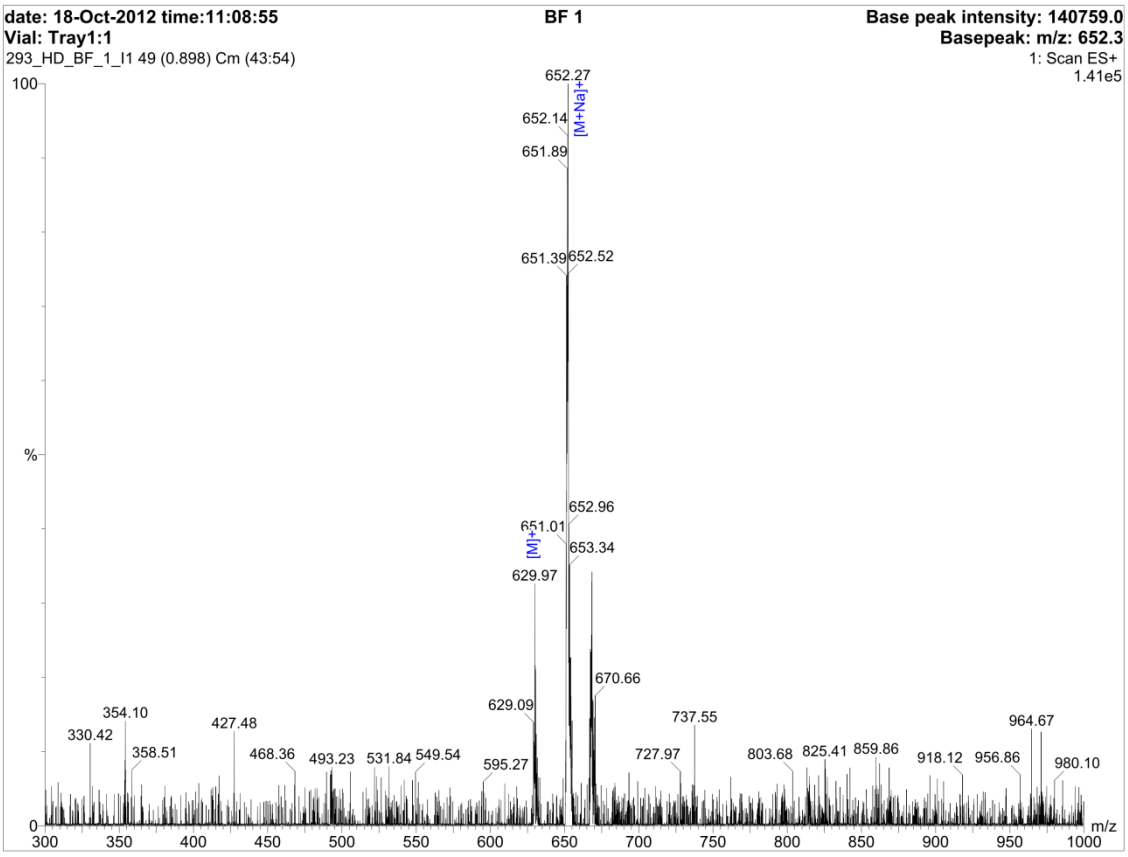

Figure S34: mass spectrum of **3e**.

Compound **3f**:

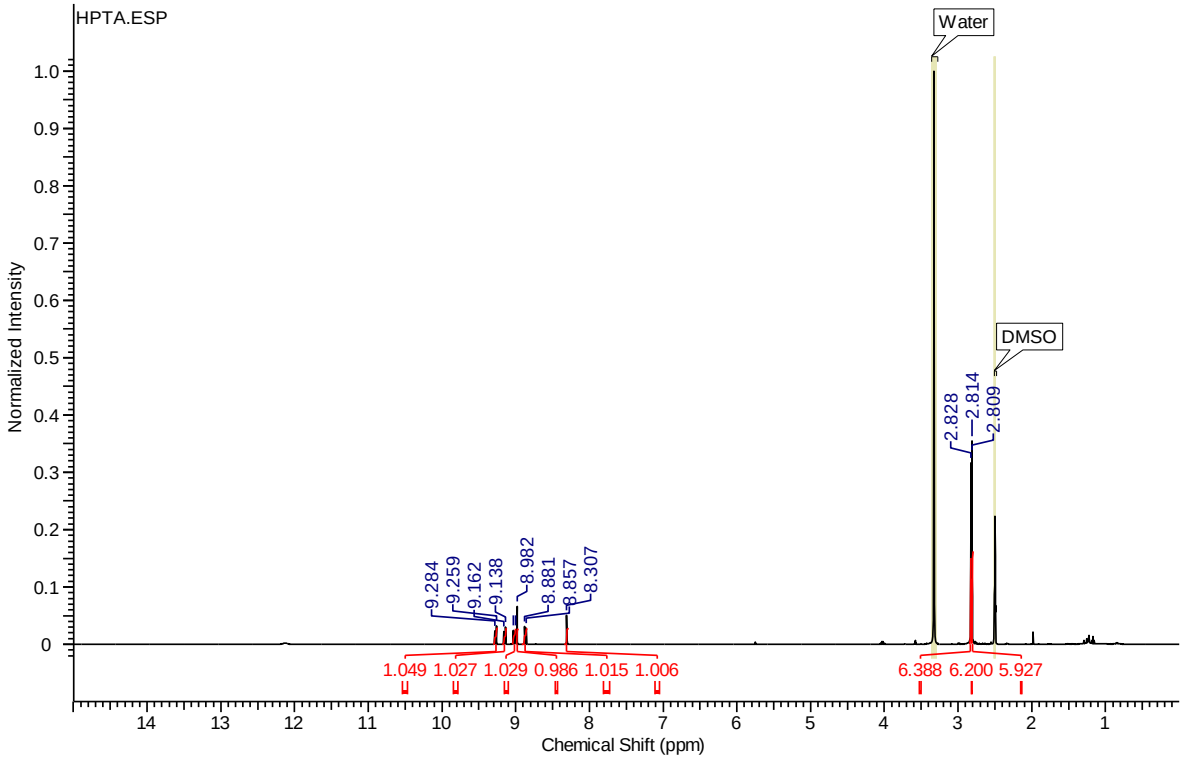

Figure S35: ^{1}H-NMR spectrum of **3f**.

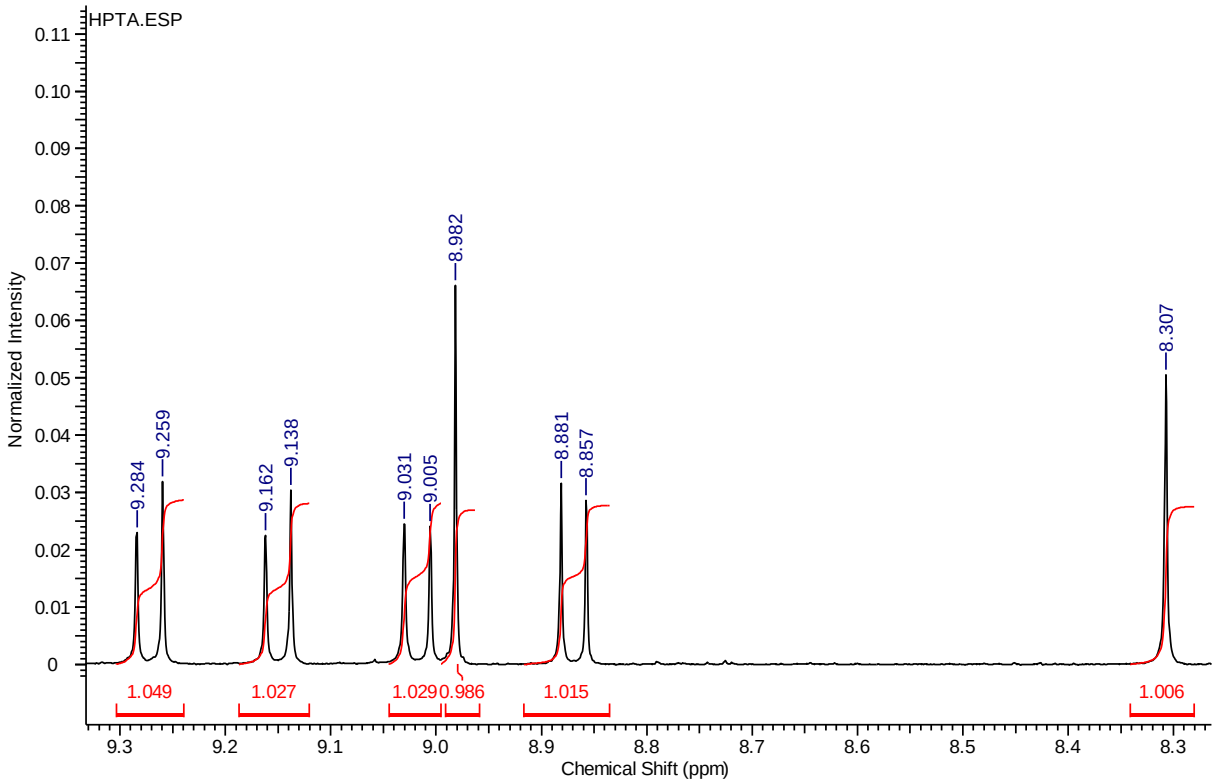

Figure S36: ^{1}H-NMR spectrum of **3f** (zoomed).

http://xlink.rsc.org/?doi=C3PP50404B

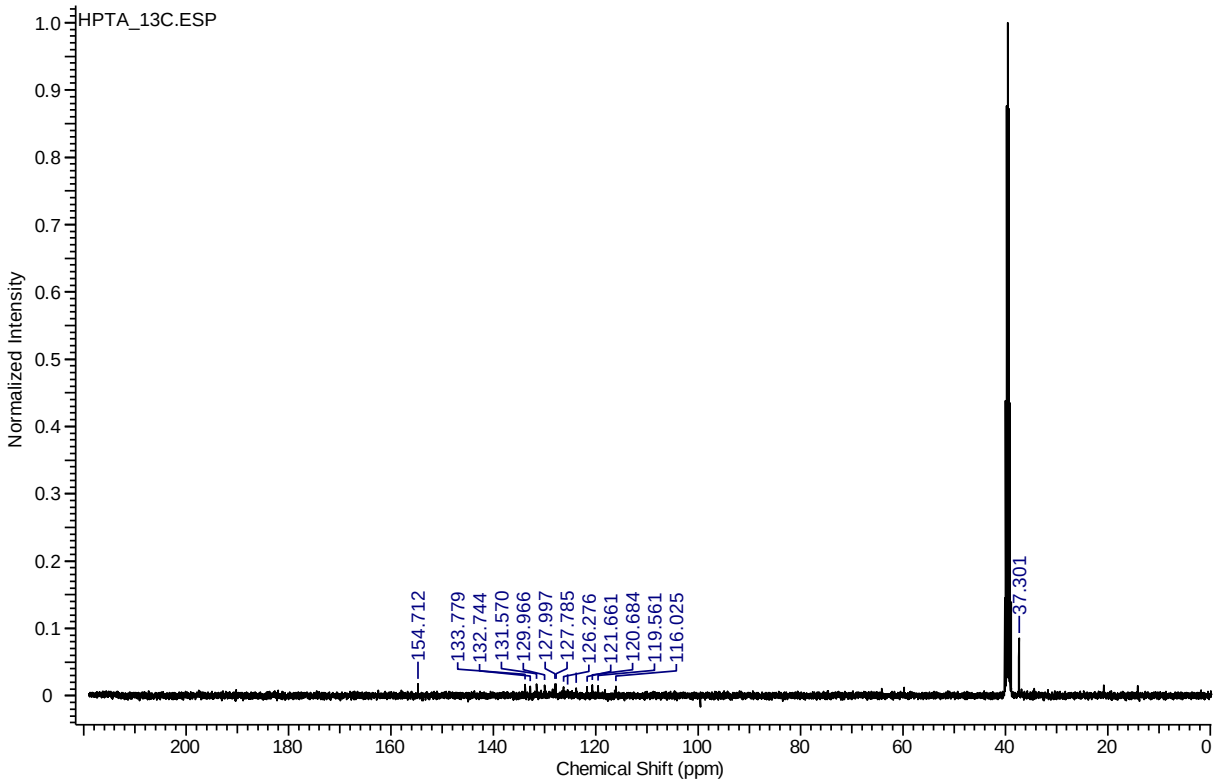

Figure S37: ^{13}C-NMR spectrum of **3f**.

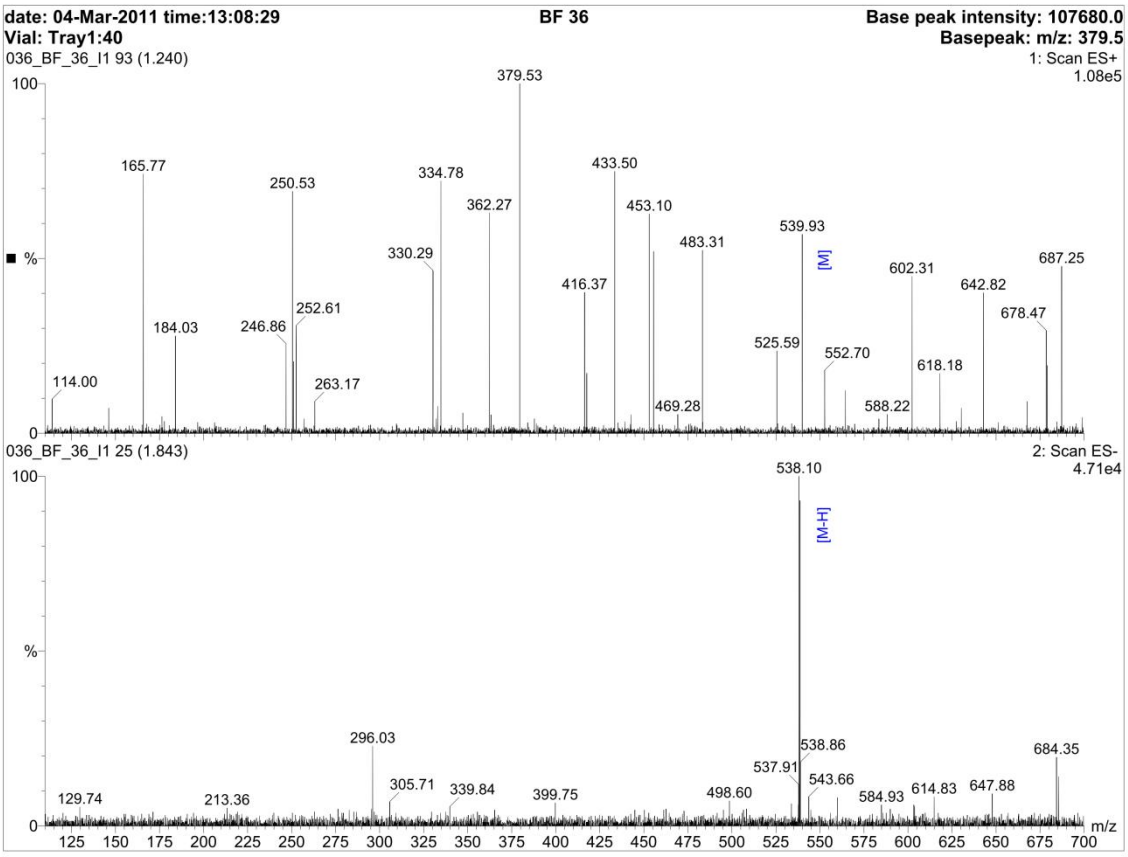

Figure S38: mass spectrum of **3f.**

References:

[S1] J. Widengren, B. Terry, R. Rigler, *Chem. Phys.* **1999**, *249*, 259–271.

http://xlink.rsc.org/?doi=C3PP50404B

5.2 M. Vester, T. Staut, J. Enderlein and G. Jung, , *J. Phys. Chem. Lett.*, 2015, 6, 1149-1154

„Photon Antibunching in a Cyclic Chemical Reaction Scheme“

THE JOURNAL OF PHYSICAL CHEMISTRY Letters

Letter

pubs.acs.org/JPCL

Photon Antibunching in a Cyclic Chemical Reaction Scheme

Michael Vester,[†] Tobias Staut,[†] Jörg Enderlein,[‡] and Gregor Jung*[,†]

[†]Biophysikalische Chemie, Universität des Saarlandes, Campus B2.2, 66123 Saarbrücken, Germany

[‡]III. Physikalisches Institut für Biophysik und Komplexe Systeme, Georg-August-Universität, Friedrich-Hund-Platz 1, 37077 Göttingen, Germany

Supporting Information

ABSTRACT: The direct observation of chemical reactions on the single-molecule level is an ultimate goal in single-molecule chemistry, which also includes kinetic analyses. To analyze the lifetime of reaction intermediates, very sophisticated excitation schemes are often required. Here we focus on the kinetic analysis of the ground-state proton transfer within the photocycle of a photoacid. In detail, we demonstrate the determination of the bimolecular rate constant of this process with nanosecond resolution. The procedure relies on the exploration of a purely quantum-optical effect, namely, photon antibunching, and thus on evaluating interphoton arrival times to extract the reaction rate constant.

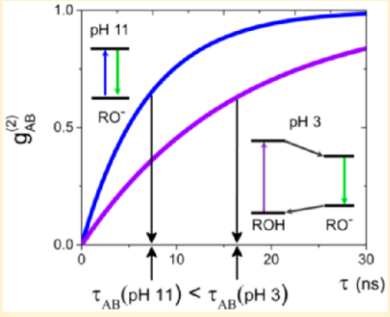

In the past few years, efforts were taken to visualize chemical reactions on the single-molecule level.[1−5] The interpretation of such experiments is mainly based on the evaluation of spectral shifts, which occur during the chemical reaction. A kinetic analysis of reaction intermediates could provide a better understanding of underlying reaction mechanisms. To monitor the time evolution of transient species, complex excitation schemes are often necessary.[6,7] We will determine the lifetime of a reaction intermediate by exploration of photon-antibunching, a purely quantum-optical effect.

Individual quantum emitters such as atoms, semiconductor nanocrystals, nanodiamonds, or single molecules are characterized by so-called photon antibunching.[8−13] This term indicates that these systems emit photons, which are temporally well-separated, and that no two photons are emitted simultaneously. Thus, it is possible to distinguish between classical and nonclassical light emission.[14−16] Beyond its fundamental meaning for quantum optics, the observation of antibunching also serves as the ultimate proof for the presence of individual emitters in single-molecule experiments.[10,11,17−20] Moreover, the antibunching amplitude can be utilized for determining the number of fluorophores.[21−23] Thus, the stoichiometry of biochemical complexes or aggregates can be determined.[24] Rate constants of photophysical processes[25,26] or even of conformational fluctuations[27,28] are also accessible with antibunching. Finally, super-resolution microscopy is performed using second- and higher-order correlation functions.[29−31] These examples provide applications of photon antibunching. Despite this interplay between molecular science and quantum optics, antibunching has not been exploited to measure chemical reaction rates so far. Consequently, the question arises of how a system has to look like for providing chemical rate constants from antibunching.

We previously introduced several photoacids, that is, an aromatic alcohol, which exhibits a considerably higher acidity in the excited state than in the ground state.[32] In the present study, we use the photoacid tris(2,2,2-trifluoroethyl)-8-hydroxypyrene-1,3,6-trisulfonate (Figure 1A) because of its pronounced photostability, high fluorescence quantum yield (Φ_F = 0.87), and sufficient water solubility.[32] This compound and its conjugated base represent a pair of two-level quantum systems, coupled by a chemical reaction in the ground and the electronically excited state (Figure 1B).[32] Reaction conditions can be tuned in such a way that a full photocycle, the so-called Förster-cycle, is traversed once the photoacid is excited. A contribution of the triplet state to the photodynamics can be neglected. (See the Supporting Information (SI VIII) for details.)

Upon photoexcitation of the ROH species with λ_{exc} = 445 nm, the acidity is raised from pK_a = 4.7 by roughly seven orders of magnitude to pK_a* = −2.8. This change of the acidity constant, ΔpK_a, corresponds to a difference of the electronic transition energies of the photoacid and its conjugated base according to eq 1.[33]

$$\Delta \mathrm{p}K_a = \frac{h(\nu_{ROH} - \nu_{RO^-})}{kT \ln(10)} \quad (1)$$

where ν_{ROH} and ν_{RO^-} correspond to the frequencies of the emission maxima of ROH and RO$^-$, respectively. A proton is transferred to nearby water molecules within a few picoseconds.[34] This process is called excited-state proton transfer

Received: February 9, 2015
Accepted: March 12, 2015

DOI: 10.1021/acs.jpclett.5b00280
J. Phys. Chem. Lett. 2015, 6, 1149−1154

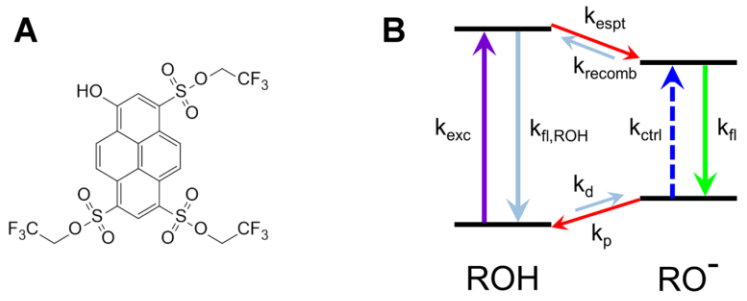

Figure 1. (A) Chemical structure of the photoacid tris(2,2,2-trifluoroethyl)-8-hydroxypyrene-1,3,6-trisulfonate of this study. (B) Förster cycle of the photoacid. Depicted are the rate constants within the photocycle: k_{exc}, excitation; $k_{fl,ROH}$, fluorescence of the acidic form; k_{espt}, excited-state proton transfer; k_{recomb}, geminate recombination; k_{fl}, fluorescence of the basic form; k_p, reprotonation in the ground state; k_d, deprotonation in the ground state. k_{ctrl} is applied in the control experiment for directly exciting the conjugated base at pH 11. Colored: mandatory for discussion. Gray: negligible under experimental conditions. (See the text for details.)

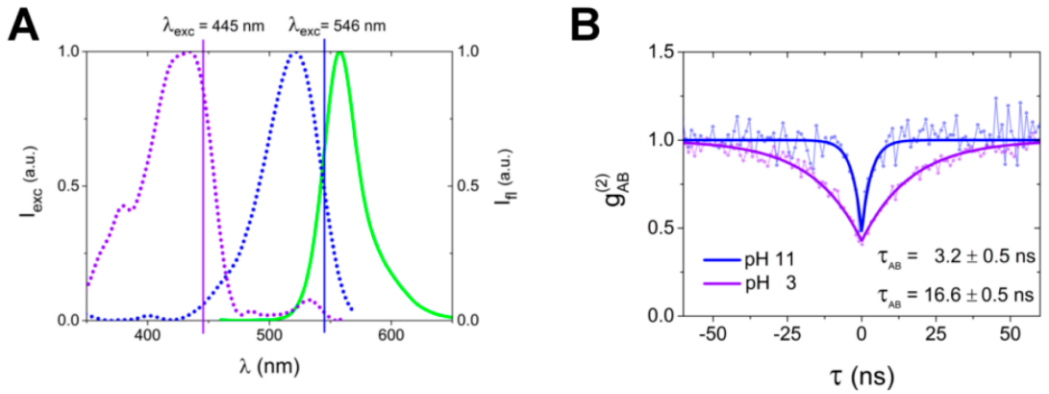

Figure 2. (A) Fluorescence excitation (dotted lines) and fluorescence emission (full line) spectra of the photoacid at pH 11 (blue curve) and pH 3 (purple curve). (B) Recorded autocorrelation $g_{AB}^{(2)}(\tau)$ at pH 11 (blue; 20 mM buffer concentration, I_{exc} = 880 kW/cm^2) and at pH 3 (purple; 20 mM buffer concentration, I_{exc} = 200 kW/cm^2). Monoexponential fits are shown as solid lines. Color code as in Figure 1B.

(ESPT), generating the corresponding base in its excited state. Subsequently, a fluorescence photon is emitted. Afterward, reprotonation in the ground state occurs, reforming the photoacid, and the photocycle is completed. pH 3 < p$K_{A,GS}$ is chosen for the experiments to ensure that the ground-state equilibrium is largely shifted toward the photoacid at the beginning of a photocycle (Figure 2A). Because the transition wavelengths of both two-level systems are optically well-separated according to eq 1, reexcitation of the conjugated base is largely avoided (Figure 2A). In a kinetic perspective, the conjugated base is regarded as intermediate; that is, it is not stable in a thermodynamic sense. Because the reprotonation is a bimolecular[35] process, the lifetime of this intermediate depends on the concentration of the reprotonation counterpart. The reexcitation and consequently the emission of another photon can then only take place after base-proton recombination. In other words, the minimum time between two photons emitted from the same molecule is exactly the time the molecule needs to complete one photocycle (Figure 1B) because photons are emitted only upon excitation of the acidic state. Therefore, it should be possible to increase antibunching by adjusting the reprotonation rate. Conversely, this means the reprotonation rate, that is, the decay kinetics of the intermediate, should be accessible by analyzing the antibunched fluorescence. For an optimal measurability, the reprotonation rate should be as low as possible.

Antibunching is seen as a dip of the second-order correlation function $g_{AB}^{(2)}(\tau)$ at short correlation times. The second-order correlation function is proportional to the probability of detecting a second photon at some lag time τ after the detection of a first photon.[25] For a single two-level system, $g_{AB}^{(2)}(\tau)$ increases monoexponentially starting from τ = 0. The antibunching dip at τ = 0 is a hallmark of the impossibility to detect two photons from a single emitter during one photocycle. The normalization procedure to obtain $g_{AB}^{(2)}(\tau)$ out of the measured autocorrelation $g_M^{(2)}(\tau)$ can be found in the Supporting Information (SI VII).

Initially, we performed an antibunching experiment at pH 11 ≫ pK_a, where the corresponding base is excited at λ_{exc} = 546 nm (Figure 2B). Here the system should behave as a classical two-level system, and the characteristic time of the antibunching should be related to the sum of the excitation and the fluorescence rate constant by $k_{ctrl} + k_{fl} = 1/\tau_{AB}$.[25,36] k_{crtl} is composed of I_{exc}, and the absorption cross section and amounts to roughly 180 MHz. Actually, the characteristic time is found to be significantly smaller than the fluorescence lifetime of the molecule (τ_{AB} = 3.2 ± 0.5 ns < 6.1 ± 0.1 ns = $\tau_{fl} = 1/k_{fl}$), as expected. In contrast, at pH 3 < pK_a, excitation of the photoacid at λ_{exc} = 445 nm provides an apparently slower antibunching

DOI: 10.1021/acs.jpclett.5b00280
J. Phys. Chem. Lett. 2015, 6, 1149−1154

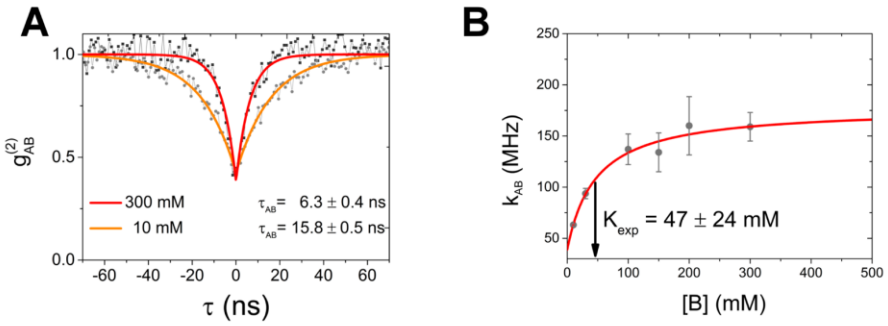

Figure 3. (A) $g_{AB}^{(2)}(\tau)$ at different citrate buffer concentrations [B]. The full lines result from monoexponential fits. (B) Plot of experimental antibunching decay rate constants versus the total buffer concentration [B]. The fit according to eq 2 is shown as full line.

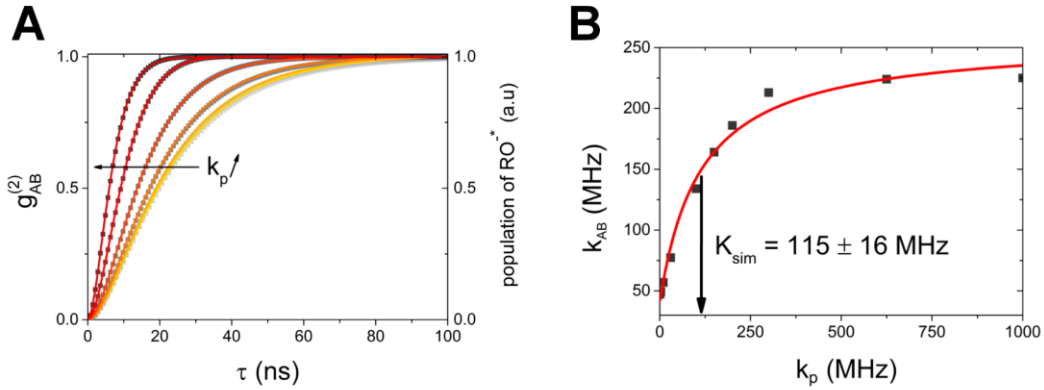

Figure 4. (A) $g_{AB}^{(2)}(\tau)$ obtained by solving the three-level scheme analytically (eq 3, dotted curves) for different reprotonation rate constants. These $g_{AB}^{(2)}(\tau)$ are compared with numerical solutions of the four-level scheme (solid lines; see also eq S1 in the Supporting Information). (B) k_{AB} as obtained from a monoexponential fit of the analytical $g_{AB}^{(2)}(\tau)$ plotted versus theoretical reprotonation rate constants k_p. The full line depicts the fit according to eq 10.

time (τ_{AB} = 16.6 ± 0.5 ns > τ_{fl} = 6.1 ± 0.1 ns =1/k_{fl}), which can be traced back to the photochemical delay (Figure 2B). Please note that the emissive state is identical in both experiments (Figure 2A).

As previously stated, the reprotonation of the conjugated base in the electronic ground state is a bimolecular reaction. Because protonation capability is restricted not only to "free" protons but also to weaker acids, that is, buffer molecules, a dependence on their concentration is expected. Moreover, this procedure enables us to drive the kinetics from a cyclic reaction scheme to a two-level system. To quantify this effect, the measurements with excitation of the photoacid are repeated at varying buffer concentration (Figure 3A). pH 3 was chosen because lower pH values would hide any buffer effects due to rapid reprotonation by ubiquitous protons and larger pH values would, however, populate the conjugated base to a higher amount. The obtained antibunching time constants from monoexponential fits are plotted versus the total buffer concentration (Figure 3B). The experimental rate constants nicely follow a saturation behavior according to eq 2.

$$k_{AB} = k_{0,exp} + \frac{k_{s,exp}[B]}{K_{exp} + [B]} \quad (2)$$

Here [B] is the total concentration of the buffer, $k_{0,exp}$ is an offset, and $k_{0,exp}$ + $k_{s,exp}$ is the maximally obtainable antibunching rate constant. The saturation constant K_{exp} corresponds to the buffer concentration where k_{AB} = $k_{0,exp}$ + $k_{s,exp}$/2. $k_{0,exp}$ is obtained as 39 ± 14 MHz, $k_{s,exp}$ is obtained as 139 ± 11 MHz, and K_{exp} is 47 ± 24 mM (Figure 3B). The maximally observable antibunching rate constant, $k_{AB,max}$, is 178 ± 18 MHz and thus larger than k_{fl}. A direct comparison with the control experiment at pH 11 in Figure 2B, however, is misleading as different excitation conditions (λ_{exc}, I_{exc}) are employed.

To understand the antibunching kinetics quantitatively, $g_{AB}^{(2)}(\tau)$ is derived from the coupled kinetics of the quantum system under investigation. Actually, its simulation (Figure 4A,B and Supporting Information SI I) enables us to connect the buffer concentration dependence (eq 2 and depicted in Figure 3B) to the bimolecular reprotonation rate constant k_p in Figure 1B. For that purpose, the time-dependent population of the four involved states was examined (Supporting Information (SI I)).[25,36,37]

Numerical calculations, based on available experimental data, were performed to estimate the influence of the reverse chemical processes (Figure 1B, gray arrows) on the kinetics.[32,34] We used k_{fl} as determined from time-correlated single-photon counting (k_{fl} = 160 MHz), k_{espt} from fluorescence upconversion measurements (k_{espt} = 250 GHz),[34] k_{recomb} from pK_a^* = −log(k_{espt}/k_{recomb}) = −2.8, and k_{exc} from the excitation intensity and the absorption cross section. In particular, the

DOI: 10.1021/acs.jpclett.5b00280
J. Phys. Chem. Lett. 2015, 6, 1149−1154

minor absorbance of the anionic species at pH 3, corresponding to <10% of the whole population, was expected to distort $g_{AB}^{(2)}(\tau)$. However, we found that reprotonation kinetics in the excited state ($k_{recomb} \approx 400$ MHz $\ll k_{espt} \approx 250$ GHz) has no impact on the autocorrelation function. Moreover, the deprotonation in the ground state can be neglected as long as the forward reaction rate is at least about one magnitude larger than the reverse reaction rate. (See Figure II in the Supporting Information (SI I).) In addition, we verified that the population of the excited photoacid is close to zero for all times, as the ESPT rate constant is about three orders of magnitude larger than all of the other rate constants in the four-level system.[34] Thus, the four-level scheme can be reduced to a three-level description (eq 3) without loss of significance (Figure 4A).

$$\frac{d}{dt}\begin{pmatrix}[ROH]\\ [RO^{-*}]\\ [RO^{-}]\end{pmatrix} = \begin{pmatrix}-k_{exc} & 0 & k_p\\ k_{exc} & -k_{fl} & 0\\ 0 & k_{fl} & -k_p\end{pmatrix}\begin{pmatrix}[ROH]\\ [RO^{-*}]\\ [RO^{-}]\end{pmatrix} \tag{3}$$

$$\begin{pmatrix}[ROH]\\ [RO^{-*}]\\ [RO^{-}]\end{pmatrix}_{t=0} = \begin{pmatrix}0\\ 0\\ 1\end{pmatrix} \tag{4}$$

The initial condition (eq 4) was chosen because the molecule is prepared in its anionic ground state after the emission of the first photon. $g_{AB}^{(2)}(\tau)$ finally becomes (eqs 5−9; see Supporting Information (SI II) for details)

$$g_{AB}^{(2)} = 1 - \frac{\sigma}{2\Delta}\{\exp(s_1|\tau|) - \exp(s_2|\tau|)\} - \frac{1}{2}\{\exp(s_1|\tau|) + \exp(s_2|\tau|)\} \tag{5}$$

$$s_{1,2} = 1/2(-\sigma \pm \Delta) \tag{6}$$

$$\sigma = k_{exc} + k_{fl} + k_p \tag{7}$$

$$\rho = k_{exc}k_{fl} + k_{exc}k_p + k_{fl}k_p \tag{8}$$

$$\Delta = \sqrt{\sigma^2 - 4\rho} \tag{9}$$

In general, the full solution turns out to be composed of two exponentials with varying amplitudes for different k_p. As the experimental data are fitted well by monoexponentials, which is likely due to inherent shot noise and timing jitter of the detectors,[37] we reduce the analytical solution to the experimentally accessible functions (Supporting Information (SI III)). Antibunching time constants, which were obtained in this manner, also follow a saturation-like behavior when plotted versus k_p (Figure 4B).

$$k_{AB} = k_{0,sim} + \frac{k_{s,sim}k_p}{K_{sim} + k_p} \tag{10}$$

In this coarse-grained approach, $k_{0,sim}$ is 25 ± 4 MHz, $k_{s,sim}$ is 194 ± 7 MHz, and K_{sim} is 115 ± 16 MHz. These values should be connected to the experimentally determined data $k_{0,exp}$, $k_{s,exp}$, and K_{exp} for accessing the bimolecular reprotonation rate constant by citric acid and by ubiquitous protons. Two limiting situations of the analytical solutions (eqs 5−9) are studied before explaining the curve progression for varying buffer concentrations (Figure 3B) and reprotonation rate constants (Figure 4B), respectively.

In the limiting case of a very fast reprotonation ($k_p \gg k_{exc}$, k_{fl}) at high buffer concentrations (see Supporting Information (SI IV) for details), the $g_{AB}^{(2)}$ function approaches that of the two-level case, where the molecule cycles only between ROH in the electronic ground state and the excited RO^{-*}, in agreement with atomic or molecular two-level systems. The experimental and the simulated $k_{AB,max}$ should coincide in this limit.

$$k_{AB} \approx k_{exc} + k_{fl} - \frac{k_{exc}k_{fl}}{k_{exc} + k_{fl} - k_p} \approx k_{exc} + k_{fl} = k_{AB,max} \tag{11}$$

$k_{s,sim} = 194$ MHz corresponds to a value of $k_{AB,max} = 219$ MHz, and thus it is considerably too large compared with the experimental value of 178 MHz. However, the simulated data points in Figure 4B level off much faster than approximated by the saturation fit. In other words, the simulated k_{AB} does not exceed $k_{exc} + k_{fl}$, as predicted by eq 11. It should be emphasized that the offset, $k_{0,sim}$, in Figure 4B corresponds to the excitation rate, which was set to 30 MHz as realistic starting point for the calculations. (See later.)

In the limit of slow reprotonation kinetics, that is, $k_{fl} \gg k_{exc}$, k_p, the antibunching rate constant, can be well described by the sum of the excitation rate and the reprotonation rate constant.

$$k_{AB} \approx k_{exc} + k_p - \frac{k_{exc}k_p}{k_{exc} - k_{fl} + k_p} \approx k_{exc} + k_p \tag{12}$$

At millimolar or larger buffer concentrations (as long as $k_p \ll k_{fl}$ is fulfilled), k_p is composed of the rate constant for reprotonation by buffer molecules, $k_p(HB^+)$, and the rate constant for reprotonation by protons, $k_p(H^+)$. The experimental $k_{0,exp} = 39 \pm 14$ MHz should comply with the sum of k_{exc} and $k_p(H^+)$ as only the buffer concentration is varied. Using an excitation rate constant of $k_{exc} \approx 30$ MHz for $I_{exc} = 200$ kW/cm^2, the experimentally determined rate constant for protonation by ubiquitous protons is on the order of 10 MHz, in approximate agreement with an almost diffusion-limited rate constant for direct protonation by H^+ at pH 3.[34,35]

The remaining parameter K can be interpreted in the following way. At this reprotonation rate constant, where $k_{AB} = k_0 + k_s/2$, antibunching changes from chemical to electronic saturation. Below, reprotonation is rate-limiting, and eq 12 can be applied when $k_p < k_{fl}$ (i.e., $k_{AB} \approx k_{exc} + k_p$). Under these experimental conditions, k_{AB} can be interpreted by chemical kinetics and allows for assessing decay constants of intermediates. At higher buffer concentration, the former three-level system converges toward the well-known two-level system with $k_{AB} \approx k_{exc} + k_{fl}$ (eq 11).

To bring the experimental antibunching time constants at varying buffer concentrations in agreement with the bimolecular reprotonation rate constant of buffer molecules, $k_p([HB^+])$ is adjusted manually. A matching of $k_{AB}([B])$ (Figure 3B) with $k_{AB}(k_p)$ (Figure 4B) indeed can be achieved with a bimolecular rate constant for the ground-state reprotonation around 2×10^9 M^{-1} s^{-1}. This value is close to the value for phosphate-buffer-mediated fluorescein protonation, as determined by fluorescence correlation spectroscopy (FCS)[35] (2.8×10^8 M^{-1} s^{-1} in phosphate buffer), and comparable to the bimolecular rate constant determined by FCS at pH 4 and excitation of RO^- (3.5×10^8 M^{-1} s^{-1}, Supporting Information (SI V)). It should be mentioned that, however, the latter obtained

DOI: 10.1021/acs.jpclett.5b00280
J. Phys. Chem. Lett. 2015, 6, 1149−1154

bimolecular rate constant only serves as a lower limit for the antibunching experiment. Because citric acid has three close-lying pK_a values (3.13, 4.76, 6.4),[38] the most abundant species at pH 3, that is, mostly triply protonated citrate, likely exhibits considerably higher protonation rate constants than doubly protonated citrate, the predominant form at pH 4 where FCS was performed. The same is true for comparison with phosphate-assisted reprotonation. Even more, the higher bimolecular rate constant in the antibunching experiment could hint, to some extent, to a preoriented photoacid buffer encounter pair.[39,40] Such a loose complex in the ESPT reaction might lead to higher reprotonation rates in the ground state than provided by the limit of diffusion-controlled reaction dynamics.

In summary, reprotonation rate constants were obtained by analyzing photon antibunching, that is, interphoton arrival times, when $k_p \ll k_{fl}$ (eq 12) holds true. The key step was the manipulation of the lifetime of an intermediate in a cyclic reaction scheme. It should be emphasized that the decay kinetics of an intermediate can be determined from the antibunching modulation, which otherwise requires technically more demanding excitation schemes like pump−dump−probe spectroscopy.[41] Our kinetic analysis, however, sets an upper limit to this method, which works well only if electronic saturation is avoided. In the future, we will use the antibunching modulation to investigate the influence of different electrostatic environments on the proton back-transfer. Also, modulation of antibunching by electrical fields that stabilize charge separation is anticipated. Finally, we imagine that electron-transfer processes can modulate antibunching as well.[42]

■ ASSOCIATED CONTENT

Supporting Information

Derivation of $g_{AB}^{(2)}(\tau)$ with respective numerical calculations; FCS data; material and methods, especially normalization procedure to obtain $g_{AB}^{(2)}(\tau)$; and the influence of intersystem crossing on $g^{(2)}(\tau)$. This material is available free of charge via the Internet at http://pubs.acs.org.

■ AUTHOR INFORMATION

Corresponding Author

*E-mail: g.jung@mx.uni-saarland.de.

Notes

The authors declare no competing financial interest.

■ ACKNOWLEDGMENTS

We thank Christoph Becher and Roland Albrecht (Quantum Optics Group, Saarland University) for technical support and Björn Finkler (Biophysical Chemistry, Saarland University) for providing the photoacid. Initial experiments long ago were assisted by A. Schiller (Inorganic and Analytical Chemistry, Friedrich-Schiller University, Jena).

■ REFERENCES

(1) Rybina, A.; Lang, C.; Wirtz, M.; Grußmayer, K.; Kurz, A.; Maier, F.; Schmitt, A.; Trapp, O.; Jung, G.; Herten, D.-P. Distinguishing Alternative Reaction Pathways by Single-Molecule Fluorescence Spectroscopy. *Angew. Chem., Int. Ed.* **2013**, *52*, 1−5.

(2) Wirtz, M.; Grueter, A.; Rebmann, P.; Dier, T.; Volmer, D. A.; Huch, V.; Jung, G. Two-Color Emissive Probes for Click Reactions. *Chem. Commun.* **2014**, *50*, 12694−12697.

(3) Blum, S. A. Location Change Method for Imaging Chemical Reactivity and Catalysis with Single-Molecule and -Particle Fluorescence Microscopy. *Phys. Chem. Chem. Phys.* **2014**, *16*, 16333−16339.

(4) Christ, T.; Kulzer, F.; Bordat, P.; Basché, T. Watching the Photo-Oxidation of a Single Aromatic Hydrocarbon Molecule. *Angew. Chem., Int. Ed.* **2001**, *40*, 4192−4195.

(5) Kiel, A.; Kovacs, J.; Mokhir, A.; Krämer, R.; Herten, D.-P. Direct Monitoring of Formation and Dissociation of Individual Metal Complexes by Single-Molecule Fluorescence Spectroscopy. *Angew. Chem., Int. Ed.* **2007**, *46*, 3363−3366.

(6) Herzog, T. T.; Ryseck, G.; Ploetz, E.; Cordes, T. The Photochemical Ring Opening Reaction of Chromene as Seen by Transient Absorption and Fluorescence Spectroscopy. *Photochem. Photobiol. Sci.* **2013**, *12*, 1202−1209.

(7) Rudolf, P.; Buback, J.; Aulbach, J.; Nuernberger, P.; Brixner, T. Ultrafast Multisequential Photochemistry of 5-Diazo Meldrum's Acid. *J. Am. Chem. Soc.* **2010**, *132*, 15213−15222.

(8) Lounis, B.; Orrit, M. Single-Photon Sources. *Rep. Prog. Phys.* **2005**, *68*, 1129−1179.

(9) Kimble, H. J.; Dagenais, M.; Mandel, L. Photon Antibunching in Resonance Fluorescence. *Phys. Rev. Lett.* **1977**, *39*, 691−695.

(10) Hübner, C. G.; Zumofen, G.; Renn, A.; Herrmann, A.; Müllen, K.; Basché, T. Photon Antibunching and Collective Effects in the Fluorescence of Single Bichromophoric Molecules. *Phys. Rev. Lett.* **2003**, *91*, 093903.

(11) Moerner, W. E. Single-Photon Sources Based on Single Molecules in Solids. *New J. Phys.* **2004**, *6*, 1−21.

(12) Ambrose, W. P.; Basché, T.; Moerner, W. E. Detection and Spectroscopy of Single Pentacene Molecules in a P-Terphenyl Crystal by Means of Fluorescence Excitation. *J. Chem. Phys.* **1991**, *95*, 7150−7163.

(13) Basché, T.; Moerner, W. E.; Orrit, M.; Talon, H. Photon Antibunching in the Fluorescence of a Single Dye Molecule Trapped in a Solid. *Phys. Rev. Lett.* **1992**, *69*, 1516−1519.

(14) Brunel, C.; Lounis, B.; Tamarat, P.; Orrit, M. Triggered Source of Single Photons Based on Controlled Single Molecule Fluorescence. *Phys. Rev. Lett.* **1999**, *83*, 2722−2725.

(15) Alléaume, R.; Treussart, F.; Courty, J.-M.; Roch, J.-F. Photon Statistics Characterization of a Single-Photon Source. *New J. Phys.* **2004**, *6*, 1−24.

(16) Galland, C.; Brovelli, S.; Bae, W. K.; Padilha, L.; Meinardi, F.; Klimov, V. Dynamic Hole Blockade Yields Two-Color Quantum and Classical Light from Dot-in-Bulk Nanocrystals. *Nano Lett.* **2013**, *13*, 321−328.

(17) Eisaman, M. D.; Fan, J.; Migdall, A.; Polyakov, S. V. Invited Review Article: Single-Photon Sources and Detectors. *Rev. Sci. Instrum.* **2011**, *82*, 071101.

(18) Rezus, Y. L. A.; Walt, S. G.; Lettow, R.; Renn, A.; Zumofen, G.; Götzinger, S.; Sandoghdar, V. Single-Photon Spectroscopy of a Single Molecule. *Phys. Rev. Lett.* **2012**, *108*, 093601.

(19) Bradac, C.; Gaebel, T.; Naidoo, N.; Sellars, M. J.; Twamley, J.; Brown, L. J.; Barnard, A. S.; Plakhotnik, T.; Zvyagin, A. V.; Rabeau, J. R. Observation and Control of Blinking Nitrogen-Vacancy Centres in Discrete Nanodiamonds. *Nat. Nanotechnol.* **2010**, *5*, 345−349.

(20) Ambrose, P. W.; Goodwin, P. M.; Enderlein, J.; Semin, D. J.; Martin, J. C.; Keller, R. A. Fluorescence Photon Antibunching from Single Molecules on a Surface. *Chem. Phys. Lett.* **1997**, *269*, 365−370.

(21) Weston, K. D.; Dyck, M.; Tinnefeld, P.; Müller, C.; Herten, D.-P.; Sauer, M. Measuring the Number of Independent Emitters in Single-Molecule Fluorescence Images and Trajectories Using Co-incident Photons. *Anal. Chem.* **2002**, *74*, 5342−5349.

(22) Ta, H.; Wolfrum, J.; Herten, D.-P. An Extended Scheme for Counting Fluorescent Molecules by Photon-Antibunching. *Laser Phys.* **2009**, *20*, 119−124.

(23) Ta, H.; Kiel, A.; Wahl, M.; Herten, D.-P. Experimental Approach to Extend the Range for Counting Fluorescent Molecules Based on Photon-Antibunching. *Phys. Chem. Chem. Phys.* **2010**, *12*, 10295−10300.

(24) Sýkora, J.; Kaiser, K.; Gregor, I.; Bönigk, W.; Schmalzing, G.; Enderlein, J. Exploring Fluorescence Antibunching in Solution to

DOI: 10.1021/acs.jpclett.5b00280
J. Phys. Chem. Lett. 2015, 6, 1149−1154

Determine the Stoichiometry of Molecular Complexes. *Anal. Chem.* **2007**, *79*, 4040−4049.
(25) Mets, Ü.; Widengren, J.; Rigler, R. Application of the Antibunching in Dye Fluorescence: Measuring the Excitation Rates in Solution. *Chem. Phys.* **1997**, *218*, 191−198.
(26) Becher, C.; Kiraz, A.; Michler, P.; Imamoglu, A.; Schoenfeld, W. V.; Petroff, P. M.; Zhang, L.; Hu, E. Nonclassical Radiation from a Single Self-Assembled InAs Quantum Dot. *Phys. Rev. B* **2001**, *63*, 121312.
(27) Nettels, D.; Schuler, B. Subpopulation-Resolved Photon Statistics of Single-Molecule Energy Transfer Dynamics. *IEEE J. Sel. Top. Quantum Electron.* **2007**, *13*, 990−995.
(28) Brucale, M.; Schuler, B.; Samori, B. Single-Molecule Studies of Intrinsically Disordered Proteins. *Chem. Rev.* **2014**, *114*, 3281−3317.
(29) Schwartz, O.; Levitt, J. M.; Tenne, R.; Itzhakov, S.; Deutsch, Z.; Oron, D. Superresolution Microscopy with Quantum Emitters. *Nano Lett.* **2013**, *13*, 5832−5836.
(30) Cui, J.-M.; Sun, F.-W.; Chen, X.-D.; Gong, Z.-J.; Guo, G.-C. Quantum Statistical Imaging of Particles without Restriction of the Diffraction Limit. *Phys. Rev. Lett.* **2013**, *110*, 153901.
(31) Gatto Monticone, D.; Katamadze, K.; Traina, P.; Moreva, E.; Forneris, J.; Ruo-Berchera, I.; Olivero, P.; Degiovanni, I. P.; Brida, G.; Genovese, M. Beating the Abbe Diffraction Limit in Confocal Microscopy via Nonclassical Photon Statistics. *Phys. Rev. Lett.* **2014**, *113*, 143602.
(32) Finkler, B.; Spies, C.; Vester, M.; Walte, F.; Omlor, K.; Riemann, I.; Zimmer, M.; Stracke, F.; Gerhards, M.; Jung, G. Highly Photostable "Super"-Photoacids for Ultrasensitive Fluorescence Spectroscopy. *Photochem. Photobiol. Sci.* **2014**, *13*, 548−562.
(33) Weller, A. Protolytische Reaktionen Angeregter Oxyverbindungen. *Z. Phys. Chem.* **1958**, *17*, 224−245.
(34) Spies, C.; Shomer, S.; Finkler, B.; Pines, D.; Pines, E.; Jung, G.; Huppert, D. Solvent Dependence of Excited-State Proton Transfer from Pyranine-Derived Photoacids. *Phys. Chem. Chem. Phys.* **2014**, *16*, 9104−9114.
(35) Widengren, J.; Terry, B.; Rigler, R. Protonation Kinetics of GFP and FITC Investigated by FCS - Aspects of the Use of Fluorescent Indicators for Measuring pH. *Chem. Phys.* **1999**, *249*, 259−271.
(36) Fleury, L.; Segura, J. M.; Zumofen, G.; Hecht, B.; Wild, U. P. Nonclassical Photon Statistics in Single-Molecule Fluorescence at Room Temperature. *Phys. Rev. Lett.* **2000**, *84*, 1148−1151.
(37) Neu, E.; Steinmetz, D.; Riedrich-Möller, J.; Gsell, S.; Fischer, M.; Schreck, M.; Becher, C. Single Photon Emission from Silicon-Vacancy Colour Centres in Chemical Vapour Deposition Nano-Diamonds on Iridium. *New J. Phys.* **2011**, *13*, 025012.
(38) Bates, R.; Pinching, G. Resolution of the Dissociation Constants of Citric Acid at 0 to 50°, and Determination of Certain Related Thermodynamic Functions. *J. Am. Chem. Soc.* **1949**, *71*, 1274−1283.
(39) Mohammed, O. F.; Pines, D.; Dreyer, J.; Pines, E.; Nibbering, E. T. J. Sequential Proton Transfer through Water Bridges in Acid-Base Reactions. *Science* **2005**, *310*, 83−86.
(40) Mohammed, O. F.; Pines, D.; Nibbering, E. T. J.; Pines, E. Base-Induced Solvent Switches in Acid-Base Reactions. *Angew. Chem., Int. Ed.* **2007**, *46*, 1458−1461.
(41) Kennis, J. T. M.; Larsen, D. S.; van Stokkum, I. H. M.; Vengris, M.; van Thor, J. J.; van Grondelle, R. Uncovering the Hidden Ground State of Green Fluorescent Protein. *Proc. Natl. Acad. Sci. U. S. A.* **2004**, *101*, 17988−17993.
(42) Ma, X.; Mews, A.; Kipp, T. Determination of Electronic Energy Levels in Type-II CdTe-Core/CdSe-Shell and CdSe-Core/CdTe-Shell Nanocrystals by Cyclic Voltammetry and Optical Spectroscopy. *J. Phys. Chem. C* **2013**, *117*, 16698−16708.

DOI: 10.1021/acs.jpclett.5b00280
J. Phys. Chem. Lett. 2015, 6, 1149−1154

Supporting Information (SI) to

Photon Antibunching in a Cyclic Chemical Reaction Scheme

Michael Vester [a], *Tobias Staut* [a], *Jörg Enderlein* [b] *and Gregor Jung* [a]*

[a] Biophysikalische Chemie, Universität des Saarlandes, 66123 Saarbrücken, Germany.

[b] III. Physikalisches Institut für Biophysik und Komplexe Systeme, Georg-August-Universität, Friedrich-Hund-Platz 1, 37077 Göttingen, Germany.

* Prof. Dr. Gregor Jung, Universität des Saarlandes, Campus B2 2, 66123 Saarbrücken, Germany, g.jung@mx.uni-saarland.de

(S I) **Evolution of [RO^{-*}](t) – numerical calculations**

Influence of reverse chemical processes on kinetics.

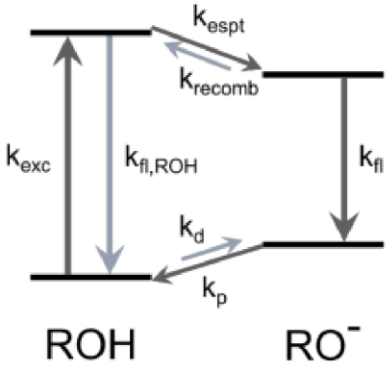

Fig. I(a): Förster cycle: 4-level-scheme, containing seven rate constants.

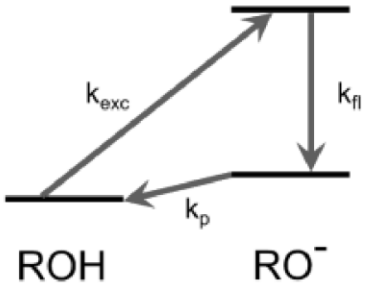

Fig. I(b): Reduced Förster-cycle.

To judge the influence of the reverse chemical processes, i.e. excited-state recombination k_{recomb} and ground-state deprotonation k_d, as well as the fluorescence decay of the photoacid with the decay rate $k_{fl,ROH}$, on the kinetics, the four-level-scheme in Fig. I(a) was solved numerically using 4th order Runge-Kutta procedure.

$$\frac{d}{dt}\begin{pmatrix}[ROH]\\ [ROH^*]\\ [RO^{-*}]\\ [RO^-]\end{pmatrix}=\begin{pmatrix}-(k_{exc}+k_d) & k_{fl,ROH} & 0 & k_p\\ k_{exc} & -(k_{espt}+k_{fl,ROH}) & k_{recomb} & 0\\ 0 & k_{espt} & -(k_{fl}+k_{recomb}) & 0\\ k_d & 0 & k_{fl} & -k_p\end{pmatrix}\cdot\begin{pmatrix}[ROH]\\ [ROH^*]\\ [RO^{-*}]\\ [RO^-]\end{pmatrix} \qquad \text{(S1)}$$

$$\frac{d}{dt}\begin{pmatrix}[ROH]\\ [ROH^*]\\ [RO^{-*}]\\ [RO^-]\end{pmatrix}_{t=0}=\begin{pmatrix}0\\0\\0\\1\end{pmatrix} \qquad \text{(S2)}$$

The result for the excited-state population of the anion was compared to $g_{AB}^{(2)}(\tau)$, i.e. the normalized population of the excited anion state, which was obtained analytically by adopting a three-level scheme without the excited acidic form (eq. (3), (4) in the manuscript). We used as input in the calculations the experimentally available data (see manuscript: $k_{exc} \approx 30$ MHz, $k_{fl} = 160$ MHz, $k_{espt} = 250$ GHz, $k_{recomb} \approx 400$ MHz, $k_{fl,ROH} = 210$ MHz) and varied k_p between 30 MHz and 300 MHz covering all experimentally accessible rate constants for reprotonation. k_d

was altered with respect to k_p (see Fig. II). In all three cases, data points of the numerical simulations are indistinguishable from the simplified analytical solutions as long as the forward reaction rate constant is larger than the rate constant for the reversed process by at least a factor of 3. We conclude that the population of the excited acidic state ROH* and the processes depicted as light gray arrows in Fig. I(a) can be neglected when describing the generation of consecutive photons.

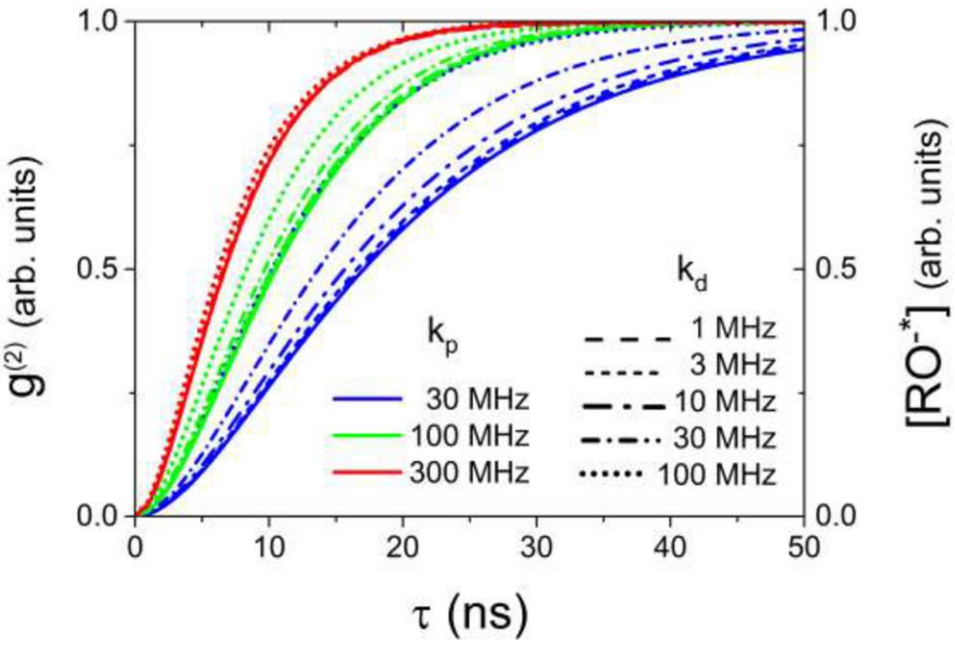

Fig. II: Comparison between four-state kinetics (Fig. I(a)) and three-state kinetics (Fig. I(b)). The solid curves represent the analytically obtained $g_{AB}^{(2)}(\tau)$ from the three-level scheme. The different dotted lines show the time-dependent, normalized population of RO^{-*} for the four-level case. Also the influence of different ground-state deprotonation rates on the evolution of the basic excited state is shown. k_{exc}, k_{fl}, k_{espt}, k_{recomb}, $k_{fl,ROH}$ were set to 30 MHz, 160 MHz, 250 GHz, 400 MHz and 210 MHz. For three different reprotonation rates k_p the deprotonation rate k_d was varied.

(S II) **Three-state kinetics and $g^{(2)}$**

The four level-scheme is reduced to a three level one, which consists of the excitation of ROH to RO^{-*}, the fluorescence decay of RO^{-*} and the protonation of RO^- to reform ROH with the rate constants k_{exc}, k_{fl} and k_p (Fig. I(b)).

$$\frac{d}{dt}\begin{pmatrix}[ROH]\\ [RO^{-*}]\\ [RO^-]\end{pmatrix}=\begin{pmatrix}-k_{exc} & 0 & k_p\\ k_{exc} & -k_{fl} & 0\\ 0 & k_{fl} & -k_p\end{pmatrix}\cdot\begin{pmatrix}[ROH]\\ [RO^{-*}]\\ [RO^-]\end{pmatrix},\quad \begin{pmatrix}[ROH]\\ [RO^{-*}]\\ [RO^-]\end{pmatrix}_{t=0}=\begin{pmatrix}0\\0\\1\end{pmatrix} \tag{S3}$$

The resulting eigenvalues:

$$0,\quad s_{1,2}=-\tfrac{1}{2}\sigma\pm\tfrac{1}{2}\sqrt{\sigma^2-4\rho} \tag{S4}$$

$$\sigma=k_{exc}+k_{fl}+k_p,\ \rho=k_{exc}k_{fl}+k_{exc}k_p+k_{fl}k_p \tag{S5}$$

The time-dependent population of RO^{-*} is obtained as:

$$[RO^{-*}](t)=\frac{k_{exc}k_p}{s_1s_2}+\frac{k_{exc}k_p}{s_1(s_1-s_2)}\exp(s_1t)+\frac{k_{exc}k_p}{s_2(s_2-s_1)}\exp(s_2t) \tag{S6}$$

$[RO^{-*}](t)$ is normalized to $[RO^{-*}]_{t\to\infty}$ to receive the autocorrelation, $g_{AB}^{(2)}(\tau)$.

$$g^{(2)}(\tau)=\frac{[RO^{-*}](t)}{[RO^{-*}(\infty)]}=1+\frac{s_2}{s_1-s_2}\exp(s_1t)+\frac{s_1}{s_2-s_1}\exp(s_2t) \tag{S7}$$

Eq. (S7) is rearranged for obtaining eq. (S8). This shows, that the $g_{AB}^{(2)}(\tau)$ is real-valued for every combination of k_p, k_{exc} and k_{fl}.

$$g^{(2)}(\tau)=1-\frac{\sigma}{2\sqrt{\sigma^2-4\rho}}\{\exp(s_1t)-\exp(s_2t)\}-\frac{1}{2}\{\exp(s_1t)+\exp(s_2t)\} \tag{S8}$$

(S III) **Monoexponential vs. Biexponential decay of $g^{(2)}$**

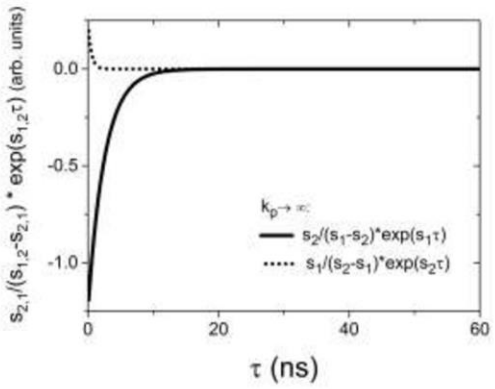

Fig. III(a): The two monoexponential contributions to $g_{AB}^{(2)}(\tau)$ (eq. (S7)) in the limiting case of $k_p \to \infty$. Exp($s_2\tau$) decays much faster than exp($s_1\tau$). Moreover, the amplitude of exp($s_2\tau$) is much smaller.

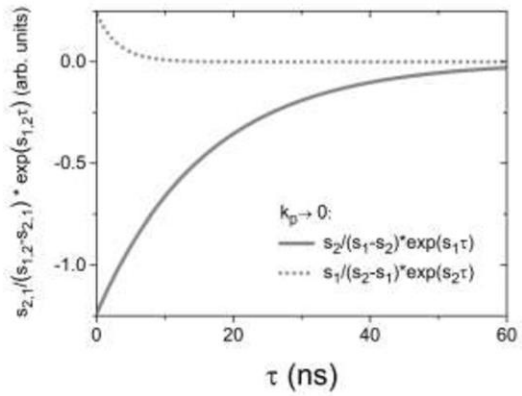

Fig. III(b): The two monoexponential contributions to $g_{AB}^{(2)}(\tau)$ (eq. (S7)) in the limiting case of $k_p \to 0$. The exp($s_2\tau$) decays also much faster than exp($s_1\tau$) in this limit.

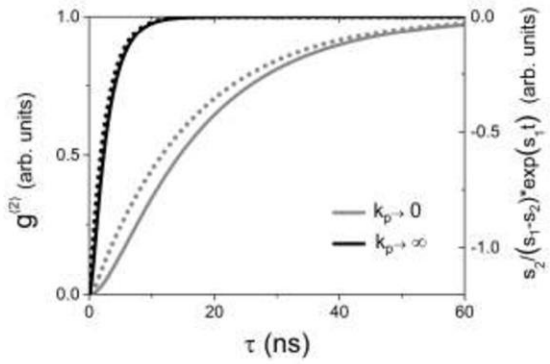

Fig. III(c): Resulting $g_{AB}^{(2)}(\tau)$ (eq. (7)) for the two limiting cases of k_p. Additionally, the respective exp($s_1\tau$) are shown as dotted lines.

Fig. III(a) and III(b) contain the two exponentials, which build up the $g_{AB}^{(2)}(\tau)$, for the two limiting cases of $k_p << k_{fl}, k_{exc}$ and $k_p >> k_{fl}, k_{exc}$, respectively. For a given k_p, the exp($s_1\tau$) increases much slower than exp($s_2\tau$). Fig. III(c) shows, that the $g_{AB}^{(2)}(\tau)$ is mainly determined by

the slower rate constant s_1 in the nanosecond time range in the two limiting cases. Thus, $g_{AB}^{(2)}(\tau)$ is well described by monoexponentials in these cases, which is in particular true as the depth of the dip at $\tau = 0$ is hardly discernible in the experimental measurement due to background contributions.

(S IV) **Approximation of k_{AB}**

As was stated above, only the slower exponential has to be taken into account when modeling the antibunching. Accordingly, the smaller rate constant can be simplified, when regarding the limiting case of $k_p << k_{fl}, k_{exc}$.

$$\sqrt{\sigma^2 - 4\rho} = \sqrt{\left(k_{exc} - k_{fl} + k_p\right)^2 - 4k_{exc}k_p} \tag{S9}$$

$$= \left(k_{exc} - k_{fl} + k_p\right)\sqrt{1 - \frac{4k_{exc}k_p}{\left(k_{exc} - k_{fl} + k_p\right)^2}} \tag{S10}$$

$$\approx \left(k_{exc} - k_{fl} + k_p\right)\sqrt{1 - \frac{4k_{exc}k_p}{\left(k_{exc} - k_{fl} + k_p\right)^2} + \frac{\left(2k_{exc}k_p\right)^2}{\left(k_{exc} - k_{fl} + k_p\right)^4}} \tag{S11}$$

$$= \left(k_{exc} - k_{fl} + k_p\right)\sqrt{\left(1 - \frac{2k_{exc}k_p}{\left(k_{exc} - k_{fl} + k_p\right)^2}\right)^2} \tag{S12}$$

$$= \left(k_{exc} - k_{fl} + k_p\right)\left(1 - \frac{2k_{exc}k_p}{\left(k_{exc} - k_{fl} + k_p\right)^2}\right) \tag{S13}$$

$$= k_{exc} - k_{fl} + k_p - \frac{2k_{exc}k_p}{k_{exc} - k_{fl} + k_p} \tag{S14}$$

In case of $k_p < k_{exc} < k_{fl}$ eq. (S15) is valid.

$$\left(\frac{2k_{exc}k_p}{\left(k_{exc} - k_{fl} + k_p\right)^2}\right)^2 \ll \frac{4k_{exc}k_p}{\left(k_{exc} - k_{fl} + k_p\right)^2} \tag{S15}$$

$$k_{AB} = \frac{1}{2}\left(\sigma + \sqrt{\sigma^2 - 4\rho}\right) = k_{exc} + k_p - \frac{k_{exc}k_p}{k_{exc} - k_{fl} + k_p} \tag{S16}$$

For the other limiting case of $k_p >> k_{fl}, k_{exc}$:

$$\sqrt{\sigma^2 - 4\rho} = \sqrt{\left(k_{exc} + k_{fl} - k_p\right)^2 - 4k_{exc}k_{fl}} \tag{S17}$$

$$= \left(k_{exc} + k_{fl} - k_p\right)\sqrt{1 - \frac{4k_{exc}k_{fl}}{\left(k_{exc} + k_{fl} - k_p\right)^2}} \tag{S18}$$

$$\approx \left(k_{exc} + k_{fl} - k_p\right)\sqrt{1 - \frac{4k_{exc}k_{fl}}{\left(k_{exc} + k_{fl} - k_p\right)^2} + \frac{\left(2k_{exc}k_{fl}\right)^2}{\left(k_{exc} + k_{fl} - k_p\right)^4}} \tag{S19}$$

$$= \left(k_{exc} + k_{fl} - k_p\right)\sqrt{\left(1 - \frac{2k_{exc}k_{fl}}{\left(k_{exc} + k_{fl} - k_p\right)^2}\right)^2} \quad \text{(S20)}$$

$$= \left(k_{exc} + k_{fl} - k_p\right)\left(1 - \frac{2k_{exc}k_{fl}}{\left(k_{exc} + k_{fl} - k_p\right)^2}\right) \quad \text{(S21)}$$

$$= k_{exc} + k_{fl} - k_p - \frac{2k_{exc}k_{fl}}{k_{exc} + k_{fl} - k_p} \quad \text{(S22)}$$

In case of $k_p >> k_{exc}, k_{fl}$, eq. (S23) is valid.

$$\left(\frac{2k_{exc}k_{fl}}{\left(k_{exc} + k_{fl} - k_p\right)^2}\right)^2 \ll \frac{4k_{exc}k_{fl}}{\left(k_{exc} + k_{fl} - k_p\right)^2} \quad \text{(S23)}$$

$$k_{AB} = \frac{1}{2}\left(\sigma + \sqrt{\sigma^2 - 4\rho}\right) = k_{exc} + k_{fl} - \frac{k_{exc}k_{fl}}{k_{exc} + k_{fl} - k_p} \quad \text{(S24)}$$

(S V) **FCS data**

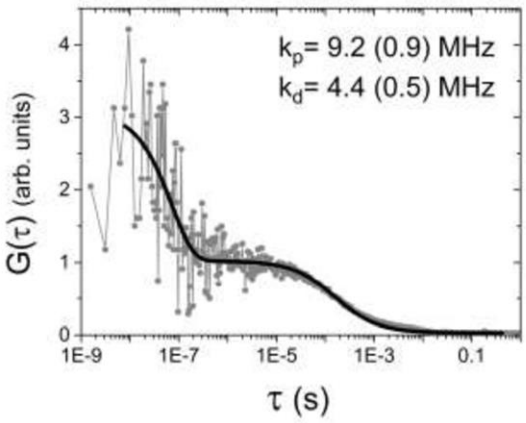

Fig. IV(a): Example curve of FCS data at pH 4.0 and 10 mM citrate buffer.

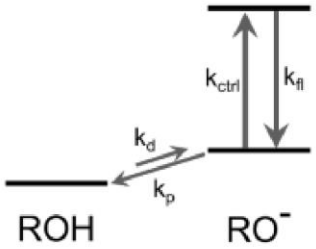

Fig. IV(b): Excitation scheme for the FCS measurement.

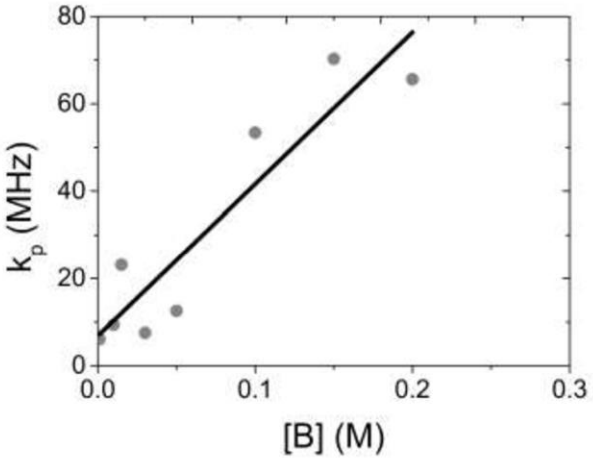

Fig. IV(c): Determination of the bimolecular rate constant of the ground state protonation at pH 4 by FCS. A linear fit yields $k_{p,bi}(HB^+)$= 3.5 ± 0.6 ×10^8 $M^{-1}s^{-1}$ and $k_0(H^+)$= 7.0 ± 5.0 MHz.

(S VI) **Material and Methods**

A diluted solution of the photoacid [24,33] (~ 1 nM) at pH 11.0 was created with a buffer solution of Sigma Aldrich (20 mM, HPCE grade). For the measurement at pH 3, buffer solutions were made from citric acid and Trisodiumcitrate-dihydrate.

Confocal Set-Up

A diluted solution (~ 1 nM) of the photoacid was excited with cw radiation at 445 nm (Coherent OBIS 445-LX) or with cw radiation at 488 nm (Soliton Picarro) in a confocal microscope. The set-up is based on a Zeiss AxioVert 200 with an immersion objective (water, Zeiss ApoChromat, 63x, 1.2 N.A.). Collected fluorescence was focused through a pinhole of 50 µm diameter.

Measurement time

The measurement time was in the range of approximately three to four hours depending on the buffer concentration of the sample.

Measurement of the second order correlation function

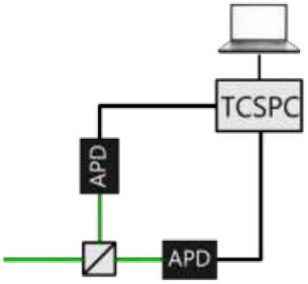

Fig. V(a): The fluorescence is split, detected, and correlated.

n_1	n_2
x	
	x
x	
x	
	x
x	x
x	
	x
x	x
	x

Fig. V(b): Detection events are written into two lists and are correlated afterwards.

Collected fluorescence light passes a 50-50 beam splitter and is focused onto two avalanche photon detectors (APD, Perkin Elmer SPCM-AQR-14), which are connected to a time-correlated single photon counting module (Picoquant Picoharp 300).

The measurement is performed in the T2 mode, which yields binary files containing the arrival times of all detected photons. To further process the binary files, the workgroup of Christoph becher kindly supplied us with a C-routine [30]. Only a short description will be given here, for a more detailed description please consult reference R1. In a pre-analysis step, for each detector a binary file (L1 and L2) is generated containing the respective photon arrival times. The main program computes the histogram $g^{(2)}(\tau)$, where τ is the time between two photon events on different detectors. Therefore, bins of width τ_{bin} have to be defined.[1] This implies a bin number of $n_{max} = T/\tau_{bin}$, where T is the total displayed $g^{(2)}(\tau)$ histogram time width. Then, the lag times $\tau_{i,j}$, given by $\tau_{i,j} = t_{L2,i} - t_{L1,j}$ are calculated one by one, where $t_{L1,j}$ ($t_{L2,i}$) are the photon arrival times in L1 (L2). The lag times are evaluated for each event in L1, but the respective events in L2 are limited to those at times $t_{L2,i}$ for which

$$t_{L1,j} - \frac{T}{2} \leq t_{L2,i} \leq t_{L1,j} + \frac{T}{2}$$

holds. In order to be able to plot $g^{(2)}(\tau)$, the $\tau_{i,j}$ have to be sorted into the respective bins with the central time t_c given by

$$t_c = -\frac{T}{2} + \frac{2n+1}{2}\tau_{bin}$$

where $n \in [0, 1, \ldots, n_{max}\text{-}1]$.

Programmatically the sorting is done by incrementing the number of occurrences in the bin for which

[1] τ_{bin} was set to 1 ns for our experiments.

$$t_c - \frac{\tau_{bin}}{2} \leq \tau_{i,j} < t_c + \frac{\tau_{bin}}{2}$$

holds by 1 for each $\tau_{i,j}$. This yields an ASCII formatted list containing lag times and their number of occurrences. This $g^{(2)}$ histogram is not yet normalized.

(S VII) **Normalization procedure to obtain $g_{AB}^{(2)}(\tau)$**

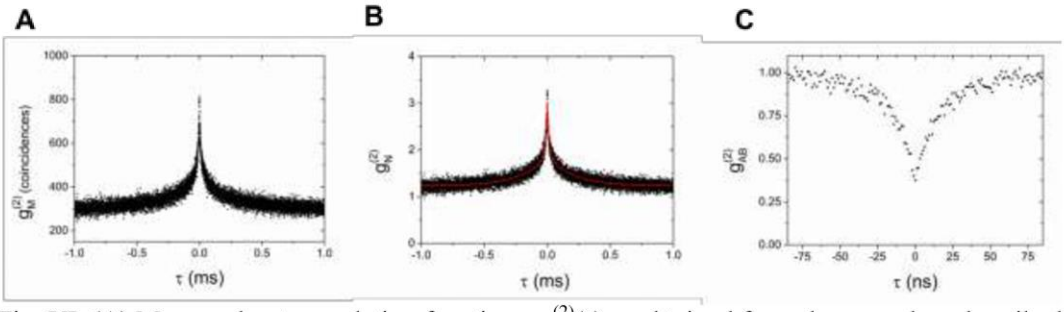

Fig. VI: (A) Measured autocorrelation function $g_M^{(2)}(\tau)$ as obtained from the procedure described in S VI. (B) Normalized correlation function $g_N^{(2)}(\tau)$. (C) Properly normalized autocorrelation function $g_{AB}^{(2)}(\tau)$.

The $g_M^{(2)}(\tau)$ histogram, which is obtained by the procedure described above, is normalized by a factor $t \cdot \tau_{bin} \cdot r_1 \cdot r_2$ according to eq. (S25) to give $g_N^{(2)}(\tau)$, where t is the total measurement time, τ_{bin} the chosen width of the time bins and r_1 and r_2 the count rates on APD_1 and APD_2.[R2] Each process that induces fluctuations in the fluorescence light contributes to the autocorrelation function. Assuming freely diffusing molecules, which also undergo intersystem crossing (for experimental proof see S VIII), the autocorrelation function consists of three respective contributions, $g_{diff}^{(2)}$ for the diffusion part and $g_T^{(2)}$ for the triplet contribution. $g_{AB}^{(2)}$ accounts for antibunching. Assuming a separation of time scales ($\tau_{diff} \approx$ 100-200 µs, $\tau_T \approx 1$ µs and $\tau_{AB} \approx$ 1-10 ns), $g^{(2)}$ can be written as (S25).[R3]

$$g_M^{(2)} = g_{diff}^{(2)} \cdot g_T^{(2)} \cdot g_{AB}^{(2)} \cdot t \cdot \tau_{bin} \cdot r_1 \cdot r_2 = g_N^{(2)} \cdot t \cdot \tau_{bin} \cdot r_1 \cdot r_2 \qquad \text{(S25)}$$

The $g_N^{(2)}$ decays biexponentially as can be seen in Fig. VI (B). These two exponentials correspond to $g_T^{(2)}$ and $g_{diff}^{(2)}$; the respective decay times are around 1-3 µs and 150 µs. We are aware of the fact that the assumption of an exponential decay of $g_{diff}^{(2)}$ causes an error, especially at longer correlation times. Therefore, $g_{AB}^{(2)}$ does not approach $g_{AB}^{(2)} = 1$ for longer lag times when dividing $g_N^{(2)}$ by $g_T^{(2)} \cdot g_{diff}^{(2)}$. Nevertheless, $g_{AB}^{(2)}$ is normalized such that $g_{AB}^{(2)}(\pm\infty) = 1$ is fulfilled.

(S VIII) **Influence of intersystem crossing on the second order correlation function**

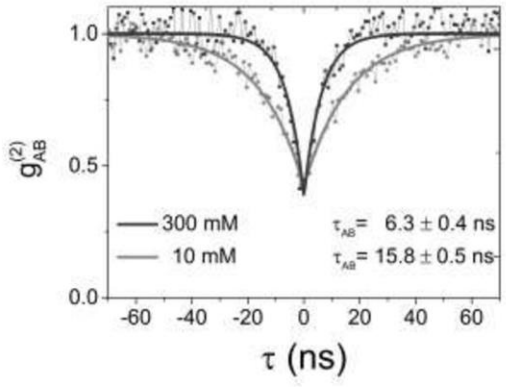

Fig. VII(a): Experimental autocorrelation of the photoacid at pH 3 in the nanosecond time-range. Solid lines represent monoexponential fits.

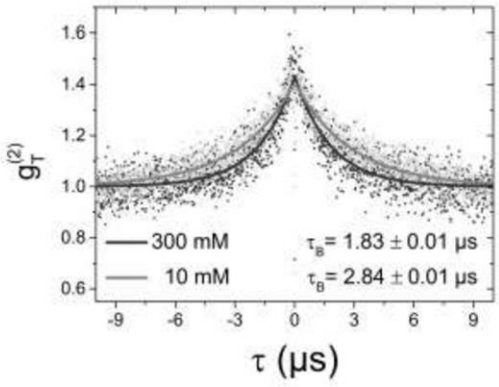

Fig. VII(b): Same measurements, but in the microsecond time-range. Solid lines represent monoexponential fits.

At this point the bunching behavior of $g^{(2)}$ should be mentioned. Bunching can be satisfactorily explained by intersystem-crossing (ISC). Due to the low quantum yield for ISC and the different time scales for ISC, this process did not play any role in the antibunching experiment. Both the intersystem crossing (ISC) rate k_{ISC} and the rate k_T, with which the triplet state is depopulated, are independently determined by fluorescence correlation spectroscopy (FCS). Intensity dependent FCS measurements yield an ISC rate constant of 1.4 (0.1) MHz and a common rate constant for triplet decay of about 0.7 (0.3) MHz, which is close to the expected value due to triplet quenching [R4]. Thus, at $I_{exc} = 200$ kW/cm^2, a bunching contrast of $C = k_{ISC}(200\ \text{kW/cm}^2)\ k_T^{-1} = 0.36$ is expected. The mean value of the experimental values for C is 0.37 (Tab. SI). Furthermore, the bunching decay rate increases with increasing buffer concentration. We attribute this finding to a higher amount of photocycles per time window at higher buffer concentrations providing additional evidence for electronic saturation according to eq. (11).

Tab. SI: Overview of the experimental antibunching k_{AB} and the bunching rate constants k_B and the contrast $C = k_{ISC}/k_T$ of the $g_T^{(2)}$-function.

[B] / mM	k_{AB} / MHz	k_B / kHz	C / 1
300	159 ± 14	519	0.31
200	160 ± 29	549	0.43
150	134 ± 19	468	0.38
100	137 ± 15	500	0.46
30	94 ± 5	392	0.22
10	63 ± 1	315	0.41

References:

(R1) dissertation of D. Steinmetz, Saarland University, 2011.

(R2) Fox, M., Quantum Optics, OMS in AOLP, 2012.

(R3) Nettels, D., Gopich, I.V., Hoffmann, A., Schuler, B., PNAS, 2007, 104, 2655.

(R4) Hübner, C.G., Renn, A., Renge, I., Wild, U.P., J. Chem. Phys., 2001, 115, 9619

5.3 M. Vester, A. Grüter, B. Finkler, R. Becker and G. Jung, *PCCP*, 2016, Accepted Manuscript

„Biexponential Photon Antibunching: Recombination Kinetics within the Förster-Cycle in DMSO“

PCCP

Accepted Manuscript

Biexponential Photon Antibunching: Recombination Kinetics within the Förster-Cycle in DMSO

Michael Vester[a], Andreas Grüter[a], Björn Finkler[a], Robert Becker[a], Gregor Jung[a]

[a]Biophysical Chemistry, Saarland University, 66123 Saarbrücken, Germany

Abstract

Time-resolved experiments with pulsed-laser excitation are the standard approach to map the dynamic evolution of excited states, but ground-state kinetics remain hidden or require pump-probe schemes. Here, we exploit the so-called photon antibunching, a purely quantum-optical effect related to single molecule detection to assess the rate constants for a chemical reaction in the electronic ground state. The measurement of the second-order correlation function $g^{(2)}$, i.e. the evaluation of inter-photon arrival times is applied to the reprotonation in a Förster-cycle. We find that the antibunching of three different photoacids in the aprotic solvent DMSO significantly differs from the behavior in water. The longer decay constant of the biexponential antibunching t_l is linked to the bimolecular reprotonation kinetics of the fully separated ion-pair, independent of the acidic additives. The value of the corresponding bimolecular rate constant, $k_p = 4 \times 10^9\ M^{-1}s^{-1}$ indicates diffusion-controlled reprotonation. The analysis of t_l also allows for the extraction of the separation yield of proton and the conjugated base after excitation and amounts to approximately 15 %. The shorter time component t_s is connected to the decay of the solvent-separated ion pair. The associated time constant for geminate reprotonation is approximately 3 ± 1 ns in agreement with independent tcspc experiments. These experiments verify that the transfer of quantum-optical experiments to problems in chemistry enables mechanistic conclusions which are hardly accessible by other methods.

Introduction

View Article Online
DOI: 10.1039/C6CP00718J

Proton transfer plays an important role in biochemistry and physiology, like in enzymatic catalysis[1], ATP synthesis[2], triggering of calcium-channels[3,4], or protein environments[5,6] and it is one of the most fundamental reaction types in chemistry. To study proton transfer reactions and enlighten their underlying mechanisms, so-called photoacids were implemented as molecular triggers for proton transfer in the past few decades.[7–13] More than 60 years ago Förster was the first to explain an increase in the acidity of a pyrenol based molecule, namely HPTS (8-hydroxypyrene-1,3,6-trisulfonic acid, pyranine), upon excitation. The acidity constant, pK_a, falls by six orders of magnitude and a corresponding red shift of its fluorescence in water is observed.[14] The so-called Förster cycle, in which the conjugated base is formed after excited-state proton transfer (ESPT) and reprotonation occurs in the electronic ground state to generate the photoacid again, was derived from steady-state fluorescence spectroscopy.[15]

The implementation of more sophisticated, time-resolved experiments allowed for a sharper view onto processes following photoexcitation down to the femtosecond regime. Pyranine and cyanonaphthols as well as quinoline-derivativs were investigated by fs-pump-probe[16–22], fluorescence upconversion[23–26], IR-pump-probe[27–29] and time-correlated single photon counting[30] instrumentation. These experiments were carried out in protic-polar solvents like water, water-alcohol mixtures[31], short-chain alcohols[32] and also in dmso[33]. In this way, additional species, which show up before the freely diffusing conjugated base is generated in its excited state, have been proven, and both their formation and decay kinetics were determined with fs-resolution.[21,26,28,34–40] It turned out, that, after excitation and intramolecular charge transfer, the proton is released to form a strongly hydrogen-bonded ion pair (HBIP) within up to 10 picoseconds in the case of HPTS,[19,20] in which the protonated acceptor molecule resides nearby the anionic species without any additional solvent molecule in between (Fig. 1 a)). Within tens of picoseconds, the so-called solvent-separated ion pair (SSIP) is created, in which

View Article Online
DOI: 10.1039/C6CP00718J

the photobase and the protonated solvent molecule are separated by at least one up to some few solvent molecules.[19,20] In the SSIP, the proton diffuses inside the centrosymmetric, attractive potential of the negatively charged corresponding base[41]. Due to the electrostatic interaction, proton and base can reform ROH* with a certain recombination probability. In water, this geminate recombination takes place within approximately 3 ps.[20] If proton and anionic base do not recombine, diffusion takes place until both ions are fully separated (fully-separated ion pair, FSIP).[19,20] Now, both proton and anion move independently from each other.

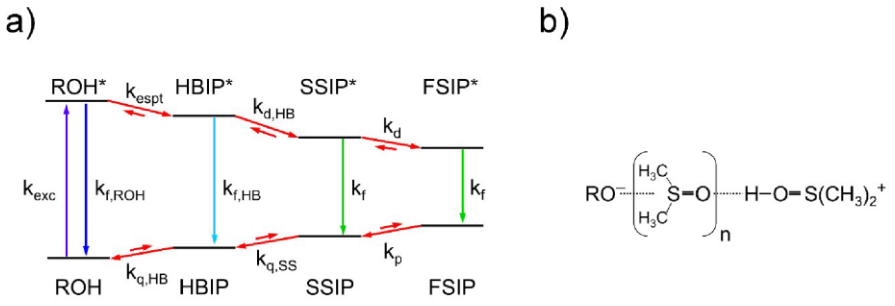

Figure 1: a) Eigen-Weller scheme. b) RO^- ---H-dmso$^+$ ion-pair. The number of dmso molecules is n = 0 for the HBIP, and for the FSIP n >> 1. In the SSIP the proton is separated by few solvent molecules from the anion, but still moves within the Coulomb potential of RO^-.

Taken together, kinetics in the excited states is understood well so far. The reprotonation in the ground state should proceed in an analogue manner. Base and proton diffuse together in close proximity to form the SSIP. Subsequently, the approach continues until the HBIP is created and, finally, proton and anion recombine. The processes described above are usually depicted in the so-called Eigen-Weller scheme (Fig. 1 a)).

Common to all ultrafast techniques implemented to study proton transfer is the initial preparation of the molecules in their excited state; afterwards the excited state potential surface is mapped. The ground state kinetics of HBIP and SSIP is not easily accessible in that way. Their associated decay rate constants, which may not necessarily be the same as in the excited states, are not accessible.

View Article Online
DOI: 10.1039/C6CP00718J

Here, we bridge this gap by analyzing the so-called photon antibunching, a purely quantum-optical effect with no classical analogue. Under cw-illumination, individual quantum emitters, such as single atoms, semiconductor nanocrystals, nanodiamonds and molecules, provide a stream of photons well separated in time. The emission is antibunched then, because exactly one photon is generated per photocycle.[42–46] Photon antibunching is experimentally captured by measuring the second-order correlation function $g^{(2)}$. This latter function $g^{(2)}$ is a measure for the time needed to detect a second photon after the initial detection of a first photon[47], i.e. the time it takes to undergo a full photocycle. A common time-correlated single photon counting instrumentation is needed to run the $g^{(2)}$-measurement, in which the timing device is started with the detection of a first photon, i.e. in the moment, in which the molecule is prepared in its ground state. As a consequence, $g^{(2)}$ usually depends on the kinetics of each step in the photocycle, i.e. the excitation step and the fluorescence in the case of a two-level system. The associated rate constants can be determined by analyzing the antibunching decay.[44,48,49] We see the great benefit in analyzing the $g^{(2)}$ function in the fact that the complete kinetic information of the whole photocycle is stored therein. It should be mentioned, that additional information is embedded in the relative amplitudes of $g^{(2)}$. The stoichiometry of biochemical complexes or aggregates[50] can be yielded in that way.

Recently, we were able to extract the chemical rate constants in a cyclic chemical reaction scheme, namely the reprotonation rate constant in the ground state within the Förster-cycle in water.[51] In the following we transfer these experiments to the proton transfer in dmso. Three different, recently described photoacids[30,52,53] are investigated together with different acidic additives. Evidence is provided that exclusively the system H^+/dmso is probed with our approach. We find that the antibunching behavior apparently differs from the previously studied antibunching in water. As in the aprotic solvent dmso the proton mobility is slowed down

View Article Online
DOI: 10.1039/C6CP00718J

compared to protic solvent, measuring $g^{(2)}$ allows for separating both the SSIP and the FSIP decay kinetics. A simplified expression approximates the kinetics within the framework of Fig. 1 a). Hence, the separation yield of proton and anionic base is experimentally accessible.

Experimental

View Article Online
DOI: 10.1039/C6CP00718J

We use the photoacids Tris(1,1,1,3,3,3-hexafluoropropan-2-yl) 8-hydroxypyrene-1,3,6-trisulfonate (**1**), Tris-(2,2,2-trifluoroethyl)-8-hydroxypyrene-1,3,6-trisulfonate (**2**), and 8-Hydroxy-N,N′,N″-trimethoxy-N,N′,N″-trimethylpyrene-1,3,6- trisulfonamide (**3**), which were synthesized in our lab.[52] Their structures and their most relevant properties are found in table 1. Whereas the ground state acidities in water are close within one order of magnitude, excited state acidities span more than 2.5 orders of magnitude.

Table 1: Photophysical and photochemical properties of the photoacids used in this study.[52]

property		(1)	(2)	(3)
structure		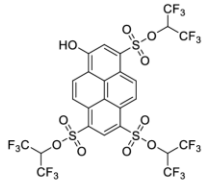	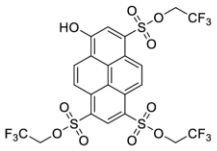	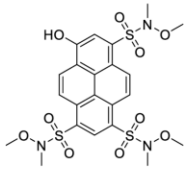
λ_{abs}/nm	ROH	449	440	438
	RO^-	576	568	568
λ_{em}/nm	ROH	c	c	506
	RO^-	580	574	576
τ_f / ns	ROH	0.2	0.4	1.4
	RO^-	5.6	5.6	5.7
pK_a		[a]4.4	[a]4.7	[b]5.6
pK_a*		-3.9	-2.7	-1.2

λ_{abs} : absorption wavelength in dmso, λ_{em} emission wavelength in dmso, τ_f fluorescence lifetime in dmso, [a] pK_a values in water by FCS, [b] pK_a values in water by absorption titration, pK_a* values in water by Förster-calculation. [c] cannot be determined due to high ESPT rate constant.

Each of (**1**) - (**3**) is dissolved in dmso (purchased from Acros chemicals, dimethyl sulfoxide, 99.7+%, Extra Dry over Molecular Sieve, AcroSeal®). Dmso is vacuum-distilled before use to

further reduce background. Although the water content continuously increased during measurement and was on average 10 % or below, the decay constants of antibunching do not change significantly during the four hours of measurement time (see SI 1). For the actual correlation measurements, the solutions are further diluted down to roughly 1 nM. For the kinetic analysis of the Förster-cycle, trifluoroacetic acid (tfa; Lancaster chemicals, 99 %), d-tfa (Sigma-Aldrich, 99.5 atom % D) or methanesulfonic acid (msa, Sigma-Aldrich, ≥ 99 %) is added to the solutions to shift the ground-state equilibrium towards the acidic form of the photoacid (Fig. 2 (a)). Concentrations of these additives up to 300 mM are used. Excitation is achieved with cw radiation at λ_{exc} = 445 nm (Coherent, OBIS 445-LX) (in the case of the Förster-cycle experiment), with cw radiation at λ_{exc} = 546 nm (Guided Color Technologies, fiber laser FL546) in the control experiment without addition of tfa. Fluorescence is collected in a home-built confocal microscope (Zeiss, AxioVert 200) with an immersion objective (Zeiss, α-Plan-Fluar 100x/1.45 oil), focused through a pinhole of 50 µm diameter and passed an emission filter (AHF, 570/60 ET Bandpass), a 50-50 beam splitter and, finally, focused onto two avalanche photon detectors (Perkin Elmer, SPCM-AQR-14). These two APDs are connected to the input channel (Ch 1) and the sync channel (Ch 0) of a time-correlated single photon counting module (Picoquant, Picoharp 300). The antibunching measurements are run in the so-called T2 mode, in which a binary file is created containing all arrival times of all detected photons. The obtained data is correlated by a commercial software (Picoquant, SymPhoTime 64) thus providing the second-order correlation function $g^{(2)}$.

In this procedure, the overall second-order correlation function is obtained, which consists of every process that leads to fluorescence fluctuations, that is diffusion, photobleaching, singlet-triplet transitions and antibunching.[54,55] If these processes occur on timescales, which are well separated, the respective attributions can be split.[56–59] The process of interest, in this case the antibunching decay, can then be treated independently. In the actual experiment diffusion takes

View Article Online
DOI: 10.1039/C6CP00718J

place in some 100 µs, photobleaching even occurs on a much longer time scale, if at all. Bunching kinetics are found in the range of 3 -7 µs at low tfa concentrations (0 to roughly 3 mM) and 0.2 – 0.1 µs at high tfa concentrations (> 30 mM, see SI 2). The longest antibunching decay times are about 150 ns (around 1 mM) and shorter at higher tfa concentrations, i.e. 5 to 10 ns (> 300 mM), thus differ from triplet dynamics by at least one order of magnitude. Therefore, we independently analyze antibunching with strong support from theory.[56–59] During the analysis of $g_{AB}^{(2)}$, i.e. the antibunching decay of $g^{(2)}$ which is obtained by the separation of time scales, is normalized such that $g_{AB}^{(2)}(\pm\infty) = 1$ is fulfilled.[51]

Results

Spectra of compound (**2**) are depicted in Fig. 2. Without addition of tfa, the three compounds are almost fully deprotonated in the ground-state. Addition of tfa leads to the population of the respective ROH state. As we run the antibunching experiments at [tfa] > 1 mM up to 300 mM, all the three compounds are fully neutralized. After excitation of ROH, fluorescence almost exclusively (≈ 95 %) arises from the RO^-* state in case of (**1**) and (**2**) (Fig. 2 b)). However, (**3**) still shows some noteworthy emission of the ROH* state[52] (SI 3). The preponderance of RO^-* emission is explained by a very fast ESPT (pK_a* ≈ -4 – -1). In summary, chemical conditions can be established so that the Förster-cycle takes place very efficiently.

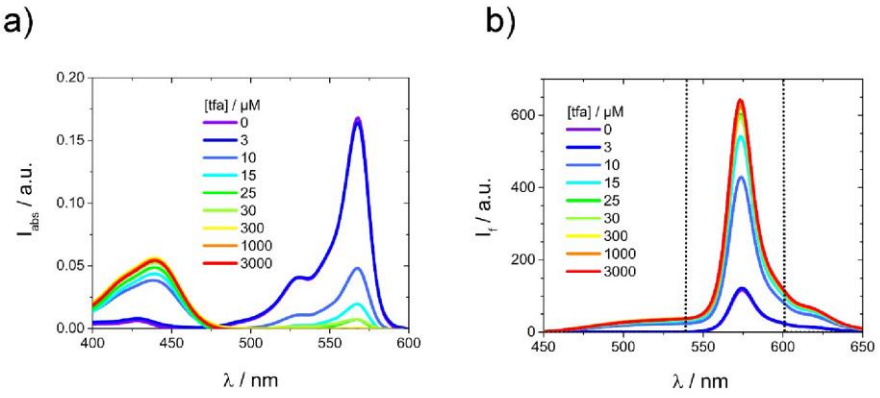

Figure 2: Absorption a) and emission (excitation at 410 nm) b) spectra of (**2**) in dmso at different tfa concentrations. The transmission profile of the emission filter (570/60 ET Bandpass) is illustrated in black dotted lines.

Antibunching experiments are carried out at various tfa concentrations (Fig. 3). At tfa concentrations in the order of 1 mM, $g^{(2)}$ decays biexponentially with a short-time (t_s) and a long-time (t_l) component (Fig. 3 a)). The former time-constant is about 10 ns, t_l is roughly 160 ns in this example. Astonishingly, we retrieve values for t_l at low proton concentrations, which are longer than the average time needed for excitation, $t_{exc} = 1/k_{exc} \approx 30$ ns. At tfa concentrations higher than 10 mM, the biexponential decay collapses to a monoexponential

curve (Fig. 3 b)). If the tfa concentration is further increased, $g^{(2)}$ approaches the antibunching decay, which is obtained when the molecule only cycles between the RO^{-}* and the RO^{-} state under excitation at 546 nm (red curve, Fig. 3 b)). Here, the antibunching decay time (5.1 ± 0.2 ns) is smaller than the fluorescence lifetime of the RO^{-} form (5.6 ns from tcspc) as expected from theory.[49]

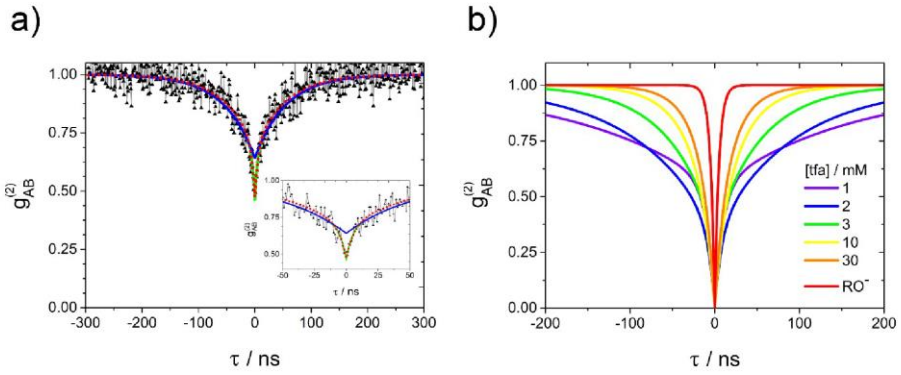

Figure 3: (a) Experimental $g^{(2)}$ function of (**1**) at 3 mM tfa. red: biexponential decay, blue: long-time component, green: short-time component. (b) Normalized $g^{(2)}$ of (**1**) at different tfa concentrations. These are normalized fit functions of the experimental data for better visualization (for experimental correlation functions see SI 4). Antibunching measurement of the pure RO^{-} emission under RO^{-} excitation yields the red curve.

Fig. 4 provides a comparison of the decay constants t_s and t_l of the three photoacids in dmso at various tfa concentrations. The other photoacids (**2**) and (**3**) show an analogue behavior with respect to t_l and t_s. Neither t_l nor t_s systematically depend on their respective pK_a or pK_a*. The short time-component, $t_s = 8.5 \pm 0.8$ ns, turns out to be constant with respect to the proton concentration (Fig. 4 a)). The apparent tendency of (**3**) to slightly lower values of t_s likely arises from some contribution of the ROH emission as can be noticed in the emission spectrum (SI 3). For increasing tfa concentrations, the long-time components, t_l, levels off for all three compounds (Fig. 4 b)). The saturation behavior is better seen when the corresponding rate constant, k_l, is plotted against [tfa] (Fig. 4 c)). We obtain values for k_l for all three compounds, which are smaller than $k_{exc} = 30$ MHz. However, a linear proportionality to [tfa] is only found

View Article Online
DOI: 10.1039/C6CP00718J

below 10 mM (Fig. 4 d)). Again, no significant impact of the proton donor (methanesulfonic or d-tfa instead of tfa, SI 5, SI 6) on the long-time decay is noticed. Because of these findings, the observed reprotonation behavior is supposed to be universal, i.e. to be solely dependent on the solvent properties.

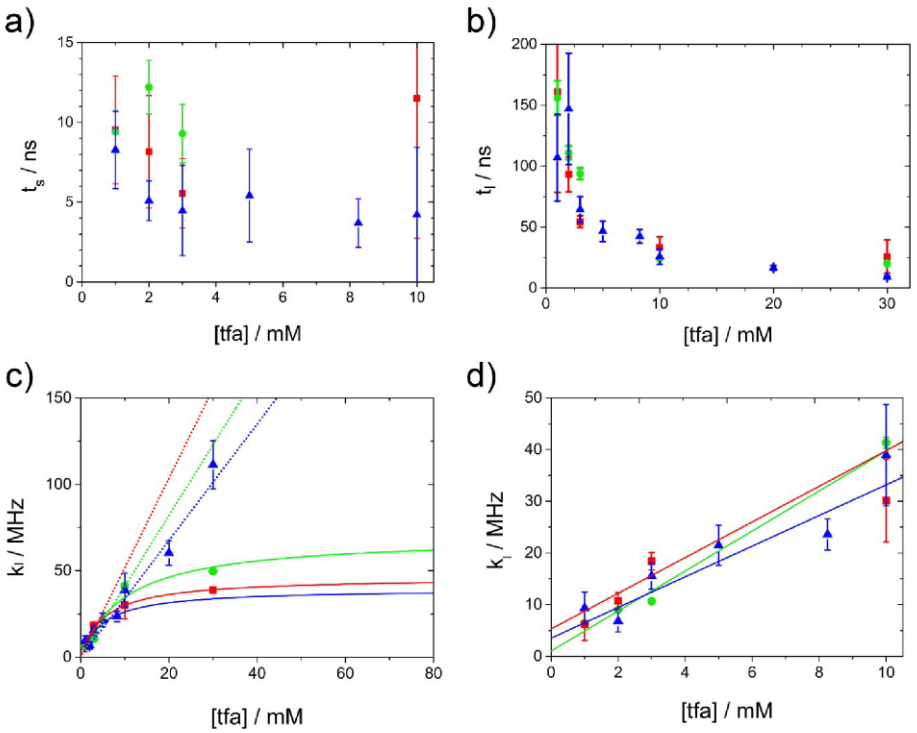

Figure 4: a) t_s against tfa concentration. The compound (**1**) is depicted in red, (**2**) in green and (**3**) in blue. The apparent tendency for (**3**) to slightly lower values of t_s likely arises from some contribution of the ROH emission (SI 3). b) Dependence of t_l on the tfa concentration. c) Rate constant k_l against tfa concentration. d) Linear relationship between k_l and [tfa] in the mM range.

Discussion

View Article Online
DOI: 10.1039/C6CP00718J

Different kinetic models were assessed for describing the experimental behavior of $g^{(2)}$. It turned out that the experimental, biexponential behavior with decay times $t_l > 1/k_{exc}$ only can be reproduced if two emissive species with different recombination kinetics contribute to the detected fluorescence. Within the Eigen-Weller scheme, at least three of the four specimen provide fluorescence in distinguishable spectral ranges. The ROH* emission is hardly, or only to some amount for (**3**), detected in the experiment (Fig. 2 b)). The HBIP* emission is expected to lie in between the emission of ROH* and FSIP*, blue-shifted to that of RO^-*.[60,61] Except from these experimental studies, our previous solvatochromic studies[53] with various hydrogen-bonding donor solvents also allow for estimating the emission wavelength range of the HBIP: We conclude from the higher acidity of protonated dmso compared to hexafluoroisopropanol that $\lambda_{em}(\text{HBIP}) << \lambda_{em}(RO^-$ in HfiPrOH$) \approx 550$ nm. Furthermore, the lifetime of the intermediate HBIP is presumably short[60]. Thus, the rate constant k_{espt} describes the formation of the SSIP*.[30,52] Summed up, the populations of the ROH* and the HBIP* state are close to zero for all times under experimental conditions[51] and the Eigen-Weller scheme is reduced to a more suitable five-level scheme (Fig. 5 a)).

View Article Online
DOI: 10.1039/C6CP00718J

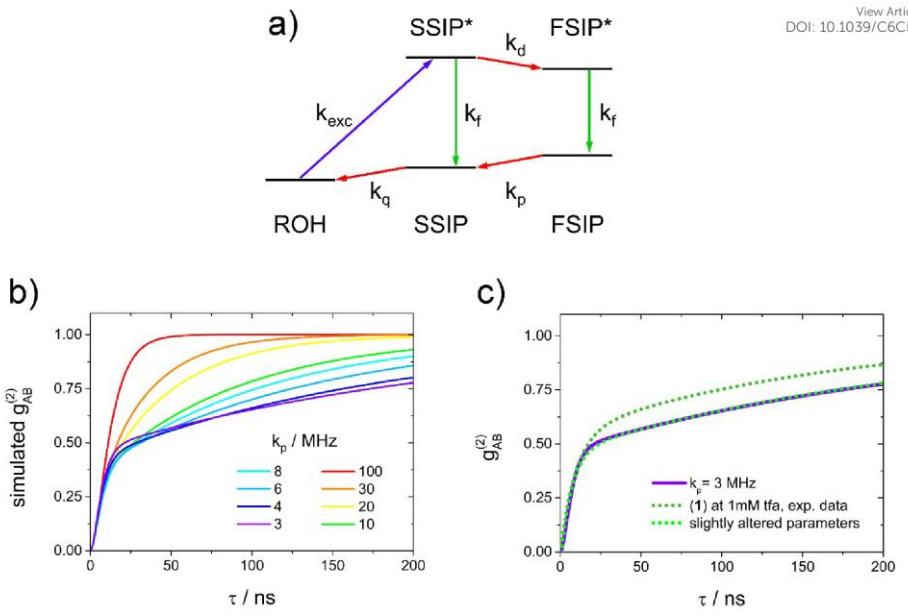

Figure 5: a) Simplified 5-level-scheme.
b) Simulation of the numerical solutions of the 5-level scheme at different reprotonation rate constants k_p. k_{exc} was set to 30 MHz, k_f to 180 MHz, k_q to 330 MHz and k_d to 10 MHz, which corresponds to tfa concentrations about 3 mM.
c) Comparison of numerical calculation and experimental data (**1** at [tfa] = 1 mM). Choosing of slighty altered fit parameters, which still lie within the error margins of the measurement, leads to a curve that fits the simulation well.

The system of coupled, differential equations, which corresponds to the five-level scheme, is solved numerically (SI 7) on the basis of independently accessible experimental data as far as possible. In this process, k_{exc} is set to 30 MHz, k_f to 180 MHz, k_d to 10 MHz, k_q to 330 MHz and k_p is varied. k_{exc} was derived from the extinction coefficient[52], and k_f from lifetime measurements[52]. k_d was, first, approximated based on former experiments[51] and later-on verified by further simulations (see SI 8). $1/k_q$ tentatively matches 3 ns, which we extract from the experimental t_s = 8.5 ns. Since the molecules are either prepared in the SSIP state or in the FSIP state after the detection of the first photon at $\tau = 0$, the initial populations of the remaining states are set to zero. Due to the relative amplitudes, which we observe experimentally (table 4

View Article Online
DOI: 10.1039/C6CP00718J

in SI), [SSIP](0) = 0.33 and [FSIP](0) = 0.67 are chosen as starting conditions for the simulations. Assuming the same brightness and similar fluorescence decay rate constant of the SSIP* and the FSIP* (see SI 9), $g^{(2)}$ can be derived from the sum of the respective excited state populations[62]. $g^{(2)}$, which are obtained in this manner, show a biexponential decay for low reprotonation rate constants k_p, which becomes monoexponential for higher k_p. Thus, simulated $g^{(2)}$ comply with the experimental behavior (Fig. 5 c)). An even better agreement between simulation and experiment is achieved when k_l, k_s and A_l, A_s are slightly altered, within the error margin of the experiment.

We simplify the five-level scheme in order to obtain approximate analytical expressions for $g^{(2)}$ (SI 10). Suchlike approximation is intended to explain the fact that we find $t_l > t_{exc} = 1/k_{exc}$ and to extract chemical information from the antibunching experiment, which is otherwise only obtained from comparison of simulated with experimental data. Due to the distinct separation of k_f and k_d, we are able to describe the five-level scheme as a combination of a cyclic three-level sub system and a two-state super scheme (Fig. 6).

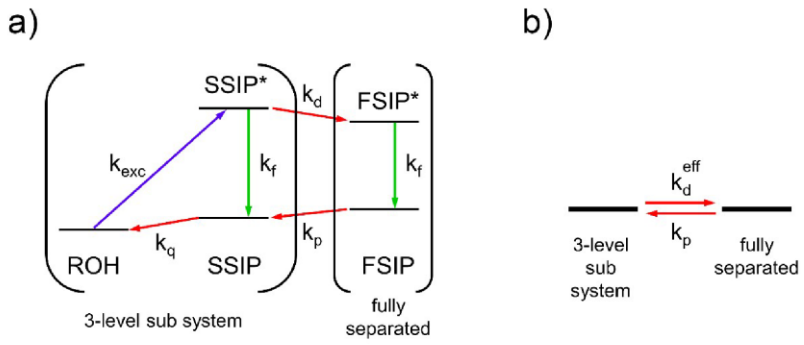

Figure 6: a) Approximate description of the five-level scheme for low [tfa]. An analytical expression of $g^{(2)}$ is derived from combining the 3-level sub system with the 2-state super system (b).

Previously, three-level systems containing the S_0, S_1 and a triplet state T_1 were simplified in an analogue manner,[63–65] for which a separation of time scales of the singlet-singlet and the singlet-

View Article Online
DOI: 10.1039/C6CP00718J

triplet transitions was provided. In our case, the three-level sub system consists of the states ROH, SSIP* and SSIP, which was already solved analytically[51] (Fig. 6 a)). In the two-state super system, these three states are unified in one system and the second state corresponds to the arrangement, in which proton and anion are fully separated (Fig. 6 b)). k_p describes diffusive reprotonation and corresponds to the reprotonation rate constant in the five-level description of the Eigen-Weller scheme. k_d^{eff} is the effective rate constant for the FSIP* formation and is k_d multiplied by the likelihood of SSIP* excitation (E1).

$$k_d^{eff} = k_d \frac{k_{exc}}{k_{exc} + k_f} \quad \text{(E1)}$$

The time scale of FSIP creation and FSIP decay and the time needed to cycle the three-level scheme differ enough to assume a separation of time scales. This assumption is valid at least at low proton concentrations in the lower mM range ($t_s \approx 10$ ns vs. $t_l \approx 150$ ns) (see SI 2).

As the molecule is either prepared in the SSIP state or in the FSIP state after the detection of the first photon, the following boundary conditions are chosen. If the three-level scheme is initially cycled, the molecule is prepared in the SSIP state, i.e. [SSIP](t = 0) = 1 is selected. If the ion-pair is fully separated at t = 0, [FSIP](t = 0) = 1 is picked for the two-level sub system (Fig. 6 b)). The analytical expressions for [SSIP*] and [FSIP] are given in table 2. $g^{(2)}$ is then derived from the linear combination of these two populations with variable amplitudes. Please note that no distinction is made between FSIP and FSIP*in the mathematical description of the combined system in Fig. 6 b) and table 2.

View Article Online
DOI: 10.1039/C6CP00718J

Table 2: Analytical expressions for [SSIP*] and [FSIP*]. In a coarse-grained approach, $g^{(2)}$ is derived from the linear combination of these two populations.

	three-level sub-system	two-state super system
	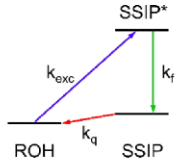	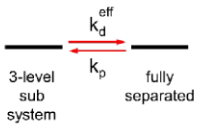
decay constants	$s_{1,2} = {}^1/_2(-\sigma \pm \Delta)$ (E2) $\sigma = k_{exc} + k_f + k_q$ (E3) $\rho = k_{exc}k_f + k_{exc}k_q + k_f k_q$ (E4) $\Delta = \sqrt{\sigma^2 - 4\rho}$ (E5)	$s_3 = -(k_d + k_p)$ (E7)
excited-state populations	$[SSIP^*](t)$ (E6) $= \frac{k_{exc}k_q}{s_1 s_2} + \frac{k_{exc}k_q}{s_1(s_2 - s_1)} exp(s_1 t)$ $+ \frac{k_{exc}k_q}{s_2(s_1 - s_2)} \exp(s_2 t)$	$[FSIP](t)$ (E8) $= \frac{k_d^{eff}}{k_d^{eff} + k_p}$ $- \frac{k_p}{k_d^{eff} + k_p} exp(-(k_d^{eff} + k_p)t)$

The solution for [SSIP*], which describes the fast recombination kinetics, is composed of two exponentials, of which only s_1 is physically meaningful for the time resolution of the experiment.[51] s_1 is simplified for didactic reason (see SI 11) and (E9) is obtained.

$$t_s \equiv -\frac{1}{s_1} \approx \frac{\sigma}{\rho} \approx \frac{1}{k_{exc} + k_f} + \frac{1}{k_q} = t_{classical} + t_q \quad \text{(E9)}$$

The experimental short time component t_s is composed of the sum of the "classical" antibunching decay time $t_{classical} = (k_{exc}+k_f)^{-1}$ and the time needed for reprotonation within the SSIP, $t_q = 1/k_q$. Under excitation with 546 nm at 200 kW/cm^2, which also corresponds to $k_{exc} \approx 30$ MHz, $t_{fl,AB} = (k_{exc}+k_{fl})^{-1} = 5.1 \pm 0.2$ ns is obtained. Taking (E9) and $t_s = 8.5 \pm 0.8$ ns into account, the reprotonation time t_q is obtained as 3 ± 1 ns. t_q in the exited state is also

View Article Online
DOI: 10.1039/C6CP00718J

recorded by TCSPC with excitation of the ROH species and a proton concentration up to 1 M (see SI 12). Independently, the time needed for excited state reprotonation is obtained as 2.5 ± 0.1 ns and nicely verifies the validity of our model.

The decay kinetics of the FSIP on a longer timescale is determined by both k_d^{eff} and k_p. According to (E7), [FSIP](t), thus the experimentally obtainable long-time component of the $g^{(2)}$ decay, is fairly independent from the excitation rate constant k_{exc} at low proton concentrations. Consequently, values for the long-time component of $g^{(2)}$ are indeed obtained that are longer than $t_{exc} = 1/k_{exc}$. Finally, in order to extract the bimolecular rate constant for diffusive reprotonation k_l([tfa]) is analyzed at low [tfa] (Fig. 4 d)).[51,66] A linear fit of the long time component at low proton concentrations, where our model splitting is valid (Fig. 6), yields the bimolecular rate constant for the reprotonation k_p^{bi} as the slope. Its value is about $4 \pm 1 \times 10^9\ M^{-1}s^{-1}$ and thus diffusion-controlled (Fig. 4 d)). Please note that the three-level + two-level approximation may break down in the case of higher proton concentrations ([tfa] > 10 mM) as the separation of time scales is not valid any more. The saturation behavior of k_l is therefore not comprised within the model of Fig. 6. To estimate the probability Φ_{esc} for the proton to leave the Coulombic cage of the anion, k_d is assessed. k_d^{eff} is obtained from the linear fit of k_l([tfa]) as 4 ± 1 MHz as the intercept. (E8) yields k_d as 30 ± 7 MHz.

$$\Phi_{esc} = \frac{k_d}{k_d + k_f} \qquad \text{(E10)}$$

The escape probability (E10) is then about 15 ± 4 %. At the end, some remarks about the amplitudes A_l, A_s are noteworthy. The simulation in Fig. S11 and S12 b) as well as equations (E6) and (E8) provide evidence that the partition among the relative amplitudes is very sensitive to k_{exc} whereas the constants k_l and k_s are not dependent thereon to same amount (Fig. S12 a)). We therefore attribute their distribution in table 4 in the SI, at least in parts, to varying excitation conditions within the Gaussian shape of the focused laser beam. Although we used the relative amplitudes as starting point for the calculations (see eq. S5), the amplitudes for the long and

View Article Online
DOI: 10.1039/C6CP00718J

short time decays are not a measure for the escape probability, as one would assume. Complicated dependencies of amplitudes were previously described for strongly coupled 4-level systems.[67,68] In addition, the limited time resolution and the contribution of ROH emission in the case of (**3**), may aggravate an accurate extraction of A_l and A_s. We therefore renounced an analysis of the amplitudes in the antibunching experiment. Moreover, slight changes of the amplitudes while the time constants are kept within the error limits, lead to a better agreement between experiment and simulation in Fig. 5 c).

View Article Online
DOI: 10.1039/C6CP00718J

Conclusions

We studied the ground-state reprotonation within the Förster-cycle of three photoacids in the aprotic solvent dmso. Antibunching analysis was chosen as experimental method as the associated decay constant contains information about all rate constants within the photocycle. The exponential decay of $g_{AB}^{(2)}$ yielded two different time components. The longer decay constant was linked to the bimolecular reprotonation kinetics of FSIP by acid. The value of the corresponding bimolecular rate constant, $k_p^{bi} = 4 \times 10^9\ M^{-1}s^{-1}$, indicates diffusion-controlled reprotonation and is, thus, comparable to that by buffer molecules in water.[51] Analysis of k_I also allowed to extract k_d, from which an escape probability of the proton of approximately 15 ± 4 % could be deduced. The shorter time component was connected to the decay of the SSIP and was hidden in the $g_{AB}^{(2)}$ in water due to the inherent fast proton-diffusion therein. $t_s \approx 8.5$ ns is roughly the sum of the "classical" decay time, $t_{classical}$ and the time found for geminate reprotonation from SSIP to ROH, t_q. The latter time constant was $t_q = 3 \pm 1$ ns in agreement with independent tcspc experiments.

Acknowledgement

We thank Mina Mohammadi-Kambs (work group for biological experimental physics, Saarland University) for her support in theoretical calculations and Bernd Morgenstern (work group for inorganic chemistry, Saarland University) for carrying out the NMR titration experiment. Financial support was provided by the German Science Foundation (JU650/5-1 and 7-1).

Literature

1 S. Y. Reece and D. G. Nocera, *Annu. Rev. Biochem.*, 2009, **78**, 673–699.

2 P. D. Boyer, *Nature*, 1999, **402**, 247–249.

3 I. Bogeski, R. Kappl, C. Kummerow, R. Gulaboski, M. Hoth and B. A. Niemeyer, *Cell Calcium*, 2011, **50**, 407–423.

4 J. P. Vessey, A. K. Stratis, B. A. Daniels, N. Da Silva, M. G. Jonz, M. R. Lalonde, W. H. Baldridge and S. Barnes, *J. Neurosci.*, 2005, **25**, 4108–4117.

5 E. Freier, S. Wolf and K. Gerwert, *Proc. Natl. Acad. Sci. USA*, 2011, **108**, 11435–11439.

6 H. Ishikita and K. Saito, *J. R. Soc. Interface*, 2014, **11**, 1–17.

7 M. Gutman, E. Nachliel and S. Kiryati, *Biophys. J.*, 1992, **63**, 281–290.

8 L. M. Tolbert and J. E. Haubricht, *J. Am. Chem. Soc.*, 1994, **116**, 10593–10600.

9 K. J. Tielrooij, M. J. Cox and H. J. Bakker, *ChemPhysChem*, 2009, **10**, 245–251.

10 R. L. A. Timmer, M. J. Cox and H. J. Bakker, *J. Phys. Chem. A*, 2010, **114**, 2091–2101.

11 B. K. Paul and N. Guchhait, *J. Lumin.*, 2012, **132**, 2194–2208.

12 L. M. Tolbert and K. M. Solntsev, *Acc. Chem. Res.*, 2002, **35**, 19–27.

13 M. G. Kuzmin, I. V Soboleva, V. L. Ivanov, E.-A. Gould, D. Huppert and K. M. Solntsev, *J. Phys. Chem. B*, 2014, **119**, 2444–2453.

14 T. Förster, *Naturwissenschaften*, 1949, **6**, 186–187.

15 T. Förster, *Z. Elektrochemie*, 1950, **54**, 42–46.

16 R. Simkovitch, S. Shomer, R. Gepshtein and D. Huppert, *J. Phys. Chem. B*, 2014, **119**, 2253–2262.

17 R. Simkovitch, S. Shomer, R. Gepshtein, M. E. Roth, D. Shabat and D. Huppert, *J. Photochem. Photobiol. A Chem.*, 2014, **277**, 90–101.

18 L. Genosar, B. Cohen and D. Huppert, *J. Phys. Chem. A*, 2000, **104**, 6689–6698.

19 R. Gepshtein, P. Leiderman, L. Genosar and D. Huppert, *J. Phys. Chem. A*, 2005, **109**,

9674–9684.

View Article Online
DOI: 10.1039/C6CP00718J

20 P. Leiderman, L. Genosar and D. Huppert, *J. Phys. Chem. A*, 2005, **109**, 5965–5977.

21 D. B. Spry, a. Goun and M. D. Fayer, *J. Phys. Chem. A*, 2007, **111**, 230–237.

22 E. Pines, D. Pines, Y. Ma and G. R. Fleming, *ChemPhysChem*, 2004, **5**, 1315–1327.

23 E.-A. Gould, A. V. Popov, L. M. Tolbert, I. Presiado, Y. Erez, D. Huppert and K. M. Solntsev, *Phys. Chem. Chem. Phys.*, 2012, **14**, 8964–8973.

24 R. Ghosh and D. K. Palit, *Photochem. Photobiol. Sci.*, 2013, **12**, 987–995.

25 R. Simkovitch, R. Gepshtein and D. Huppert, *J. Phys. Chem. A*, 2015, **119**, 1797–1812.

26 M. Veiga-Gutiérrez, A. Brenlla, C. Carreira Blanco, B. Fernández, S. A. Kovalenko, F. Rodríguez-Prieto, M. Mosquera and J. L. P. Lustres, *J. Phys. Chem. B*, 2013, **117**, 14065–14078.

27 M. L. Donten, P. Hamm and J. VandeVondele, *J. Phys. Chem. B*, 2011, **115**, 1075–1083.

28 O. F. Mohammed, D. Pines, J. Dreyer, E. Pines and E. T. J. Nibbering, *Science (80-.).*, 2005, **310**, 83–86.

29 T. H. van der Loop, F. Ruesink, S. Amirjalayer, H. J. Sanders, W. J. Buma and S. Woutersen, *J. Phys. Chem. B*, 2014, **118**, 12965–12971.

30 C. Spies, S. Shomer, B. Finkler, D. Pines, E. Pines, G. Jung and D. Huppert, *Phys. Chem. Chem. Phys.*, 2014, **16**, 9104–9114.

31 D. Huppert and E. Kolodney, *Chem. Phys.*, 1981, **63**, 401–410.

32 A. V. Popov, E.-A. Gould, M. A. Salvitti, R. Hernandez and K. M. Solntsev, *Phys. Chem. Chem. Phys.*, 2011, **13**, 14914–14927.

33 I. V. Gopich, K. M. Solntsev and N. Agmon, *J. Chem. Phys.*, 1999, **110**, 2164–2174.

34 O. F. Mohammed, D. Pines, E. T. J. Nibbering and E. Pines, *Angew. Chem. Int. Ed.*, 2007, **46**, 1458–1461.

35 O. F. Mohammed, J. Dreyer, B.-Z. Magnes, E. Pines and E. T. J. Nibbering,

ChemPhysChem, 2005, **6**, 625–636.

View Article Online
DOI: 10.1039/C6CP00718J

36 M. Rini, B.-Z. Magnes, E. Pines and E. T. J. Nibbering, *Science*, 2003, **301**, 349–352.

37 M. Rini, D. Pines, B.-Z. Magnes, E. Pines and E. T. J. Nibbering, *J. Chem. Phys.*, 2004, **121**, 9593–9610.

38 A. A. Freitas, F. H. Quina and A. A. L. Maçanita, *J. Phys. Chem. A*, 2011, **115**, 10988–10995.

39 N. Agmon, *J. Phys. Chem. A*, 2005, **109**, 13–35.

40 M. Eigen, *Angew. Chem. Int. Ed.*, 1964, **3**, 1–72.

41 E. Pines, D. Huppert and N. Agmon, *J. Chem. Phys.*, 1988, **88**, 5620–5630.

42 B. Lounis and M. Orrit, *Rep. Prog. Phys.*, 2005, **68**, 1129–1179.

43 H. J. Kimble, M. Dagenais and L. Mandel, *Phys. Rev. Lett.*, 1977, **39**, 691–695.

44 T. Basché, W. E. E. Moerner, M. Orrit and H. Talon, *Phys. Rev. Lett.*, 1992, **69**, 1516–1519.

45 C. Brunel, B. Lounis, P. Tamarat and M. Orrit, *Phys. Rev. Lett.*, 1999, **83**, 2722–2725.

46 W. E. Moerner, *New J. Phys.*, 2004, **6**, 1–21.

47 J. Bernard, L. Fleury, H. Talon and M. Orrit, *J. Chem. Phys.*, 1993, **98**, 850–859.

48 P. W. Ambrose, P. M. Goodwin, J. Enderlein, D. J. Semin, J. C. Martin and R. A. Keller, *Chem. Phys. Lett.*, 1997, **269**, 365–370.

49 Ü. Mets, J. Widengren and R. Rigler, *Chem. Phys.*, 1997, **218**, 191–198.

50 J. Sýkora, K. Kaiser, I. Gregor, W. Bönigk, G. Schmalzing and J. Enderlein, *Anal. Chem.*, 2007, **79**, 4040–4049.

51 M. Vester, T. Staut, J. Enderlein and G. Jung, *J. Phys. Chem. Lett.*, 2015, **6**, 1149–1154.

52 B. Finkler, C. Spies, M. Vester, F. Walte, K. Omlor, I. Riemann, M. Zimmer, F. Stracke, M. Gerhards and G. Jung, *Photochem. Photobiol. Sci.*, 2014, **13**, 548–562.

53 C. Spies, B. Finkler, N. Acar and G. Jung, *Phys. Chem. Chem. Phys.*, 2013, **15**, 19893–

19905.

View Article Online
DOI: 10.1039/C6CP00718J

54 M. Gösch and R. Rigler, *Adv. Drug Deliv. Rev.*, 2005, **57**, 169–190.

55 O. Krichevsky and G. Bonnet, *Rep. Prog. Phys.*, 2002, **65**, 251–297.

56 I. V. Gopich and A. Szabo, *J. Chem. Phys.*, 2006, **124**, 154712.

57 D. Nettels, I. V. Gopich, A. Hoffmann and B. Schuler, *Proc. Natl. Acad. Sci. USA*, 2007, **104**, 2655–2660.

58 D. Nettels and B. Schuler, *IEEE J. Sel. Top. Quantum Electron.*, 2007, **13**, 990–995.

59 I. V. Gopich, D. Nettels, B. Schuler and A. Szabo, *J. Chem. Phys.*, 2009, **131**, 095102.

60 R. Simkovitch, K. Akulov, S. Shomer, M. E. Roth, D. Shabat, T. Schwartz and D. Huppert, *J. Phys. Chem. A*, 2014, **118**, 4425–4443.

61 T. Kumpulainen, B. H. Bakker and A. M. Brouwer, *Phys. Chem. Chem. Phys.*, 2015, **17**, 20715–20724.

62 P. Schwille, F. J. Meyer-Almes and R. Rigler, *Biophys. J.*, 1997, **72**, 1878–1886.

63 J. Widengren, R. Rigler and Ü. Mets, *J. Fluoresc.*, 1994, **4**, 255–258.

64 J. Widengren, U. Mets and R. Rigler, *J. Phys. Chem.*, 1995, **99**, 13368–13379.

65 A. Schönle, C. Von Middendorff, C. Ringemann, S. W. Hell and C. Eggeling, *Microsc. Res. Tech.*, 2014, **77**, 528–536.

66 J. Widengren, B. Terry and R. Rigler, *Chem. Phys.*, 1999, **249**, 259–271.

67 A.-M. Boiron, B. Lounis and M. Orrit, *J. Chem. Phys.*, 1996, **105**, 3969–3974.

68 G. Jung, C. Bräuchle and A. Zumbusch, *J. Chem. Phys.*, 2001, **114**, 3149–3156.

Electronic Supplementary Material (ESI) for Physical Chemistry Chemical Physics.

Supporting Information

(1) Sequential correlation of the photon stream

To study the influence of the water content, which did not exceed on average 10 Vol-% and below, on the $g^{(2)}$ decay, the fluorescence signal of (**2**) at 2 mM tfa concentration is analyzed in more detail. The photon stream, which was recorded over 4 hours, is equally split and is correlated for each of the four hours of measurement time. The separate correlations of each hour of measurement time do not yield significant deviations from each other with respect to the decay constants within the error margin of the experiment. We conclude that the behavior of H^+ in dmso is not significantly altered up to a water content of 10 Vol-%.

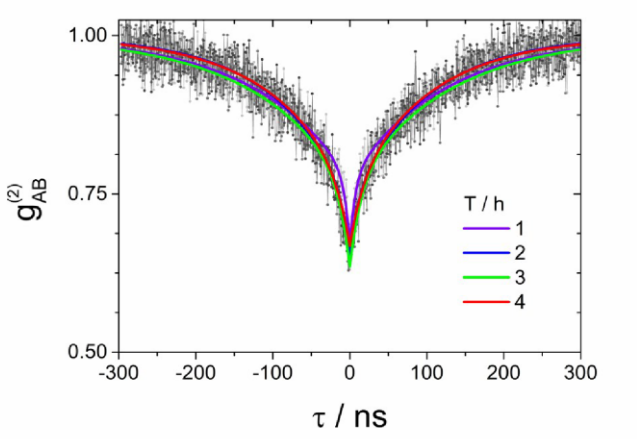

Fig. S1: Experimental correlation function of (**2**) at 2 mM tfa concentration. Each full hour of the photon stream, which was recorded over 4 hours, is correlated separately. The same result is obtained in other runs, where one-hour cut-outs could be studied.

Tab. 1: Fit parameters of $g_{AB}^{(2)}$. t_l: long-time component, t_s: short-time component. The dt are the respective errors, A_l, A_s correspond to the relative, unnormalized amplitudes.

T / h	t_l / ns	dt_l / ns	t_s / ns	dt_s / ns	A_l	A_s
1	122	11	7	2	0.25	0.11
2	103	10	12	4	0.26	0.09
3	124	16	14	3	0.24	0.12
4	99	12	15	6	0.25	0.08

(2) Triplet kinetics

The $g^{(2)}$ function, which is obtained in the experiment, is dependent on each process that leads to fluorescence fluctuations, that is diffusion, photobleaching, singlet-triplet transitions and antibunching.[1,2] If these processes occur on timescales, which are different enough, the respective contributions can be segregated: The process of interest, in this case the antibunching decay, can then be treated separately.[3–6] Diffusional time constants of single molecules in solvents with viscosities around 1 mPa·s usually lie in the order of 100 µs, the photobleaching occurs on a much longer time scale, if at all.[7]

To prove the separation of the triplet and the antibunching time scales, we determine the intersystem crossing rate constant (isc, k_{isc}) and the rate constant for the depopulation of the triplet state, k_{risc} in two experiments in dmso. In the first one, the deprotonated form is excited with 546 nm and the intensity is varied (Fig. S2, left). 10 µM of $CsCO_3$ is added as base to ensure that no other species than the FSIP is excited. The intensity independent isc-rate k_{isc} constant is determined with equation S1, where k_{isc}^{eff} is the isc rate constant at a given excitation rate. In the second experiment, the ROH is excited with 445 nm and k_{isc} is determined in a similar manner (Fig. S2, right). Here, the proton concentration is varied instead of k_{exc}.

$$k_{isc}^{eff} = \frac{k_{isc} k_{exc}}{k_f + k_{exc}} \qquad \text{(S1)}$$

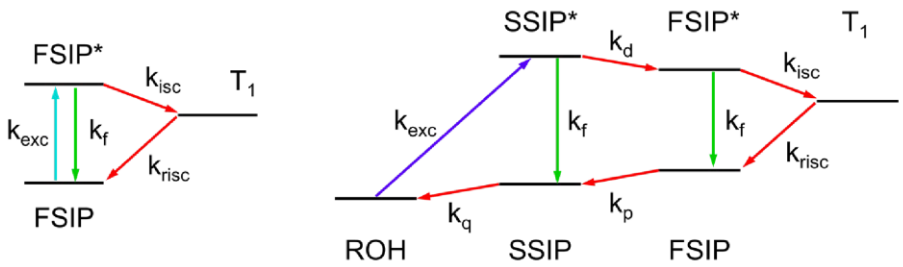

Fig. S2: Excitation schemes for the investigation of the triplet kinetics. Left: the deprotonated form is excited with 546 nm. Right: In the "Förster-cycle" experiment the ROH form is excited with 445 nm.

Tab. 2: Triplet kinetics of the photoacids used in this study in dmso. The second column lists the intensity independent rate constants for intersystem crossing. The third one provides the effective isc rate constants at 30 MHz excitation rate, which is implemented in the antibunching experiment. Together with the rate constant for bunching time constant t_B, k_{risc}, the triplet lifetime at k_{exc} = 30 MHz is obtained (fifth column).

		at k_{exc} = 30 MHz		at k_{exc} = 30 MHz
Photoacid	k_{isc} / MHz	k_{isc}^{eff} / MHz	k_{risc} / MHz	t_B / µs
(1)	0.98 ± 0.03	0.13 ± 0.01	0.63 ± 0.07	1.5
(2)	1.15 ± 0.04	0.26 ± 0.01	0.74 ± 0.03	1.3
(3)	0.85 ± 0.06	0.15 ± 0.02	1.41 ± 0.14	0.7

Tab. 3: The dependence of the effective inter-system crossing rate constant k_{isc}^{eff} and the bunching time t_B of the photoacid (**2**) on the proton concentration during the Förster-cycle experiment.

[msa] / mM	k_{isc}^{eff} / kHz	k_{risc} / kHz	t_B / µs
1	4 ± 3	144 ± 72	6.757
3	28 ± 7	230 ± 36	3.876
10	4 ± 1	35 ± 3	0.256
30	9 ± 1	81 ± 8	0.111
100	11 ± 1	75 ± 7	0.163

$$t_B = \frac{1}{k_{isc}^{eff} + k_{risc}} \qquad \text{(S2)}$$

In the case of ROH excitation at various proton concentrations the time constant t_B (S2), on which bunching occurs, lies in the range of 6.8 µs and 0.1 µs. The corresponding antibunching decay times (the t_1 component) range from ≈ 150 ns at 1 mM proton concentration to below 10 ns at > 30 mM proton concentrations.

Thus, the antibunching decay is at least 10 times faster than the triplet associated kinetics. We conclude that antibunching and triplet decay can be separately analyzed.

It is noteworthy that the time constant of the photon bunching, t_B, decreases as the proton concentration increases. We explain this unexpected bahaviour by proton quenching of the triplet state, which has been observed in the fluorescence of 2-Naphthol in a similar manner.[8]

(3) Spectral properties of (3)

The absorption spectra of (**3**) resemble those of compounds (**1**) and (**2**). The emission spectra of (**3**) show a stronger ROH emission than in the case of (**1**) and (**2**). The "contamination" of the analyzed photon stream by ROH photons likely explains the tendency of shorter t_s in the antibunching of compound (**3**) (see Fig. 4 a)).

a) b)

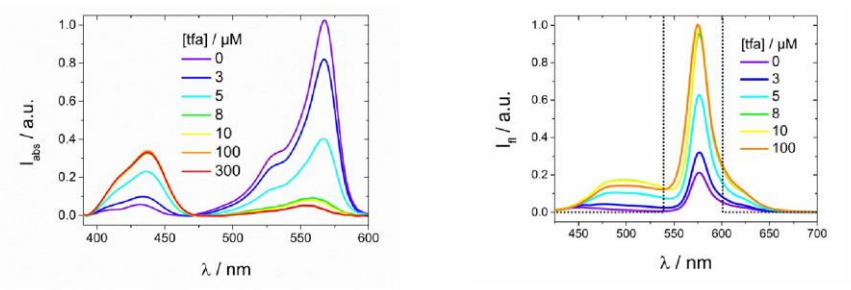

Fig. S3: Absorption a) and emission c) spectra of compound (**3**). The transmission profile of the emission filter (570/60 ET Bandpass) is also depicted in c).

(4) Experimental autocorrelation functions

Experimental correlation functions of the three photoacids (**1**)-(**3**) at 1, 2 and 3 mM tfa concentration are shown in Fig. S4 a), c) and d). The normalized fit curves are depicted in the manuscript in Fig. 3 b). Table 4 gives an overview of the associated fit parameters.

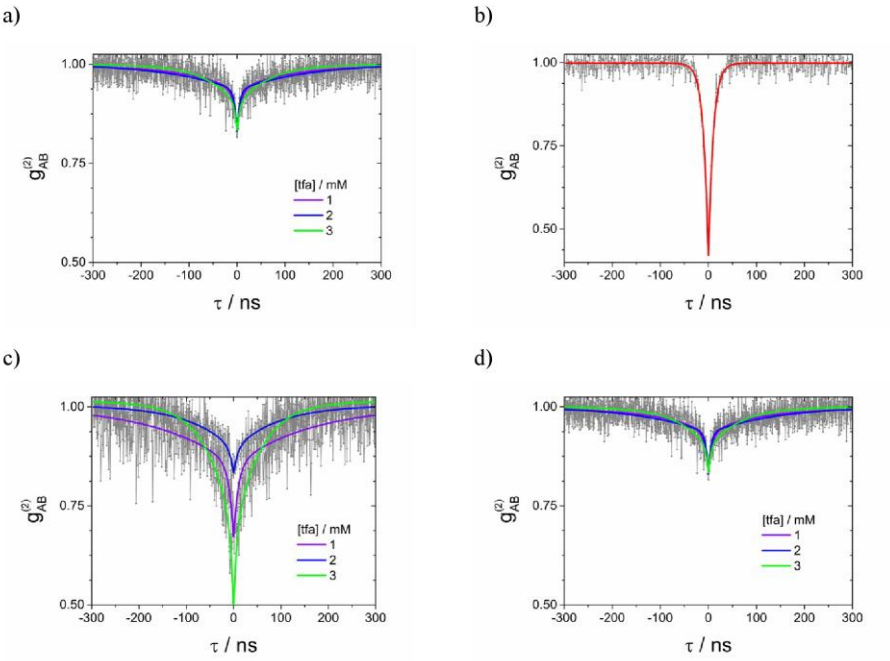

Fig. S4: Experimental correlation functions of compounds (**1**)-(**3**). a) Compound (**2**) at 1-3 mM tfa concentration. b) Compound (**2**) at 100 mM tfa. c)-d) Photoacids (**1**) and (**3**) at 1-3 mM tfa.

Tab. 4: Fit parameters of the $g_{AB}^{(2)}$ of (**1**)-(**3**) at 1-3 mM tfa concentration.

Compound	[tfa] / mM	t_l / ns	dt_l / ns	t_s / ns	dt_s / ns	A_l / %	A_s / %
(1)	1	161	83	9.5	3.4	46	54
	2	93	14	8.2	3.5	66	34
	3	54.4	5	5.6	2.2	66	34
(2)	1	156	14.2	9.3	1.3	64	36
	2	111	5.7	12.2	1.7	72	28
	3	93.8	4.7	9.3	1.8	74	26
(3)	1	107	35.6	8.3	2.4	40	60
	2	147	45.6	5.1	1.3	39	61
	3	64.4	10.6	4.8	2.8	61	39

(5) Antibunching decay with addition of methanesulfonic acid

To find out whether the progression of $k_l(c)$ depends on the proton donating acid or not, the antibunching measurement is repeated with methanesulfonic acid (msa) instead of trifluoroacetic acid (tfa). The influence of the proton donor on the long time component of the antibunching, respectively k_l, is negligible in the linear range, from which the bimolecular reprotonation rate constant k_p^{bi} is extracted (Fig. S5 left). Consequently, this hints to a common mechanistic reason behind the ground-state reprotonation in the linear regime. Both plots differ only in the saturation range. We ascribe this difference to slightly different dissociation of msa and tfa in dmso, which we proved by NMR spectroscopy (not shown). As a consequence, a certain acid concentration leads to a higher decay rate constant in the case of msa.

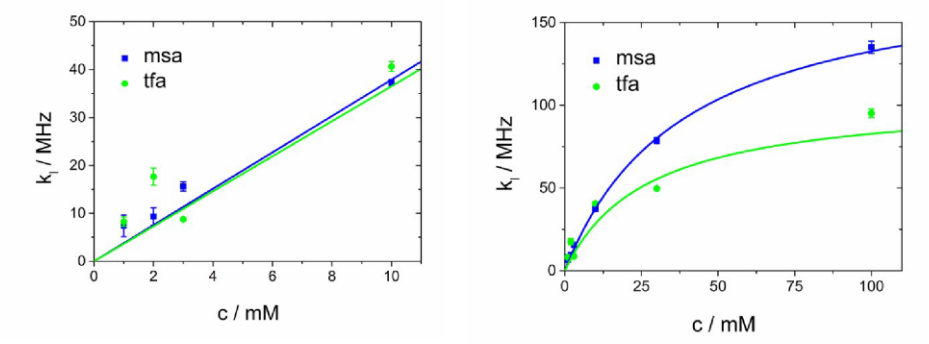

Fig. S5: Dependence of antibunching decay rate constants on proton acid concentration in the linear range and in the range of 0-100 mM.

(6) Isotope-effect

The progression of k_l(tfa) is compared to that of k_l(d-tfa) (Fig. S6), whose bimolecular rate constants differ by 5 %. This is similar to the error in the determination of the bimolecular rate constant for the different photoacids. Consequently, no clear isotope effect is detected.

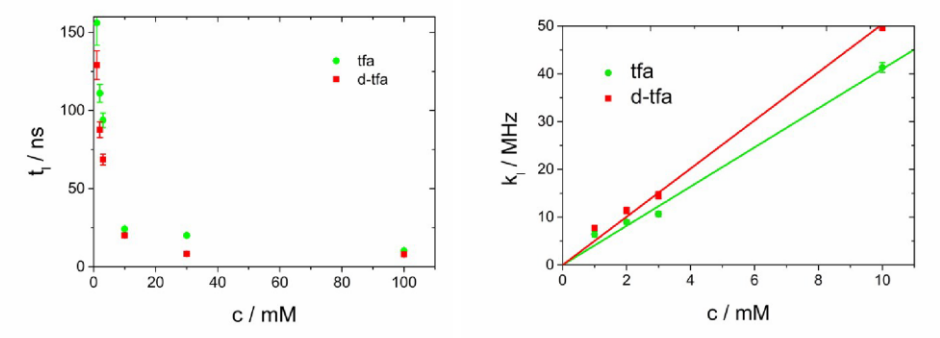

Fig. S6: Investigation of the kinetic isotope effect. The long-time decay constants (left) and decay rate constants (right) over the added amount of tfa and d-tfa, respectively. The bimolecular rate constant for protonation k_p^{bi} by tfa is 4.1 ± 0.2 x 10^9 $M^{-1}s^{-1}$ and by d-tfa 5.0 ± 0.2 x 10^9 $M^{-1}s^{-1}$.

(7) 5-states-system

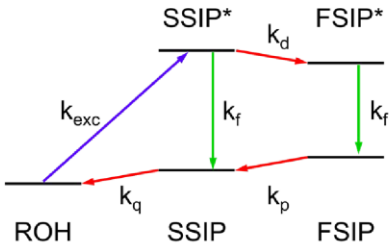

Fig. S7: 5-level-scheme.

Equation S1 collects the transitions within the 5-level-scheme.

$$\frac{d}{dt}\begin{pmatrix} FSIP^* \\ FSIP \\ ROH \\ SSIP^* \\ SSIP \end{pmatrix} = \begin{pmatrix} -k_f - s & 0 & 0 & k_d & 0 \\ k_f & -k_p - s & 0 & 0 & 0 \\ 0 & 0 & -k_{exc} - s & 0 & k_q \\ 0 & 0 & k_{exc} & -k_f - k_d - s & 0 \\ 0 & k_p & 0 & k_f & -k_q - s \end{pmatrix} \begin{pmatrix} FSIP^* \\ FSIP \\ ROH \\ SSIP^* \\ SSIP \end{pmatrix} \tag{S3}$$

or

$$\frac{d}{dt}\begin{pmatrix} FSIP^* \\ FSIP \\ ROH \\ SSIP^* \\ SSIP \end{pmatrix} = \underline{K} \begin{pmatrix} FSIP^* \\ FSIP \\ ROH \\ SSIP^* \\ SSIP \end{pmatrix} \tag{S4}$$

For the numerical calculations, $k_{exc} = 30$ MHz, $k_f = 180$ MHz, $k_d = 10$ MHz and $k_q = 330$ MHz are set and k_p is varied. S5 is chosen as initial condition as the molecule is either in the SSIP state or in the FSIP state after the emission of a photon. The distribution among FSIP and SSIP is chosen according to the amplitudes of the antibunching decays.

$$\frac{d}{dt}\begin{pmatrix} FSIP^* \\ FSIP \\ ROH \\ SSIP^* \\ SSIP \end{pmatrix}_{t=0} = \begin{pmatrix} 0 \\ 1/3 \\ 0 \\ 0 \\ 2/3 \end{pmatrix} \tag{S5}$$

(8) Dissociation constant k_d

In order to estimate the magnitude of k_d, $g_{AB}^{(2)}$ is simulated taking the 5-level scheme as basis. In the present case, k_{exc} was set to 30 MHz, k_f to 180 MHz, k_q to 330 MHz and k_p to 3 MHz. k_d is changed in the range of 3 to 30 MHz. k_f fits the fluorescence rate constant and the assumed k_p roughly matches the experimental k_p at 1 mM tfa based on a bimolecular rate constant of about 4 x 10^9 $M^{-1}s^{-1}$.

The obtained, simulated curves are compared to experimental $g_{AB}^{(2)}$ at 1 mM tfa (Fig. S8 a)). The comparison hints to experimental k_d in the range of 3 to 60 MHz. These values were initially used as input for other numerical calculations. Besides, k_d much lower than 3 MHz is not in agreement with the experiment. k_d significantly higher than 30 MHz leads to $g_{AB}^{(2)}$, which also strongly deviates from experimentally seizable correlation functions (Fig. S8 b)). We learn from suchlike simulations that k_d likely lies in the range between ≈ 1 and 60 MHz. Thus, we conclude that k_d is considerably smaller than k_f which allows us to introduce the approximation in (S9).

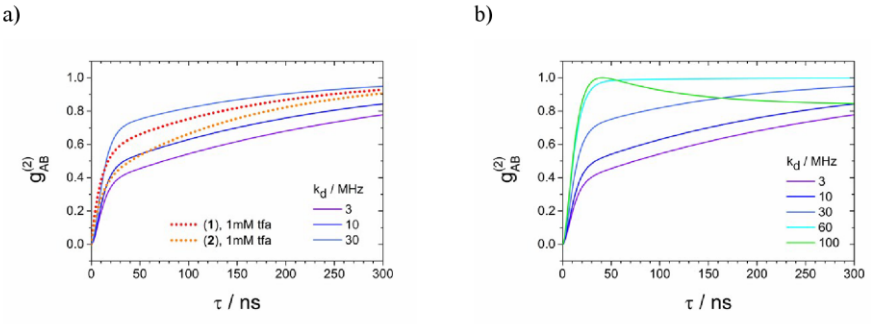

Fig. S8: a) Comparison of experimental correlation functions at 1 mM tfa and simulated data at different k_d. The simulated data is obtained by numerically solving the 5-state scheme. k_{exc} was set to 30 MHz, k_f to 180 MHz (corresponding to fluorescence lifetime), k_q to 330 MHz and k_p to 3 MHz, which roughly fits the experimental k_p at 1 mM tfa. k_d is in the range of 3 to 30 MHz at tfa concentrations between 1 to 5 mM. b) Simulated $g^{(2)}$ for k_d between 3 and 100 MHz. At k_d higher than 60 MHz, $g^{(2)}$ is no longer biexponential with two amplitudes of the same sign and, hence, do not reproduce experimental behavior.

(9) TCSPC data: Comparison of SSIP* and FSIP*

During the derivation of the $g^{(2)}$ of the five-level scheme, the SSIP* and FSIP* are assumed to decay in a similar manner. Figure S9 a) depicts the fluorescence decay of compound (**2**), which are obtained with excitation of the ROH form (405 nm) and the RO^- form (470 nm) respectively. In both cases, the RO^- fluorescence is observed. Although different excitation schemes are applied, the respective tcspc data show monoexponential decays. The associated decay constants differ by 3 % and less (Tab. 5). The apparent difference between 405 nm and 470 nm excitation in the case of (**3**) is due to the buildup of the RO^{-}* population. This buildup is less obvious is the case of (**2**) because of its distinctly higher espt rate constant. Hence, the assumption of similar decay constants of SSIP* and FSIP* is backed by the tcspc data.

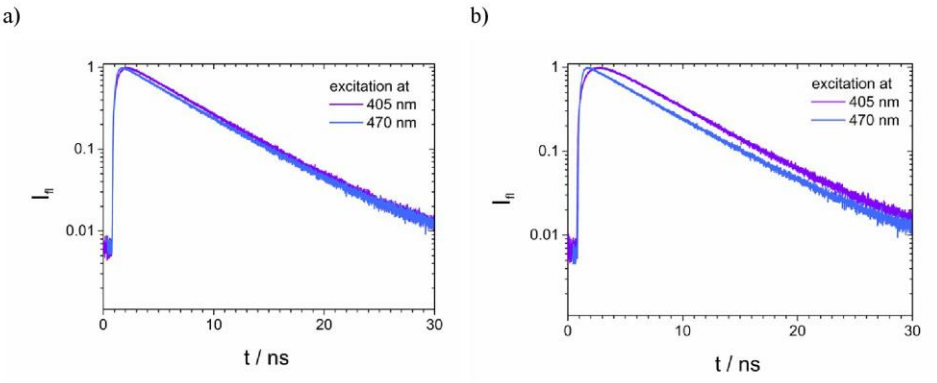

Fig. S9: Fluorescence decay of a) (**2**) and b) (**3**) in dmso with excitation at 405 nm and 470 nm. The emission filter is 570/60 ET Bandpass.

Tab. 5: Decay constants of the (**2**) and (**3**) fluorescence. The error is between 1 and 2 %.

	t / ns
(**2**), exc. at 405 nm	5.61
(**2**), exc. at 470 nm	5.78
(**3**), exc. at 405 nm	5.56
(**3**), exc. at 470 nm	5.62

(10) 3-state-system plus 2-state-system

The goal is to obtain a valid approximation of $g_{AB}^{(2)}$, which ought to be chemically interpretable. Therefore, analytical expressions for the SSIP* and the FSIP* population are obtained by splitting the five-level Eigen-Weller scheme into a 3-level-scheme and a 2-level-scheme.

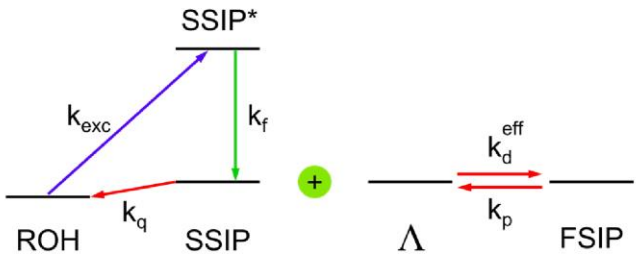

Fig. S10: Combination of 3-level and 2-level-scheme.

The transitions within the 3-level sub scheme are combined in the equations

$$\frac{d}{dt}\begin{pmatrix} ROH \\ SSIP^* \\ SSIP \end{pmatrix} = \begin{pmatrix} -k_{exc}-s & 0 & k_q \\ k_{exc} & -k_f-s & 0 \\ 0 & k_f & -k_q-s \end{pmatrix}\begin{pmatrix} ROH \\ SSIP^* \\ SSIP \end{pmatrix} \tag{S6}$$

or

$$\frac{d}{dt}\begin{pmatrix} ROH \\ SSIP^* \\ SSIP \end{pmatrix} = \underline{K_3}\begin{pmatrix} ROH \\ SSIP^* \\ SSIP \end{pmatrix} \tag{S7}$$

The molecule is found in the SSIP after the emission of a photon from the SSIP* state. Therefore, S6 is set as initial condition.

$$\frac{d}{dt}\begin{pmatrix} ROH \\ SSIP^* \\ SSIP \end{pmatrix}_{t=0} = \begin{pmatrix} 0 \\ 0 \\ 1 \end{pmatrix} \tag{S8}$$

$$det\underline{K_3} = -s\left(s^2 + s\left(k_{exc}+k_f+k_q\right) + k_{exc}k_f + k_{exc}k_q + k_f k_q\right) = -s(s_2-s)(s_3-s) \tag{S9}$$

with $s_1 = 0,\ s_{2,3} = -\frac{1}{2}\left(\sigma \pm \sqrt{\sigma^2 - 4\rho}\right)$ (S10)

and $\sigma = k_{exc}+k_f+k_q,\ \rho = k_{exc}k_f + k_{exc}k_q + k_f k_q$ (S11)

The implementation of the residue theorem (each pole of $\underline{K_3}$ is separated from the fraction and becomes an exponential function) leads to S12.

$$[X](t) = \sum_{i=1}^{3} \frac{det\underline{X}}{det(\underline{K_3})} exp(s_i t) \tag{S12}$$

The matrices $\underline{X}$ in S12 account for the initial conditions. So, the $\underline{SSIP^*}$ matrix, which corresponds to the SSIP* state is given by S12.

$$\underline{SSIP^*} = \begin{pmatrix} -k_{exc} - s & 0 & k_q \\ k_{exc} & 0 & 0 \\ 0 & -1 & -k_q - s \end{pmatrix} \tag{S13}$$

Then, the determinant of $\underline{SSIP^*}$ is

$$|\underline{SSIP^*}| = -k_{exc} k_q \tag{S14}$$

This finally leads to

$$[SSIP^*](t) = \frac{k_{exc} k_q}{s_2 s_3} + \frac{k_{exc} k_q}{s_2(s_3 - s_2)} exp(s_2 t) + \frac{k_{exc} k_q}{s_3(s_2 - s_3)} exp(s_3 t) \tag{S15}$$

For the 2-level-system equation S16 is valid.

$$\frac{d}{dt}\begin{pmatrix} FSIP \\ \Lambda \end{pmatrix} = \begin{pmatrix} -k_p - s & k_d^{eff} \\ k_p & -k_d^{eff} - s \end{pmatrix}\begin{pmatrix} FSIP \\ \Lambda \end{pmatrix} \tag{S16}$$

k_d^{eff} is given by (E1):

$$k_d^{eff} = k_d \frac{k_{exc}}{k_{exc} + k_f} \tag{E1}$$

In S16, Λ accounts for transitions within the three-level system.

S17 is chosen as boundary condition, because the system is in the FSIP state the moment just after the emission from the FSIP* state.

$$\frac{d}{dt}\begin{pmatrix} FSIP \\ \Lambda \end{pmatrix}_{t=0} = \begin{pmatrix} 1 \\ 0 \end{pmatrix} \tag{S17}$$

or

$$Det\underline{K_2} = -s\left(s + k_p + k_d^{eff}\right) \tag{S18}$$

with $s_4 = 0,\ s_5 = -(k_p + k_d^{eff})$ (S19)

Again, the residue theorem leads to

$$[X](t) = \sum_{i=4}^{5} \frac{det\underline{X}}{det(\underline{K_2})} exp(s_i t) \tag{S20}$$

In the present case:

$$[FSIP](t) = \frac{k_d^{eff}}{k_p + k_d^{eff}} - \frac{k_p}{k_p + k_d^{eff}} exp(-(k_p + k_d^{eff})t) \tag{S21}$$

$g^{(2)}$ is approximated by a linear combination of [SSIP*] and [FSIP].

$$g^{(2)} \propto \frac{1}{N_g}([SSIP^*] + [FSIP]) = 1 + \frac{A_2}{N_g} exp(s_2 t) + \frac{A_3}{N_g} \exp(s_3 t) - \frac{A_5}{N_g} exp(s_5 t) \tag{S22}$$

with

$$N_g = \frac{k_{exc} k_q}{s_2 s_3} + \frac{k_d^{eff}}{k_p + k_d^{eff}} \tag{S23}$$

$$A_2 = \frac{k_{exc} k_q}{s_2(s_3 - s_2)},\ A_3 = \frac{k_{exc} k_q}{s_3(s_2 - s_3)},\ A_5 = \frac{k_d^{eff}}{k_p + k_d^{eff}} \tag{S24}$$

Fig. S11 a) shows numerical solutions of the five-level Eigen-Weller scheme for various excitation rate constants k_{exc}. As input k_f = 180 MHz, k_d = 10 MHz, k_q = 330 MHz and k_p = 3 MHz is used. Thereby, k_q matches the SSIP reprotonation rate constant we determined in the antibunching experiment. In the experiment, k_d is in the range of 3 - 30 MHz (see SI 8), so k_d is set to 10 MHz for the following calculation. k_p = 3 MHz is expected at 1-3 mM tfa concentration. The predicted dependency of the amplitudes of the $g^{(2)}$ function (eq. S22-S24) is reflected by experimental correlation functions as depicted in Fig. S11 b).

a) b)

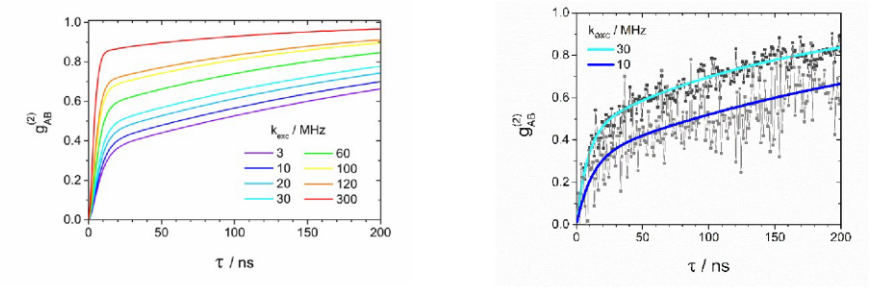

Fig. S11: a) Numerical solutions of the 5-level scheme for different k_{exc}. b) Experimental correlation functions at different excitation rate constants. These have been normalized to be comparable with the simulated curves.

In summary, k_l only changes by a factor of 2 when k_{exc} is raised from 3 MHz to 100 MHz, i.e. by a factor of about thirty (Fig. S12 a)). Based on that, the long-time component of $g_{AB}^{(2)}$ only shows a minor dependence on the applied excitation rate. The splitting of the 5-level scheme into the 3-level and the two level system is valid in a good approximation, especially at $k_{exc} \approx$ 3-100 MHz in the time range between 0 and 200 ns. The influence of k_{exc} on the relative amplitudes A_l and A_s is shown in Fig. S12 b). In the range of 0 to 300 MHz, A_l monotonically decreases as A_s increases. Also this behavior is described by our model, where A_5, which is associated with the long-time component, decreases as k_{exc}, thus also k_d^{eff}, increases. Accordingly, the 3-level-2-level approximation also describes that experimental behavior well. However, the most sensitive parameter to a variation of k_{exc} is the distribution among the amplitudes which might partially explain the experimental variation in table 4.

a) b)

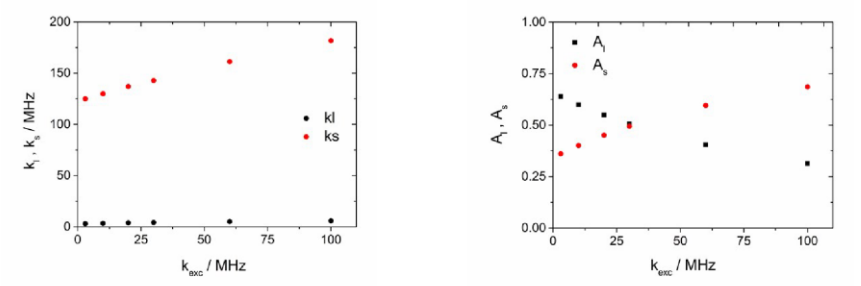

Fig. S12: a) Dependence of k_l and k_s on the excitation rate constant k_{exc}. b) Dependence of the relative amplitudes A_l and A_s on k_{exc}.

(11) Simplification of s_1 for didactic reasons

$$s_1 = {}^1/_2\left(-\sigma+\sqrt{\sigma^2-4\rho}\right) \quad \text{(S25)}$$

$$= {}^1/_2\left(-\sigma+\sigma\sqrt{1-\frac{4\rho}{\sigma^2}}\right) \quad \text{(S26)}$$

$$\approx {}^1/_2\left(-\sigma+\sigma\left(1-\frac{14\rho}{2\sigma^2}\right)\right) \quad \text{(S27)}$$

$$= -\frac{\rho}{\sigma} \quad \text{(S28)}$$

The approximation of the square root is assumed to be valid because of $\rho << \sigma$.

$$t_s \equiv -\frac{1}{s_1} \approx \frac{\sigma}{\rho} \quad \text{(S29)}$$

$$= \frac{k_q+k_{exc}+k_f}{k_qk_f+k_{exc}k_q+k_fk_{exc}} \quad \text{(S30)}$$

$$\approx \frac{k_q}{k_qk_f+k_{exc}k_q+k_fk_{exc}}+\frac{k_{exc}+k_f}{k_qk_f+k_{exc}k_q+k_fk_{exc}} \quad \text{(S31)}$$

Approximation: $k_{exc} \approx \frac{1}{6}k_f$ and $k_{exc} \approx \frac{1}{10}k_q$ thus $k_{exc} \ll k_f, k_q$

$$t_s \equiv -\frac{1}{s_1} \approx \frac{1}{k_f+k_{exc}}+\frac{1}{k_q} \quad \text{(S32)}$$

(12) TCSPC data: Geminate recombination

The fluorescence decay of the protonated form of (**2**) is shown in Fig. S13 with excitation at 405 nm, detection at 470/40 nm and with 1 mM and 1 M tfa concentration. The biexponential fit provides two time components. The short one is associated with the sum of k_f and k_{espt}, the long one with the recombination in the excited state. The diffusion-assisted geminate recombination in the excited state also explains the deviation of the decay curves from a purely biexponential behavior.[9,10] In the consequence, geminate recombination takes place within ≈ 2.5 ns. Less than 10 % of the molecules recombine in the excited state, which can be derived from the relative amplitudes A_1 and A_2. Therefore, the approximation [ROH*](t) ≈ 0 is valid in dmso with proton concentrations between 1 to 300 mM.

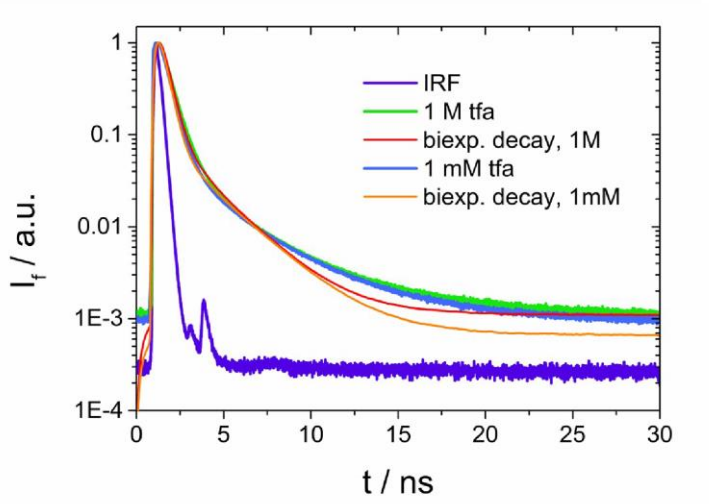

Fig. S13: Fluorescence decay of the protonated form of (**2**). Excitation at 405 nm, detection at 470/40.

Tab. 6: Parameters obtained from biexponential reconvolution fit of the tcspc data. t_1 and t_2 are the decay constants, A_1 and A_2 the respective, relative amplitudes.

	t_1 / ns	A_1	t_2 / ns	A_2
1 mM	0.401 ± 0.009	0.96 ± 0.02	2.58 ± 0.06	0.04 ± 0.01
1 M	0.468 ± 0.011	0.95 ± 0.01	2.49 ± 0.07	0.05 ± 0.01

(13) Literature

1 M. Gösch and R. Rigler, *Adv. Drug Deliv. Rev.*, 2005, **57**, 169–190.

2 O. Krichevsky and G. Bonnet, *Rep. Prog. Phys.*, 2002, **65**, 251–297.

3 I. V. Gopich and A. Szabo, *J. Chem. Phys.*, 2006, **124**, 154712.

4 D. Nettels, I. V. Gopich, A. Hoffmann and B. Schuler, *Proc. Natl. Acad. Sci. USA*, 2007, **104**, 2655–2660.

5 D. Nettels and B. Schuler, *IEEE J. Sel. Top. Quantum Electron.*, 2007, **13**, 990–995.

6 I. V. Gopich, D. Nettels, B. Schuler and A. Szabo, *J. Chem. Phys.*, 2009, **131**, 095102.

7 B. Finkler, C. Spies, M. Vester, F. Walte, K. Omlor, I. Riemann, M. Zimmer, F. Stracke, M. Gerhards and G. Jung, *Photochem. Photobiol. Sci.*, 2014, **13**, 548–562.

8 C. M. Harris and B. K. Selinger, *J. Phys. Chem.*, 1980, **84**, 891–898.

9 E. Pines, D. Huppert and N. Agmon, *J. Chem. Phys.*, 1988, **88**, 5620–5630.

10 N. Agmon, E. Pines and D. Huppert, *J. Chem. Phys.*, 1988, **88**, 5631–5638.

6. Ausblick

Im Fokus dieser Arbeit stand die Analyse des Zeitabstandes abstandshaltender Photonen, d.h. der assoziierten Zeitkonstante τ_{AB}. Klassische Experimente mit Zwei-Zustandssystemen wurden zunächst auf zyklische Vier-Zustandssysteme ausgedehnt. In diesen waren die beiden emissiven Spezies ROH und RO^- über Protolysegleichgewichte im angeregten Zustand und im Grundzustand gekoppelt. Die Kombination aus dem sehr schnellem ESPT und der relativ langsamen Grundzustandsreprotonierung führte zu einer Abhängigkeit von τ_{AB} von der Reprotonierungsrate k_p. Somit können allgemeine Bedingungen ausgemacht werden, um eine Grundzustandskinetik unter Ausnutzung des Antibunching zu analysieren. In einem zyklischen Anregungsschema müssen zwei Spezies in ihrem Grundzustand und ihrem angeregten Zustand miteinander im Gleichgewicht stehen. Die Reaktion muss im angeregten Zustand so schnell ablaufen, dass das emissive Produkt rasch gebildet wird. Gleichzeitig muss die Reaktion im Grundzustand geschwindigkeitsbestimmend sein, also langsam genug ablaufen. So ist eine Ausdehnung der Experimente auf PET Reaktionen (Engl., Photoinduced Electron Transfer) denkbar, in denen ein Elektron nach optischer Anregung übertragen wird. Ionenpaare werden sowohl beim ESPT als auch beim PET gebildet. Das sollte außerdem eine Möglichkeit bieten, die Kinetik des Antibunchings mit elektrischen Feldern zu manipulieren. Es sollte so zumindest theoretisch möglich sein, beispielsweise die Protonenübertragung im Grundzustand zu verlangsamen. Als praktische Limitierung ist hier allerdings die molekulare Helligkeit zu sehen. Wird die Grundzustandsreaktion zu sehr verlangsamt, ist die Dauer eines Photozyklus zu hoch. Damit wäre die Emissionsrate pro Molekül zu gering um in erträglicher Messzeit eine gute Statstik zu erreichen.

Die Antibunching-Experimente wurden um Versuche im Lösemittel DMSO erweitert. Das emissive, intermediär gebildete SSIP führte zu einer kurzen Zerfallskomponente in $g^{(2)}_{AB}$. Damit konnte die komplexere Kinetik des Grundzustandsprotonentransfers, einer konsekutiven Reaktion, durch das biexponentielle Antibunching erfasst werden. Hierfür war eine Reihe weiterer Bedingungen notwendig. Im zyklischem Reaktionsschema mussten erstens zwei emissive Spezies, SSIP und FSIP, miteinander im Gleichgewicht stehen. Zweitens musste der Zerfall des SSIP auf der ns-Skala stattfinden. Drittens mussten bei der bimolekularen Bildung des SSIP aus dem FSIP Proton und RO^- zunächst zueinander diffundieren. Das führte zu einer Abhängigkeit der langsamen Komponente von τ_{AB} von der vorliegenden Protonenkonzentration. So war es möglich diese Reaktion so zu verlangsamen, dass das biexponentielle Verhalten von $g^{(2)}_{AB}$ zu Tage trat. In ähnlicherweise könnten weitere zyklische

Systeme untersucht werden, die eine konsekutive Reaktionsfolge zwischen emissiven Spezies beinhalten.

7. Literaturverzeichnis

1 T. Funatsu, Y. Harada, M. Tokunaga, K. Saito and T. Yanagida, *Nature*, 1995, 374, 555–559.

2 A. Rybina, C. Lang, M. Wirtz, K. Grußmayer, A. Kurz, F. Maier, A. Schmitt, O. Trapp, G. Jung and D. P. Herten, *Angew. Chem. Int. Ed.*, 2013, **52**, 6322–6325.

3 S. A. Blum, *PCCP*, 2014, **16**, 16333.

4 N. M. Esfandiari and S. A. Blum, *JACS*, 2011, **133**, 18145–18147.

5 R. H. Goldsmith and W. E. Moerner, *Nat. Chem.*, 2010, **2**, 179–186.

6 A. Kiel, J. Kovacs, A. Mokhir, R. Krämer and D.-P. Herten, *Angew. Chem. Int. Ed.*, 2007, **46**, 3363–3366.

7 K. Naito, T. Tachikawa, S. Cui, A. Sugimoto, M. Fujitsuka and T. Majima, *JACS*, 2006, **128**, 16430–16431.

8 M. Börsch, M. Diez, B. Zimmermann, R. Reuter and P. Gräber, *FEBS Lett.*, 2002, **527**, 147–152.

9 S. Y. Reece and D. G. Nocera, *Annu. Rev. Biochem.*, 2009, **78**, 673–699.

10 J. P. Vessey, A. K. Stratis, B. A. Daniels, N. Da Silva, M. G. Jonz, M. R. Lalonde, W. H. Baldridge and S. Barnes, *J. Neurosci.*, 2005, **25**, 4108–4117.

11 I. Bogeski, R. Kappl, C. Kummerow, R. Gulaboski, M. Hoth and B. A. Niemeyer, *Cell Calcium*, 2011, **50**, 407–423.

12 P. D. Boyer, *Nature*, 1999, **402**, 247–249.

13 L. M. Tolbert and J. E. Haubricht, *JACS*, 1994, **116**, 10593–10600.

14 D. B. Spry, A. Goun and M. D. Fayer, *J. Phys. Chem. A*, 2007, **111**, 230–237.

15 L. M. Tolbert and K. M. Solntsev, *Acc. Chem. Res.*, 2002, **35**, 19–27.

16 J. T. Hynes, T.-H. Tran-Thi and G. Granucci, *J. Photochem. Photobiol. A Chem.*, 2002, **154**, 3–11.

17 O. F. Mohammed, J. Dreyer, B.-Z. Magnes, E. Pines and E. T. J. Nibbering, *ChemPhysChem*, 2005, **6**, 625–636.

18 B. Zelent, J. M. Vanderkooi, R. G. Coleman, I. Gryczynski and Z. Gryczynski, *Biophys. J.*, 2006, **91**, 3864–3871.

19 S. K. Mondal, S. Ghosh, K. Sahu, P. Sen and K. Bhattacharyya, *J. Chem. Sci.*, 2007, **119**, 71–76.

20 R. L. A. Timmer, M. J. Cox and H. J. Bakker, *J. Phys. Chem. A*, 2010, **114**, 2091–2101.

21 O. F. Mohammed, D. Pines, J. Dreyer, E. Pines and E. T. J. Nibbering, *Science*, 2005,

310, 83–86.

22 T. Förster, *Naturwissenschaften*, 1949, **6**, 186–187.

23 T. Förster, *Z. Elektrochemie*, 1950, **54**, 42–46.

24 A. Douhal, F. Lahmani and A. H. Zewail, *Chem. Phys.*, 1996, **207**, 477–498.

25 M. T. Htun, A. Suwaiyan and U. K. A. Klein, *Chem. Phys. Lett.*, 1995, **243**, 506–511.

26 E. Pines, D. Pines, Y.-Z. Ma and G. R. Fleming, *ChemPhysChem*, 2004, **5**, 1315–1327.

27 I. Presiado, R. Gepshtein, Y. Erez and D. Huppert, *J. Phys. Chem. A*, 2011, **115**, 7591–7601.

28 I. Presiado, N. Karton-Lifshin, Y. Erez, R. Gepshtein, D. Shabat and D. Huppert, *J. Phys. Chem. A*, 2012, **116**, 7353–7363.

29 R. Simkovitch, S. Shomer, R. Gepshtein, D. Shabat and D. Huppert, *J. Phys. Chem. A*, 2014, **118**, 1832–1840.

30 R. Simkovitch, S. Shomer, R. Gepshtein and D. Huppert, *J. Phys. Chem. B*, 2015, **119**, 2253–2262.

31 C. Spies, S. Shomer, B. Finkler, D. Pines, E. Pines, G. Jung and D. Huppert, *PCCP*, 2014, **16**, 9104.

32 E.-A. Gould, A. V. Popov, L. M. Tolbert, I. Presiado, Y. Erez, D. Huppert and K. M. Solntsev, *PCCP*, 2012, **14**, 8964–8973.

33 R. Simkovitch and D. Huppert, *J. Phys. Chem. A*, 2015, **119**, 1973–1982.

34 D. Huppert and E. Kolodney, *Chem. Phys.*, 1981, **63**, 401–410.

35 A. V. Popov, E.-A. Gould, M. A. Salvitti, R. Hernandez and K. M. Solntsev, *PCCP*, 2011, **13**, 14914–14927.

36 I. V. Gopich, K. M. Solntsev and N. Agmon, *J. Chem. Phys.*, 1999, **110**, 2164–2174.

37 T. Kumpulainen, B. H. Bakker, M. Hilbers and A. M. Brouwer, *J. Phys. Chem. B*, 2015, **119**, 2515–2524.

38 O. F. Mohammed, D. Pines, E. T. J. Nibbering and E. Pines, *Angew. Chem. Int. Ed.*, 2007, **46**, 1458–1461.

39 R. Gepshtein, P. Leiderman, L. Genosar and D. Huppert, *J. Phys. Chem. A*, 2005, **109**, 9674–9684.

40 P. Leiderman, L. Genosar and D. Huppert, *J. Phys. Chem. A*, 2005, **109**, 5965–5977.

41 M. Rini, B.-Z. Magnes, E. Pines and E. T. J. Nibbering, *Science*, 2003, **301**, 349–352.

42 S.-Y. Park, Y.-S. Lee and D.-J. Jang, *PCCP*, 2008, **10**, 6703–6707.

43 J. T. M. Kennis, D. S. Larsen, I. H. M. van Stokkum, M. Vengris, J. J. van Thor and R. van Grondelle, *PNAS*, 2004, **101**, 17988–17993.

44 L. J. G. W. Van Wilderen, I. P. Clark, M. Towrie and J. J. Van Thor, *J. Phys. Chem. B*, 2009, **113**, 16354–16364.

45 H. J. Kimble, M. Dagenais and L. Mandel, *Phys. Rev. Lett.*, 1977, **39**, 691–695.

46 T. Basché, W. E. Moerner, M. Orrit and H. Talon, *Phys. Rev. Lett.*, 1992, **69**, 1516–1519.

47 B. Lounis and M. Orrit, *Rep. Prog. Phys.*, 2005, **68**, 1129–1179.

48 L. Fleury, J.-M. Segura, G. Zumofen, B. Hecht and U. P. Wild, *Phys. Rev. Lett.*, 2000, **84**, 1148–1151.

49 C. Kurtsiefer, S. Mayer, P. Zarda and H. Weinfurter, *Phys. Rev. Lett.*, 2000, **85**, 290–293.

50 T. Plakhotnik, E. A. Donley and U. P. Wild, *Annu. Rev. Phys. Chem.*, 1997, **48**, 181–212.

51 M. Vester, T. Staut, J. Enderlein and G. Jung, *J. Phys. Chem. Lett.*, 2015, **6**, 1149–1154.

52 M. Vester, A. Grüter, B. Finkler, R. Becker and G. Jung, *PCCP*, 2016, Accepted Manuscript.

53 L. G. Arnaut and S. J. Formosinho, *J. Photochem. Photobiol. A Chem*, 1993, 75, 1–20.

54 K. K. Smith, K. J. Kaufmann, D. Huppert and M. Gutman, *Chem. Phys. Lett.*, 1979, **64**, 522–527.

55 N. Agmon, *J. Phys. Chem. A*, 2005, **109**, 13–35.

56 R. Simkovitch, S. Shomer, R. Gepshtein, M. E. Roth, D. Shabat and D. Huppert, *J. Photochem. Photobiol. A Chem*, 2014, **277**, 90–101.

57 B. Finkler, C. Spies, M. Vester, F. Walte, K. Omlor, I. Riemann, M. Zimmer, F. Stracke, M. Gerhards and G. Jung, *Photochem. Photobiol. Sci.*, 2014, **13**, 548–562.

58 W. Bartok, P. J. Lucchesi and N. S. Snider, *JACS*, 1962, **84**, 1842–1844.

59 G. Jung, S. Gerharz and A. Schmitt, *PCCP*, 2009, **11**, 1416–1426.

60 M. Gutman and E. Nachliel, *Biochim. Biophys. Acta*, 1990, **1015**, 391–414.

61 S. J. Formosinho and L. G. Arnaut, *J. Photochem. Photobiol. A Chem*, 1993, **75**, 21–48.

62 E. L. Wehry and L. B. Rogers, *JACS*, 1965, **87**, 4234–4238.

63 S. G. Schulman, W. R. Vincent and W. J. M. Underberg, *J. Phys. Chem.*, 1981, **85**, 4068–4071.

64 E. Pines and G. R. Fleming, *Chem. Phys.*, 1994, **183**, 393–402.

65 E. Pines, D. Huppert and N. Agmon, *J. Chem. Phys.*, 1988, **88**, 5620–5630.

66 K. M. Solntsev, D. Huppert and N. Agmon, *J. Phys. Chem. A*, 1999, **103**, 6984–6997.

67 M. Prémont-Schwarz, T. Barak, D. Pines, E. T. J. Nibbering and E. Pines, *J. Phys. Chem. B*, 2013, **117**, 4594–4603.

68 A. Weller, *Z. f. Phys. Chem.*, 1958, **17**, 224–245.

69 N. Agmon, W. Rettig and C. Groth, *JACS*, 2002, **124**, 1089–1096.

70 W. H. Fang, *J. Chem. Phys.*, 2000, **112**, 1204.

71 C. Spies, B. Finkler, N. Acar and G. Jung, *PCCP*, 2013, **15**, 19893.

72 L. N. Silverman, D. B. Spry, S. G. Boxer and M. D. Fayer, *J. Phys. Chem. A*, 2008, **112**, 10244–10249.

73 D. B. Spry, A. Goun, C. B. Bell and M. D. Fayer, *J. Chem. Phys.*, 2006, **125**, 144514.

74 N. Agmon, E. Pines and D. Huppert, *J. Chem. Phys.*, 1988, **88**, 5631–5638.

75 K. M. Solntsev, D. Huppert and N. Agmon, *Phys. Rev. Lett.*, 2001, **86**, 3427–3430.

76 J. Ditkovich, T. Mukra, D. Pines, D. Huppert and E. Pines, *J. Phys. Chem. B*, 2015, **119**, 2690–2701.

77 L. Giestas, C. Yihwa, J. C. Lima, C. Vautier-Giongo, A. Lopes, A. L. Macanita and F. H. Quina, *J. Phys. Chem. A*, 2003, **107**, 3263–3269.

78 R. Simkovitch, N. Karton-Lifshin, S. Shomer, D. Shabat and D. Huppert, *J. Phys. Chem. A*, 2013, **117**, 3405–3413.

79 M. Rini, D. Pines, B.-Z. Magnes, E. Pines and E. T. J. Nibbering, *J. Chem. Phys.*, 2004, **121**, 9593–9610.

80 M. Veiga-Gutiérrez, A. Brenlla, C. Carreira Blanco, B. Fernández, S. A. Kovalenko, F. Rodríguez-Prieto, M. Mosquera and J. L. P. Lustres, *J. Phys. Chem. B*, 2013, **117**, 14065–14078.

81 C. Clower, K. M. Solntsev, J. Kowalik, L. M. Tolbert and D. Huppert, *J. Phys. Chem. A*, 2002, **106**, 3114–3122.

82 V. Thomas, U. Rivard, P. Maurer, A. Bruhács, B. J. Siwick and R. Iftimie, *J. Phys. Chem. Lett.*, 2012, **3**, 2633–2637.

83 K. J. Tielrooij, M. J. Cox and H. J. Bakker, *ChemPhysChem*, 2009, **10**, 245–251.

84 S. Rakshit, R. Saha, P. K. Verma and S. K. Pal, *Photochem. Photobiol.*, 2012, **88**, 851–859.

85 J. A. Syage, *J. Phys. Chem.*, 1995, **99**, 5772–5786.

86 V. Vojinovic, S. Mentus and V. Komnenic, *J. Serb. Chem. Soc.*, 2003, **68**, 497–504.

87 N. Agmon, *Chem. Phys. Lett.*, 1995, **244**, 456–462.

88 Ü. Mets, J. Widengren and R. Rigler, *Chem. Phys.*, 1997, **218**, 191–198.

89 M. Gösch and R. Rigler, *Adv. Drug Deliv. Rev.*, 2005, **57**, 169–190.

90 J. Widengren, Ü. Mets and R. Rigler, *J. Phys. Chem.*, 1995, **99**, 13368–13379.

91 C. G. Hübner, G. Zumofen, A. Renn, A. Herrmann, K. Müllen and T. Basché, *Phys. Rev.*

Lett., 2003, **91**, 093903.

92 C. Brunel, B. Lounis, P. Tamarat and M. Orrit, *Phys. Rev. Lett.*, 1999, **83**, 2722–2725.

93 W. E. Moerner, *New J. Phys.*, 2004, **6**, 1–21.

94 J. Bernard, L. Fleury, H. Talon and M. Orrit, *J. Chem. Phys.*, 1993, **98**, 850–859.

95 C. Bradac, T. Gaebel, N. Naidoo, M. J. Sellars, J. Twamley, L. J. Brown, A. S. Barnard, T. Plakhotnik, A. V. Zvyagin and J. R. Rabeau, *Nat. Nanotechnol.*, 2010, **5**, 345–349.

96 W. E. Moerner and M. Orrit, *Science (80-.).*, 1999, **283**, 1670–1676.

97 A.-M. Boiron, B. Lounis and M. Orrit, *J. Chem. Phys.*, 1996, **105**, 3969–3974.

98 M. Orrit and J. Bernard, *Phys. Rev. Lett.*, 1990, **65**, 2716–2719.

99 C. Becher, A. Kiraz, P. Michler, A. Imamoglu, W. V. Schoenfeld, P. M. Petroff, L. Zhang and E. Hu, *Phys. Rev. B*, 2001, **63**, 121312.

100 K. D. Weston, M. Dyck, P. Tinnefeld, C. Müller, D.-P. Herten and M. Sauer, *Anal. Chem.*, 2002, **74**, 5342–5349.

101 H. Ta, A. Kiel, M. Wahl and D.-P. Herten, *PCCP*, 2010, **12**, 10295–10300.

102 J. Sýkora, K. Kaiser, I. Gregor, W. Bönigk, G. Schmalzing and J. Enderlein, *Anal. Chem.*, 2007, **79**, 4040–4049.

103 E. Neu, D. Steinmetz, J. Riedrich-Möller, S. Gsell, M. Fischer, M. Schreck and C. Becher, *New J. Phys.*, 2011, **13**, 025012.

104 D. Nettels and B. Schuler, *IEEE J. Sel. Top. Quantum Electron.*, 2007, **13**, 1077.

105 D. Nettels, I. V. Gopich, A. Hoffmann and B. Schuler, *PNAS*, 2007, **104**, 2655–2660.

106 T. Sandén, G. Persson, P. Thyberg, H. Blom and J. Widengren, *Anal. Chem.*, 2007, **79**, 3330–3341.

107 M. Nothaft, S. Höhla, F. Jelezko, N. Frühauf, J. Pflaum and J. Wrachtrup, *Nat. Commun.*, 2012, **3**, 628.

108 O. Schwartz, J. M. Levitt, R. Tenne, S. Itzhakov, Z. Deutsch and D. Oron, *Nano Lett.*, 2013, **13**, 5832–5836.

109 D. Gatto Monticone, K. Katamadze, P. Traina, E. Moreva, J. Forneris, I. Ruo-Berchera, P. Olivero, I. P. Degiovanni, G. Brida and M. Genovese, *Phys. Rev. Lett.*, 2014, **113**, 143602.

110 P. Schwille, S. Kummer, A. A. Heikal, W. E. Moerner and W. W. Webb, *PNAS*, 2000, **97**, 151–156.

111 E. L. Elson, *Biophys. J.*, 2011, **101**, 2855–2870.

112 P.-O. Gendron, F. Avaltroni and K. J. Wilkinson, *J. Fluoresc.*, 2008, **18**, 1093–1101.

113 U. Meseth, T. Wohland, R. Rigler and H. Vogel, *Biophys. J.*, 1999, **76**, 1619–1631.

114 J. Ries and P. Schwille, *Bioessays*, 2012, **34**, 361–368.

115 O. Krichevsky and G. Bonnet, *Rep. Prog. Phys.*, 2002, **65**, 251–297.

116 J. Widengren, R. Rigler and Ü. Mets, *J. Fluoresc.*, 1994, **4**, 255–258.

117 C. Ringemann, A. Schönle, A. Giske, C. von Middendorff, S. W. Hell and C. Eggeling, *ChemPhysChem*, 2008, **9**, 612–624.

118 S. Rüttinger, P. Kapusta, M. Patting, M. Wahl and R. Macdonald, *J. Fluoresc.*, 2010, **20**, 105–114.

119 J. Widengren and C. A. M. Seidel, *PCCP*, 2000, **2**, 3435–3441.

120 C. Eggeling, J. Widengren, R. Rigler and C. A. M. Seidel, *Anal. Chem.*, 1998, **70**, 2651–2659.

121 S. R. Aragón and R. Pecora, *Biopolymers*, 1975, **14**, 119–137.

122 M. Eigen and R. Rigler, *PNAS*, 1994, **91**, 5740–5747.

123 T. Wohland, R. Rigler and H. Vogel, *Biophys. J.*, 2001, **80**, 2987–2999.

124 B. Hinkeldey, A. Schmitt and G. Jung, *ChemPhysChem*, 2008, **9**, 2019–2027.

125 S. Veettil, N. Budisa and G. Jung, *Biophys. Chem.*, 2008, **136**, 38–43.

126 A. M. Huynh, J. Menges, M. Vester, T. Dier, V. Huch, D. A. Volmer and G. Jung, *ChemPhysChem*, 2016, **17**, 433–442.

127 W.-T. Yip, D. Hu, J. Yu, D. A. Vanden Bout and P. F. Barbara, *J. Phys. Chem. A*, 1998, **102**, 7564–7575.

128 J. Widengren and R. Rigler, *Bioimaging*, 1996, **4**, 149–157.

129 C. G. Hübner, A. Renn, I. Renge and U. P. Wild, *J. Chem. Phys.*, 2001, **115**, 9619–9622.

130 J. Widengren, B. Terry and R. Rigler, *Chem. Phys.*, 1999, **249**, 259–271.

131 E. Brooks Shera, N. K. Seitzinger, L. M. Davis, R. A. Keller and S. A. Soper, *Chem. Phys. Lett.*, 1990, **174**, 553–557.

132 S. Nie, D. T. Chiu and R. N. Zare, *Science*, 1994, **266**, 1018–1021.

133 W. P. Ambrose, P. M. Goodwin and J. P. Nolan, *Cytometry*, 1999, **36**, 224–231.

134 W. P. Ambrose, P. M. Goodwin, J. Enderlein, D. J. Semin, J. C. Martin and R. A. Keller, *Chem. Phys. Lett.*, 1997, **269**, 365–370.

135 P. C. Beaumont, D. G. Johnson and B. J. Parsons, *J. Chem. Soc. Faraday Trans.*, 1993, **89**, 4185–4191.

136 N. I. Shank, K. J. Zanotti, F. Lanni, P. B. Berget and B. A. Armitage, *JACS*, 2009, **131**, 12960–12969.

137 G. Y. Mitronova, V. N. Belov, M. L. Bossi, C. A. Wurm, L. Meyer, R. Medda, G. Moneron, S. Bretschneider, C. Eggeling, S. Jakobs and S. W. Hell, *Chem. Eur. J.*, 2010,

16, 4477–4488.

138 C. Reichhardt, *Solvents and Solvent Effects in Organic Chemistry*, VCH Verlagsgesellschaft, 2nd edn., 1988.

139 J. A. Veerman, M. F. Garcia-Parajo, L. Kuipers and N. F. van Hulst, *Phys. Rev. Lett.*, 1999, **83**, 2155–2158.

140 P. Tamarat, A. Maali, B. Lounis and M. Orrit, *J. Phys. Chem. A*, 2000, **104**, 1–16.

8. Abkürzungsverzeichnis

<C>	mittlere Konzentration
<N>	mittlere Teilchenzahl
ΔpK_s	Änderung der pK_s Werte durch optische Anregung
^1L_a	Zustand der durch Anregung mit Licht erreicht wird, das parallel zur Längsachse des Pyrens polarisiert ist
^1L_b	Zustand der durch Anregung mit Licht erreicht wird, das quer zur Längsachse des Pyrens polarisiert ist
1N	1-Naphthol
2CP	2-Cyanophenol
2N	2-Naphthol
5,8DCN2	5,8-Dicyano-2-naphthol
5CN2	5-Cyano-2-naphthol
ATP	Adenosintriphosphat
d.h.	das heißt
$D_{DMSO}(H^+)$	Diffusionskoeffizient des Protons in DMSO
$D_{H2O}(H^+)$	Diffusionskoeffizient des Protons in Wasser
DMSO	Dimethylsulfoxid
Du	Dunkelzustand
e.g.	exempli gratia, zum Beispiel
Engl.	Englisch
ESPT	Protonentransfer aus dem angeregten Zustand, Engl. Excited State Proton Transfer
FCS	Fluoreszenzkorrelationsspektroskopie, Engl. Fluorescence Correlation Spectroscopy
FITC	Fluoreszeinisothiocyanat
FRET	Förster-Resonanz-Energie-Transfer
fs	Femtosekunde
FSIP	Engl., Fully-Separated Ion-Pair
$g^{(2)}$	Korrelationsfunktion 2. Ordnung
$g^{(2)}_{AB}$	Antibunching-Zerfall von $g^{(2)}$
$g^{(2)}_{bl}$	Einfluss des Photobleichens auf $g^{(2)}$
$g^{(2)}_{diff}$	Diffusionsteil der $g^{(2)}$ Funktion
$g^{(2)}_{Du}$	Bunching-Zerfall von $g^{(2)}$

$g^{(2)}_{rot}$	Rotationszerfall von $g^{(2)}$
Glg.	Gleichung
HBIP	Engl., Hydrogen-Bonded Ion-Pair
HPTA	8-Hydroxypyren-1,3,6-Trisulfonamid
HPTS	8-Hydroxypyren-1,3,6-Trisulfonat
i.e.	id est, das heißt
I_{exc}	Anregungsintensität
k_{bl}	Ratenkonstante des Photobleichens
k_{blS}	Ratenkonstante des Photobleichens aus einem Singulettzustand
k_{blT}	Ratenkonstante des Photobleichens aus einem Triplettzustand
$k_{c/-c}$	Ratenkonstante einer chemischen Hin- / Rückreaktion
k_d	Ratenkonstante des diffusionskontrollierten Zerfalls des SSIP im ersten angeregten Zustand
$k_{Du/-Du}$	Ratenkonstante in / aus dem Dunkelzustand
k_{espt}	Ratenkonstante des Protonentransfers aus dem ersten angeregten Zustand
k_{exc}	Anregungsratenkonstante
k_f	Fluoreszenzratenkonstante der Basenspezies, des FSIP und des SSIP
$k_{f,ROH}$	Fluoreszenzratenkonstante der Säurespezies
k_{gr}	Ratenkonstante der geminanten Rekombination
k_{isc}	Interkombinationsratenkonstante
$k_{p/-p}$	Ratenkonstante der diffusionskontrollierten Reprotonierung / Deprotonierung
k_q	Ratenkonstante der unimolekularen Reprotonierung innerhalb des SSIP
k_{risc}	Ratenkonstante, mit der das Triplettniveau entleert wird
K_s	Säurestärke im Grundzustand
K_s^*	Säurestärke im ersten angeregten Zustand
nm	Nanometer
ns	Nanosekunde
P	Phenol
ps	Pikosekunde
R6G	Rhodamin 6G
RO^-	Säure in deprotonierter Form
ROH	Säure in protonierter From
S / HS^+	Solvensmolekül / protoniertes Solvensmolekül
s.g.	sogenannt

S_0	elektronischer Grundzustand
S_1	erster angeregter elektronischer Zustand
SSIP	Engl., Solvent-Separated Ion Pair
T_1	erstes Triplettniveau
TCSPC	zeitkorreliertes Einzelphotonenzählen, Engl. Time-Correlated Single Photon Counting
TFA	Trifluoressigsäure, Engl. Trifluoroacedic acid
u.a.	unter anderem
V_{eff}	konfokales Volumen
vgl.	vergleiche
z_0	Rayleigh-Länge
σ	Hammet-Koeffizient
ω_0	minimaler Strahlradius, Abfall der Laserintensität auf $1/e^2$
B / HB^+	Akzeptormolekül / protoniertes Akzeptormolekül
τ	Korrelationszeit
τ_{AB}	Zeitkonstante des Antibunchings
τ_B	Zeitkonstante des Bunchings
τ_{diff}	Diffusionsdauer
τ_f	Fluoreszenzlebensdauer
τ_{rot}	Rotationszeit

9. Abbildungsverzeichnis

10. Auflistung aller wissenschaftlichen Beiträge

10.1 Publikationen in internationalen Fachzeitschriften

- B. Finkler, C. Spies, M. Vester, F. Walte, K. Omlor, I. Riemann, M. Zimmer, F. Stracke, M. Gerhards und G. Jung, „Highly Photostable „Super"-Photoacids for Ultrasensitive Fluorescence Spectroscopy", *Photochem. Photobiol. Sci.*, 2014, **13**, 548–562.
- M. Vester, T. Staut, J. Enderlein und G. Jung, „Photon Antibunching in a Cyclic Chemical Reaction Scheme", *J. Phys. Chem. Lett.*, 2015, **6**, 1149–1154.
- M. Vester, A. Grüter, B. Finkler, R. Becker und G. Jung, „Biexponential Photon Antibunching: Recombination Kinetics within the Förster-Cycle in DMSO", *PCCP*, 2016, Accepted Manuscript.
- A.-M. Huynh, J. Menges, M. Vester, T. Dier, V. Huch, D. A. Volmer und Gregor Jung, „Monofluorination and Trifluoromethylation of BODIPY Dyes for Prolonged Single-Molecule Detection", *ChemPhysChem*, 2016, **17**, 433-442.

10.2 Konferenzbeiträge: Vorträge

- Vester, M., Jung, G., Proton Transfer Kinetics from Photon Antibunching, *Methods and Applications of Fluorescence*, **2015**.
- Vester, M., Jung., G., Chemically Expanded Antibunching, *Tagung der Deutschen Bunsen-Gesellschaft für Physikalische Chemie*, **2014**.

10.3 Konferenzbeiträge: Poster

- Vester, M., Finkler, B., Jung, G., Single Molecule Spectroscopy on Proton Transfer, *Picoquant Single Molecule Workshop*, **2014**.
- Vester, M., Finkler, B., Jung, G., Modern Optics with Pyrene-based Photoacids", *Methods and Applications of Fluorescence*, **2013**.
- Vester, M., Finkler, B., Jung, G., Quantum Optics with Photoacids, *Tagung der Deutschen Bunsen-Gesellschaft für Physikalische Chemie*, **2013**.
- Vester, M., Finkler, B., Jung, G., Quantum Optics and Photochemistry, *Gesellschaft Deutscher Chemiker, Fachgruppe Photochemie*, **2012**.

10.4 Bachelorthesen

- Melissa Teubner:
  „Untersuchung von Photosäuren auf Pyrenbasis im Doppelresonanzexperiment“
- Alexander Pelz:
  „Stabilitätsuntersuchungen von siRNA-Nanoplexen mit Fluoreszenzmethoden“
- Alexander Grandjean:
  „Fluoreszenzspektroskopische Charakterisierung von Photosäure-Cyclodextrin Komplexen“
- Robert Becker:
  „Spektroskopische Analyse von Pyrenderivaten in aprotischem Solvens“